

University of Oxford
Department of Materials

Quantitative Studies of Gas Porosity in Cast Aluminium & the Determination of Melt Quality

Julian L. Malisano
St Catherine's College

A thesis submitted for the degree of Doctor of Philosophy in Materials

Trinity 2018

Abstract

Quantitative Studies of Gas Porosity in Cast Aluminium & the Determination of Melt Quality

Julian L. Malisano
St Catherine's College

DPhil Thesis
Trinity 2018

Gas porosity is one of the major defects that forms during solidification in cast aluminium alloys. Hydrogen, oxide films, and TiB_2 based grain refiner are all known to play a role in the formation of gas porosity, however their individual influences are not fully understood, necessitating further investigation.

In this work, metallography and low resolution X-Ray Computed Tomography (XCT), i.e. *macro-CT*, have been employed to study the effects of hydrogen, oxide films, and TiB_2 grain refiner on the structure of porosity formed in Al-7Si samples that were cast using the Reduced Pressure Test (RPT). Porosity in the centres of castings that were solidified under atmospheric pressure is also examined using high resolution XCT, i.e. *micro-CT*.

The studies of the structure of the porosity provided insight into the respective effects that the aforementioned factors play in the nucleation and growth of bubbles in the material during solidification. The results suggested that hydrogen provides the impetus for gas porosity formation, and the fuel for the expansion of the nucleated bubbles, while oxide films, and TiB_2 grain refiner particles - probably TiB_2 clusters - act as bubble nuclei, and provide a means for the hydrogen to come out of solution and form the bubble. The higher the oxide film content of a melt, the greater the fraction of hydrogen that may be released from solution. Another finding was that Premetz and PoDFA analysis proved unreliable for measuring the oxide film content of a melt; it was concluded that this due to their insensitivity to small oxide films. SEM microanalysis or the use of the RPT are therefore needed in order to measure melt oxide film content.

The results provided new insight into the RPT and how it may be used as a measure of melt quality. In line with the current wisdom, the volume fraction of porosity was shown to indicate the combined hydrogen and oxide film content of the melt, while the pore number density was shown to be indicative of the oxide film content in the material.

To Guglielmo and Maria Malisano,
who showed me anything is possible.

Preface

Personal Acknowledgements

I extend my deepest thanks to those closest to me, to my parents and to my grandparents, who, though giving me every opportunity in life, have ultimately made this possible. To Carla, who has enabled me to endure, and to her family, who have taken me in as one of their own.

Next, I thank those who have guided me through this academic gauntlet. First and foremost I thank my supervisor Prof Keyna O'Reilly, and my industrial mentor, Mr Phil Enright of N-Tec ltd. Next I thank Dr Kumar Sundaram, and Mr Ian Hughes and Mr Simon Pepperell at N-Tec Ltd, my industrial mentors in this project, who have helped me with so much, and have been an endless source of practical foundry-wisdom. I also would like to thank Dr Paul Evans at TSC for providing us with access to Premetz for this work.

Next, I thank Dr Andrew Lui for performing the macro-CT scans, which have proved so important for this work. I thank Mr Trevor Knibbs, Mr Robin Vincent, and Mr Gideon Ring, the behind-the-scenes technicians who have helped put together the various bits and bobs required for the experimental work, and often as last minute requests.

Finally, I thank my friends. To those from my undergraduate studies, thank you for helping me reach great heights. To my friends here in Oxford, thank you for making this a truly memorable experience.

Conferences

Oral Presentations at the *National Student Conference in Metallic Materials* (NSCiMM) 2016 & 2017, held in Sheffield, United Kingdom. Awarded the *Best Presentation* at the 2016 edition.

Attended *Tomography for Scientific Advancement* (ToSCA) 2016, held in Bath, United Kingdom.

Poster Presentation at *SP 17: 6th Decennial International Conference on Solidification Processing*, held in Old Windsor, United Kingdom. The presented work was published in the conference proceedings [1].

Funding Acknowledgements

The North Star Imaging (NSI) ImigiX instrument used for macro-CT imaging was supported by the EPSRC grant EP/J013501/1.

The Zeiss Xradia 510 Versa instrument used for micro-CT imaging, and the FEI Avizo software package that was used to process and segment the macro-CT and micro-CT data were supported by the EPSRC grant EP/M02833X/1.

Contents

Part I Background 1

Chapter 1 Introduction 1

1.1 Background 1

1.2 Thesis Overview 2

Chapter 2 Gas Porosity in Cast Aluminium 5

2.1 Melt Quality 5

2.2 The Driving Forces for Porosity Formation 6

2.3 Hydrogen in Aluminium 11

2.4 Mechanisms of Porosity Formation 18

2.5 Oxide Films 25

2.6 The Reduced Pressure Test 36

2.7 Melt Quality Control 40

2.8 Grain Refiner's Effect on Porosity 42

Chapter 3 Quantitative Porosity Assessment & X-Ray Computed Tomography 43

3.1 A Brief Overview of Metallographic Analysis 43

3.2 Limitations of 2D Analyses 44

3.3 Overview of X-Ray CT 46

3.4 Fundamental Principles of X-Ray CT 47

3.5 Studies of Oxides Films & Bifilms 53

3.6 Quantitative Digital Image Analysis for X-Ray CT 54

Part II Materials & Methods 64

Chapter 4 Foundry & General Characterisation Methods 65

4.1 Materials & Melt Preparation 65

4.2 Measurement of Melt Hydrogen Content 68

4.3 Melt Cleanliness Measurement & Oxide Characterisation 68
4.4 The Reduced Pressure Test 71
4.5 Melt Quality Experimental Procedures 76
4.6 Grain Refiner Addition Experimental Procedures 84
Chapter 5 Porosity Characterisation Methods 88
5.1 Porosity Analysis by Metallography 89
5.2 Porosity Analysis using Macro-CT 97
5.3 Porosity Analysis using Micro-CT 108
Chapter 6 Evaluation of Porosity Characterisation Methods 115
6.1 Metallographic Analysis of Porosity 115
6.2 Porosity Analysis by Macro-CT 120
6.3 Metallography vs Macro-CT 131
6.4 Evaluation of Macro-CT using Micro-CT 142
6.5 Micro-CT Analysis of Porosity 154
Part III Main Results 155
Chapter 7 Melt Quality Experiments 156
7.1 Summary of Experiments & Melt Compositions 156
7.2 Melt Quality Change in Response to Melt Treatments 157
7.3 Melt Cleanliness Change in Response to Melt Treatments 163
7.4 Sample Classification 177
7.5 Volume Fraction of Porosity 180
7.6 Changes in Pore Structure with Hydrogen Content 181
7.7 Comparative Analysis of Porosity in Clean & Dirty Metal 191
7.8 Meta-Analysis of the Porosity in the RPT Samples 203
7.9 Micro-CT Analysis of Porosity in APT Samples 215
7.10 Summary of Results 217
Chapter 8 Grain Refiner Addition Experiments 218

8.1 Summary of Experiments & Melt Compositions 218
8.2 Melt Grain Refiner & Inclusion Population Assessment 219
8.3 Change in Grain Structure 230
8.4 Volume Fraction of Porosity 232
8.5 Changes in the Structure of Pores 236
8.6 Micro-CT Analysis of Atmospheric Porosity 246
8.7 Summary of Results 248

Part IV Discussion 249

Chapter 9 The Effect of Melt Quality on Porosity Formation 250

9.1 The Efficacy of the Melt Treatments in Manipulating Melt Quality 250
9.2 Complexities in the Assessment of Oxide Films 255
9.3 Oxide Film Morphology 260
9.4 Melt Quality & the Formation of Porosity during the RPT 261
9.5 Effects of Hydrogen & Oxide Films on the Structure of Pores 264
9.6 Melt Quality & the Formation of Porosity under Atmospheric Pressure 266
9.7 Pore Formation in the Dross Layer 268
9.8 Determination of Melt Quality Using the RPT 269

Chapter 10 Effect of Grain Refiner on Porosity Formation 272

10.1 Effect of Grain Refiner Addition on Grain Structure 272
10.2 Origins of Endogenous Borides & their Effect on Porosity 274
10.3 The Role of TiB_2 on Gas Porosity Formation 277

Part V Conclusions 281

Chapter 11 Conclusions & Future Work 282

11.1 Conclusions 282
11.2 Recommendations of Future Work 285

Reference List 289

Appendicies

Contents....1

Appendix I **Supplementary Background Information**....2

I.1 Summary of Hydrogen Measurement Techniques....2

I.1.1 Bubble Formation Techniques....2

I.1.2 Direct Measurement Techniques....3

I.1.3 Gas Recirculation Techniques....3

I.1.4 Electrochemical Techniques....4

I.2 Inclusion Assessment using LiMCA....5

Appendix II **Supplementary Material on the Materials & Methods**....6

II.1 Hydrogen Analysis using LECO....6

II.1.1 Procedure....6

II.1.2 Comparison of AlScan and LECO....7

II.2 Volume Fraction of Porosity Uncertainty Analysis....9

II.2.1 Sources of Uncertainty....9

II.2.2 Maximum Variation....10

II.3 Supplementary Material to the Porosity Characterisation Methods....12

Appendix III **Supplementary Material for Part III**....20

III.1 Experiment DMX....20

III.1.1 Procedure....20

III.1.2 Results....21

III.1.3 Discussion on the Effect of Upgassing on Melt Cleanliness....26

III.2 SEM Analysis of the 'Particle Cluster' Inclusions Present in CM1....28

III.3 Additional Metallographic Measurements....30

III.3.1 Melt Quality Experiments....30

III.3.2 Grain Refiner Addition Experiments 33

III.4 Grain Refiner Addition Studies: Solidification Curves 36

Appendix IV **Ancillary Experimental Work RPT Porosity Retention Experiments** 38

IV.1.1 Experimental Procedures 40

IV.1.2 Melt Compositions 43

IV.1.3 RPT Duration & Retained Porosity 44

IV.1.4 Temperature-Time Solidification Curves 47

IV.1.5 Solid Fraction Calculations 48

IV.1.6 Ancillary Studies using an Al-3Si Alloy 49

IV.1.7 Metallographic Analysis 51

IV.1.8 Discussion 59

References In The Appendices 66

Part I
Background

Chapter 1

Introduction

1.1 Background

In 1888 mankind's view of aluminium would change forever with the inception of the commercial Hall-Heroult electrochemical smelting process, which made the production of metallic aluminium viable on an industrial scale [2]. Aluminium would no longer be viewed as a precious metal, but instead a relatively inexpensive commodity that could be used to produce a wide range of engineering components for use in nearly any industry.

Today there is great emphasis on the control of *metal quality*, which generally refers to the number of defects inside the material and directly governs the overall quality of the products produced from it [3], [4]. Many critical defects arise from the liquid metal, known as the *melt*, and carry through into the metal when it is cast. This has therefore put great emphasis on the control of *melt quality* to avoid defects in the cast metal. This is done by subjecting the molten metal to a number of treatments to remove impurities, hydrogen, and inclusions prior to casting (**Figure 1.1**) [4], [5].

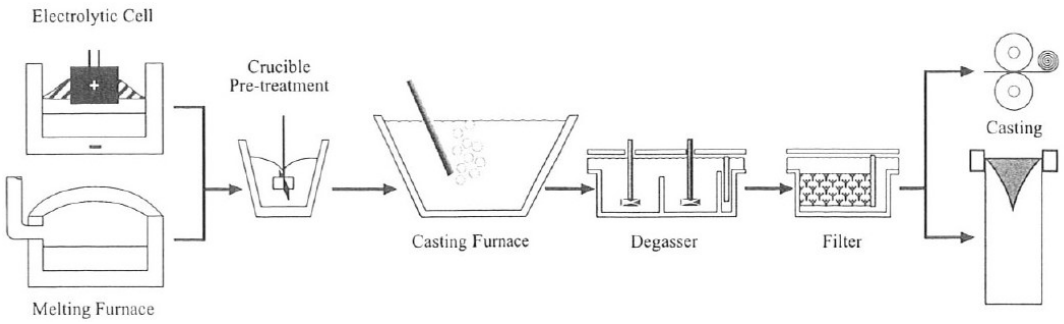

Figure 1.1 A typical sequence of melt processing steps prior to casting. From Waite [5].

One particularly detrimental defect is *gas porosity*. It is known that that the dissolved hydrogen content and number of inclusions – solids present in the melt above its liquidus – are the impetus for gas porosity, though the mechanisms by which they act are not well understood.

There is a growing body of evidence from the last two decades that has very strongly implicated oxide film inclusions, particularly bifilm inclusions, with gas porosity [6]–[11]. Such inclusions form naturally on the surface of the melt, but are entrained into the metal during processing and pouring [3]. However, there is still much that is not well understood – for example, the exact roles that melt hydrogen and oxide content respectively play in forming gas porosity. What is more, the effect of other variables, such as the effect of grain refiner on the structure of porosity, are currently not well understood.

1.2 Thesis Overview

This work aims to elucidate the respective roles of **hydrogen**, **oxide films**, and **grain refiner** on the formation of gas porosity during the solidification of aluminium casting alloys. This will be approached by investigating the structure of pores, that is, their overall fraction, number, size, and shape, using metallographic analysis and X-ray Computed Tomography (X-Ray CT or XCT). The Reduced Pressure Test (RPT) will be the primary mode used to produce high-porosity castings, on which most of the analyses will be conducted.

1.2.1 Project Scope

Given that there are a wide range of potential inclusions that may be found in aluminium, it is necessary to restrict the oxide aspect of scope of this work solely to endogenous oxide films that form in unmodified binary Al-Si alloys – namely Al_2O_3. This

therefore puts species of endogenous oxides such as $MgAl_2O_4$ spinel, MgO, or SrO, that can form endogenously in the presence of magnesium or strontium solute, out of the scope of this work.

There are also a wide range of grain-refiners available on the commercial market, which necessitates that this aspect of the research be restricted to TiB_2 based grain refiners, the most common type in today's commercial market.

1.2.2 Thesis Outline

This project can broadly be broken down into three main areas of work (**Figure 1.2**). The first area is that concerning the development of the Digital Image Analysis (DIA) methodologies used for the quantitative assessment of the structure of pores from metallographic and XCT images in the subsequent experimental work.

The other two areas of work are the experimental phases. The first experimental phase investigates the individual roles of melt hydrogen and oxide film contents, key

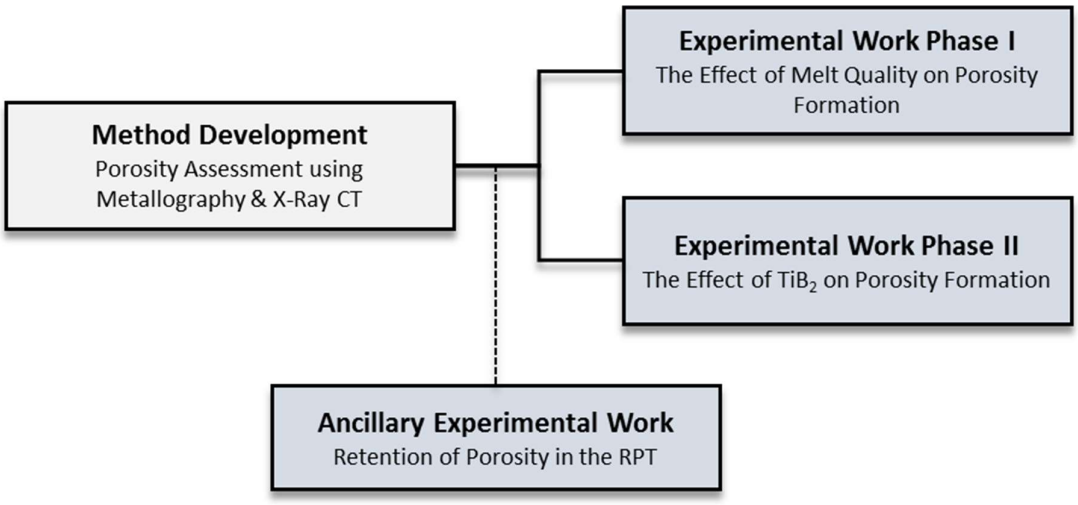

Figure 1.2 The main areas of work presented in this thesis.

constituents of the overall *melt quality*, on the formation and structure of gas porosity. The

second phase of experimental work investigates the effect of TiB_2 grain refiner on the formation and structure of gas porosity.

Ancillary experimental work was also conducted to investigate the dependency of the RPT on the solidification characteristics of experimental alloy. This proved critical in selecting appropriate parameters to ensure consistency when using the RPT in the subsequent phases of experimental work. This is not presented in the body of the thesis, but the Appendix.

Chapter 2

Gas Porosity in Cast Aluminium

Gas porosity is one of the major defects that forms in aluminium during casting. It is particularly problematic in cast alloys because they are often used in their near as-cast state, thus any porosity formed within them will remain. The presence of gas pores inside cast components can cause blistering when they are finished by heat treatment [12], which necessitates their scrapping. In cyclically loaded components used in service, the presence of porosity significantly decreases the fatigue properties [13]–[16]. Inspection of castings for gas pores therefore plays an integral role for quality control in the casthouse.

2.1 Melt Quality

Melt quality is the term that is loosely used to describe the ability of a melt to produce a quality, defect free product. There are three main criteria, to which the melt quality is inversely proportional [3]–[5], [17]:

- the dissolved gas content,
- the inclusion content, and
- compositional impurity content, namely that of alkalis or iron impurities [18].

Dissolved gas, hydrogen, and oxide film inclusions, are two very pertinent aspects of melt quality that come together to act concomitantly to form gas pores; though oxide films entrained inside the metal are a deleterious defect on their own as they act as stress raisers which deteriorate the mechanical properties of the cast component [7], [19].

2.2 The Driving Forces for Porosity Formation

In order to set the context for the coming sections, some background on the driving forces behind the porosity will be given here.

The porosity that is formed during solidification in cast aluminium is driven by two collaborative forces: (1) *hydrogen partitioning*, and (2) *shrinkage* [20]. As shown in **Figure 2.1**, depending on the degree to which each acts, pores will take on a specific morphology, and can broadly be classified accordingly. *Gas porosity*, which is driven primarily by dissolved hydrogen, forms nearly spherical pores, while *shrinkage porosity*, which as the name suggests, is driven primarily by the shrinkage mechanism, forms interdendritic pores that are complex in shape. In practice, binary classification of pores is often not so straightforward, as pores tend to be a combination of both, due to the collaborative action of the two mechanisms.

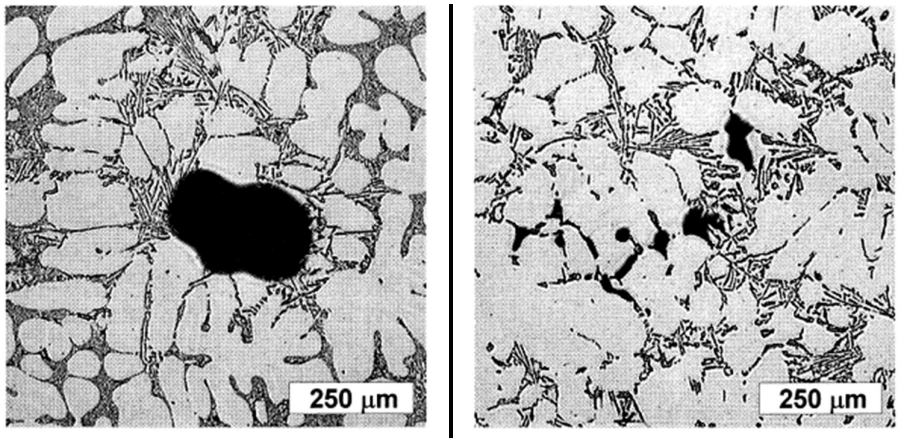

Figure 2.1 Typical examples of a) a gas pore, and b) a network of shrinkage pores in cast A356 alloy. It is important to note that the complex 3D structure of pores, especially shrinkage pores, is poorly represented in 2D slices as they are generally highly interconnected in 3D. Images from Anson et al. [20].

2.2.1 Hydrogen Partitioning & Melt Supersaturation

Hydrogen is the only gas that is soluble in aluminium to any appreciable extent and acts as the primary impetus for gas porosity formation during the solidification of aluminium alloys. As **Figure 2.2** a) illustrates, this is because its solubility decreases significantly between the solid and liquid [3], [21]. In pure aluminium this is a factor of 20 [3] decreasing from a limit of 0.69 ml $100g^{-1}$ to 0.036 ml $100g^{-1}$ at the melting point (660°C and a hydrogen pressure of 1 atm) [21], [22], which results in the segregation and build-up of hydrogen in the liquid ahead of the growing solid [23], [24], as shown in **Figure 2.2** b) and **Figure 2.3**.

Hydrogen build-up, combined with the concomitant decrease in the local solubility due to decreasing melt temperature, enrichment of the solid-liquid interface with various solute elements, such as Si or Cu [25], and the pressure drop due to shrinkage, induces hydrogen supersaturation in the liquid (**Figure 2.2** b)), which provides the impetus for

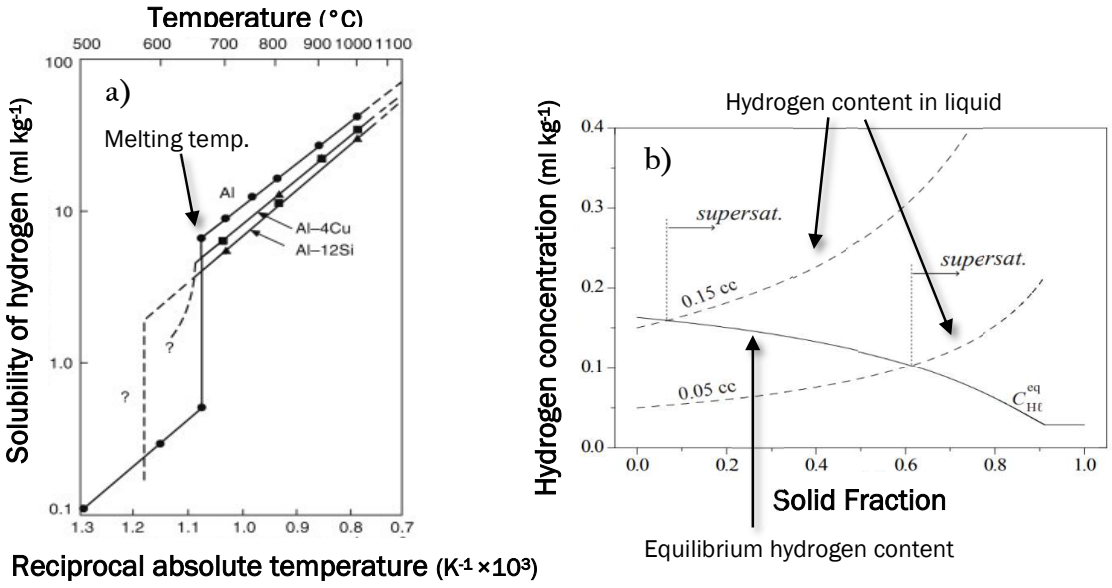

Figure 2.2 a) Hydrogen solubility in pure aluminium, Al-4Cu, and Al-12Si as a function of temperature. Adapted from Campbell [3]. b) Supersaturation of hydrogen in an Al-4.5wt%Cu alloy as a function of solid volume fraction for two differnet initial hydrogen levels (0.05 and 0.15 cc $100g^{-1}$ (ml $100g^{-}$)). Adapted from Felberbaum [24].

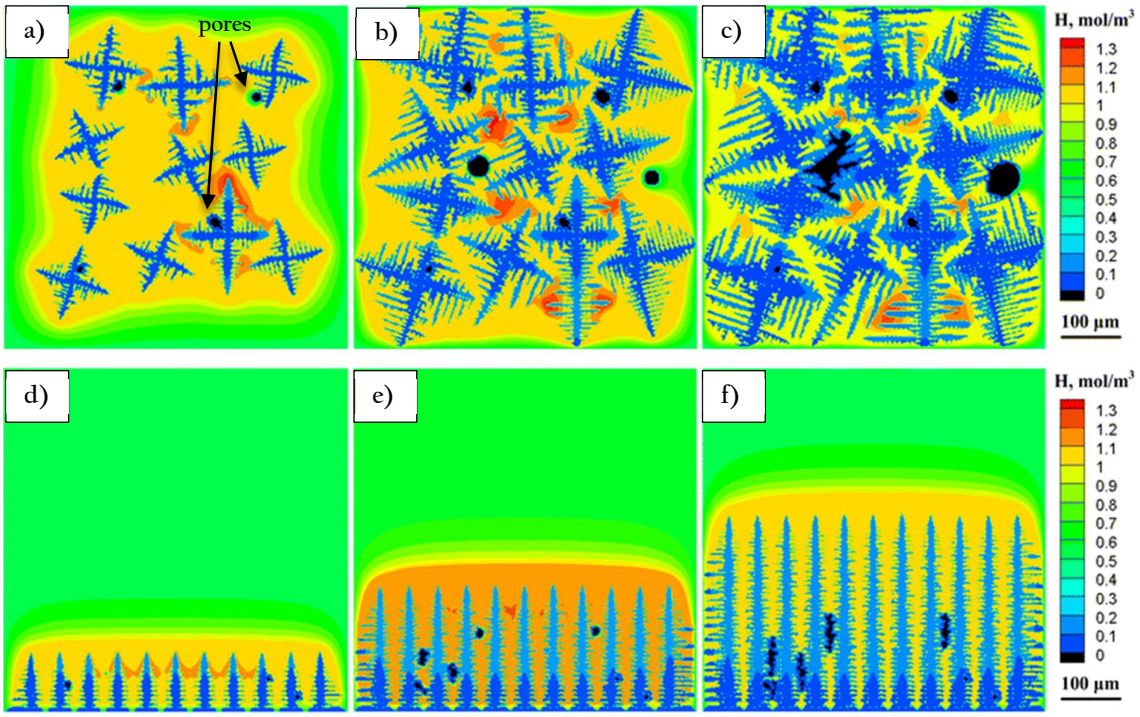

Figure 2.3 Simulation of the partitioning and build-up of hydrogen in an Al-4wt%Cu alloy during a) - c) equiaxed dendritic growth, and d) – f) columnar dendritic growth. Adapted from Gu et al. [23].

hydrogen to come out of solution and form gas pores. Increasing levels of hydrogen in the melt increase the contribution of this mechanism during the formation of porosity.

When the driving force of hydrogen dominates, pores tend to be spherical in shape. This is because they form in the liquid as a bubble. At increasing hydrogen levels, pores become increasingly spherical in shape as they form at low solid fractions, and are consequently less impinged on by the solid microstructure during their growth [20]. Conversely, when the hydrogen level is low, pores will develop the shape of the surrounding solid microstructure – and the shrinkage mechanism plays an increasingly important role in their influencing pore shape. Hence, the shape of gas pores can be used as an indication of what stage they formed at during solidification [3].

2.2.2 Solidification Shrinkage

The second key impetus that drives gas porosity formation is shrinkage, which assists the formation of gas pores by inducing a pressure drop in the liquid inside the semi-solid material. This occurs due to contraction caused by the density increase during the liquid to solid transformation, and restricted liquid metal feeding to the free volume that this creates [3].

Pure aluminium shrinks approximately 7.14% during freezing [69], although this is generally less for casting alloys as they are formulated to reduce this effect. For example, the volumetric expansion of β-Si which is formed in most Si-containing casting alloys results in a reduction of the overall shrinkage of the alloy. Eutectic Al-12.6Si alloys shrink only 4.4% [71], and an Al-7Si alloy – the type of alloy used in this work – shrinks ~5.77% as it solidifies with approximately 50% eutectic.

The resulting pressure drop varies from region to region in the casting and ultimately depends on the permeability of the dendritic structure and the ability of the liquid to feed the free voids created by the shrinkage [26], [27].

A number of authors have arrived at different conclusions about the exact magnitude of the pressure drop that occurs in the liquid of the mushy zone, which varies strongly with the solidification mode (directional or equiaxed) and the alloy. It has been estimated to range from less than ~0.75 kPa (0.008 atm) [26] to ~200kPa (~2 atm) [28]. However, it depends not only on the alloy, but also the solidification mode (equiaxed or columnar) and the cooling rate, due to their influence on liquid feeding to the solidifying regions [29].

The presence of eutectic solidification in casting alloys hugely reduces the degree of the pressure drop compared to wider freezing range alloys [3]. This is because

interdendritic liquid channels increase with increasing eutectic fraction (which is generally high in casting alloys), which increases liquid feeding. Hence the shrinkage mechanism is most significant in wide freezing range alloys that form a low fraction of eutectic.

2.3 Hydrogen in Aluminium

2.3.1 Absorption & Solubility

Hydrogen is the only elemental gas with an appreciable solubility in aluminium [21], [22], [30], [31]. It is absorbed into molten aluminium in order to attain thermodynamic equilibrium of the hydrogen partial pressure (P_{H_2}) with its surrounding environment [3],[21]. Absorption into solution occurs when P_{H_2} of the environment is larger than that of the melt –as is usually the case – and will come out of solution when the P_{H_2} in the melt is greater than that of the environment. This latter case is often referred to as *off-gassing*. The equilibrium concentration (in ml $100g^{-1}$) is described by Sievert's equation [3], [31], [32]:

$$S = \sqrt{k_{eq}}\sqrt{P_{H_2}} = C_{alloy}S_o\sqrt{P_{H_2}} \tag{2.1}$$

Where k_{eq} is the equilibrium constant, which is not actually a constant and depends on melt temperature and composition, and is therefore usually expressed as the product of C_{alloy}, the alloy correction factor, and S_o, the equilibrium concentration of hydrogen at 1 atm in pure aluminium. In pure aluminium S_o follows [33]:

$$\mathrm{Log}_{10}S_o = 2.726 - \frac{2692}{T} \tag{2.2}$$

Where *T* is the melt temperature in Kelvin. It should be noted that there are many slight variations in the constants that have been reported for this relationship [25],[34], though those given in Sigworth's equation in 2.2 are considered the most reliable. The strong temperature dependence of S_o on *T* is shown in **Figure 2.4**.

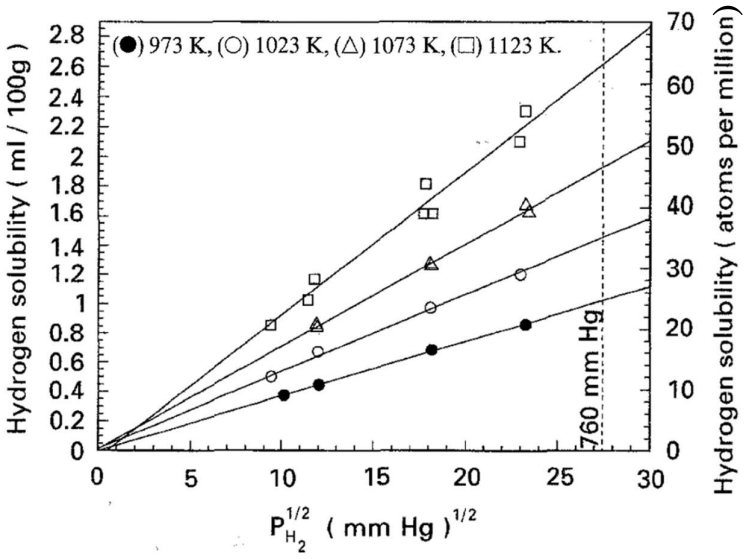

Figure 2.4 Solubility of hydrogen in pure aluminium versus square root of the hydrogen partial pressure for different temperatures. From Liu et al. [35]

The effect of the alloy composition on S is accounted for by C_{alloy}. As shown in **Figure 2.5**, some elements have the effect of increasing hydrogen's solubility while others have the effect of decreasing it. Anyalebechi [25] suggested the following relationship for multicomponent alloys:

$$\mathrm{Log}_{10} C_{alloy} = k_{Mg} W_{Mg} + k_{Cu} W_{Cu} + k_{Si} W_{Si} + k_{Zn} W_{Zn} \qquad (2.3)$$

Where k_x and W_x are the correction factor and weight percentage of element x in the alloy. There is a wide variability in the reported values of k_x for each element (a comparison for some common alloying elements is shown in **Table 2.1**), which can lead to significant differences in the calculated hydrogen solubility depending on which values are used. Interestingly, despite some solutes (Si and Cu) reducing the solubility in the liquid, modelling suggests that they may have the opposite effect in the solid and increase hydrogen's solubility [36].

Overall the effect of melt composition and C_{alloy} on hydrogen solubility is currently not well understood, especially in multicomponent alloys where the agreement between

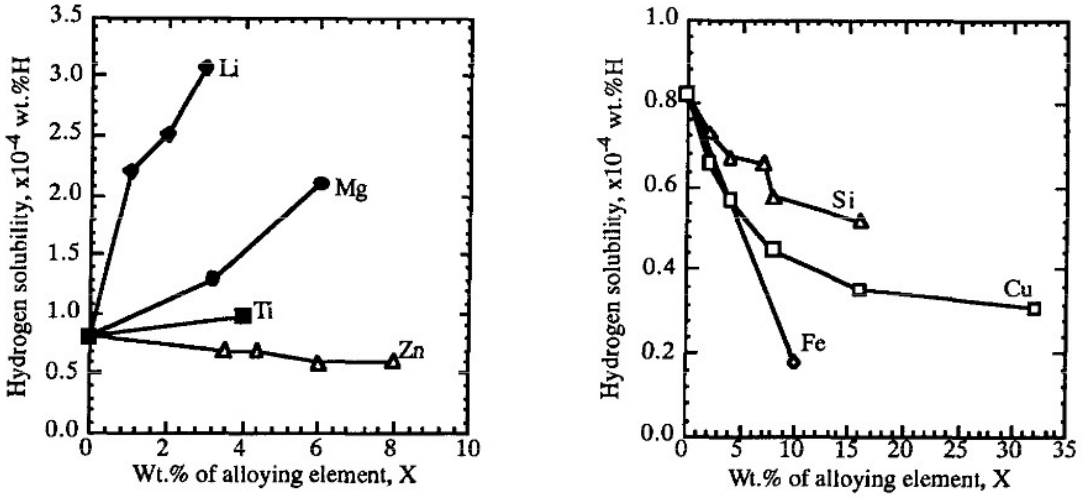

Figure 2.5 The individual effects of various elements on the solubility of hydrogen in molten aluminium. Source Anyalebechi [25].

Table 2.1 Correction factors for common alloying elements.

Element	Correction Factor (k_x)	
	Anyalebechi [25]	AlScan [34]
Mg	0.066	0.017
Si	-0.019	-0.0119
Cu	-0.033	0.0269

predicted values and empirically determined values is poor [36], [37]. Therefore calculated values of S in alloys should be taken as a guide, rather than a precise value.

2.3.2 Sources of Hydrogen

The major exogenous sources of hydrogen for molten aluminium during melt processing and casting are [3], [21]:

- atmospheric water vapour,
- damp charge materials and tools (which can also pose a severe safety hazard),
- moisture absorbed into refractory materials – such as crucibles, graphite rotors, and furnace linings,

- combustion-by-products of the combustion process in hydrocarbon fuelled furnaces, and
- paint, oil and cutting fluids, and other hydrogenous contaminants may constitute an additional source when using recycled scrap as the charge material [17].

Hydrogen already occluded inside the actual charge material itself can also constitute a major endogenous source for the melt.

Hence, in practice, it is not possible to fully eliminate hydrogen from the casting environment.

When molecular hydrogen, or more commonly, water or water vapour, contacts molten aluminium, it disassociates by the following endothermic reaction using energy supplied from the heat of the melt [21], [22]:

$$3H_2O(g) + 2Al(l) \rightarrow Al_2O_3(s) + 3H_2(g) \quad (2.4)$$

The change in the associated free energy is very high [21], giving the reaction a great drive to proceed. The free H_2 gas then disassociates to dissolve into solution [21]:

$$H_2 \rightarrow 2H \quad (2.5)$$

The omnipresent surface film of aluminium oxide (Al_2O_3) acts as a barrier to hydrogen at the surface of the melt and tends to impede absorption [21], [30] due to the low mobility of hydrogen as H^+ cations (protons) across it. There have been few studies that have investigated this, but one study (of an alumina membrane used to control the flux of hydrogen in chemical plants) suggested that it could be as low as 6.5×10^{-18} cm^2 s^{-1} in γ-alumina at room temperature [42]. Hydrogen therefore preferentially diffuses into the melt through cracks in the oxide which act as short circuit paths, or may dissolve directly into the melt from the atmosphere when the oxide skin is disturbed – such as by melt skimming, sampling, or turbulent pouring [43]. Hence, the uptake of hydrogen is not

straightforward to model or predict in real situations given it is controlled by kinetic limitations, namely the presence and staccato breakage of oxide. Warke et al. [38] showed using a rotary impeller, that the rate of hydrogen pickup was strongly dependent on the rate of film breakage.

2.3.3 Diffusion of Hydrogen in Aluminium

Diffusion of hydrogen in molten aluminium is rapid at $3.2 \times 10^{-7} m^2 s^{-1}$ at the melting point [39], [40]. This is so rapid that many models of porosity formation have simply tended to neglect diffusion all together and instead used the lever rule of hydrogen mass conservation to describe its build up in the solidifying material [41]. In contrast hydrogen diffusion in the solid is much slower, which results in the decreased mobility of hydrogen in solidifying, semi-solid alloys, which can be described by the effective diffusion coefficient **<*D*>** (**Figure 2.6**) [26], [40].

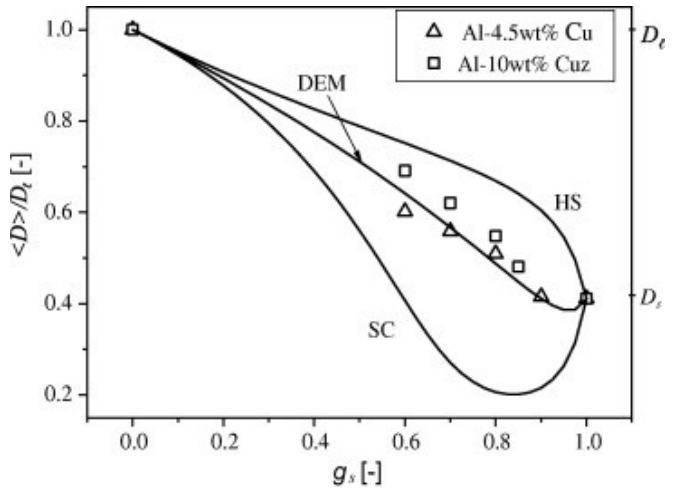

Figure 2.6 Effective hydrogen diffusion coefficient in a semi-solid material (<*D*>) as a function of the solid fraction (g_S) as a fraction of the liquid diffusion coefficient (D_l). It shows the comparison of the model developed by Felberbaum et al. [89] (DEM), compared with Maxwell-type (HS), and self-consistent (SC) approximations. From Felberbaum et al. [40].

2.3.4 Hydrogen Measurement using the AlScan

Monitoring of the hydrogen level is essential in ensuring that the melt quality kept is within specification, and if necessary, degassing treatments be applied.

There are several techniques for determining the hydrogen content of aluminium [42], however, the scope here will be restricted to the AlScan, which has been considered the reference technology for hydrogen measurement in industry for many years [5], [43]. Details of other common techniques have been given in Appendix I.1.

A schematic diagram of the AlScan is shown in **Figure 2.7** a). The device works by recirculating an inert carrier gas – usually nitrogen – through a porous probe that is submerged in the melt, and which is permeable to hydrogen but not to molten aluminium (**Figure 2.7** b)). Because the inert gas is devoid of hydrogen, hydrogen diffuses from the melt into the inert gas within, driven to attain equilibrium with it (as described in Section 2.3.1) [21], [34]. The reverse can also happen, with hydrogen in the gas dissolving back into the melt.

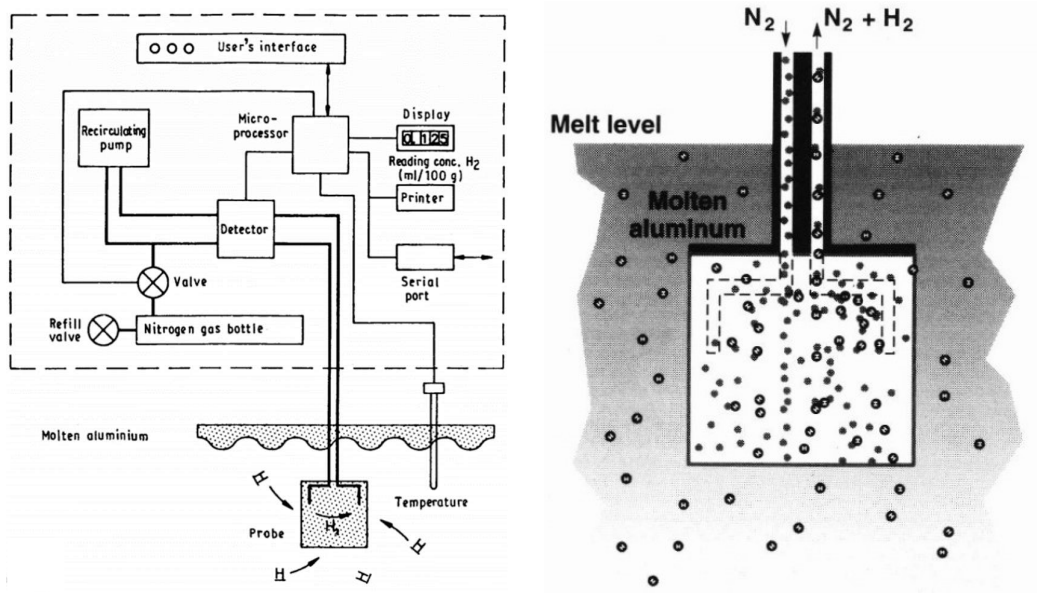

a) b)

Figure 2.7 Schematic diagram of a) the AlScan instrument, from Samuel et al. [44]; and b) an AlScan probe, showing the method of hydrogen pickup, Anyalebechi from [42].

Once in the carrier gas hydrogen exists as H_2, and a cathetometer located down the gas circuit measures the thermal conductivity of the gas, which is proportional to P_{H_2}. Using the P_{H_2} the concentration of hydrogen in the melt can be estimated by relating it to the equilibrium concentration in the instrument's gas circuit using a form of Sievert's equation [34]:

$$S = S_0 \, CF_T \, CF_A \sqrt{P_{H_2}} \tag{2.6}$$

Where S_0 is the baseline solubility, and is taken as a constant 0.92 ml $100g^{-1}$ at 700°C in pure aluminium. CF_T and CF_A are the temperature and alloy correction factors, which correct for variations in temperature from 700°C and variations in composition from pure Al, respectively. They are given as:

$$CF_T = \exp\left(\frac{6.531(T - 700)}{T + 273}\right) \tag{2.7}$$

$$CF_A = 10\text{^}(k_{Mg}W_{Mg} + k_{Cu}W_{Cu} + k_{Si}W_{Si}) \tag{2.8}$$

Where T in this case is given in °C, and k_x and W_x are respectively the correction factors (**Table 2.1**) and weight percentages of the alloying elements. Note only Mg, Cu, and Si are accounted for. Moreover, as mentioned above, those values do differ from that given in the literature, thus errors may increase with increasing alloy content. Thus it should be considered that the AlScan gives an estimate, rather than an exact value of the hydrogen content of alloys.

One of the major issues with older models of the AlScan is that the polymer gas pump components are susceptible to moisture absorption, which may contribute to erroneously higher values in the measured hydrogen level [45]. Anecdotal evidence has suggested that this issue is most pronounced in Mg containing alloys [46].

2.4 Mechanisms of Porosity Formation

Gas pores are the result of the entrapment of bubbles that formed in the metal above the solidus temperature during solidification. Recall from Section 2.2 that supersaturation of hydrogen in the liquid and the pressure drop in the mushy-zone are the driving forces for bubble formation. For the formation of a spherical pore of radius *r* this can be expressed as [3], [39], [47]:

$$P_g - P_{eq} \geq P_{atm} + P_{met} - P_d + \frac{2\gamma_{l-g}}{r} \tag{2.9}$$

Where P_g is the actual hydrogen partial pressure in the melt, P_{eq} is the equilibrium hydrogen partial pressure; P_{atm} is the overhead pressure of the melt, P_{met} is the pressure from the metallostatic pressure head and P_d is the pressure drop induced by shrinkage – all of which constitute the pressure in the surrounding liquid; and γ_{l-g} is the interfacial energy between the liquid and gas phase.

2.4.1 Bubble Nucleation

Nucleation is the first step in the formation of a bubble, though in solidifying aluminium the mechanism by which this occurs is currently not well understood.

Classical Nucleation Theory

According to Fisher's classical (and somewhat dated) nucleation theory [48], gas bubbles nucleate from small embryos in the liquid through a mechanism analogous to the classical nucleation of a solid from a liquid [39]. The supersaturation of hydrogen and the pressure drop in the liquid can both be thought of as suppling work to 'fracture' the liquid and to form a bubble. The reversible change in free energy associated with the homogeneous (ΔG_{hom}) and heterogeneous (ΔG_{he}) nucleation of a spherical bubble or bubble cap of radius *r* on a planar surface can be expressed [48] as follows.

$$\Delta G_{hom} = 4\pi r^2 \gamma_{l-g} + \frac{4}{3}\pi r^3 \Delta P \tag{2.10}$$

$$\Delta P = P_l - P_i \tag{2.11}$$

$$\Delta G_{het} = \Delta G_{hom} \frac{2 + 3\cos\theta + \cos^3\theta}{4} \tag{2.12}$$

Where P_l is the pressure in the surrounding liquid, P_i is the internal gas pressure in the bubble, and θ is the contact or wetting angle (**Figure 2.8** a)).

In contrast to the heterogeneous nucleation of solids, the total free energy in this case is reduced when the contact angle increases – representing poor wetting of the nucleant substrate. This implies that surfaces that form *in situ* during solidification are not viable nucleation substrates, because their direct formation from the melt implies that they are well wetted.

For a bubble to survive and continue to grow, it must exceed a critical radius r^*[48]:

$$r^* = -\frac{2\gamma_{l-g}}{\Delta P} \tag{2.13}$$

Using this, Fisher [48] has gone on to derive a critical pressure at which the liquid 'fractures' and a bubble is formed. Estimates by Campbell [49] have put this critical pressure of the order of 30,000 atmospheres for homogeneous nucleation.

Like in most nucleation scenarios encountered in casting, one would expect for bubbles to nucleate heterogeneously rather than homogenously due to the reduced energy requirements. For nucleation on a planar interface, Campbell [49] went on to estimate that even for a contact angle of 160° (the largest that had been observed at the time), heterogeneous nucleation would require a critical pressure of 1,500 atm (~152,000 kPa). Even in the case of N_2 bubble nucleation in liquid water, heterogeneous nucleation on planar hydrophobic surfaces ($\theta > \sim 120°$) has been shown to require

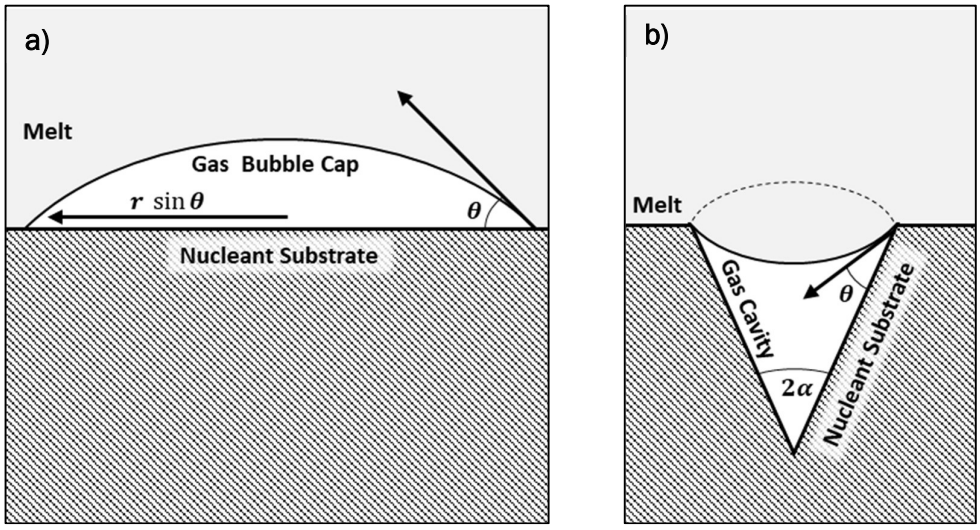

Figure 2.8 Heterogeneous nucleation of a bubble on a) a planar substrate, and b) within a crevice on the surface of a nucleant substrate.

relatively large supersaturation pressures of 100+ atmospheres [50]. This stresses the importance of another factor, the surface micro-topology of the nucleant substrate.

The presence of small crevices on a substrate such as an inclusion (**Figure 2.8** b)) can further assist in reducing the energy associated with heterogeneous nucleation. This has been called *pseudo-classical nucleation* [51]. If the crevice is sufficiently sharp and the particle is poorly wetted, then the melt will not be able to completely fill the crevice, leaving a hollow cavity [52], [53]. Hydrogen may therefore diffuse into these cavities, and given there is adequate supersaturation and pressure drop from shrinkage in the liquid, a bubble will emerge from the crevice [51].

Tiwari and Beech [47] performed SEM on the surface of alumina that was skimmed from the top of molten aluminium, and found it to contain numerous pores and cracks that ranged in size from 5 to 40 µm. They went on to suggest that such cracks in entrained oxide fragments may act as nucleation sites, as they found alumina associated with pores in their cast samples. Dantzig and Rappaz [39] have estimated that if the smallest critical radius of the bubble cap (radius of curvature) for nucleation from a Al_2O_3

crevice that is between 10 and 100 μm, the corresponding critical pressure would be ~20 to 200kPa, which they have suggested is a plausible pressure that may be achieved in the mushy zone. Therefore if a bubble cap was able to emerge from a crevice on Al_2O_3, it is feasible that it would be able to grow.

The wettability (contact angle) of Al_2O_3 has been reported to range significantly, from about 140 to 80° over temperatures between 750 and 1100°C [54], [55]*. Generally the wetting of the interface is initially high, and decreases with increasing contact time and temperature [56]. If an oxide film was to be entrained into the melt and a high contact angle was developed between it and molten aluminium, then its non-wetted face could act as an excellent bubble nucleus.

* Contact angle is usually measured using the sessile drop method, where a drop of molten aluminium is placed atop the test material substrate. The major challenge with this approach is that the aluminium drop develops a surface layer of Al_2O_3 which prevents liquid-substrate contact and influences the surface tension. Bao et al. [55] have performed some reliable experiments that showed that the contact angle of molten aluminium with Al_2O_3 in the absence of the surface film was 149 to 156°at 1100°C.

Bifilm Initiation

Because of the seeming impossibility of heterogeneous nucleation of bubbles, Campbell [3], [6] has instead proposed that bifilms, folded fragments of oxides, are the active nucleants for bubbles in aluminium. As will be detailed further in Section 2.5.1, bifilms are fragments of oxide, folded with their non-wetted faces touching, and a small pocket of air enveloped within, that are entrained in the melt.

During solidification, the small air-pockets within bifilms act as pre-existing embryos for bubble formation [3], [6], [7]. These embryos are already larger than r^*, which alleviates the need for classical-style bubble nucleation. Hydrogen diffuses into these embryos through cracks in the oxide and grows them into pores [57]. Hydrogen's ingress is again driven by its supersaturation in the liquid and its need to attain equilibrium with the internal atmosphere inside the bifilm [39], [57], and the pressure drop from shrinkage plays a further role in unfurling (opening up) bifilms into pores [3]. **Figure 2.9** shows diagrammatically the gradual expansion and eventual unfurling of a bifilm to form a bubble.

The bifilm initiation mechanism is evidenced by the direct observations of Raiszadeh and Griffiths [57], who, using *in situ* x-ray radiography, observed the expansion of an air-

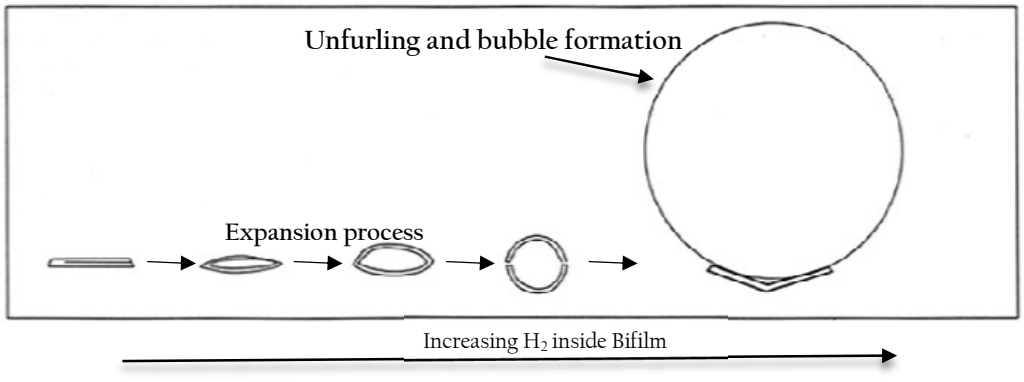

Figure 2.9 The expansion and unfurling process of a bifilm. Adapted from Campbell [49].

bubble due to the inward diffusion of hydrogen in a supersaturated melt. Experiments by Yao et al. [11] found that by pouring metal through a filter at a height above the casting, the volumetric pore number density increased – indicating more instances of bubble nucleation in the material when there were more bifilms in the material. Similar results were also reported by Tiryakioglu et al. [8] who found that increasing the turbulence of melt pouring increased the number of pores in the sample – indicating that there were a greater number of bifilms present in the material acting as pore nuclei. However, one of the key issues with these experiments where the melt is poured, is that it momentarily simultaneously breaks the oxide film and significantly increases the surface area to volume ratio of the melt – which presents an opportunity for hydrogen to diffuse into the melt, which itself may increase the volume and number of pores that are formed.

In conclusion, the evidence suggests that pores may nucleate heterogeneously inside cavities on inclusions, or by the unfurling of bifilms. Of these two mechanisms bifilm initiation theory currently seems to be the most widely accepted by recent authors [7], [58]–[60]. There is a need for further studies to confirm which of these mechanism is dominant, and under which conditions.

2.4.2 Bubble Growth

Following nucleation a bubble begins to grow. Growth in the liquid is controlled by the inward diffusion of atomic hydrogen into the pore where it recombines into a molecular gas:

$$2H^+ \rightarrow H_2 \tag{2.14}$$

This is a diffusion controlled process, and as such, the growth rate depends on the mobility and the availability of hydrogen in the melt. When a growing pore is surrounded by liquid containing hydrogen, the hydrogen is fed into it solely through the liquid-gas interface. However, Atwood et al. [26] and Felberbaum et al. [40] have demonstrated that for a pore growing in the mushy-zone, hydrogen is supplied through both the liquid-gas and solid-gas interfaces, albeit slower in the latter case (**Figure 2.6**). Nevertheless, this means that the growth of pores becomes increasingly limited as the volume fraction of solid increases due to the reduced supply of hydrogen.

The growth of bubbles is also heavily dependent on their number in the liquid. This is because when a pore nucleates, it depletes its surroundings of hydrogen, thus limiting the nucleation and growth of surrounding pores which must compete for available hydrogen in the material. Atwood et al. [26] showed that because of this, when the number of pores (nucleated simultaneously) increases, their size must correspondingly decreased.

Given that growth is usually a diffusion controlled process it is sensitive to the cooling rate during casting, which determines the allowable time for pore growth. The overall fraction of porosity that forms increases while the average pore size decreases with slower cooling rates [11], [26], [61], [62]. If the cooling rate is very rapid, hydrogen is unable to diffuse and may remain trapped in solid solution [62].

2.5 Oxide Films

Melt cleanliness is the term that is used to describe the inclusion content of a melt, with low melt cleanliness referring to a high inclusion content and vice-versa. Generally inclusions are considered to be solids present inside the metal above the liquidus temperature. There are numerous species of inclusions that may be found in aluminium, incorporated into the melt from various sources throughout its processing lifetime.

Usually their presence is undesirable, as they can be deleterious to mechanical and fatigue properties of the metal by acting as stress raisers [15], [16], [63]–[65]. However, not all inclusions are always considered undesirable, for example TiB_2 particles are also inclusions (by the definition given above), and are routinely added to refine the grain structure and mechanical properties of the material [66].

The most prolific species of inclusions that are found in casthouse aluminium are oxide films, and, as has been discussed, have been strongly implicated with porosity.

2.5.1 Oxide Film Formation on Molten Aluminium

Alumina, Al_2O_3, forms endogenously as a result of the *quasi-instantaneous* oxidation of the melt surface due to the highly reactive nature of aluminium [10], [22], [67]. While it remains at the melt surface it plays a protective role in preventing runaway oxidation of the bulk and inhibiting hydrogen absorption due to its continuous nature [65] – though the presence of some solute elements, such as magnesium or strontium, other oxides such as $MgAl_2O_4$ and MgO, or SrO may form, which can significantly alter the morphology and protective nature of the surface oxide [58], [68], [69].

Al_2O_3 initially forms as an amorphous film that is only tens of nanometres thick. Based on a review of atomised aluminium powder by Schaffer [70], it can be estimated that the quasi-instantaneous thickness of the oxide is in the range of 5 – 15 nm. Continued oxidation causes the film to thicken and eventually begin to crystallise into γ-Al_2O_3, which begins at the melt-oxide interface (wetted side) [71]. The incubation time for this transformation has been reported to be around 5 to 10 minutes at 750°C [72]. These films remain relatively thin and flexible, but continuously thicken over time, and over time these films may thicken to be hundreds of microns thick.

Continued holding at elevated temperature results in the transformation of γ -Al_2O_3 to α-Al_2O_3, but is generally a slow process, and has been reported to occur at 750°C, although the reported temperature and times for this transformation vary widely [10], [67], [73]. During the phase transformation, oxide films may develop cracks due to the 24% decrease in the volume of the oxide [73]. This species of oxide is generally very thick, and behaves more as a plate than a film.

2.5.2 Entrainment

The oxide film that forms endogenously on the surface of aluminium melts is generally considered benign whilst it remains on the surface. However, during melt turbulence, from pouring, or nearly any sort of melt handling, the surface film is broken up and entrained in the melt, which is when it becomes a problematic inclusion [3].

2.5.3 Structure of Oxide Films

The two sides of an oxide film have very different characteristics. As **Figure 2.10** shows, the side that is formed in contact with the melt is well-wetted, while the side formed in contact with the air is poorly wetted. This gives oxides the unique and important characteristic of being both an endogenous inclusion, and also being poorly wetted – at least partially.

Quantification of the degree of non-wetting on the non-wetted side of Al_2O_3 is not currently known as the published work has (to the author's knowledge) so far focused exclusively on exogenous α-Al_2O_3, and a real oxide film would be expected to contain a combination of species (further details are given in Section 2.4.1).

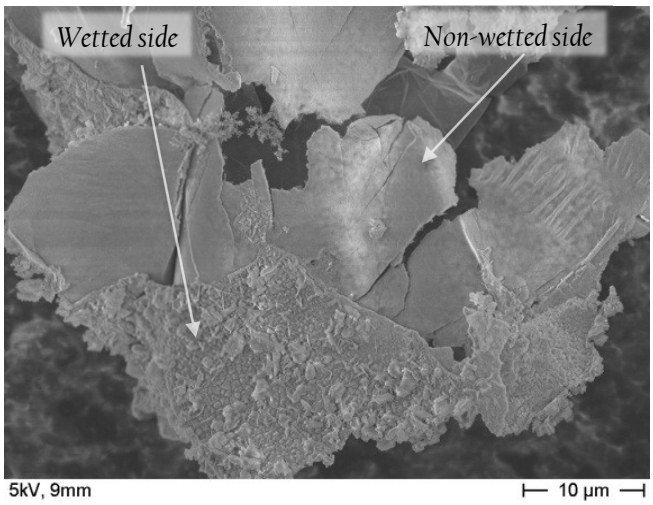

Figure 2.10 Secondary electron micrograph of an extracted γ-Al_2O_3 oxide film. Acquired by Verma during their doctoral research [74].

2.5.4 Young & Old Oxides

Because of the constantly growing and evolving morphology and phase of oxides on/in melts, some authors have found it convenient to loosely classify them as either *young-* or *old-* oxides, based on their thickness [3], [75]. Young oxides are films that have had very little time to grow, being only hundreds of nanometres thick, and appear as thin cracks inside the material [76]. These oxides are spontaneously formed and entrained when the surface of the melt is broken during pouring. Old oxides, while oxides are thicker films that have had time to grow on the surface of the melt, or originate from the surface of the charge material, that can become folded up and entrained in the material during pouring to become a bifilm.

2.5.5 Bifilms

During melt turbulence, oxides may be folded such that their non-wetted side envelops a small pocket of air, creating a bifilm as shown in **Figure 2.11** [6], [7], [49], [77]. Beyond a simple, well-defined folded fragment, bifilms can also be large, and complexly folded fragments, analogous to a scrunched-up ball of paper, that has numerous doubled over folds. The internal non-wetted faces of bifilms are initially not bonded [78], which means that they are effectively cracks in the liquid – and can subsequently be cast into the solid. As has been discussed in Section 2.4.1, it is their crack-like nature that makes them a pre-existing embryo from which a bubble may grow.

Bifilms can be either young or old oxides, provided that the oxide is thin and flexible enough to double over onto itself. Larger bifilms can be seen under the microscope, and appear as extensive cracks in the solid material (**Figure 2.12**). They have commonly been seen to intersect α- and β-Fe-intermetallic compounds [79]–[81], and occasionally with β-Si plates [6], [82], which suggests their wetted faces may act as nucleation substrates for these phases.

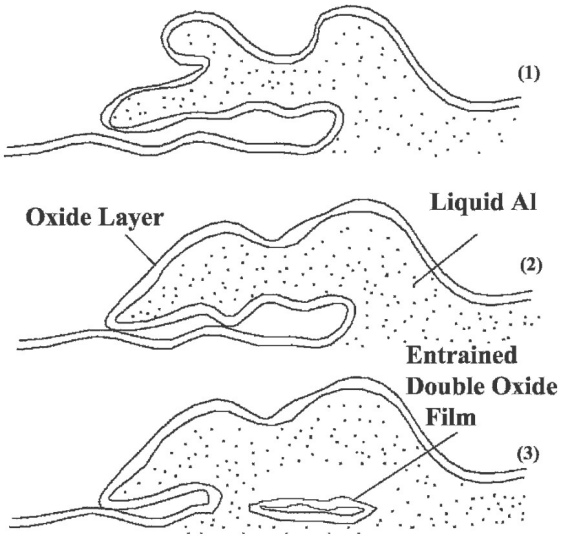

Figure 2.11 Entrainment mechanism of a bifilm. Showing (1) & (2) the folding of an oxide film over on its non-wetted faces due to turbulence, which (3) generates and entrains a bifilm. From [49].

Campbell [3] maintains that bifilms, especially those of young oxides, may only be nanometres in thickness, which makes them effectively invisible under the microscope. Therefore, there are no reported direct observations of these films, meaning that their prominence in aluminium is entirely speculative, though highly plausible. It is for this reason that the RPT has been suggested to be a suitable bifilm test (Section 2.6).

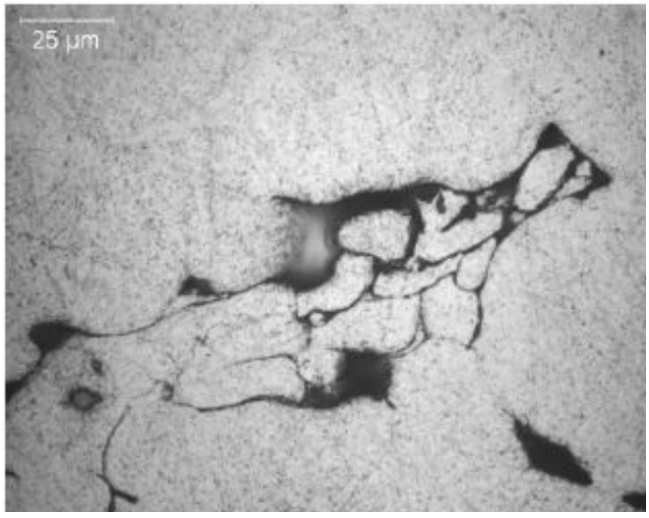

Figure 2.12 Optical micrograph showing a complexly folded bifilm. From [76].

2.5.6 Bifilm Deactivation

During extended holding inside the melt, the volume of air inside bifilms is gradually decreased [57], [83]. This occurs due to the continual reaction of the air inside them with the melt, which forms Al_2O_3, and when all the oxygen in the air is consumed, AlN [83]. The reaction is perpetuated through the continued cracking of the bifilms from the amorphous- to γ- to α-Al_2O_3 phase transformations. It has been proposed that once the atmosphere is consumed that faces of the bifilm could bond together, preventing their expansion, which 'deactivates' them – at least as pore nuclei [68], [84].

Modelling work of these reactions has indicated that these reactions could range between minutes for small bifilms, and hours for large ones, depending on the air-pocket volume and the surface area with which it can react with the melt [78]. Moreover, when hydrogen is not equilibrium between the internal bifilm atmosphere and the melt – as is the case during solidification – hydrogen will diffuse into the bifilms, which expands them and prolongs their complete bonding [57], [78]. Deactivation therefore only occurs during prolonged melt holding. In a practical casting situation where the melt is continually being treated and processed, if a bifilm were to be entrained during turbulence or melt processing, it would probably would not be deactivated during the associated timescales, and remain active inside the melt.

2.5.7 Inclusion & Oxide Film Assessment

The four most prominent techniques for assessing the inclusion content of a melt are, a combination of Prefil and Premetz, PoDFA, LiMCA, and the RPT. Here, focus will be given to the former two techniques as they were used within this work. The RPT will be discussed on its own in Section 2.6, and LiMCA is summarised in Appendix I.2

Prefil

The basic operating principle of the Prefil is shown in the diagram given in **Figure 2.13**. The device works by forcing a charge of molten metal through a ceramic foam filter using applied pneumatic pressure, to capture suspended inclusions [85]. The instrument is very similar to the PoDFA instrument but has the additional benefit of continuously measuring the weight of the filtered metal in the weigh ladle to generate a filtration curve, an approximate on-line indication of the melt cleanliness [86], [87].

During filtration suspended inclusions in the melt build up on top of the filter, which cause the filtration curve to curtail. The slope of the curve indicates the overall level of inclusions in the metal, and its curvature can be used to give a rough indication of the type of inclusions in the metal, with small particulates – such as borides or carbides – most heavily influencing the shape of the curve [46], [85], [86], [88]. However, it is only through a metallographic PoDFA analysis of the solidified filter residue that the population of the inclusion species can be determined. The metallographic analysis is made significantly easier because of the fact that inclusions are highly concentrated in the band above the filter by a factor of about 10,000 [87].

Premetz

One issue with the Prefil device, is the intrinsic variability of the filter permeability, which confounds the results of the test [85], [89], [90], though Premetz [89], an online

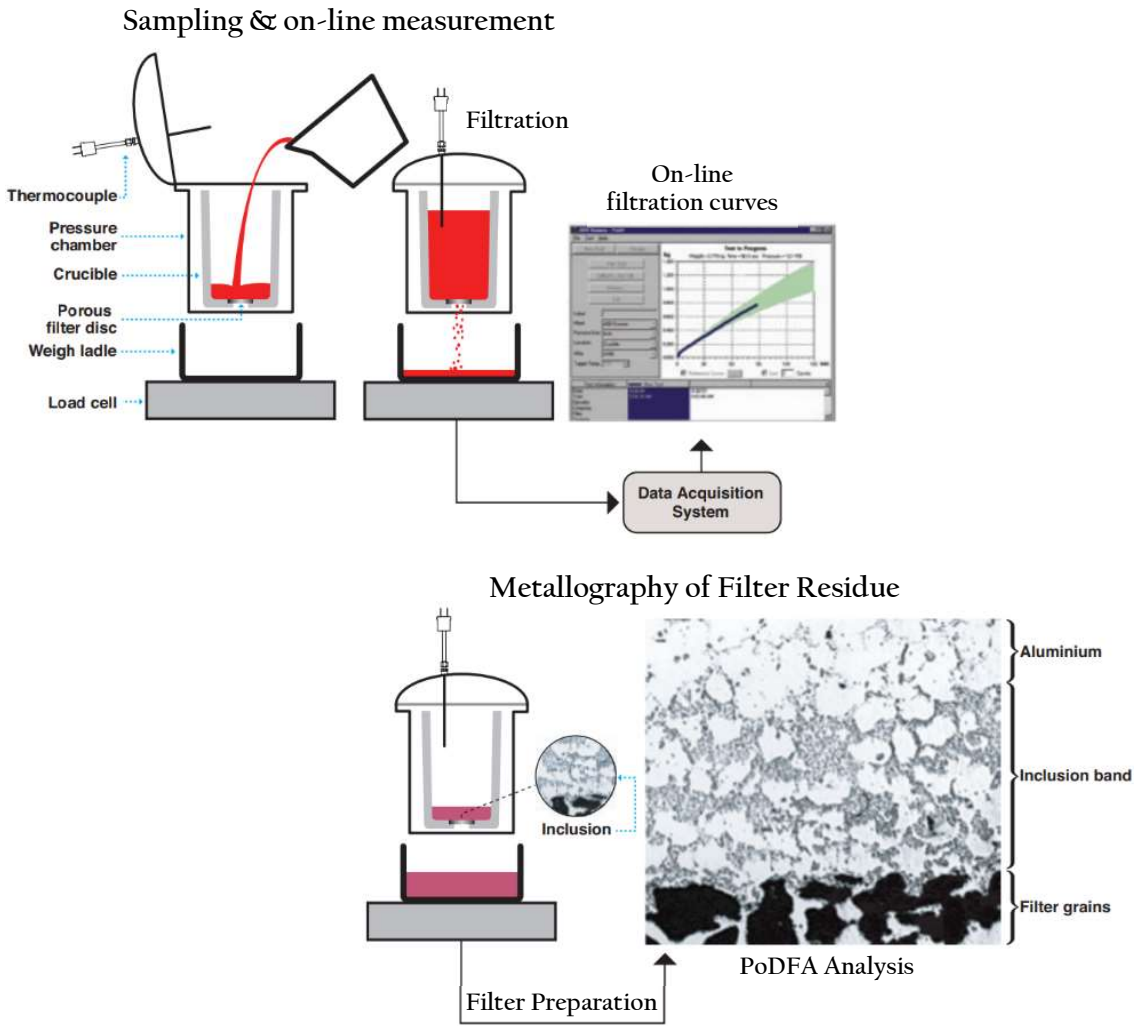

Figure 2.13 Basic operating principle of the Prefil, showing the acquisition of the filtration curve and a micrograph of the sectioned and prepared filter residue. Adapted from ABB Inc. [206].

service, can be used to correct this *post-facto*. It does so by 2 filters in series, one being the actual Prefil filter, and the other being the inclusion cake that builds up on top during filtration. The permeability of the filter cake is used to quantify the melt cleanliness with the *MC* parameter [90]:

$$MC = K\left(\frac{\sigma}{\rho_c k_c}\right) \tag{2.15}$$

Where K is influenced by melt viscosity and density, σ is the weight fraction of inclusions, and k_c and ρ_c are the permeability and density of the filter cake. **Figure 2.14**

shows the effect of Premetz slope of the filter permeability-normalised Premetz curves. In general, an MC value of 0-5 is typical of a treated, clean metal, while an MC>30 is typical of a dirty, untreated metal.

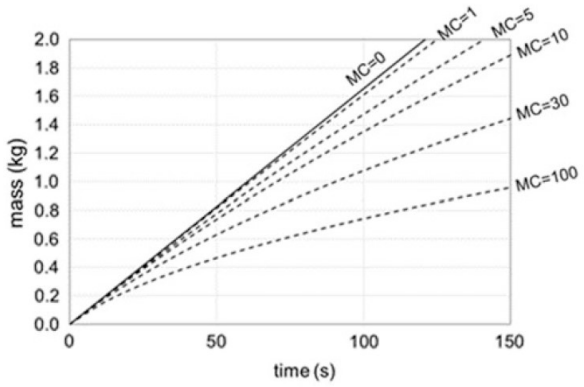

Figure 2.14 Filter-permeability normalised filtration curves for a range of MC values. From Evans et al. [85].

One of the potential limitation of the Prefil (and PoDFA), and by extension, Premetz, as pointed out by Campbell et al. [3], [75] is that small nanometre thick oxide films may not interfere with the flow rate curve, and simply pass through or closely wrap around the filter. Consequently permeability changes seen in the filtration curve will be negligible.

PoDFA Analysis

PoDFA (Porous Disk Filtration Apparatus) was the original filtration method that was developed in the 1960s by Alcan to concentrate inclusions for their subsequent measurement by metallographic analysis [85], [88]. The instrument itself is very similar to the Prefil, and is therefore not described here. Using a rigid and standardised procedure, PoDFA analysis is able to give a semi-quantitative estimate of the inclusion population inside a material. Nowadays, this analysis is performed not only on filter residues captured by PoDFA, but also on Prefil filter residues.

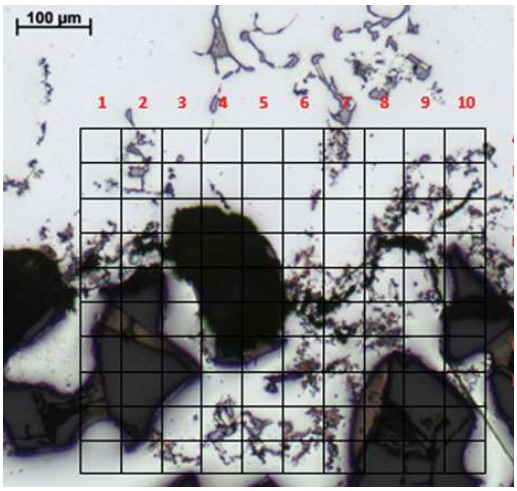

b)

1	2	3	4	5	6	7	8	9	10
	0.1				0.1	0.5			0.1
0.2	0.1	0.2	0.1		0.1	0.3	0.1	0.4	0.3
	0.1				0.2		0.6	0.4	0.2
0.3	0.2				0.2	0.1	0.1	0.1	0.3
0.4	0.2				0.5	0.3	0.1	0.3	
					0.3	0.2	0.5	0.1	
			0.2		0.4	0.2	0.6		
				0.1	0.3	0.2	0.4		0.1
			0.1	0.1	0.5	0.3			
		0.1	0.1	0.2	0.2				

a) b)

Figure 2.15 a) Example of a PoDFA analysis grid superimposed over a filter residue, and b) the estimated area fractions in the grid. From [85]

The techniques makes use of a grid analysis method (**Figure 2.15** a)), where the area fraction of each species of the concentrated inclusions above the filter is estimated by the metallographer (**Figure 2.15** b)) [85]. The exception to this is oxide films, which are counted and a note is taken of their approximate morphology (**Table 2.2**). Generally the analysis is conducted over 30-100 areas just above the filter, at 50, 100, or 200× magnification. At the end of the analysis the total area of each inclusion species is normalised by the filtered weight and reported as $mm^2\ kg^{-1}$, though the oxide content is reported as the number kg^{-1}.

Table 2.2 PoDFA classifications of oxide length and thickness [91].

Length	Short (‹ 250 µm), Medium (250 to 500 µm) or Long (› 500 µm).
Thickness	Thin (‹ 1 µm), Medium (1 to 3 µm) or Thick (› 3 µm).

The proven use of PoDFA analysis over the years has established it as the 'gold standard' against which other techniques are judged, however, it is not without its limitations, and it is important to reiterate that the technique is only semi-quantitative. The subjective nature of the area fraction estimates may lead to inherent variability in repeated measurements. Evans et al. [85] have shown PoDFA error to increase dramatically as the number of inclusions decreases. In the case of oxide films PoDFA analysis should be considered to give only an order of magnitude indication of their content [92].

Campbell [3] has pointed out that freshly entrained bifilms are on the order of tens of nanometres thick, and therefore cannot be expected to be seen by the metallographer – or may not even be captured by the filter. This has implications for small films in general – if they cannot be identified in the concentrated filtrate, they cannot be measured. This notion is supported by the results of Yao et al. [11] who found PoDFA was unable to detect small oxides, which were clearly observable using SEM.

2.6 The Reduced Pressure Test

The Reduced Pressure Test (RPT), originally known as the Straube-Pfeiffer test, is one of the oldest and simplest tests of metal quality that is still used extensively in many casthouses. It was originally developed to measure hydrogen, but it was soon recognised that it measured a convoluted combination of the melt hydrogen content and the melt cleanliness together – hence it is often considered to be a straightforward test of melt quality. It is precisely for this this reason, combined with its robustness, low cost, speed, and simplicity, that the RPT finds extensive use.

2.6.1 Basic Principles

The RPT involves taking a small sample of ~100g of metal and solidifying it under a partial vacuum inside a vacuum chamber as shown in **Figure 2.16** a). The application of the vacuum magnifies the size of gas pores, making them visible to the unaided human eye (**Figure 2.16** b)). The volume fraction of porosity is then considered to be inversely proportional to the melt quality and the vacuum level. The vacuum level is selected based on the melt quality and the amount of porosity that is expected, but is generally selected to be of the order of either 100 mBar or 10 mBar (though this varies between commercial instruments). For example, for a vacuum of 80 mBar (as used in this work), pores will be expanded to ~12.5× of their atmospheric size according to the ideal gas law. If the hydrogen level in the material is very high, selection of too low of a vacuum can result in the pores blowing out of the top of the sample.

2.6.2 The RPT as a Bifilm Test

In recent years the RPT has been increasingly used as a test for bifilms [9], [19], [65], [75], [77], [93]–[95]. It is generally considered that application of the practical vacuum during the RPT can be used as a means of unfurling and expanding them to form pores,

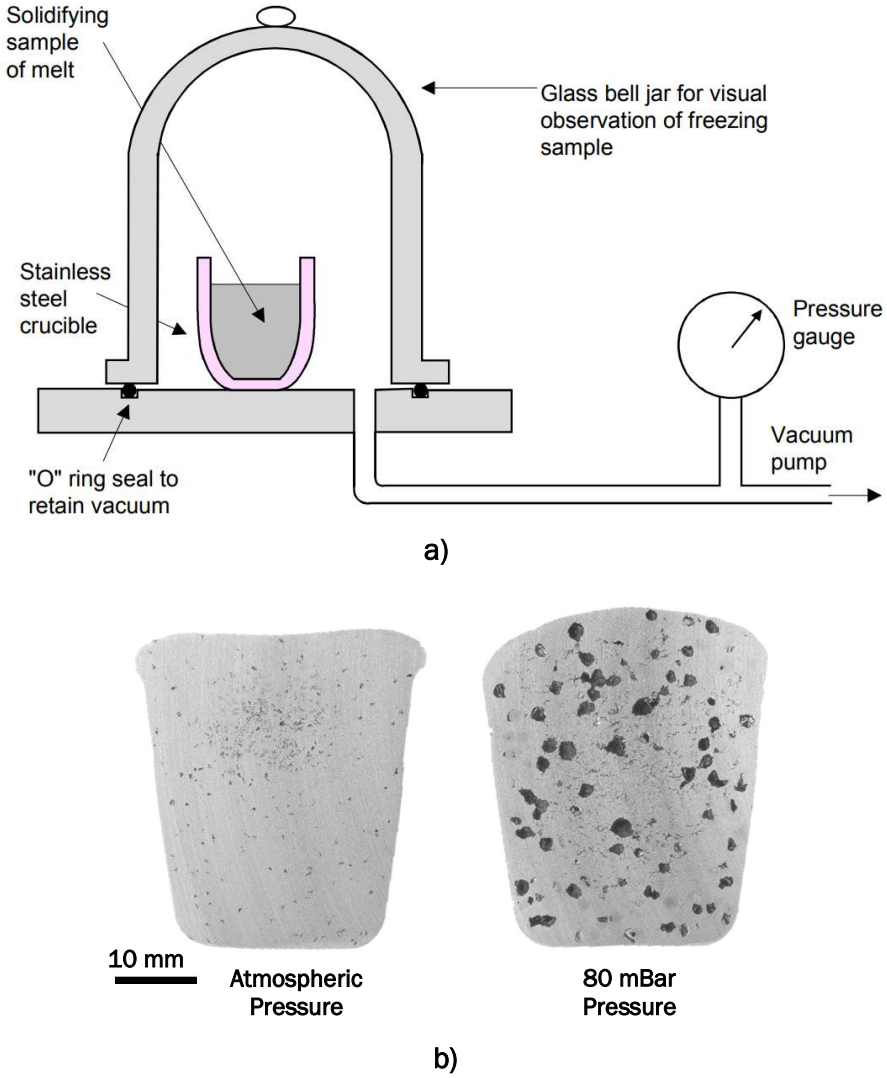

Figure 2.16 a) A simplified diagram of reduced pressure test apparatus (from Campbell and Harding [207]), and b) a comparison of porosity formed in the samples under atmospheric and reduced pressure.

allowing these otherwise too small inclusions to be examined [7], [65], [94]. Even in the absence of hydrogen, the application of reduced pressure would result in the expansion of the small air pockets inside bifilms. This of course assumes that all pores that are seen in theRPT sample are initiated by an individual bifilm.

2.6.3 Quantification

There are 3 typical methods for quantifying the RPT:

1. Bubble tests, qualitative tests where the melt quality is determined based on the appearance of the first bubble or the number of bubbles at the surface of the sample as observed by the operator through a viewing port [42], [44].
2. Density measurements, where the sample density is measured by Archimedes' Principle. The Density Index (*DI*) is commonly calculated by comparing the density of the RPT sample (ρ_{RPT}) with that of a twin sample that is solidified under atmospheric pressure (ρ_{atm}) with:

$$DI = \frac{\rho_{atm} - \rho_{RPT}}{\rho_{atm}} \times 100\% \tag{2.16}$$

3. Visual examination of the pores in the cross-sectioned sample, and qualitative comparison with a reference chart.

2.6.4 The Bifilm Index

The Bifilm Index (*BI*) was developed by Dispinar and Campbell [65], [77] in 2004 to quantify the length of pores in a sectioned RPT sample using image analysis. The *BI* is given as:

$$BI = \sum L_p \tag{2.17}$$

Where L_p is the "*maximum length of the pores*", and is the *major axis* of the pore [94].

The technique is becoming increasingly adopted to give an indication of the number of bifilms inside the metal, though at the same time the importance of hydrogen seems to be becoming increasingly overlooked, and is sometimes not measured at all. Its effect has

been shown to strongly increase the size of pores [62], [96], so it would therefore be expected that the total *BI* would be strongly dependent on this.

Finally, the theory considers that all pores in the RPT are initiated by bifilms, therefore for this reason it would seem more logical to directly measure the pore number density, which would give a direct measurement of the bifilms. That being said, Campbell and Dispinar [7] have shown that the BI correlates with the number of pores (**Figure 2.17**).

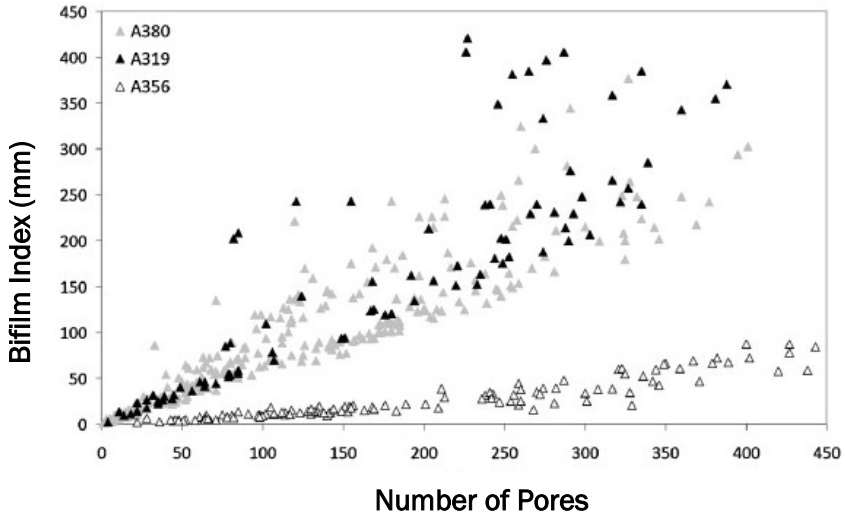

Figure 2.17 Bifilm index versus number of pores. The bifilm index is the total length of bifilms observed in an area of a metallographic sample. From Dispinar and Campbell [7].

2.7 Melt Quality Control

In order to control the hydrogen and inclusion content and keep the melt quality within specification, casthouses subject their metal to a number of pre-casting treatments (as can be appreciated from **Figure 1.1**). Here, only two treatment processes with relevance to this work will be covered; for an extended overview of the numerous other melt quality control techniques, the reader is referred to the works of others [3]–[5], [17].

2.7.1 Flotation & Sedimentation of Inclusions

Melt holding is one of the most straightforward methods that can remove entrained inclusions by floating or sedimenting them from the melt. Inclusions with a lower density have a propensity to float, while those with a higher density have a propensity to sink and sediment. The rate at which an inclusion moves through the melt during flotation or settling is governed by Stokes's law, and depends on its cross-sectional area and its relative density difference to the melt [97].

Oxide films have a slightly higher density that molten aluminium, which would suggest that they would sink. However, the complex structure of oxide films, and especially oxide bifilms, confound this reasoning as they may entrap pockets of air when they are entrained in the melt. This in turn gives them a highly variable buoyancy. Those with large pockets of entrapped air will float faster – as is the case with most dross – however, those with small air pockets, may be essentially neutrally buoyant [6], which means that holding will prove ineffective in removing them. Flotation may be facilitated by bubbling gas through the melt, as the bubbles may collect suspended inclusions as they pass through the melt and float them out. This way inclusions that would normally

sink may be floated to the surface of the melt, where they may be entrapped by the dross layer, which can simply be skimmed from the melt.

TiB_2 grain refiner (and endogenous $(Ti,V)B_2$ [98]) particles have a tendency to sediment out of the melt due to their much higher density (~4.5 g cm^{-3}) compared to molten aluminium, causing them to rapidly sink once added to the melt, though this is highly dependent on the particle size [99]. As TiB_2 settles through the melt, it may collide with and build up on oxide films, which can facilitate their sedimentation. Once sedimented, the melt above can be cast off, free of them.

2.7.2 Degassing

Degassing processes work on the basis of removing hydrogen from the melt by floating it out inside bubbles of an inert gas - usually argon – that is passed through it [33], [100], [101]. The low P_{H_2} of the inert gas drives hydrogen to diffuse from the melt into the bubbles, which then float out of the material [64], [102]–[104]. The process is also widely considered to have a cleaning effect on the melt as the passage of bubbles through the melt also has the effect of picking up inclusions from the metal [4], [33], [101], [103].

There are a variety of means for degassing, which include degassing tablets, use of a submerged lance, or by rotary degassing, though the latter is by far the most efficient from the perspective of hydrogen removal as it is capable of generating dispersing micro-bubbles throughout the melt, which increase the process's efficiency [102], [103]. Modelling of particulate inclusion removal in molten steel demonstrated that as bubble size increases and inclusion size decreases, the probability of the removal of particulate inclusions is decreased [105], [106]. However, although degassing may be effective at removing large inclusions (such as old oxides) from the melt, it might also simultaneously

generate and entrain many small oxide film fragments from the melt's surface during this process [3], [107]. Anecdotal evidence from Enright would further support this [46].

2.8 Grain Refiner's Effect on Porosity

The mechanisms by which grain refiner nucleates and refines the grain structure in solidifying aluminium has been the subject of a considerable number of studies [108]. In contrast, grain refiner's effect on porosity formed in the material has not been widely studied, and is much less understood, as the few existing studies tend to contradict each other.

Some authors have reported an increase in the number density [109], and in the fraction of porosity and the size of pores [62] with Al-Ti-B grain refiner addition. One of the authors [109] proposed that TiB_2 particles themselves might act as nucleants for pores - however this is unlikely as it is expected that TiB_2, even the less well wetted particles, would be relatively well wetted compared to other potential nuclei inside the melt. The other author [62] speculated that this might be due to an increase in "*grain-refiner related oxide nucleation sites*", or alternatively, the increased titanium from the master alloy increased the solubility and content of hydrogen in the melt, but did not give further details.

In contrast, grain refinement has been reported to decrease the volume fraction and the size of pores [110], [111]. Modelling by Atwood and Lee [26] also showed this, and attributed it to the physical impingement by the grain structure, and by hindered feeding of hydrogen to pores due to higher fractions of solid.

In conclusion, it is difficult to confidently draw a conclusion about grain refiner's effect on porosity based on the current literature.

Chapter 3

Quantitative Porosity Assessment & X-Ray Computed Tomography

Metallography in its all-encompassing sense is the study of the microstructure of metals by microscopy. Traditionally microscopy was limited to the 2D planar analysis of sectioned metallic specimens, though today it could technically be extended to encompass X-Ray CT and other novel forms of microscopy – though generally, and in this thesis, metallography is used in its traditional 2D sense.

3.1 A Brief Overview of Metallographic Analysis

2D planar analysis of metallographic sections is the standard approach for assessing the structure of porosity in metals. Digital Image Analysis (DIA) is becoming increasingly utilised in these studies in order to extract quantitative measurements in this process. Generally this is done automatically using commercial software packages [9], [15], [60], [94], [112] or free public domain software packages such as ImageJ [113], [114]. The process is relatively straightforward when the pores are well defined – with good contrast with the image background - such as in optical micrographs. However, DIA becomes increasingly difficult for the assessment of pores on a macro-scale, such as over an entire cross section of a casting, because of difficulties in accurately segmenting the image.

The most widely used technique for quantitatively analysing porosity on a macro-scale has been the method developed by Dispinar and Campbell for RPT samples [65],

[77] – the Bifilm Index (*BI*), which has been discussed in Section 2.6.4 – using the Sigmaplot software package. The images used in the analysis contain numerous artefacts (reflections), but the strength of the *BI* measurement is that it is relatively insensitive to these artefacts [94]. The trade-off is that it is difficult to acquire meaningful measurements of other characteristics of pores because of these artefacts. There is therefore room for improvement in this field to acquire reliable measurements of porosity in this way.

3.2 Limitations of 2D Analyses

Although relatively simple compared to X-Ray CT or other novel imaging methods, the major limitation of 2D metallographic analyses is that it only 'sees' the 2D manifestations of pores on the analysis plane that randomly intersects them [115], [116], as shown in **Figure 3.1**. This means that either the maximum size (area or diameter), or some fraction thereof is measured from the analysis plane. This is problematic and misleading, especially when measuring features with complex morphologies – such as shrinkage pores, or combined shrinkage and gas pores, as shown in **Figure 3.2** [1], [15], [117]. Therefore measurements of the pore shape, size distribution, or number can be very misleading, and not representative of the true 3D manifestation of the pores. Stereological relationships can be used to estimate the 3D size and number of pores, but these relationships hinge on a number of assumptions that are not always valid [116], [118]. Moreover, the act of sectioning and preparing the sample for analysis may itself deform the pores, which further compounds the result [173], [174]. Some of these aspects will be discussed further in Section 6.1.

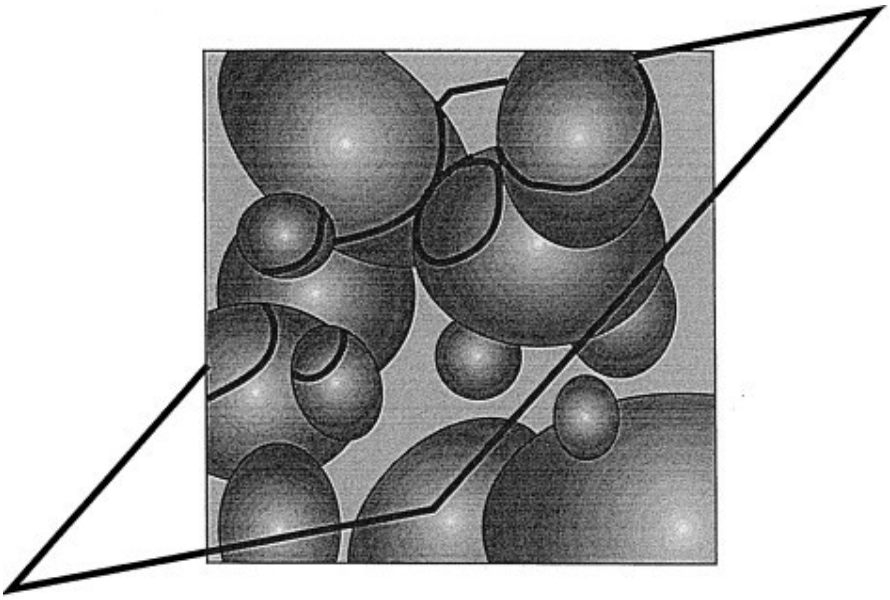

Figure 3.1 The random sectioning of pores by an analysis plane, showing that their maximum size is not always seen. Adapted from Sahagian et al. [115].

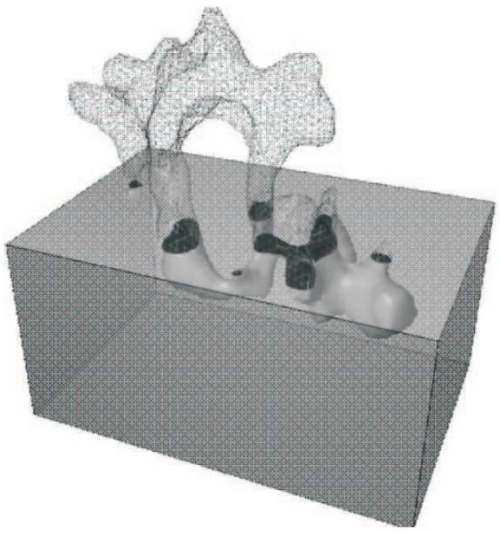

Figure 3.2 A cross section through a 3D reconstruction of a shrinkage pore, with the black regions showing the 2D manifestation on the sectioning plane. From Fintova et al. [117].

3.3 Overview of X-Ray CT

X-Ray Computed Tomography (XCT), popularly known as X-Ray CT, CT, or in the medical sphere, Computer Assisted Tomography (CAT) is a non-destructive form of microscopy with 2D and 3D imaging capabilities. The word tomography derives from the Greek '*tomos*' and '*graph*', which mean to slice or section, and image or representation, respectively [121]. This is because one way its 3D data may be viewed is as 2D cross-sectional slices. However, data may also be presented as a 3D volume, which is sometimes referred to as a *tomogram*.

Traditionally XCT was performed on materials nearly exclusively using synchrotron radiation. However, with the rise of commercial laboratory CT systems, the technique is becoming far more accessible.

3.4 Fundamental Principles of X-Ray CT

The key components of a cone-beam XCT system, the most common of the laboratory-CT machines today, and the type used in this work, is shown in **Figure 3.3** a). X-rays are generated from a source, shot through a sample, and picked up and measured by a detector on their exit from the sample, which generates a *projection image*. The sample is then rotated at small increments – usually in the range of 0.1 to 1° – and imaged at each *projection* until it has turned at least 180°. The series of *projection images* are then reconstructed into a matrix of voxels (3D pixels), which can then be used to generate a 3D volume (tomograph) or resliced into a stack of 2D images, known as slices, as illustrated in **Figure 3.3** b) and c).

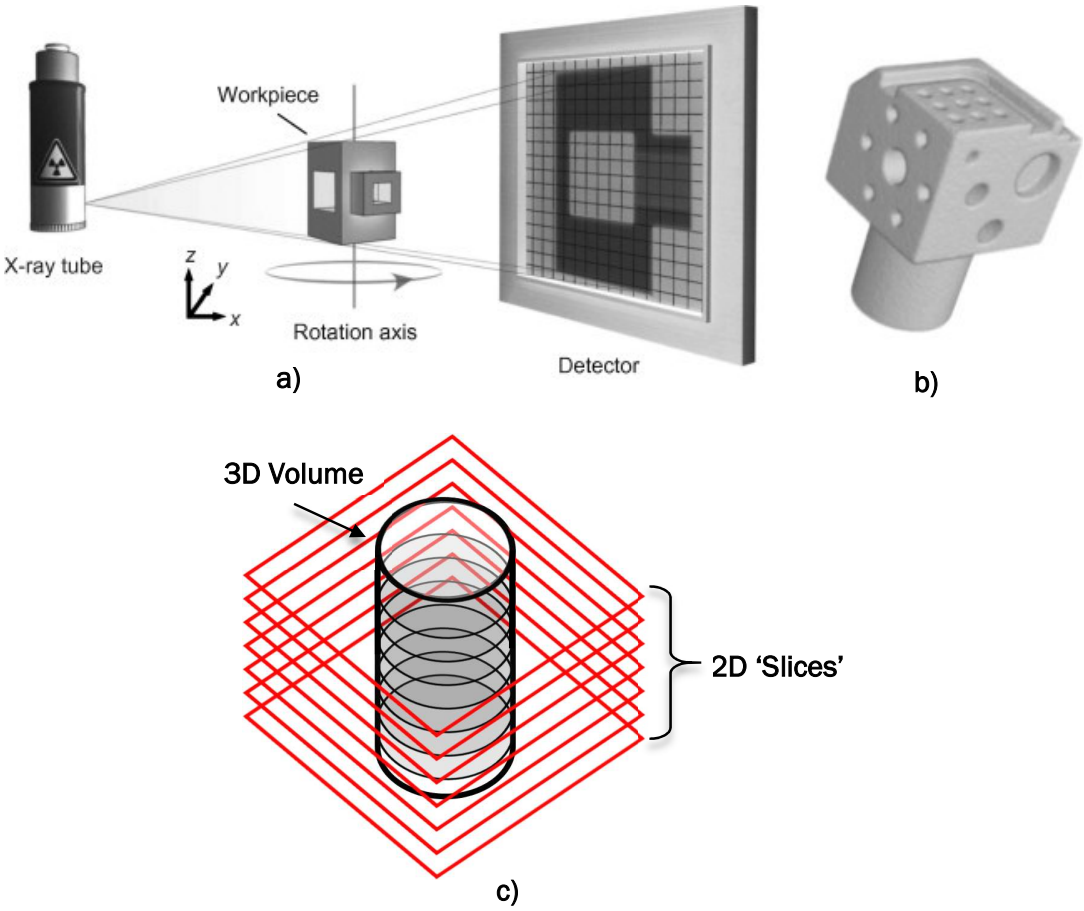

Figure 3.3 a) a typical setup of the fundamental components of a cone-beam x-ray CT instrument, b) a 3D rendering of the scanned component, both from Hiller et al. [122]; and c) an example of the representation of a 3D cylindrical volume as a series of 2D cross-sectional slices.

3.4.1 Absorption Imaging

Laboratory-CT systems often rely on differences in x-ray attenuation between phases inside the sample to generate an image. This is known as absorption imaging, which will be the focus of this section due to its relevance to this thesis. For a monochromatic beam, the intensity after passing through a material (I) is given by Beer's law [123], [124]:

$$I = I_0 \exp(-\mu_L\, x) \tag{3.1}$$

Where I_0 is the initial intensity, μ_L is the linear attenuation coefficient, and x is the distance travelled through the material. μ_L is influenced by the density of the material's phase, the atomic number of its constituents (approximately $\propto Z^3$ in the typical XCT

energy range), and is also a function of the x-ray voltage [124], [125]. This voltage dependence can be used to optimise differences in x-ray attenuation between each phase, as shown by **Figure 3.4**. By extension, this enhances their contrast in the output greyscale images. Indifferent phases should become distinctly resolvable from each other when there is a relative difference in their respective linear attenuation coefficients of more than approximately 20% [125]. When studying porosity however, there is always a significant difference in attenuation between the attenuation for all energy ranges.

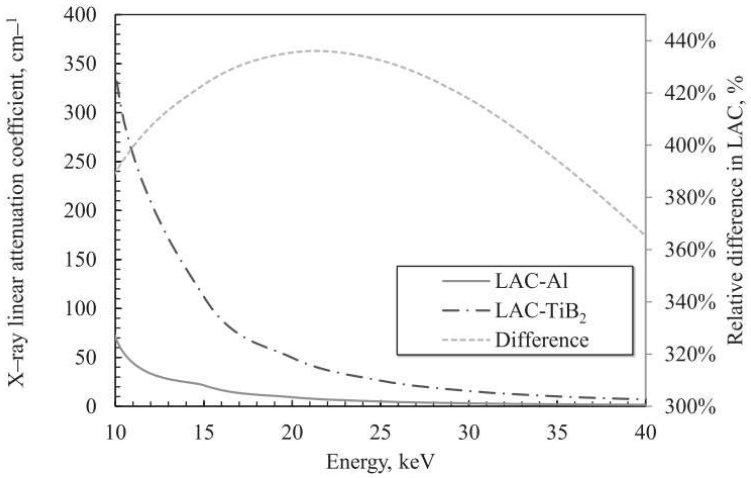

Figure 3.4 X-ray linear attenuation coefficient (LAC) of Al and TiB_2 and their relative difference. From Li et al. [125].

Unlike synchrotrons, laboratory XCT systems, like the ones used in this work, emit a polychromatic spectrum of x-rays as shown in **Figure 3.5** a). This gives rise to the *beam hardening* artefact, due to progressive scattering of the low energy x-rays as the beam passes through the sample, giving an apparent change in μ_L with the sample thickness [123], which has a darkening effect on the image as shown in **Figure 3.5** b). Beam hardening can also occur as a result of inhomogeneous sample thickness. Hence it is therefore common to apply a physical filter (which is sometimes a simple copper plate) in front of the x-ray source to 'kill off' these low energy x-rays as they exit the source [126].

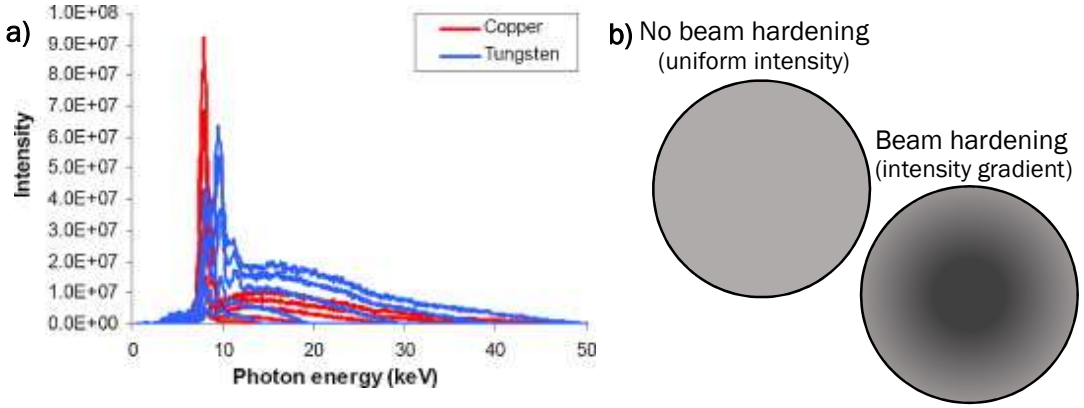

Figure 3.5 a) Polychromatic x-ray spectra generated from Cu and W sources, from Kruth et al. [126]; and b) an illustration of the Intensity drop over the thickness of a homogenous samples due to beam hardening.

3.4.2 Magnification

As shown in **Figure 3.6** the magnification of a cone-beam XCT system depends on the relative distances between the x-ray source and sample (d_{s-s}), and the sample and detector (d_{s-d}), and is known as geometric magnification (M_G) and is given as [123], [126]:

$$M_G = \frac{d_{s-s} + d_{s-d}}{d_{s-s}} \tag{3.2}$$

The Zeiss Xradia laboratory XCT system incorporates an additional optical magnification lens which provides further magnification (M_O) by taking the geometrically magnified beam, converting it to visual light through a scintillator, and then magnifying this with objective lenses - analogous to a visual light (optical) microscope. The resultant system magnification becomes: $M_G \times M_O$ [127].

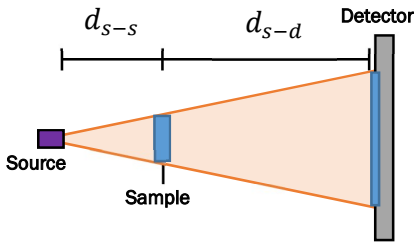

Figure 3.6 Geometric magnification in cone-beam XCT system.

3.4.3 Field of View, Voxel Size, & Spatial Resolution

Because of the finite number of pixels *N* within a detector, there is an intrinsic trade-off between the field of view (*FOV*) and the voxel size. The minimum voxel size of a system is [128]:

$$Voxel\ Size = \frac{FOV}{N} \tag{3.3}$$

Hence as the FOV increases, the voxel size must too increase. However, the minimum voxel size does not directly translate to the spatial resolution, which is the smallest resolvable unit of length in the image [126].

The spatial resolution of an XCT system is complex and is influenced by several factors, which includes the spot size of the x-ray source, the internal scattering of x-rays within the sample, mechanical imperfection during manipulation of the sample's position, and the determination of the sample's centre of rotation during reconstruction of the data [126], [128], [129].

3.4.4 Reconstruction

Several algorithms have been developed over the years for reconstructing the projection images into a 3D tomograph. An in depth discussion of these algorithms is beyond the scope of this work. However, a simplified description will be given here of

the most widely adapted reconstruction algorithm for commercial cone-beam CT systems today, the *Feldkamp algorithm* [121].

The technique is based on the *filtered back projection* algorithm, which is used for reconstruction of fan-beam XCT data [126]. Filtered back projection involves first filtering (denoising), and then projecting the intensity of each pixel in each of the projection images 'backwards' through the entire volume, as shown in **Figure 3.7**. This is repeated for each projection and the final intensity of each voxel in the volume is the summation of the back projections from each angle. The Feldkamp algorithm [130] is a type of filtered back projection algorithm applied for cone-beam tomography that corrects for the 3D conical trajectory of the back projected voxels, which do not stay in the same horizontal projection plane [126], [131]. The sharpness of the reconstructions produced by this algorithm may be improved by increasing the number of projection images acquired during the scan [126].

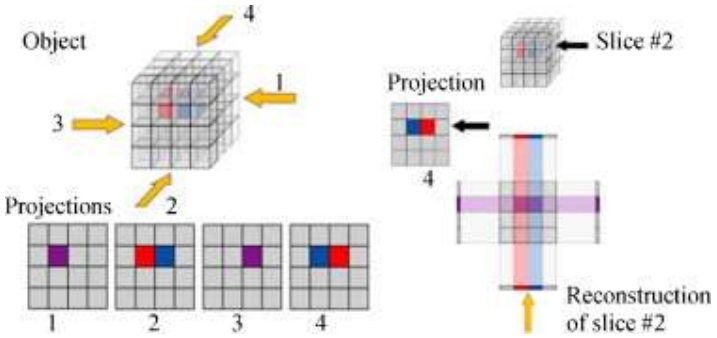

Figure 3.7 Basic principle of 'back projection reconstruction'. It shows that for each projection image (from angles 1, 2, 3, 4) that the backward projection of their intensities sums to give the intensity of the reconstructed voxel in the 3D tomograph. From Kruth et al [126].

3.5 Studies of Oxides Films & Bifilms

It is not possible to resolve oxide films or bifilms directly because of their very thin nature and low difference in attenuation coefficient with aluminium. However, an interesting study [132] was performed on the behaviour of pores in liquid metal using a synchrotron. By performing *in situ* time lapse XCT, pores have been observed to remain in the liquid, but morph in shape, which may imply they are surrounded by bifilms.

X-ray CT has been employed to characterise porosity in RPT samples to a limited extent, but, with the exception of one instance [8], have not considered it as a bifilm test. It has been used as a means of evaluating the fraction of porosity in the samples [133]–[135]. Most recently, Tiryakioglu et al. [8] used XCT to quantify changes in the size and the number of pores in RPT samples with pouring damage and the incorporation of bifilms in the material. This is perhaps the most relevant work to date to the work that is presented in this thesis.

3.6 Quantitative Digital Image Analysis for X-Ray CT

Broadly speaking, digital image analysis (DIA) can broadly be broken down into the following three steps:

1. **Image Processing**, where the operations are performed to improve the image quality for analysis.
2. **Image Segmentation**, where features of interest in the image, such as the pores, are defined and isolated from the image.
3. **Quantitative Measurement & Analysis** of the features identified during the preceding segmentation stage.

No single universally correct combination of techniques for the DIA of an image exists, but an array of potential techniques have been developed which prove effective for particular types of images (though some are better than others). Given its heavy use in this work, this section will give an overview of the key DIA principles, with focus on application to XCT images – though they are also applicable analysis of nearly any image. It should be noted that, although XCT images can be processed as a stack of 2D images, or a single 3D image, the foundational principles are usually the same.

3.6.1 Image Processing

The processing phase of XCT images commonly involves two practices: remapping and denoising.

Remapping

It has been common practice to remap XCT images from 16-bit to 8-bit to save on computational power during subsequent analyses [136]. It is imperative that during this

process the greyscale range of the image is remapped so as to include only non-zero intensity values in order to minimise losses in intensity.

Denoising

Noise is one of the major issues that manifests itself in XCT images, and should be removed in order to achieve a sound segmentation and analysis. Denoising therefore usually constitutes most of the image processing phase.

There are a number of algorithms, known as filters, which exist for image denoising. In all cases, their application is a delicate task as entails balancing noise reduction with the preservation of the image features [137], [138]. Local means (LM) filters, such as the median or Gaussian filter, are the most basic type of filter, and remove noise by replacing a pixel with some sort of average or other statistical value from its surroundings [139]. Although good at removing salt-and-pepper noise, their drawback is that they typically heavily blur the image features. The bilateral [140] and SUSAN [141] filters better preserve the sharpness of edges compared to other LM methods, but can erroneously warp features in noisy images [138].

Non-local means (NLM) type filters make use of all pixels within a large region around the target pixel or voxel, known as search window, when performing averaging [137], [138]. Such filters can more effectively remove noise whilst preserving image edges, especially weakly defined edges, compared to LM filters and other families of filters [142].

3.6.2 Segmentation

Segmentation is the process of identifying and defining the objects or regions of interest within the image as shown in **Figure 3.8**. This is a highly critical step as it is what is segmented from the image that is measured in the subsequent analysis. One must therefore remain consistent when analysing groups of the same data as the segmentation

directly effects the analysis step. Here an overview of the most common methods that have been employed for segmentation of XCT images will be given.



Figure 3.8 An example of the segmentation of the object / region of interest from an image, which in this case, is a penguin. Segmentation of a penguin from the a) input image and b) segmentation of the penguin from the image background. Adapted from Yu et al. [143].

Global Thresholding

Global thresholding is the most basic segmentation technique in which pixels are classified based on their greyscale intensity as shown in **Figure 3.9**. Commonly an image is segmented into only 2 phases (binarisation), though this can be extended to many classes.

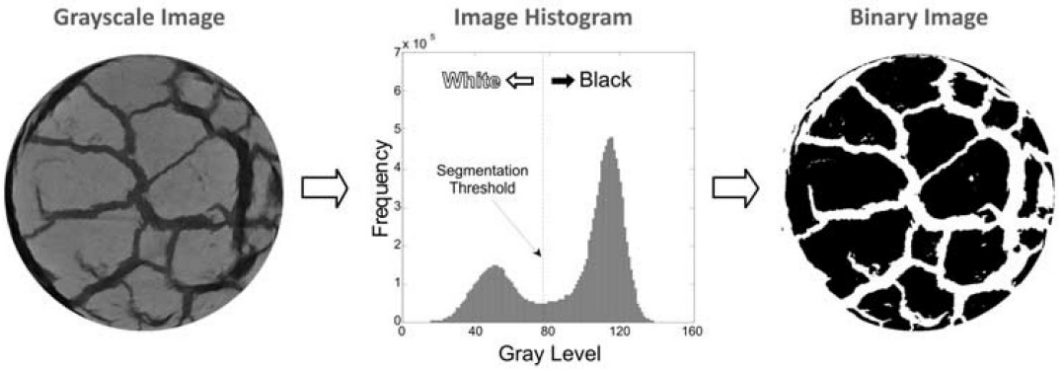

Figure 3.9 Segmentation of a micro-CT slice of bentonite-sand sample into a binary image by global thresholding. From Iassonov et al. [144].

This technique is ideal when the features of the image have significantly different greyscales to the background, and therefore is commonly used when measuring porosity in XCT images [144]. Threshold may be selected arbitrarily by the operator, or calculated. However, the former case may introduce inconsistencies in successive measurements and operator bias [145], [146], which underscores the advantage of threshold calculation. One of the most widely used methods is that developed by Otsu [147], which segments an image using the peaks of its greyscale histogram. In its original form, this method defines the threshold as the point between the two peaks of a bimodal histogram that minimises the intra-class variance (equivalent to maximising the inter-class variance), with the assumption that the peaks represent the classes or regions in the image. Because this technique works well for images with two clearly defined regions (translating into two clearly defined peaks on the histogram), it has found extensive use when thresholding micro-XCT images of porosity in various materials [148]–[152]. Compared to other methods for threshold calculation, Otsu's method has been shown to have superior accuracy when segmenting porosity in XCT images [144]. However, if the criteria of uniform image illumination, or histogram bimodality is not fulfilled significant errors may be introduced [153]. An interesting drawback of global thresholding is that objects of the same type, but different thicknesses cannot be accurately segmented, especially in the presence of beam hardening; this is illustrated in **Figure 3.10** below [121].

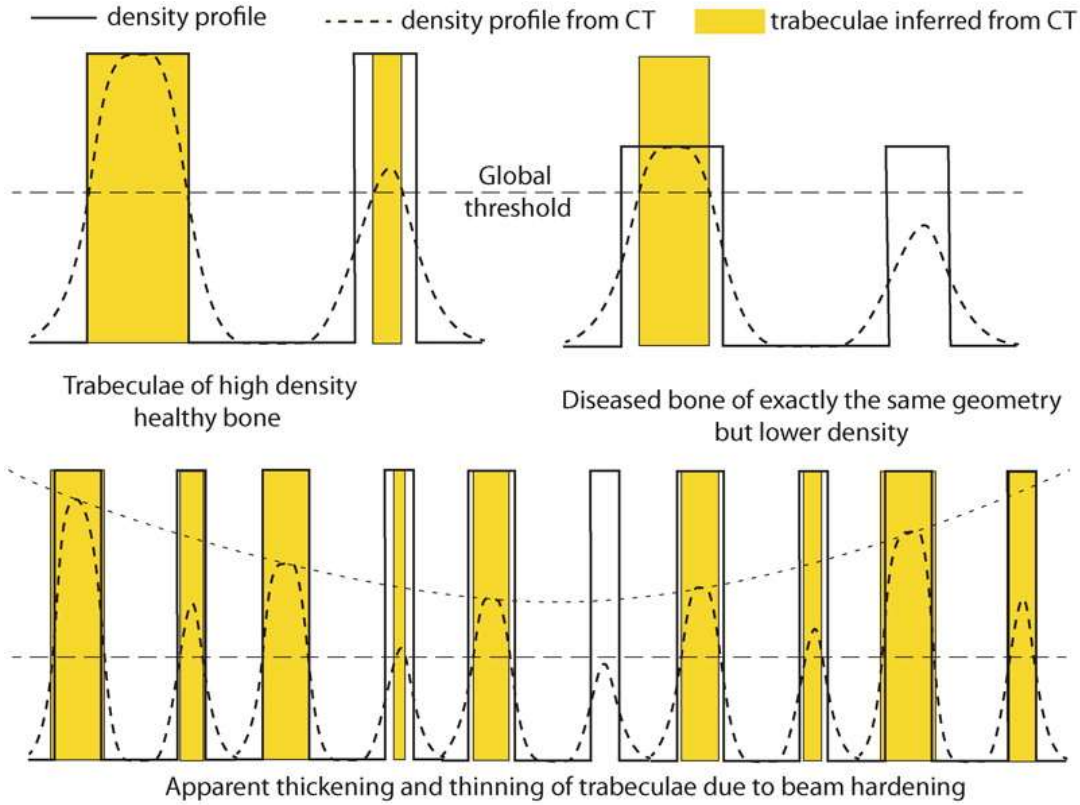

Figure 3.10 a) Wall thickness dependence of the measured thickness and density of trabeculae in bones inferred using XCT when using a global threshold, and b) this problem extended to a case containing beam hardening. Solid lines represent the actual borders, the dashed lines represent the attenuation profile seen by the XCT, and yellow regions are the area inferred by the global threshold. From Maire and Withers [121].

Watershed Transformations

Watershed Transformations are an alternative and robust family of algorithms for image segmentation [154], [155], and are useful for defining objects that contain a range of greyscales in non-uniformly illuminated images (beam hardened images). A particularly notable algorithm from this family is the *Marker Based Watershed Transformation* (MBWT) [154], [155], that is becoming increasingly used for segmentation of XCT [156]–[158]. It also finds use in splitting connected or overlapping objects in an already segmented image [139].

Watershed algorithms segment an image by region growing. The basic concept of image segmentation using watershed transformations can be explained using the following anecdotal hydrological example. A gradient image of the original input image (**Figure 3.11** a)) is treated as a topological map, with its pixel intensities representing a geographical topography as shown in **Figure 3.11** c). In the MBWT, this topographic landscape is then flooded from markers (**Figure 3.12** a)). This flooding represents the growth of the distinct regions (objects) in the image, and is governed by the gradient image, with steeper topologies flooded slower. Flooding proceeds until two adjacent 'flood waters' (the growing regions) meet, at which point the division point between them is constructed and individual objects in the image are defined (**Figure 3.12** b)).

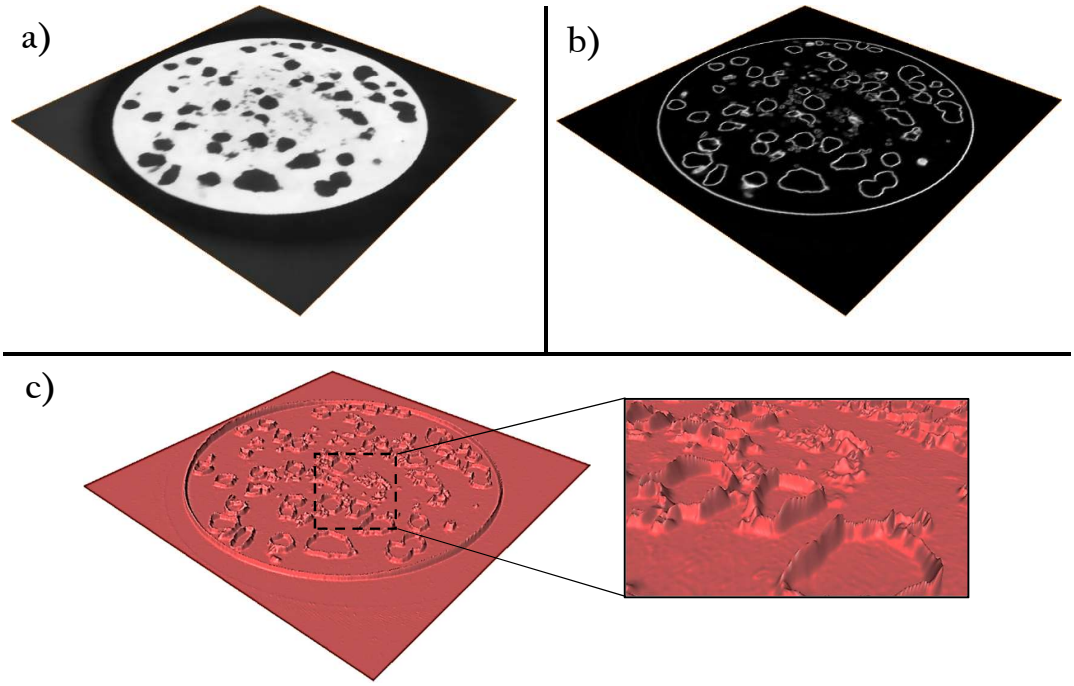

Figure 3.11 The watershed transformation procedure. a) input image, b) gradient image of the input, c) 3D rendering of the image gradient as a topological map.

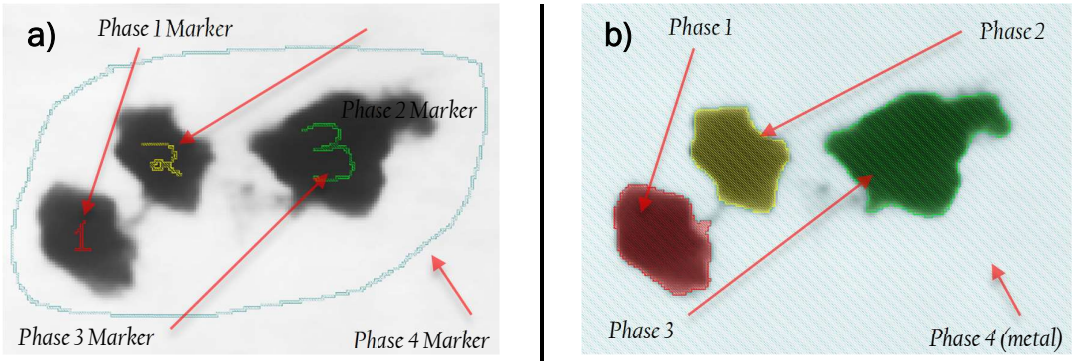

Figure 3.12 An example of marker based watershedding applied to an XCT image of porosity, showing in a) markers for 4 different objects (phases 1 to 3 are individual pores, and phase 4 is the metal substrate), represented by the colours; and b) the resultant segmented image.

The outcome of the segmentation from the MBWT depends on the quality of marker definition and also the sharpness of the gradient image. There have been a number of approaches employed for marker placement. The simplest approach is to place the markers by hand – though this can introduce possible errors and inconsistencies, not to mention it is impractical for large 3D datasets. In their seminal work Beucher and Meyer [155] used a series of top-hat operations to define markers at the centre of the objects of interest. More recently, authors [156]–[158] have used conservative operator defined global thresholds to place markers in XCT images. This is consistent with the approach recommended by the tutorials in Avizo [157].

Top-Hat Transforms

The top-hat transform is a morphological operation that can be used to enhance low contrast features in greyscale images. There are two types of top-hat transforms, the white top-hat (WTH) and the black top-hat (BTH) transform, that respectively enhance either bright or dark features from an image, irrespective of image illumination [139]. Mathematically they can be described as [155], [159]:

$$WTH = A - (A \circ B) \tag{3.4}$$

$$BTH = (A \cdot B) - A \tag{3.5}$$

Where A is the original greyscale image, $(A \circ B)$ and $(A \cdot B)$ are the resultant images after morphological opening and closing of the input image A, and B is the structuring element that performs these operations [160]. B has both shape and size, both of which are user selected to enhance the features of interest, with only features that fit within B being enhanced. The transformed images can then be thresholded to segment out the enhanced features. An example of the use of a BTH transform for image segmentation is shown in **Figure 3.13**.

The top hat only draws out small or low contrast features from the image and therefore is often used in conjunction with other techniques – such as global thresholding – to obtain a thorough image segmentation.

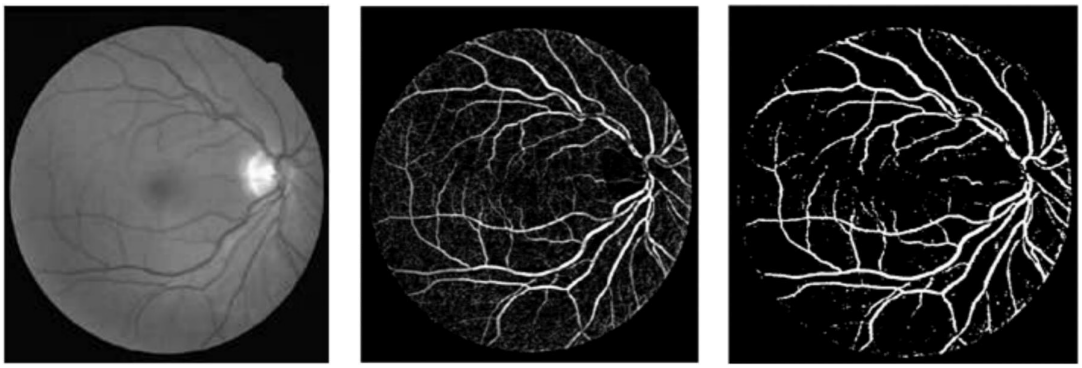

Figure 3.13 Example of the use of a black top hat (BTH) transform applied to segment vascular networks in the human retina; showing a) the input (greyscale) image, b) the BTH transformed image (greyscale), and c) the binarized image after global thresholding. A key observation is that the vascular networks have a non-uniform intensity in a). Images adapted from Khdhair et al. [159].

3.6.3 Quantitative Analysis

Quantitative measurements are performed on the objects that were defined from the image during the segmentation stage. Groups of pixels and voxels are considered to be connected and part of the same object if they share a face, vertex, or an edge (only for voxels) with their neighbours, depending on the user preference.

When performing quantitative XCT measurements it is not uncommon to impose a minimum size threshold for analysis of segmented objects. Commonly a minimum of 8 voxels has been taken as the minimum size limit [121], [128], [148], [161], as noise and sub-voxel objects cannot otherwise be resolved confidently from smaller features. In addition, it is also common to impose a limit of 125 voxels for morphological analysis, as objects smaller than this appear increasingly polygonal due their discrete voxel representation and therefore their morphologies becomes increasingly difficult to accurately measure, as is illustrated in **Figure 3.14**. The results of Patterson et al. [162] have indicated that objects should be at least 5 voxels in each dimension, in order to keep errors to a minimum. Hence resolution limits should always be kept in mind when using XCT or any form of DIA.

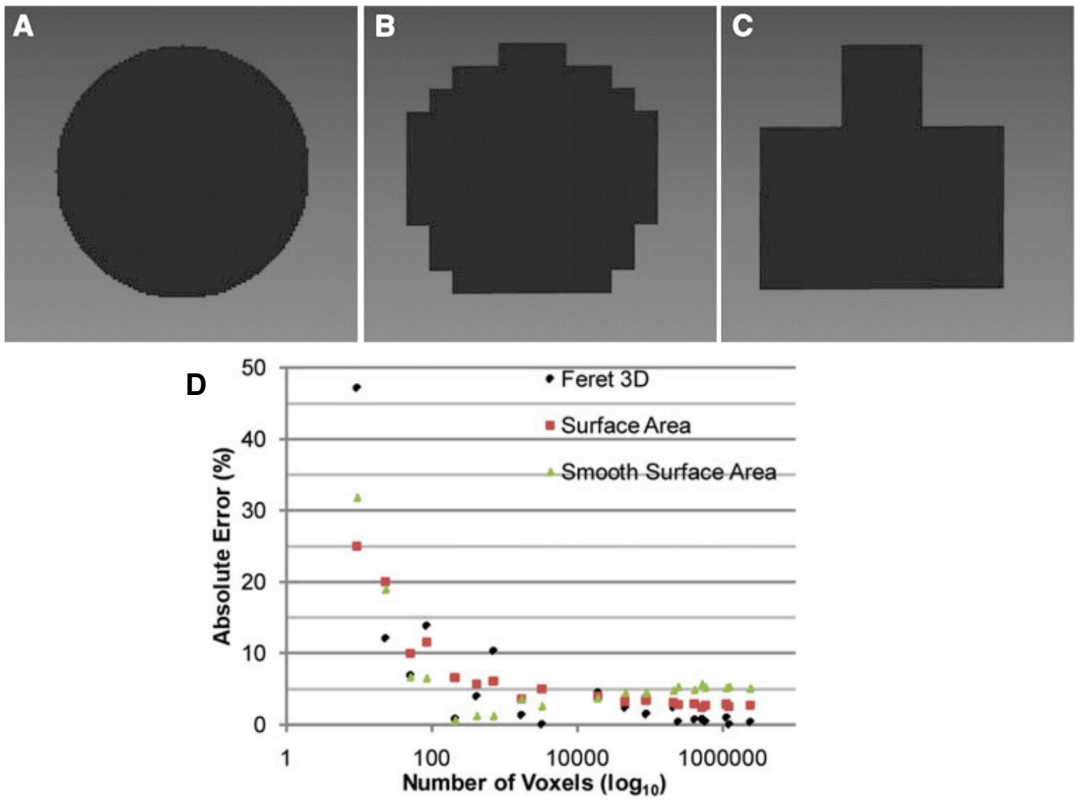

Figure 3.14 An example in the loss in the accuracy of XCT in determining the shape of a cylinder as the number of voxels decreases. Showing the cross-section of a cylinder A) 100 voxels wide, B) 11 voxels wide, and C) 3 voxels wide. D) Shows the absolute measurement error of various values of cylinders as a function of voxel size. Adapted from Patterson et al. [162].

Part II
Materials & Methods

Chapter 4

Foundry & General Characterisation Methods

The main areas of experimental work presented in this thesis are:

1. The effect of melt quality, which in this work is the combined hydrogen and oxide level of the metal, on gas porosity formation during solidification. And,
2. The effect of TiB_2 grain refiner on gas porosity formation during solidification.

This chapter lays out the foundry methods that were used when conducting the experimental work, along with some typical characterisation methods too.

4.1 Materials & Melt Preparation

4.1.1 Alloy Selection

Binary Al-7Si (wt.%) alloys were the primary experimental material that were used for the vast majority of the experimental work. This alloy was selected due to its similarity to the widely commercially used 7wt%Si casting alloys A356 and A357, which feature the desirable casting characteristics of good fluidity and low shrinkage during solidification [17], [163]. However, unlike its commercial counterparts, the binary Al-7Si experimental alloys do not (normally) form MgO or $MgAl_2O_3$ due to the absence of magnesium [71], [164]. It was believed that their absence would help in simplifying the investigations.

4.1.2 Melt Preparation

A fresh melt was made-up in house at the beginning of each experiment, using a Ramsell-Naber resistance heated furnace with an uncoated Noltina Stabil crucible. Each melt that was made was between 40 and 55 kg, as it was found that the hydrogen content of larger melts was generally more stable than smaller melts. Throughout all experiments, each melt was held at a constant temperature of $750 \pm 5°C$.

Alloying

Al-7Si alloy was produced in-house at the beginning of each experiment by adding pieces of Al-50Si master alloy waffle into a base melt comprised of commercially pure (CP) aluminium ingots and leftover Al-7Si alloy from earlier experiments. Following the addition of the waffle, the melt was held for 30 minutes and intermittently stirred to aid dissolution of the waffle and to ensure compositional homogeneity in the melt.

Because it was necessary to make up a fresh batch of metal for each experiment, one of the intrinsic errors of this research is the small variance in the composition of the alloy. The compositional tolerance was to ±0.5Si, which is in line with common commercially used tolerances [17], plus any trace impurities of other elements that were carried through from the base materials.

Holding for Hydrogen Equilibration

After alloying, all melts were held for at least one hour to allow their hydrogen content to equilibrate and stabilise to ambient levels. This prevented spontaneous change at the start of the experiment. During this time the oxide was continuously skimmed-off or skimmed aside to facilitate hydrogen uptake.

General Melt Handling Practice

Prior to the taking of samples, the oxide and dross layer at the surface of the melt was skimmed off or gently pushed to one side using an iron spoon or iron blade. This was done in an attempt to prevent its incorporation into the sample so that only the entrained oxide was sampled, but also to avoid its incorporation into the bulk of clean melts (see Section 4.5).

All tools that came into contact with the molten metal in this work were coated with boron nitride (BN) spray and dried overnight. The BN coat minimised Fe pickup into the melt from the tools, and the overnight drying was performed as a safety precaution to avoid contact of moisture with the molten metal.

4.1.3 Measurement of Alloy Composition

The alloy composition of the melt was measured using a Spectrolab LAVFA05A spark analyser optical emission spectrometer (OES) from disk mould castings. The castings that were taken at the beginning of each experiment were used for determining the melt composition.

Prior to analysis, the disk mould castings were prepared by facing them with a lathe to remove 2mm of material. Their face was then ground to a 1200 grit finish with SiC paper to improve the surface finish. To remove any embedded SiC particles, the samples were polished on a polishing wheel with water at high RPM, and then cleaned with ethanol. At least 5 measurements were taken over the face of the sample and averaged to give the reported composition. Nevertheless, minor SiC surface contamination may have remained from grinding, which would introduce a small error in the measurements.

4.2 Measurement of Melt Hydrogen Content

The melt hydrogen content in each experiment was measured using an ABB AlScan Model F – known herein as simply as the 'AlScan' - details of which have been given in Section 2.3.4. The LECO method – known herein as LECO – was used for the measurement of the hydrogen content in experiment GR1 of the grain refiner studies.

The AlScan probe and thermocouple were immersed approximately 10 cm sub-surface into the melt. Measurements with the AlScan were taken continuously, with 15 minute sampling times, using the probe oscillation function to improve hydrogen pickup by the instrument and the response of the measurements.

An alloy factor correction of 0.83 was used to account for the decreased solubility of hydrogen in Al-7Si alloys; this was calculated using Equation 2.8 [34]. The first 'breaking in' scan of each AlScan probe each day were discarded, as it is considered unreliable compared to subsequent measurements. The accuracy of this technique was taken to be 0.01 ml $100g^{-1}$ or ±5% of the measurement, whichever is higher [34].

4.3 Melt Cleanliness Measurement & Oxide Characterisation

A Prefil (ABB Inc.) was used to sample the melt in each of the experiments for subsequent melt cleanliness analysis by Premetz, PoDFA, and SEM. Details on the Prefil and these analysis techniques have been given in Section 2.5.7.

4.3.1 Melt Sampling

Samples were taken from the melt using a BN-coated ladle, taking care to avoid incorporation of the surface oxide of the melt. The sample was then poured into the Prefil by

pouring gently down the wall of the crucible so as to minimise turbulence and splashing, which would otherwise generate and entrain additional oxides. The Prefil test was initiated when the melt sample had reached a temperature of 720°C.

4.3.2 Premetz Analysis

Premetz [89] was used to correct for spurious variations in Prefil filter permeability and calculate the MC value based on the filtration curve.

4.3.3 PoDFA Assessments

The Prefil filter residues (known as the Prefil samples) were sectioned, prepared, and analysed by N-Tec Ltd. (Oxford, United Kingdom), authorised PoDFA licensees. Analysis was performed using the metallographic parameters listed in **Table 4.1**, within the area of inclusion band just above the filter as indicated in **Figure 4.1 a)**. **Figure 4.1 b)** shows a typical micrograph on which the analysis was conducted in order to give the reader an idea what can be reliably seen during the analysis.

Table 4.1 Nominal metallographic parameters used in the PoDFA analyses.

Filtered weight of metal Used for normalization	1.41 kg (nominal)
Method *Counting Method*	GRID
Optical Magnification	100×
Measured chord length of analyzed section	12.5 mm

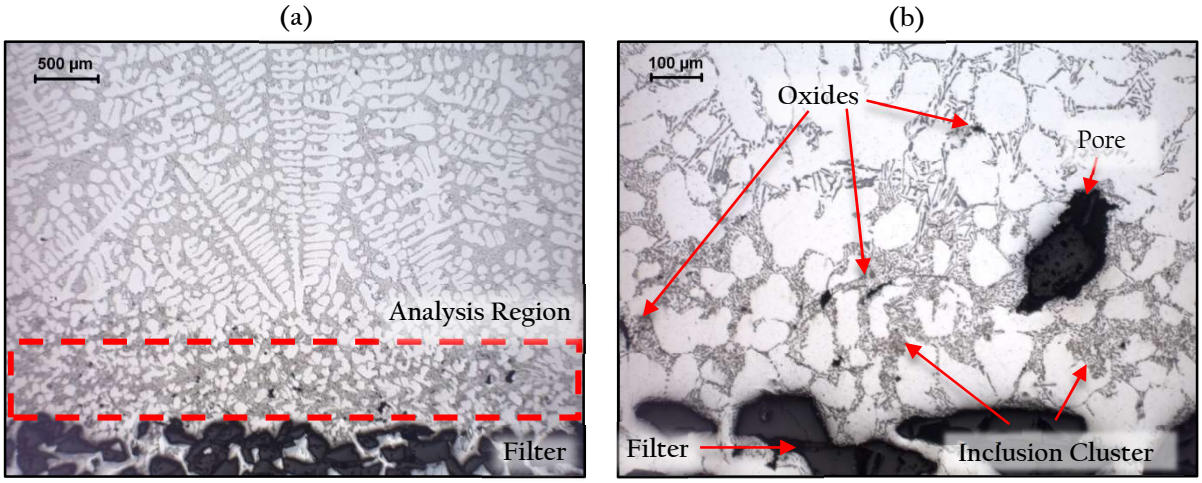

Figure 4.1 Visual light (optical) micrographs of Prefil residues showing a) the inclusion band within which the PoDFA analysis is conducted, and b) a typical micrograph taken at 100× magnification.

4.3.4 Scanning Electron Microscopy (SEM) Microanalysis

Scanning Electron Microscopy (SEM) was performed on the Prefil samples for further analysis of the inclusion populations. The samples were prepared by grinding using SiC paper to a 2000 grit finish, and then polishing to a 1 µm finish using a diamond suspension.

A Zeiss Evo was used as the standard instrument for imaging and elemental analysis. Backscattered Electron (BSE) imaging was used to observe oxides films in the samples from

the Melt Quality experiments, and analysis of the grain refiner rod in the Grain Refiner experiments; and EDX spectroscopy was used for compositional analysis of the inclusions.

High resolution SEM was performed on selected samples using a Zeiss Merlin instrument for imaging and EDX spectroscopy of small boride inclusions in the Grain Refiner Addition experiments.

4.4 The Reduced Pressure Test

The Reduced pressure test (RPT) was used as the primary mode of casting in this work, and was used to produce samples with gas pores of amplified size, which allowed the effects of hydrogen and oxide film content, and TiB_2 addition to easily be examined. The increased size of gas pores helped overcome the FOV – voxel size trade-off of XCT, which allowed for entire RPT samples to be assessed using (macro-) X-Ray CT.

The following RPT parameters and sampling procedure were adopted for use in experimental work. The RPT parameters were determined from the experimental investigation which is presented in Appendix IV.

4.4.1 RPT & APT Samples

When performing each RPT, two identical samples were taken together in the thin-walled steel cup-moulds, one of which was solidified under partial vacuum (80 mBar) inside the RPT apparatus' chamber, while the other was solidified under atmospheric pressure on top of the RPT apparatus (as shown in **Figure 4.2**). Here, for added clarity the samples that were solidified under partial vacuum will be referred to as *RPT samples* (as is the convention),

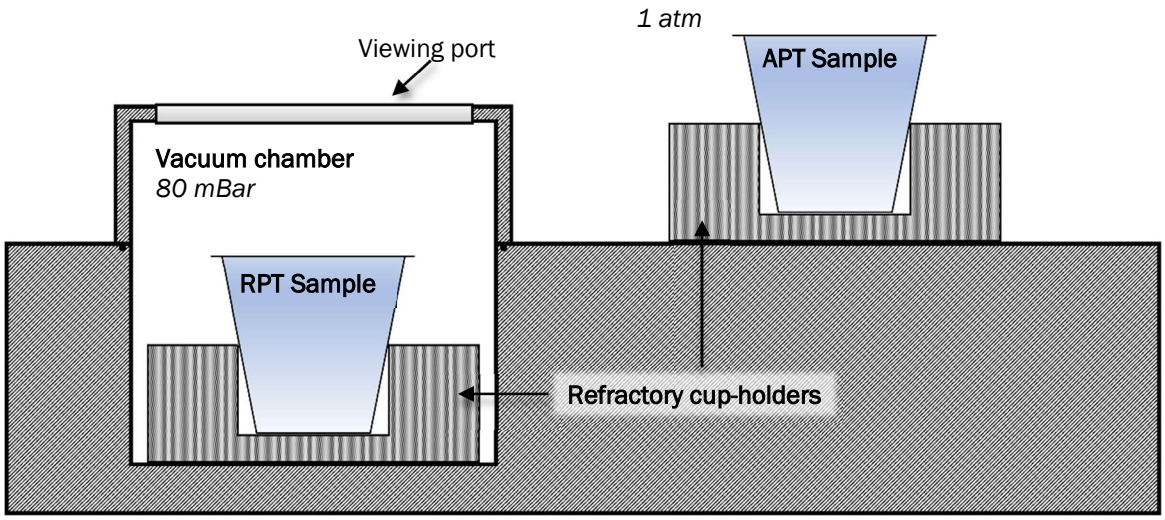

Figure 4.2 Schematic of the RPT showing RPT and APT samples.

while the samples solidified under atmospheric pressure will be referred to as *APT samples* (which is a little unorthodox).

4.4.2 RPT Procedure

Rather than the conventional approach of pouring a sample of melt into an RPT cup, in this work a sample was directly collected in the BN-coated RPT cup by immersing it into the melt using BN-coated tongs. The cup was held subsurface for 30 seconds to allow them to heat to melt temperature (750± 5°C) before it was removed, and the RPT commenced. The parameters used for the RPT in this work are given below in **Table 4.2**. The RPT took approximately 1 minute to obtain a 80 mBar vacuum after sample insertion, though with the given conditions, the samples were still in the molten state at this time. In addition, during upgassing, samples were taken on the opposite side of the crucible from the diffuser so as to avoid pickup of suspended bubbles.

Table 4.2 RPT parameters used in this work.

Parameter	Value
Vacuum pressure	80 mBar
Test (Vacuum) Duration	9 minutes
Cup temperature	750± 5°C
Cup holder temperature	Room temperature

4.4.3 Density & Volume Fraction Measurements

The first step in characterising the porosity in the RPT samples was to calculate the overall fraction of porosity (f_p) within them, which was done based on direct density measurements.

The density (ρ) of the RPT samples was determined by weighing them using an MK 1610 density balance, with a resolution 0.01 g. Standard procedure calls for each sample to first be weighed in air prior to immersion, and then again when immersed in water, which can then be used to determine the density using Archimedes' Principle. However, this does not account for open pores. Therefore, the samples was weighed again in air after immersion, with its outer surfaced dried off, so that the mass of water in the interconnected surface pores could be accounted for (at least partially). The sample density, inclusive of the open pores could then be determined using a modified equation of Archimedes' principle:

$$\rho = \frac{m_a}{m_{a_2} - m_w}\rho_w \tag{4.1}$$

Where m_a, m_w, and m_{a_2} are the mass of the sample in air, the mass when immersed, and the mass in air after immersion, respectively, and ρ_w is the density of water, 0.998 g cm^{-3}. For each measurement the sample was weighed repetitively until a stable reading was obtained

3 successive times to improve accuracy. Although the resolution of the balance was 0.01 g, the maximum measurement uncertainty was taken as ± 0.02 g, the typical variability.

The density was then used to calculate the volume fraction of porosity (f_p) in the samples:

$$f_p = \left(1 - \frac{\rho}{\rho_t}\right) \times 100\% \tag{4.2}$$

Where ρ_t is the theoretical alloy density, calculated to be 2.67 g cm^{-3} using MTData thermodynamic software with the MTAL database v6.1 [165]. This was validated with complimentary calculations using the rule of mixtures. Unless otherwise stated, this was the standard method by which f_p was determined, and not by metallography or macro-CT. The maximum variation in the calculated value of f_p is given in Appendix II.2.

For simplicity, the f_p was used in favour of the common of density index (*DI*) measurement (See Section 2.6). This was because it allowed for a single RPT sample to be cast and weighed, rather than two, but also eliminated errors arising from spurious variations in density of the APT samples. For the reader's reference, there is a linear relationship between f_p and *DI* as shown in **Figure 4.3**, and follows:

$$f_p = DI \times 1.158 \tag{4.3}$$

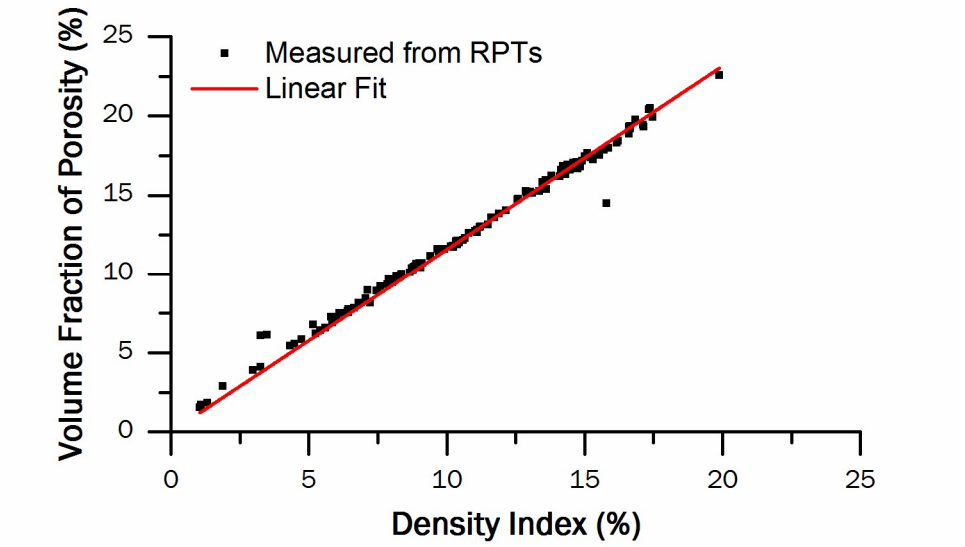

Figure 4.3 Relationship between DI and f_p for RPT samples taken during this work.

4.4.4 Advantages of this Procedure

The sampling method where the RPT cup was immersed into the melt was adopted in favour of the conventional method where the cup is pre-heated and the melt is poured into it, because it conferred the advantages of:

- Allowing better control of the initial sample temperature, ensuring that the vacuum would be applied at a consistent time before the sample began solidifying. Whereas sampling with an iron spoon may lead to variable pouring temperatures due to the siphoning of heat from the melt sample by the implement.
- Eliminating oxide entrainment during pouring of the melt, and any variability in the oxide content between samples from differences in pouring heights / melt turbulence.
- Improved the reproducibility of the sample masses. Though generally non-critical, it prevented overfilling of the metal onto the cup's brim – as may happen when pouring

with an iron spoon. Cups filled to the brim would often form abnormal porosity in this region during the RPT.

4.5 Melt Quality Experimental Procedures

In the second phase of experiments, the effect of two of the key components of melt quality, hydrogen content and oxide content, on porosity formation were investigated.

A series of experiments were conducted, in which different melt treatments or combinations of melt treatments were performed in order to manipulate the hydrogen and oxide contents of the metal. A summary of the four experiments that are presented in the body of this work is given below in **Table 4.3**, their experimental procedures are laid out in sub-sections 4.5.1 to 4.5.4, while specific details their melt treatments are described in 4.5.5. Another experiment, DMX, was also performed, though this work is presented in Appendix III.1, as it proved less critical to the thesis than the other experiments.

Table 4.3 IDs and nominal melt cleanlinesses of each experiment in this work. *Clean Metal* refers to a metal that is relatively low in entrained oxides compared to a *Dirty Metal.*

ID	Melt Treatment
CM1	**Clean Metal** Self-cleaned (holding) & upgassed.
CM2	**Clean Metal** Fluxed & upgassed.
DM	**Dirty Metal** Al-7Si Swarf chips added.
RD	**Degassed Metal (Unknown Cleanliness)** Rotary treatment.

4.5.1 Experiment CM1: Self-Cleaned & Upgassed Melt

This experiment aimed to produce a clean metal with low entrained oxide content and a range of hydrogen contents. The workflow of this experiment is shown in **Figure 4.4**. Over the course of the experiment care was taken to handle to melt with care during skimming to prevent oxide film entrainment.

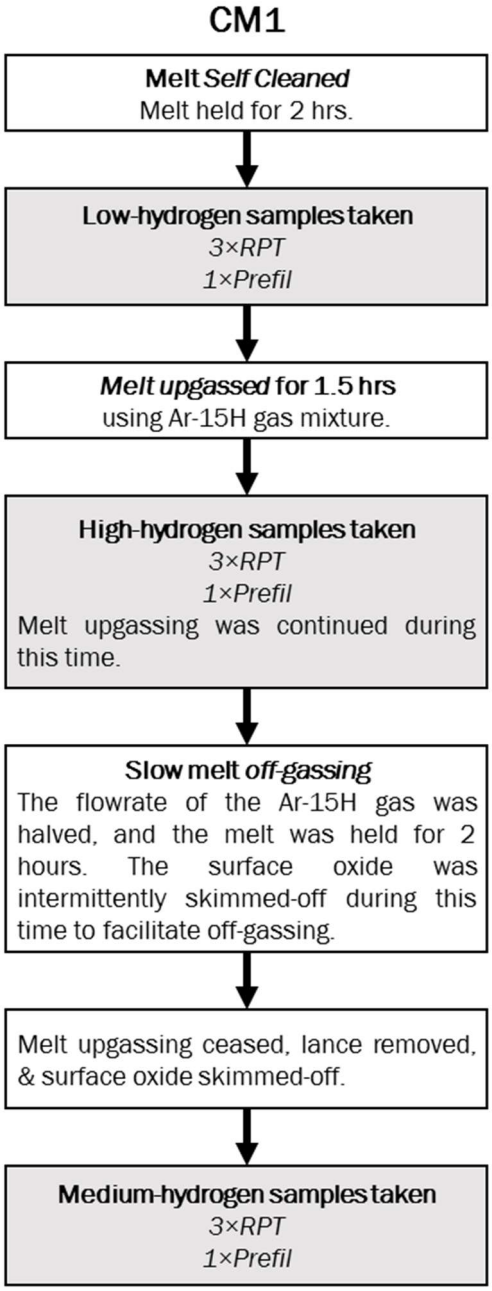

Figure 4.4 Experimental procedure for experiment CM1.

4.5.2 Experiment CM2: Fluxed & Upgassed Melt

This experiment was a follow up to CM1 with minor improvements. The melt was again cleaned and upgassed with the aim of casting RPT samples with a range of hydrogen contents from the clean melt. Over the course of the experiment care was taken to handle the melt with care during skimming to prevent oxide film entrainment. A workflow of the experiment is shown in **Figure 4.5**. Details of the fluxing are given in **Table 4.4**.

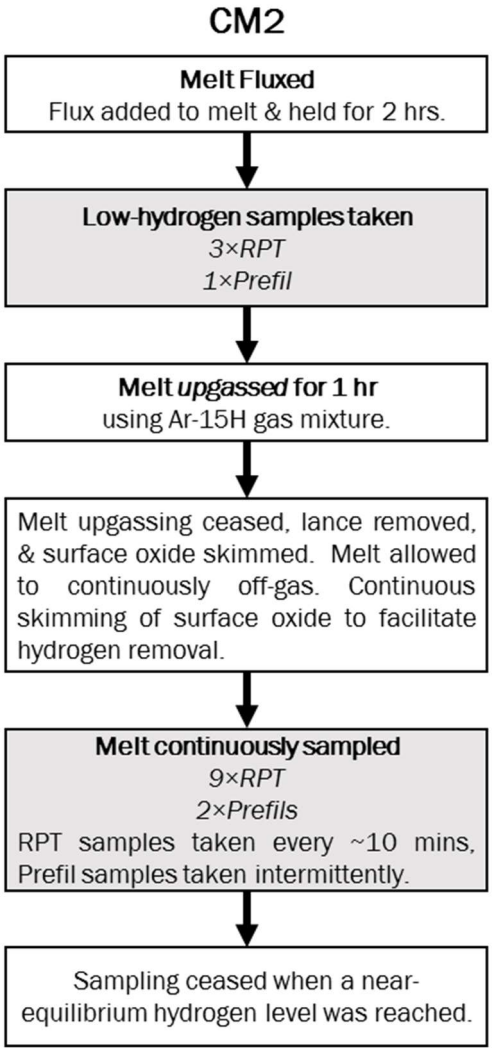

Figure 4.5 Experimental procedure for experiment CM2.

4.5.3 Experiment DM: Upgassing & Swarf Addition

An attempt was made at dirtying the melt by adding swarf chips into it to increase its oxide content. A work flow of the experiment is shown in **Figure 4.6**, and details of the dross addition are given in **Table 4.4**.

During this experiment it was necessary to manually *top-stir* the melt as shown in **Figure 4.7** in an attempt to reincorporate the oxide films prior to each sample being taken because of the propensity of the oxide films to float to the surface of the melt into dross layer over time. Following stirring, the dross layer was skimmed aside to reduce its pickup on the top of the samples. However, in practice, a portion of the dross inevitably picked up on top of the RPT samples. After the first 4 RPT samples were taken the decision was made to skim off a fraction of the dross which reduced its pickup on the top of the surfaces of the samples.

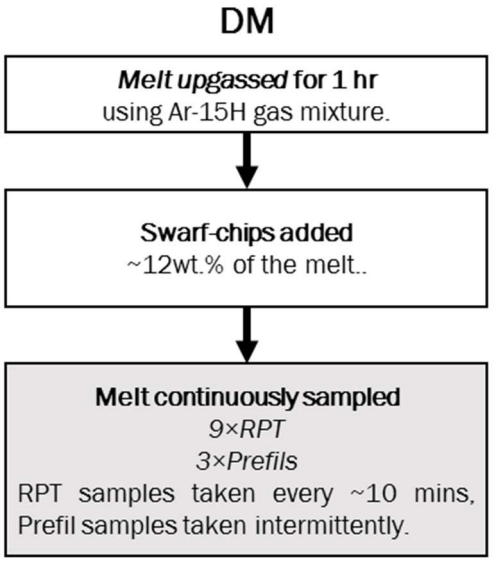

Figure 4.6 Experimental procedure for experiment DM.

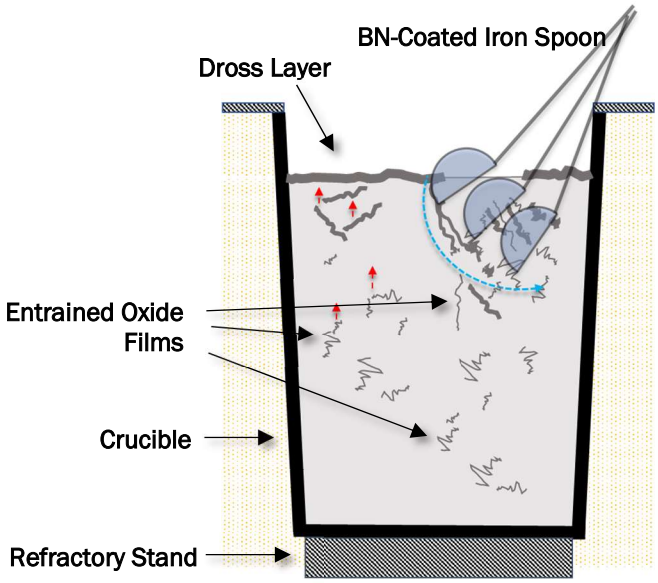

Figure 4.7 A diagram showing top-stirring technique employed in *DM* to reincorporate floated doss. The red arrows indicate the propensity of the oxide films to float out of the melt over time.

4.5.4 Experiment RD: Rotary Degassed Melt

In this experiment, the melt was rotary degassed with the aim of casting RPTs with a low hydrogen content. It was not certain as to what melt cleanliness would be obtained as this treatment is widely considered to clean metals [4], [101], but anecdotal evidence ran counter to this [46]. The experimental procedure for this experiment is shown in **Figure 4.8**, and details on the degassing procedure are listed in **Table 4.4**.

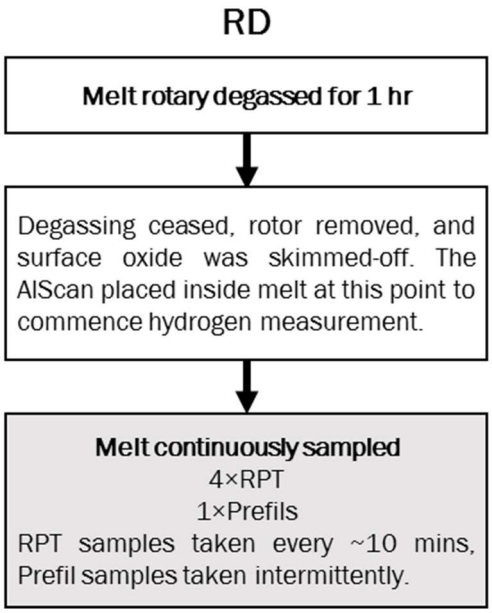

Figure 4.8 Experimental procedure for experiment RD.

4.5.5 Summary of Melt Treatments

Details of each of the specific melt treatments that were performed in these experiments are listed in **Table 4.4**.

Table 4.4 Melt treatment procedures used during the melt quality experiments.

Melt Self-Cleaning (CM1, CM2, & DM)	*Self-cleaning* was the straight approach of holding the melt for 2 hours to allow time for the flotation or sedimentation of suspended inclusions. Further information on this is given in Section 2.5.7. Floated inclusions were removed by periodically skimming-off the dross-layer during this time. Srimanosaowapak [166] estimated using Stokes' law that most of the largest inclusions would sediment out of the melt within this two-hour time frame, though very small inclusions would remain suspended inside the material. During holding and for the remainder of the experiment, the body of the melt was disturbed minimally (e.g. no stirring) to prevent resuspension of settled inclusions.
Melt Fluxing (CM1)	Flux was added to the melt at the beginning of experiment CM2 in an attempt to further lower the oxide content below that achieved in CM1. This would have also had the effect of removing any dissolved alkalis from the melt [167]. 0.08% by mass of Refinal X350XF (MQP Ltd.) flux and was stirred in manually using a BN-coated iron spoon. The melt was then held for 2 hours to allow for the flux to act. During this time the melt would have had some degree of self-cleaning of other inclusions that were not-affected by the flux.

Table 4.4 continued over page

Table 4.4 continued

Swarf-Chip Addition (DM)	Swarf chips were added to the melt at the beginning of experiment DM. The chips were produced by turning down Al-7Si ingots - that were cast off at the end of DM1 - using a metal lathe. The chips were washed in a bucket that had a continuous flow of water through it to remove any cutting fluid. A broomstick was used to vigorously stir it, in an attempt to remove any cutting fluid. The material was then dried off holding it in an oven at 300°C for 2 days. Before being added into the melt, the swarf was heated in a separate furnace to ~580°C, into the semi-solid (mushy) state, over the course of 3 hours. Prior to addition the mush was then compacted down inside the holding crucible. The mushy swarf was then added into the melt to give a nominal constitution of ~12wt.%. It was added by plunging the mushy compact subsurface, and holding it there for ~2 minutes using a BN-coated iron implement. The melt was then vigorously hand stirred for ~3 minutes to aid its incorporation. The swarf constituted ~12% by mass
Rotary Degassing (RD)	Rotary degassing was performed on the melt at the beginning of experiment RD. Details of the general effects of rotary degassing have been given in Section 2.7.2. The rotor was selected as it was the only one that is owned by the group, therefore its geometry was not matched to the crucible. The graphite rotor that was used for this treatment was pre-baked at 350°C for 4 hours prior to use to remove any trapped moisture from inside it. Degassing was performed for 1 hr using 99.998% pure argon (from BOC) as the purge gas. The rotor was driven at a high, but unknown RPM (as no tachometer was available) using a pneumatic air motor specific for the purpose of degassing aluminium.

4.6 Grain Refiner Addition Experimental Procedures

In the third phase of experiments, the effect of grain refiner on porosity was investigated. Two nearly identical experiments were conducted (**Table 4.5**), GR1 and GR2, which involved the same procedure, though the former served as a forerunner to the latter. The grain refiner master alloy rods used in this were produced by different manufacturers, so there may be a difference in the quality between them.

Table 4.5 Summary of Grain Refiner Experiments

ID	Details
GR1	**TiB_2 Addition, Forerunner to GR2** Al-3Ti-1B master alloy rod added to give a concentration of 20 ppm of B.
GR2	**Tib_2 Addition, Improvement of GR1** Al-5Ti-1B master alloy rod added to give a concentration of 40 ppm of B.

4.6.1 Experimental Procedure

A workflow of the experimental procedure used in these experiments is outlined in **Figure 4.9**. Samples were taken in four melt conditions, the *Baseline*, non-grain refined condition; the *Grain Refined* condition, the *Settled* condition, and the *Restirred* condition. Specific details on each melt condition are as follows.

Baseline Melt Condition

During the sampling of the melt in the *Baseline* condition, the melt was manually bottom-stirred to resuspend any inclusions, so that a fair comparison could be made with the *Grain Refined* melt, which was constantly stirred to keep the grain refiner suspended in the melt.

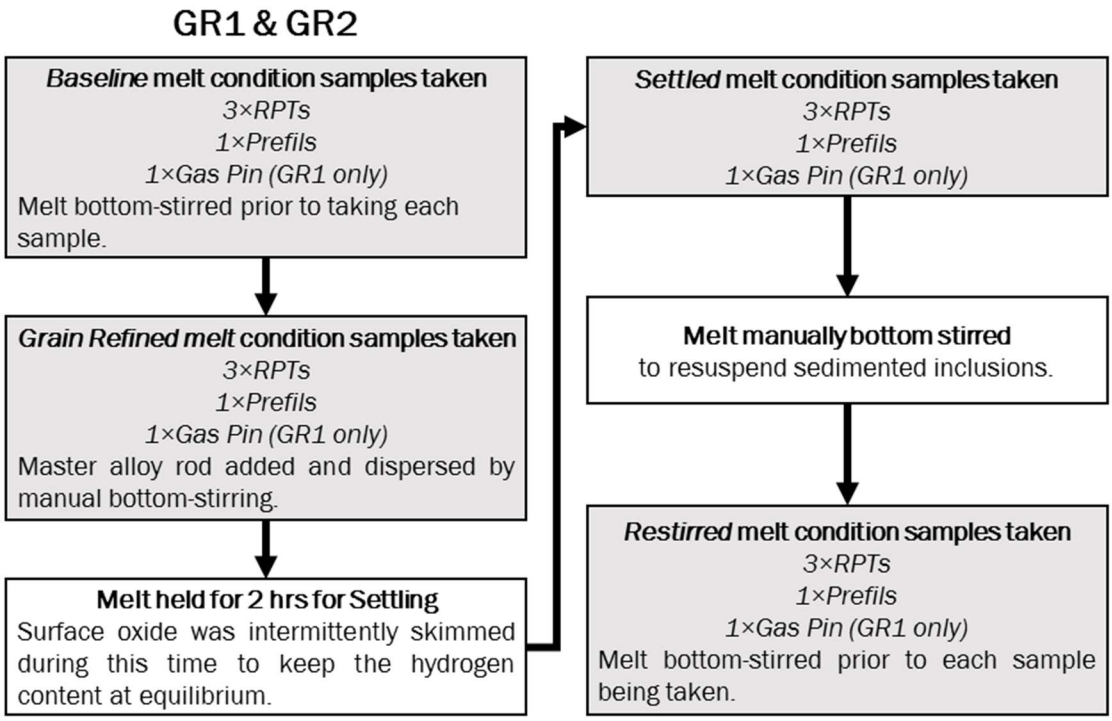

Figure 4.9 Outline of the experimental procedure of GR1 & GR2.

Grain Refined Melt Condition.

Al-3Ti-1B and Al-5Ti-1B master alloy rod was added into the melts in GR1 and GR2, respectively, to give 20ppm and 40ppm concentrations of B in the *Grain Refined* condition. Following the addition of the rod, the melt was manually mixed in by bottom stirring using a spoon to distribute the grain refiner as shown in **Figure 4.10**. In addition the melt was gently bottom stirred prior to taking each sample in this condition to ensure the TiB_2 was thoroughly dispersed.

Settled Melt Condition

When sampling the melt in the *Settled* condition care was taken to minimise incorporation of oxide or disturbance of the sedimented inclusions.

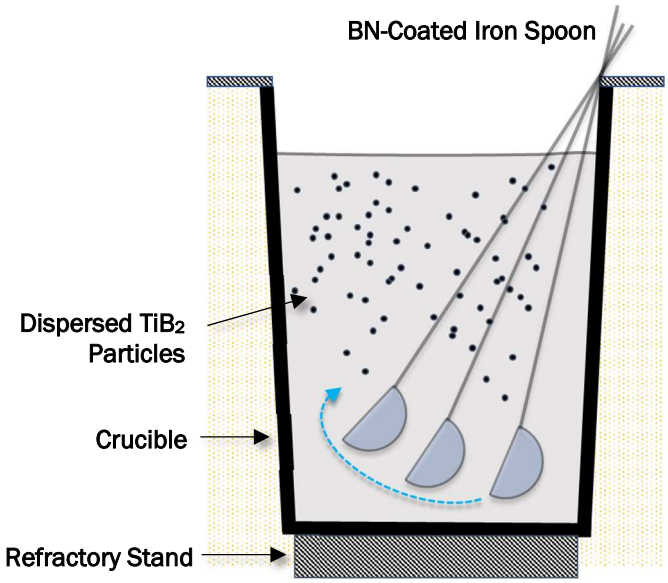

Figure 4.10 A diagram showing the bottom-stirring technique employed in the grain refiner experiments to disperse the TiB_2 particles throughout the melt.

Restirred Melt Condition

Sedimented inclusions were resuspended in the melt by bottom stirring. This was performed prior to taking each sample in this condition.

Hydrogen Measurement

It was not possible measure the melt hydrogen content in GR1 using the AlScan due to the absence of measurement probes at the time, therefore LECO was employed instead. The sampling procedure for LECO is detailed in Appendix II.1. The AlScan was used in GR2, and at least 2 hydrogen measurements were taken for each melt condition.

4.6.2 Grain Size Analysis

The grain structure of sectioned RPT samples was revealed by first grinding their surfaces to a 1200 grit finish with SiC paper and then etching. The etching was performed by Yutaro Fujisawa, a summer-research student in the research group, and was done by first immersing

the samples in a cupric chloride solution (400 ml water + 20 g $CuCl_2$) for 10 s, followed by immersion in a 69% nitric acid solution for 20 s, and cleaning in water. This procedure produced a 'macro-etch' which was used for qualitative analysis of the grain structure.

Numerous additional attempts were made to obtain a 'micro-etch' of the RPT samples so that the grain size could be quantified, though this proved difficult for the Al-7Si alloy.

Chapter 5

Porosity Characterisation Methods

The first main area of work in this project was the development of the Digital Image Analysis (DIA) methodologies for the quantitative assessment of the structure of pores. From this work came three methods, which were employed throughout this work:

- metallographic analysis of pores in whole RPT samples,
- macro-CT analysis of pores in whole RPT samples, and
- micro-CT analysis of pores in samples cut from APT samples.

The metallographic and macro-CT methods form the foundation of much of this work, whereas the micro-CT is used in a more ancillary role to examine changes in the structure of pores formed under 'normal' atmospheric pressure. This chapter will cover the methodologies behind these techniques.

5.1 Porosity Analysis by Metallography

The first step was to develop a DIA procedure using Fiji image analysis software [168] that could be used for the assessment of the porosity in sectioned RPT samples.

5.1.1 Sample Preparation

Sample preparation was a critical step for this procedure, and involved the following steps:

1. The samples were cross-sectioned longitudinally down their approximate centres using an abrasive cut-off wheel. Both halves of each casting were then prepared and analysed.
2. The cross-sectioned faces of samples were then ground with 120 grit SiC paper at 250 RPM to smooth out the cut faces, and to remove burs of material and open any unopened pores.
3. A matte black acrylic based spray paint that adhered strongly to metal was applied to the cross-sectioned faces of the samples to completely coat the insides of the pores.
4. The spray painted faces of the samples were ground back with SiC paper to remove the black spray paint from the bulk metal face of the sample, but retaining the paint inside the pores – enhancing their contrast with the metal. The samples were ground through the grits to 1200.
5. The samples were washed by spraying ethanol on their surfaces and dried using a heat-gun.

5.1.2 Image Acquisition

Images of metallographic RPT samples were acquired by scanning the prepared cross-sectioned faces with an Epson Perfection 3490 flatbed scanner at a resolution of 3200 dpi (translating to a pixel size of ~7.9 µm per pixel). As shown in **Figure 5.1**, the greyscale ranges of the input- (the metallographic samples) and output-images (the digital image) these values were both set to the fixed range of 0 to 255, and the gamma value was set to 1.0, for all images. This ensured that images captured in successive scans had comparable greyscale ranges and were not automatically truncated to different ranges by the software. It also had the benefit of reducing the prominence of reflections in the image. A scanned image of a finished metallographic sample is shown in **Figure 5.2**.

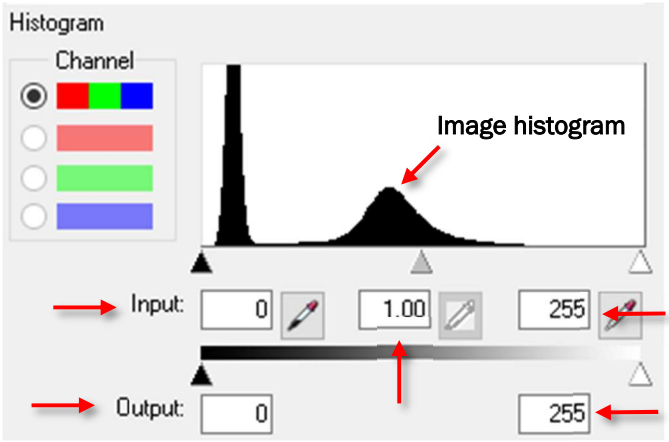

Figure 5.1 Image greyscale-mapping parameters on the EPSON Scan software user interface, with the key parameters indicated with red arrows.

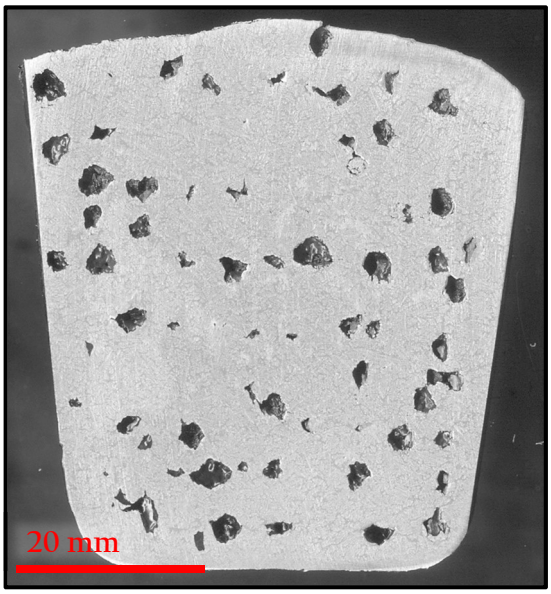

Figure 5.2 A cross-sectioned RPT sample prepared for quantitative metallography

5.1.3 Image Processing & Analysis

Processing and analysis of the scanned images was performed using Fiji [168], a plugin-inclusive distribution of ImageJ [113]. A simplified workflow of the procedure is given in Appendix II.3.

Image Processing

The 3200 dpi images were resampled to 1600 dpi (translating to a pixel size of ~15.8 µm per mm) using a bicubic interpolation algorithm to improve the signal to noise ratio. A non-local means (NLM) filter was then applied to the image using a plugin [169], [170] with the input parameters selected so that the metallic substrate was smoothed but with minimal loss in sharpness of the pore edges. An NLM filter was used as it gives better sharpness of edges compared to local means filters [137].

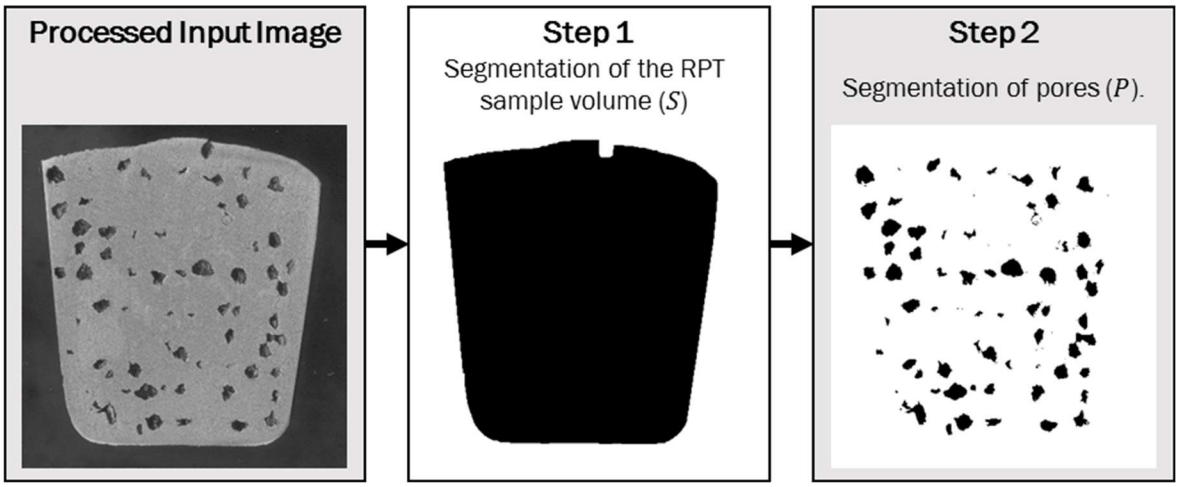

Figure 5.3 The 2 stage segmentation procedure in the metallographic images.

Image Segmentation

Segmentation of the images was performed in two main stages as indicated in **Figure 5.3**.

In Step 1, the RPT sample area (S) was segmented from the image background by global thresholding using Otsu's method [147]. The binarized image was then subjected to a sequence of morphological operations as follows:

1. erosion (50 iterations),
2. dilation (75 iterations),
3. flood-fill (fill holes), erosion
4. erosion (40 iterations).

The number of iterations for each operation was selected based on trial and error. The purpose of these operations was threefold: firstly, to remove non-contiguous pixels from the thresholded image; secondly, to fill in holes within the sample area, including open surface pores; and thirdly to shrink the analysis area away from the edges of the sample (omitting a boundary of 25 pixels) so that reflections from non-uniform grinding at the edges would be

omitted during further analysis. One limitation of this technique is that only surface pores with openings smaller than ~0.8 mm are closed by this sequence of operations.

In Step 2, the pores (P) were segmented using a combination of global-thresholding and a black top-hat (BTH) transform. During global thresholding, the threshold value was selected from the histograms of some metallographic images such that it was below the peak corresponding to the metallic substrate, as shown in **Figure 5.4**. Pores that were less than 100 pixels in area (~0.025 mm^2) were omitted from the global threshold at this stage to remove artefacts (namely reflections). This left only large gas pores in the segmented image.

The BTH transform was performed on the processed input image to draw out small features of pores which would then be combined with the global threshold image. A circular structuring element with a radius of 22 pixels (~0.35 mm) was used to transform the image. The small pore features in the transformed image were then segmented by global thresholding using a user defined threshold value of 50.

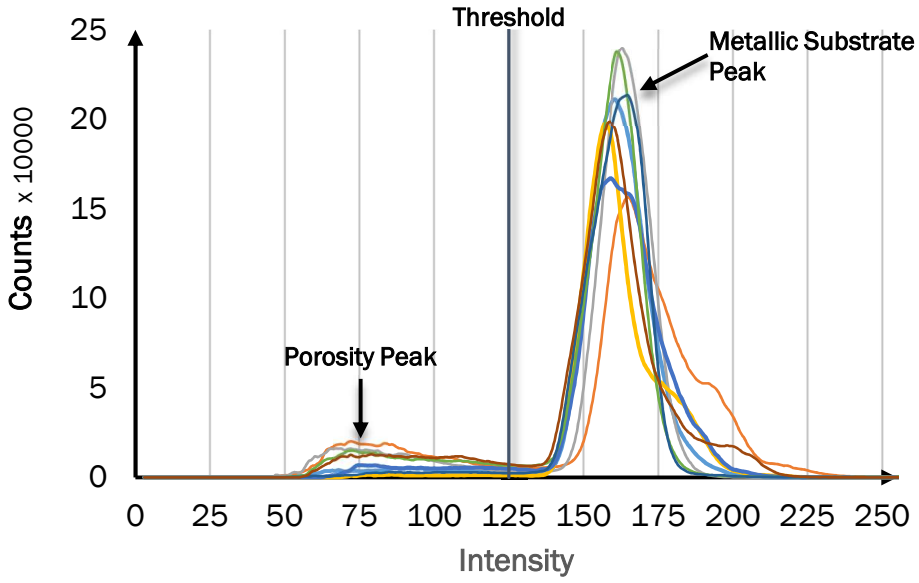

Figure 5.4 Global threshold selection for metallographic analysis.

The pores segmented by global thresholding and the BTH transform were then combined together into a single image, and were subsequently subjected to two iterations of a morphological closing operation to fill in any small holes in the pores arising from reflections or grinding marks inside them. This yielded P, an example of which is shown in **Figure 5.5**.

Analysis

The segmented images were analysed using ImageJ's inbuilt Particle Analyser feature [113] and the MorphoLibJ plugin package [171]. For each RPT sample, analysis was conducted on both halves of the sample.

Table 5.1 lists the main metrics that were measured by this technique.

Pores smaller than 44 pixels (an area = 0.0112 mm^2, or an equivalent circular diameter d_{eq}=0.12mm) were omitted from the analysis in order to prevent the incorporation of artefacts, such as scratches, spurious reflections – especially near the edges of the sample –

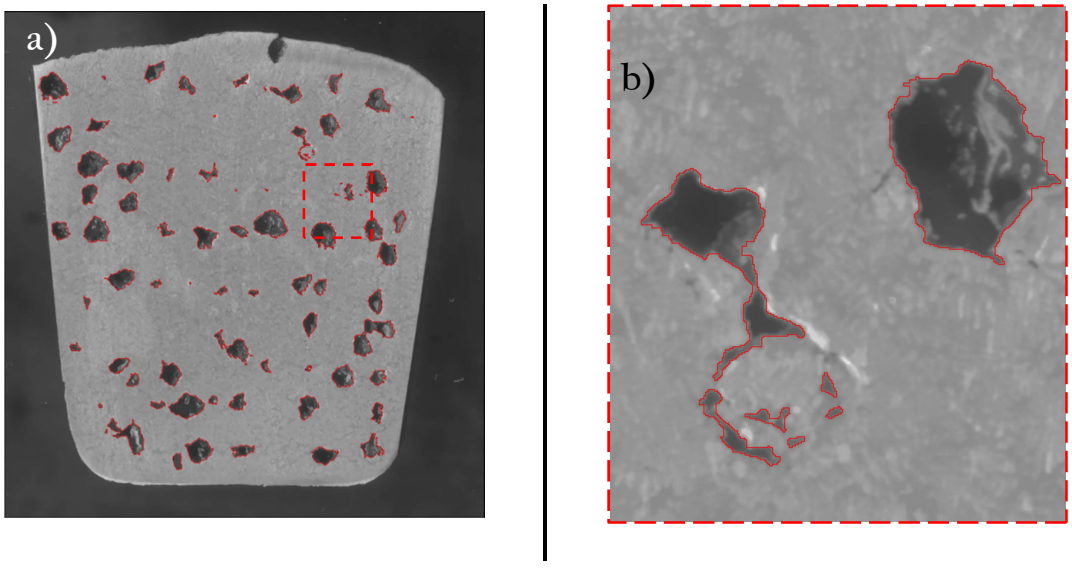

Figure 5.5 a) An example of the resulting segmentation from the metallographic analysis, and b) a close-up showing the segmentation of very fine pore features.

and silicon plates. The technique is therefore able to detect very fine features, but these very fine features are included if they are part of a pore greater than this size threshold. **Figure 5.5** b) shows, relatively small pores were still detectable by this analysis. Further details on measurements by this technique are given in Section 6.1.

Table 5.1 List of measured and derived metrics from the metallographic analysis of RPT sections..

Metric	Symbol	Description
Number of Pores	*N*	The number of pores in each sample.
Area	*A*	The area of pixels comprising a single pore.
Crofton Perimeter	*P*	An estimate of a pore's perimeter given by Crofton's Formula [172], which was measured using the MorphoLibJ plugin package [171].
Areal Pore Number Density	*PND*	The number of pores per unit area of the sample, given by: $$N_p = \frac{N}{A_{RPT}}$$ Where A_{RPT} is the area of the RPT sample.
Equivalent Diameter	D_{eq}	The equivalent circular diameter based on the pore area, given by: $$D_{eq} = \sqrt{\frac{4A}{\pi}}$$
Shape Factor (2D) or Circularity	*SF*	The degree of circularity of the pore given by [173]: $$SF = 4\pi\left(\frac{A}{P^2}\right)$$ Where $1 > SF > 0$, with pore circularity increasing towards 1.
Feret Diameter	D_F	The maximum point to point length across a pore.
Bifilm Index	*BI*	A modified version of the metric developed by Dispinar and Campbell for RPT assessment, given by [77]: $$BI = \sum D_F$$ Where, here, D_F is the Feret diameter (and not the usual 'major length' of the pore) in mm.

5.2 Porosity Analysis using Macro-CT

The second step in the area of work was to develop a workflow for assessing the porosity in the entire volumes of RPT samples using XCT. This was referred to as macro-CT.

5.2.1 Acquisition & Reconstruction

The acquisition and reconstruction of all of the macro-CT scans was performed by Dr Andrew Lui, of the Department of Materials, University of Oxford.

Acquisition

Macro-CT scans of the RPT samples were performed using a North Star Imaging (NSI) ImigiX CT machine, using the *vorteX* method. This involves performing a helical scan on the data where the sample is simultaneously moved vertically while it is rotated, giving it a cork-screw trajectory during acquisition of the projection images. The key scan parameters are given in **Table 5.2**; all scans were scanned using the *Precise* scan settings, which governs the quality of the output image.

The number of projections that contributed to each voxel, the *Equivalent number of Projections*, was 1440 for all of the scans. This can be calculated, but is not derived here, as the workings of the software are NSI proprietary and are currently pending patent approval.

Table 5.2 Macro-CT helical scan parameters.

Parameters	Value
Detector Type	*Varian PaxScan®1313DX* (16-bit)
Scan Voltage	150 kV
Current	140 µA
Focal Spot Size	20 µm
Beam Filter	0.8 mm Cu Plate
Exposure Time	500 ms
Nominal Source-Sample Distance*	230.00 mm
Nominal Sample-Detector Distance*	426.55 mm
Binning	1
Projections Averaged	2
Image Variation Limit	8%
Vortex Scan Settings	
Scan Setup	Precise
Equivalent Projections	1440
Nominal Voxel Size	44 ±1 µm

* Occasionally varied to accommodate the edges of larger samples, which resulted in a slight variation of the voxel size in these scans.

† Varied depending on the height of the sample

Reconstruction

Following acquisition, reconstruction and pre-processing of the data were performed using NSI's efx-CT software. Reconstruction was performed using NSI's VorteX algorithm, which is based on the Feldkamp algorithm [130]. The rotation axis shift was determined manually by the operator by selecting the reconstruction parameters that gave the sharpest detail in a sample cross-sectional slice of the XCT data; and a beam hardening correction factor of 0.1 was applied to the data. Finally, the data were saved as .nsidat files, NSI's

proprietary floating point image format, with a 32-bit depth – though because the analogue to digital (A/D) conversion of the detector was 16-bit depth, the images also effectively had 16-bit depths.

5.2.2 Image Processing & Analysis

The macro-CT data were processed, segmented, and quantitatively analysed using Avizo software (Thermo-FisherTM Scientific, versions 9.0 through to 9.5) as detailed in the following subsections. Unless otherwise stated, all operations were applied to the 3D image. An example 3D reconstruction and 2D slice of macro-CT data are shown in **Figure 5.6**. A flowchart and supplementary information on the segmentation procedure are given in Appendix II.3.

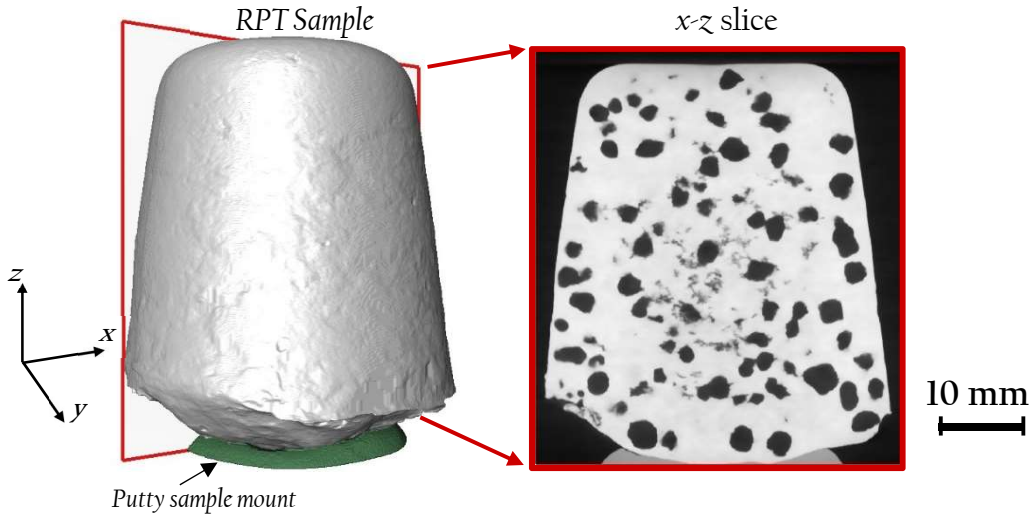

Figure 5.6 3D reconstruction & 2D slice of macro-CT data. Note that the RPT samples were usually inverted during scanning to minimise sample movement which can generate artefacts in XCT images.

Image Processing

The 32-bit image data were down-sampled to 8-bit to save on computational power for subsequent processes, with the intensity range carefully selected to include only the non-zero data range. Following conversion, the images were denoised using a non-local means (NLM) filter applied in 2D to the *x-y* planes (transverse sections) of the data. This type of filter was selected as it better preserved the sharpness of the edges of pores compared to local-means filters [138], [142], especially the edges of small less prominent pores in the image. The effect of this filter can be seen by comparing the images in **Figure 5.7**.

Segmentation

The processed images were segmented in a four-step process using as outlined in **Figure 5.8**.

In Step 1, the RPT sample from the image using the Marker Based Watershed Transform (MBWT) applied to the 3D image. The gradient image used in the process (**Figure 5.9** a)) was calculated using the Canny-Deriche method [174], and markers for this process (the points which the segmented phases/objects are initially grown from) were defined manually by the user using the *paint brush* tool at this stage as shown in **Figure 5.9** b). It should be noted that the 'image background' in this case is comprised of the black background and the sample holder (as they are not features of interest).

Although manual, the outcome is largely insensitive to operator bias provided that the markers are placed in clearly distinct regions as shown. Open pores at the surface of the segmented RPT sample were closed and filled using the following series of the following morphological operations (applied in 3D):

1. dilation (13 iterations),
2. flood-fill (fill holes), and
3. erosion (16 iterations).

Surface pores with openings smaller or equal to 26 pixels (~1.1 mm) in diameter were filled by this procedure, so that they were included in the analysis (they would otherwise be considered part of the image background). It was also necessary to omit a boundary of 3-pixels (130 µm) around the edges of the RPT samples due to beam-hardening at the sample edges, which otherwise would be problematic for subsequent thresholding and top-hat operations. This yielded the closed RPT sample volume (S) within which subsequent porosity analysis was performed.

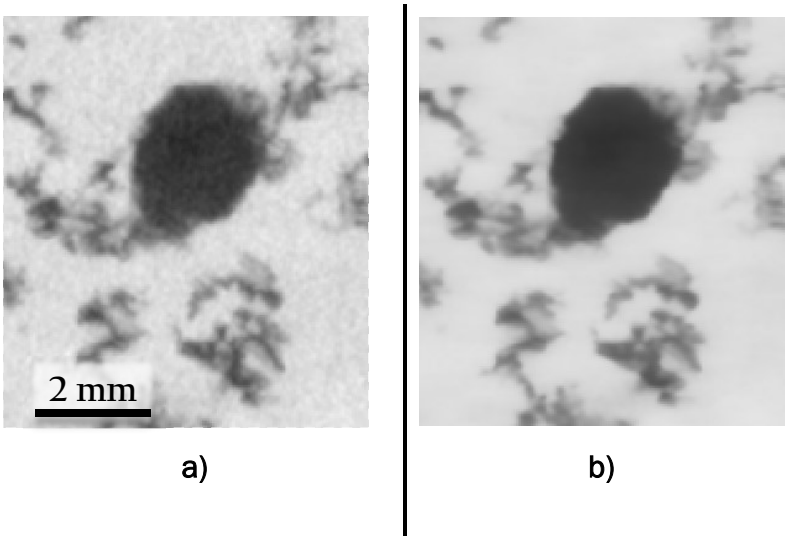

Figure 5.7 Close-up of an x-z macro-CT slice a) before and b) after denoising.

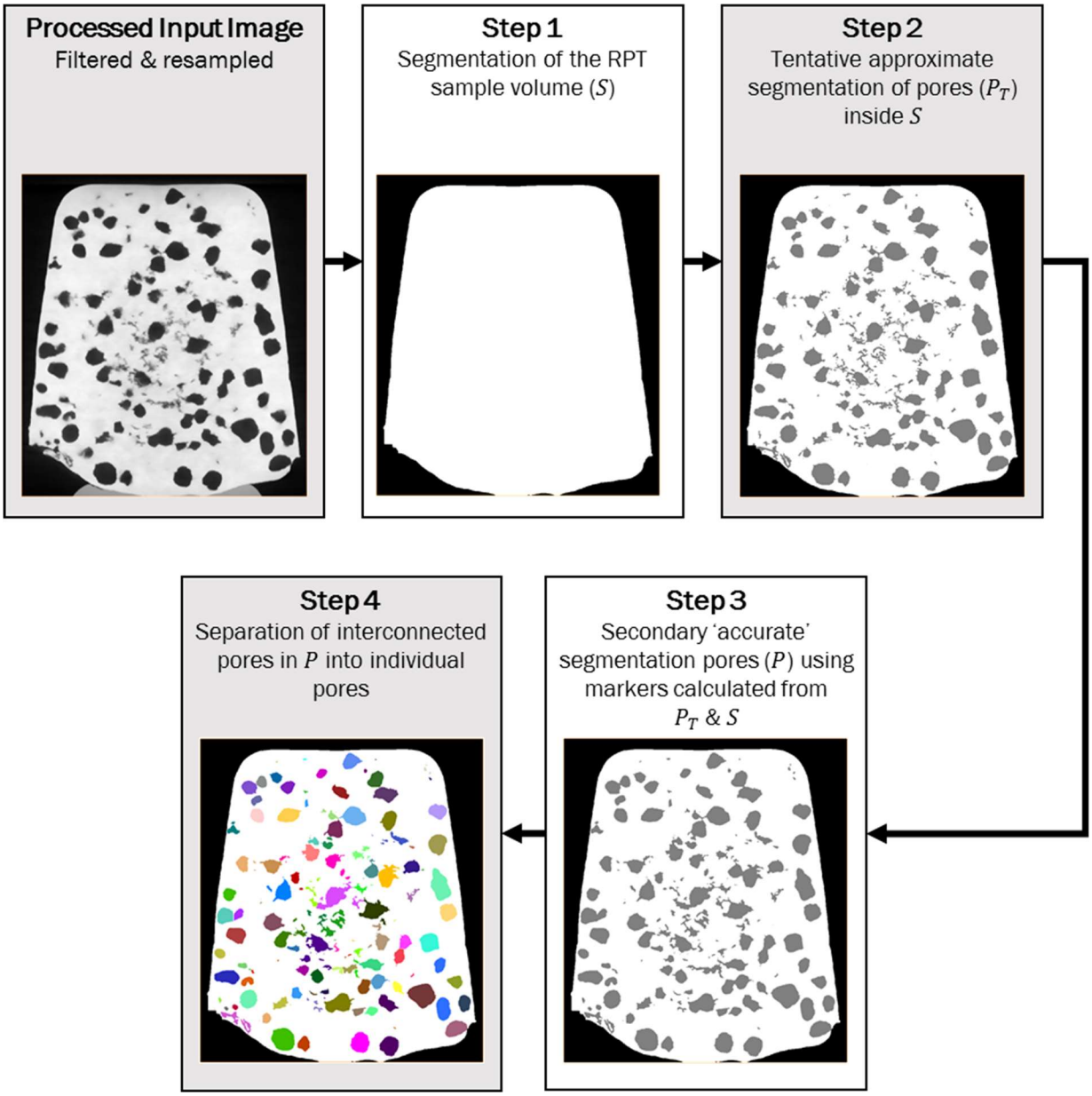

Figure 5.8 The 4 main steps for the segmentation of porosity in the macro-CT images.

In Step 2 of the segmentation procedure, a tentative segmentation of the porosity (P_T) was performed so that markers for a subsequent, more accurate MBWT of the pores could be performed. P_T was defined using a conservative global threshold of 100 to segment the prominent gas pores from the 3D image, while a 3D Black Top-Hat (BTH) transformation

using a spherical structuring element with a radius of 3 voxels, followed by a global threshold of the transformed image with a threshold value of 10 was used to define markers for the shrinkage pores. **Figure 5.10** a) shows that P_T is reasonable, but does not fully encompass the edges of the pores. The metallic substrate – now considered to be part of the background (as it is the pores that are now of interest) - was defined as $P_T - S$, that is, the 'pore-less' regions inside the sample.

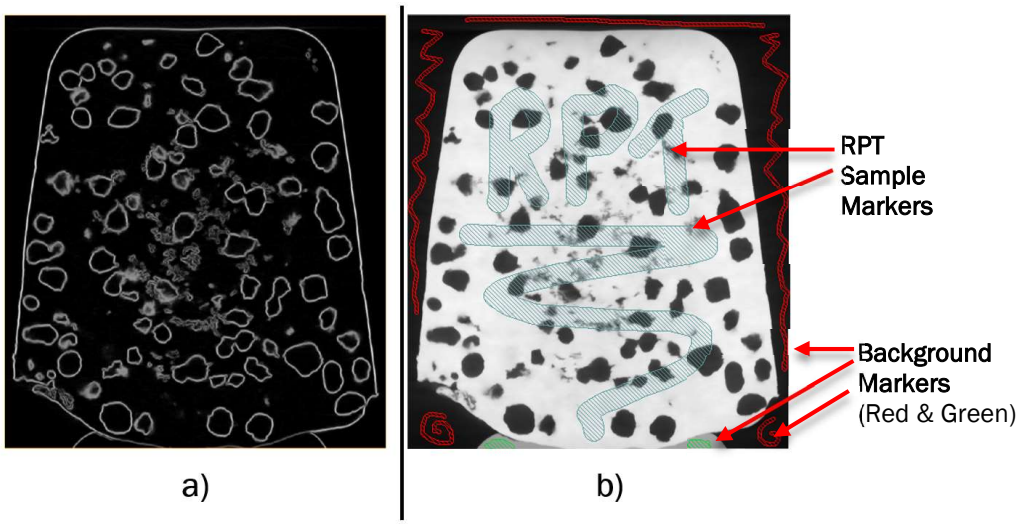

Figure 5.9 a) Gradient image, and b) user defined markers for the MBWT used to segment the RPT sample volumes, S.

In Step 3, a more accurate segmentation of the pores (P) was performed, again using the MBWT applied in 3D. The markers for this process were calculated based on P_T. Markers for P were placed at the centres of the gas pores that were defined in P_T using a combination of distance transform followed *h*-maxima transform [139], [175]. Markers for the shrinkage pores were defined using a BTH transform on the input image, which used a spherical structuring element with a radius of 1 voxel; a global threshold of 10 was then applied to the transformed image. An example of the BTH transform is given in **Figure 5.11** and shows that

it draws out the shrinkage pores and other locally darkened regions in the image. This placed numerous small markers in pores as shown in **Figure 5.10** b). Markers for the image background (metallic substrate) were defined as the regions in the sample most locally distant from P_T. This was done by again using a combination of distance transform and *h*-maxima transforms.

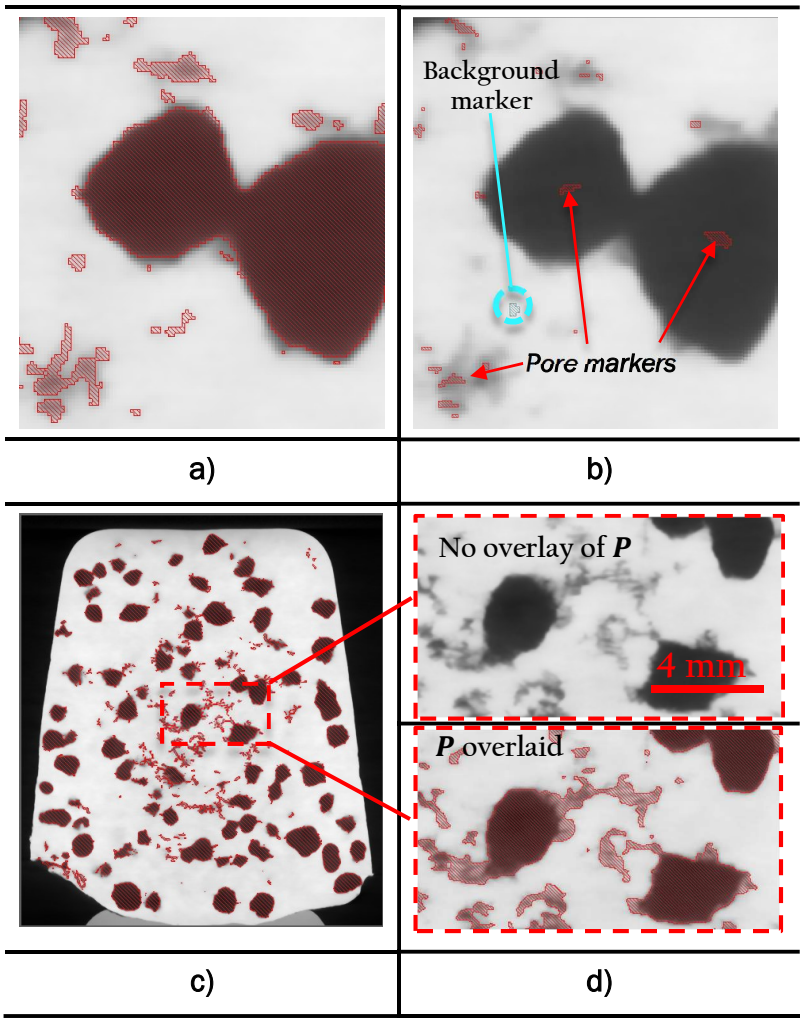

Figure 5.10 a) An example of P_T showing incomplete segmentation, b) the placement of markers for the MBWT used in Step 3 to segment P, and c) & d) examples of P overlaid on the image, illustrating the efficaccy of the procedure.

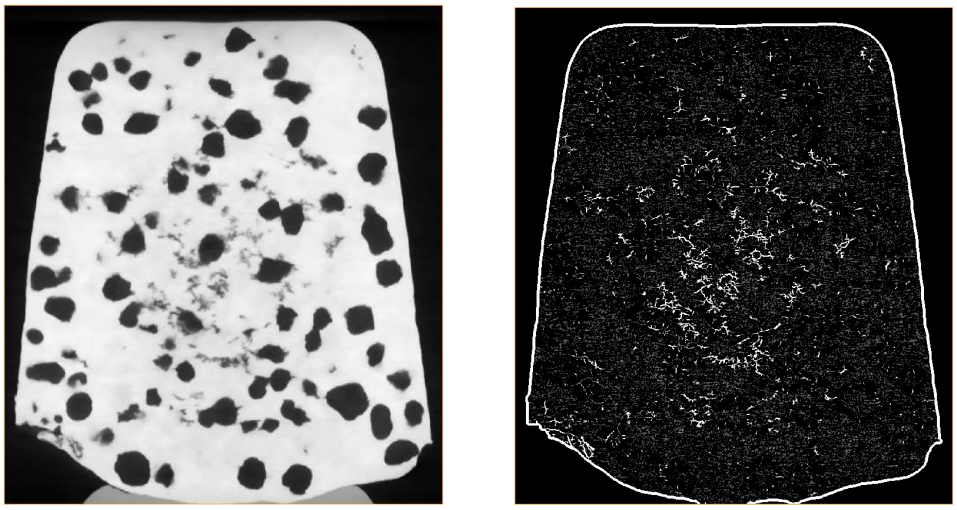

a) b)

Figure 5.11 Example of the effect of applying a b) BTH transform using a spherical structuring element with a radius of 1 to image a). Note that the image is enhanced, and the sample border has been added to aid its interpretation.

Following the MBWT segmentation, the output porosity, *P* was subjected to an AND logical operation with *S* to restrict any surface pores to inside the RPT sample, removing any 'overgrowth' of pores into the image background that might have occurred. An example of *P* in **Figure 5.10** c) and d). From **Figure 5.10** d) it can be seen that the strong large pores are precisely segmented using this technique, though for the weaker pores, there is some inevitable over segmentation of these features as their actual boundaries are not so easy to define due to their near-sub-voxel size. Nevertheless, there would otherwise be no straightforward way to define and include them in the analysis given the resolution of this scan.

Finally, in Step 4 of the segmentation procedure, *P* was separated into individual pores as shown in the example **Figure 5.12**, using Avizo's *Separate Objects* algorithm, with the user input *marker extent* set to a value of 4. This algorithm is based on a MBWT algorithm, which

splits objects using a combination of distance map, *h-maxima* and a MBWT operations. The separation of pores is further discussed in Sections 6.2.2 and 6.2.4.

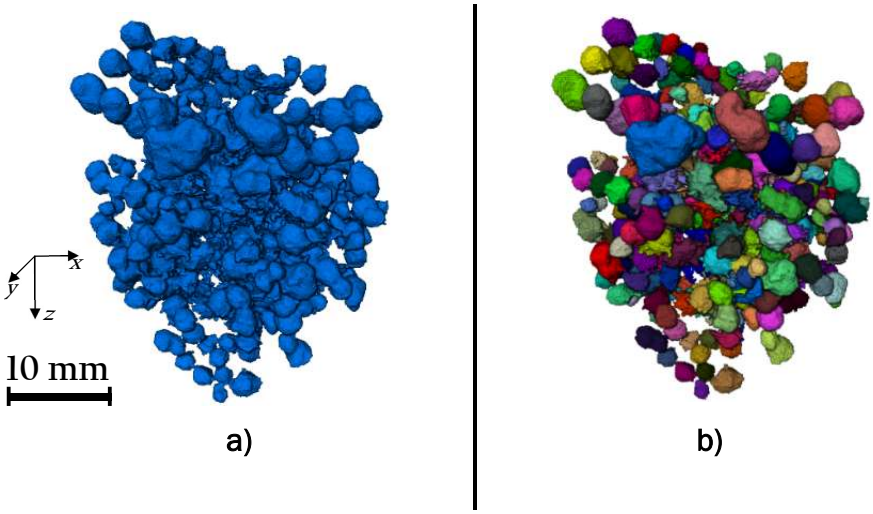

Figure 5.12 The splitting of a) a single large pore into b) its constituent pores using Avizo's 'separate objects algorithm'. The individual pores are discriminated by colour.

Analysis

P and *S* sample volumes were analysed using Avizo's inbuilt *Label Analysis* and *Global Analysis* algorithms, respectively. **Table 5.3** lists the measured parameters and derived parameters from the XCT analyses.

` Any voxels that shared a face, edge, or vertex with a neighbouring voxel were considered to be connected and part of the same object - part of the same pore. Pores smaller than 8 voxels were omitted from the analysis completely, and morphological analysis (shape factor) was only performed on pores comprised of 125 or more voxels. These limits are in line with those that have been used by others when performing similar analyses [121], [128], [148], [161].

Table 5.3 Key measurements from the macro-CT analyses

Metric	Symbol	Description
Sample Volume	V_s	Volume of the RPT sample (S).
Number of Pores	N_p	The number of (separated) pores in each sample.
Pore Volume	V_p	The area of pixels comprising a single pore.
Pore Crofton Surface Area	A	An estimate of the pore surface area using Crofton's formula [172].
Volumetric Pore Number Density	PND_V	The number of pores per unit volume of the sample, given by: $$PND = \frac{N_p}{V_s}$$
Equivalent Spherical Diameter	D_{eq}	The equivalent spherical diameter based on the pore area, given by: $$D_{eq\ 3D} = 2\sqrt[3]{\frac{3}{4\pi}V_{p,n}}$$ Where $V_{p,n}$ is the volume of pore n.
Shape Factor (3D) or Sphericity	SF	The degree of circularity of the pore given by: $$SF = \frac{\pi^{\frac{1}{3}}(6V_{p,n})^{\frac{2}{3}}}{A}$$ Where $V_{p,n}$ and A_n are the volume and surface area of pore n, respectively. $1 > SF > 0$, with pore sphericity increasing towards 1.

5.3 Porosity Analysis using Micro-CT

High resolution micro-CT scans were performed on small regions of interest cut from the centre of APT samples (**Figure 5.13**) in order to investigate changes in the structure of pores that were formed under atmospheric pressure. This was performed in order to give complimentary measurements to the RPT analyses as it was considered that the application of vacuum to RPT samples may contort the shape and structure of pores as a consequence of their expansion.

A number of additional attempts were made to try and resolve any association of TiB_2 particles with the pores, though all attempts proved unsuccessful.

5.3.1 Sample Preparation, Acquisition, & Reconstruction

Specimen Preparation

Specimens were turned from the centres of APT samples as shown in **Figure 5.13** using a lathe.

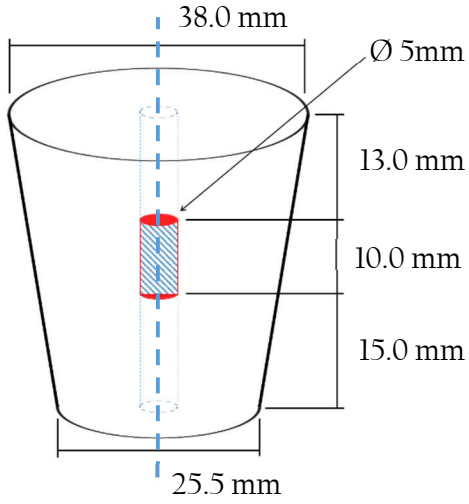

Figure 5.13 Approximate dimensions of an APT sample and the position from which the micro-CT specimens were machined.

Acquisition

A Zeiss Xradia 510 Versa was used to acquire high-resolution scans of the specimens using the parameters listed in **Table 5.4**. These scans were conventional cone-beam scans, and not helical scans like the macro-scans. The beam was aligned so that it was centred approximately midway up the height of the specimen.

Table 5.4 Micro-CT scan parameters.

Parameter	Value
Scan Voltage	80 kV
Beam Power	7 W
Focal Spot Size	20 µm
Beam Filter*	LE5
Optical Lens†	4×
Exposure Time	10 s
Source-Sample Distance	92.28 mm
Sample-Detector Distance	12.36 mm
Binning	2
Number of Projections	1601
Nominal Voxel Size	~5.9 µm

* Zeiss proprietary materials. The number indicates the filter's attenuating strength, increasing in ascending order.

† This system includes an optical magnification lens as described in Section 3.4.2.

Reconstruction

Reconstruction of the data was performed using Zeiss Reconstructor CT software. The centre of rotation shift was determined automatically by the software, and the beam hardening correction constant was chosen manually by the operator for each scan and was selected so that a uniform intensity was achieved in homogenous volumes across the

diameter of the sample as shown in Figure **5.14**. The manual choice of the beam hardening correction for each scan was a source of variability between the scans, but was necessary due to differences in the total x-ray attenuation of each sample due to their varying fractions of porosity. Finally, the data were saved as 16-Bit .txm files, a Zeiss proprietary image format.

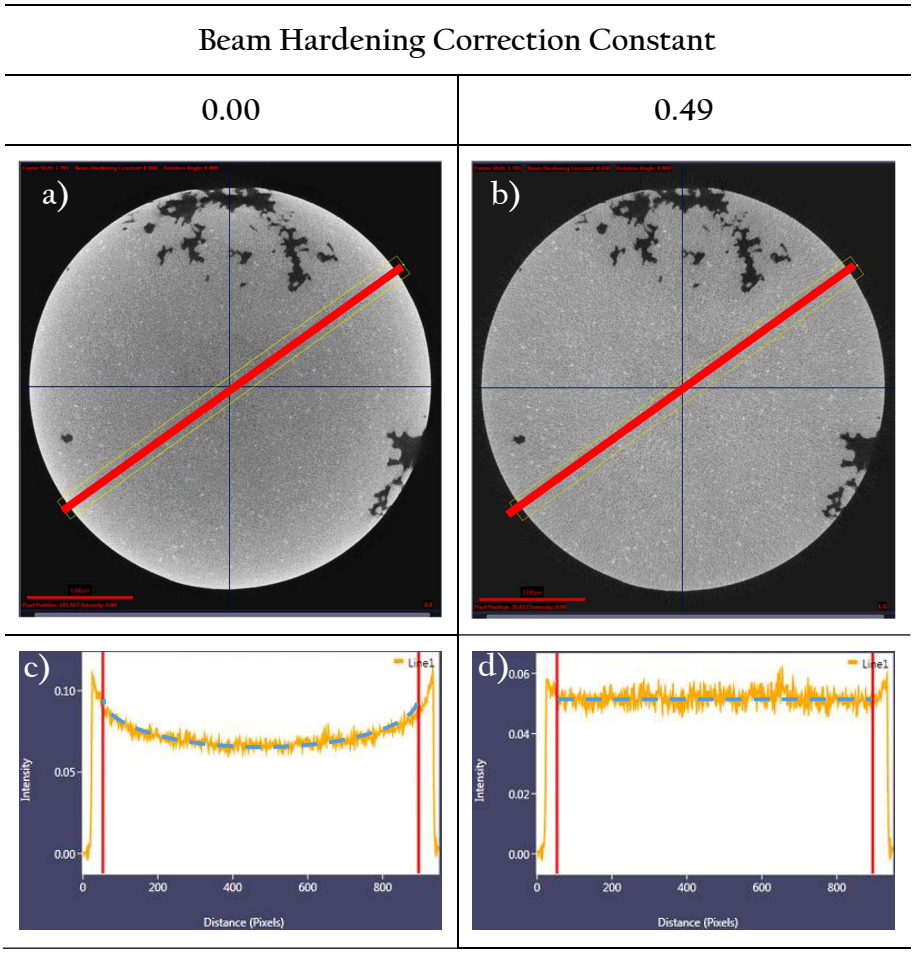

Figure 5.14 Selection of the beam hardening constant. Showing a slice of data and variation of pixel intensity along the red line a) & c) without, and b) & d) with beam hardening applied.

5.3.2 Micro-CT: Image Processing & Analysis

Following reconstruction, the micro-CT data were processed, segmented, and quantitatively analysed using Avizo software as detailed in the following subsections. Again, unless otherwise stated, all operations were applied to the 3D image. An example 3D reconstruction and 2D slice of micro-CT data are shown in **Figure 5.15**. For supplementary information on the process the reader should consult Appendix II.3.

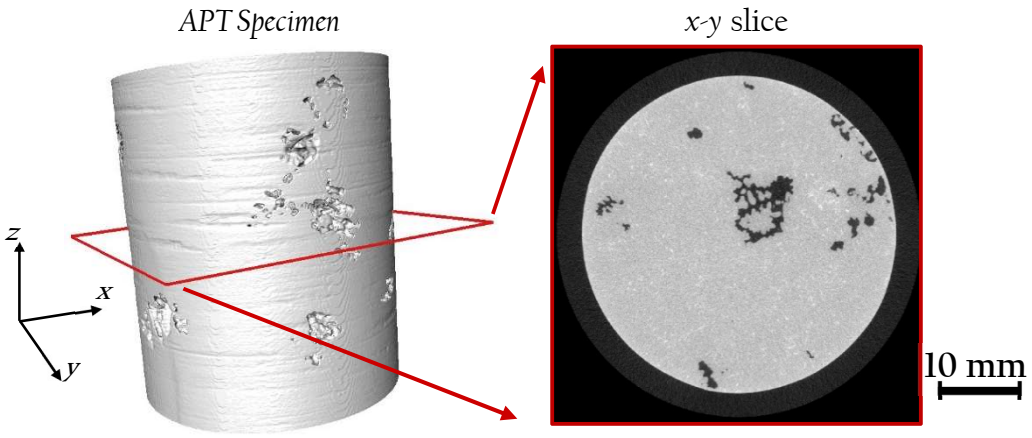

Figure 5.15 3D reconstruction & x-y slice of micro-CT data.

Image Processing

The 16-bit images were resampled to 8-bit, with the data remapped to include only the non-zero data range to minimise the loss of greyscale from the images. The images were then denoised using a non-local means (NLM) filter applied in 2D to the *x-y* planes of the image – an example of the result of this is shown in **Figure 5.16**.

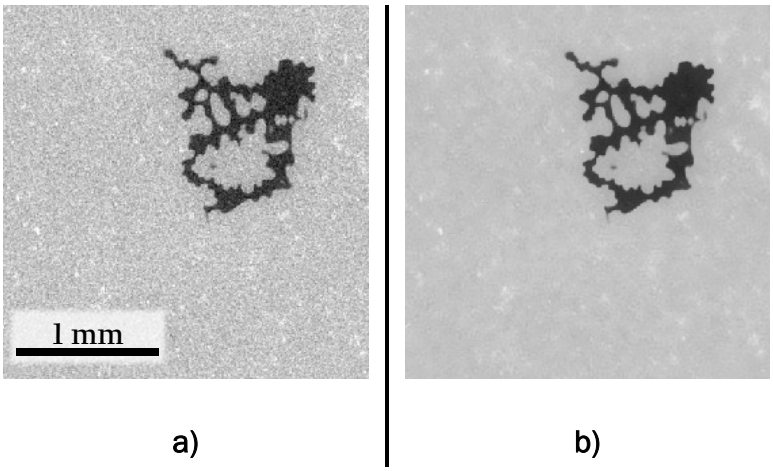

Figure 5.16 Close-up of an x-y slice of micro-CT data a) before and b) after denoising.

Segmentation

The segmentation procedure consisted of two main stages as illustrated by **Figure 5.17**. In Stage 1, the cylindrical sample volume (S) was segmented from the image background using a MBWT algorithm, with the gradient image again being calculated using the Canny-Deriche method [174], and the markers defined manually by the operator as shown in **Figure**

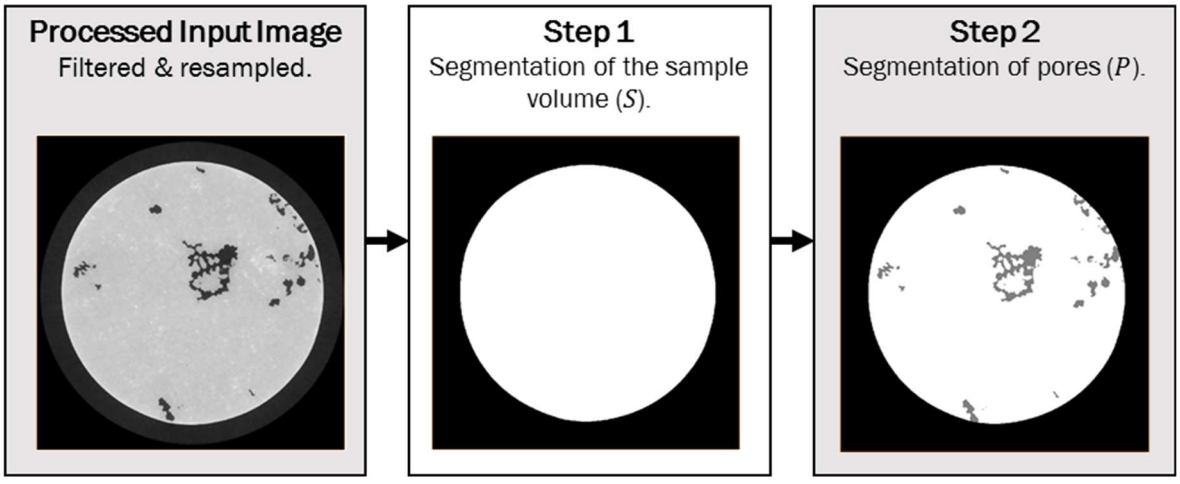

Figure 5.17 The 2 stage segmentation procedure of the porosity in the micro-CT images.

5.18 a). The segmented sample volume (**Figure 5.18** b)) was then subjected to the following series of morphological operations: 3D dilation (55 iterations), flood fill (fill-holes), fitting of a convex hull to each *x-y* slice (2D), and erosion operations (60 iterations). This closed any pores at the surface of *S* with openings smaller than approximately 177 µm (30 voxels), so that they were included in subsequent analyses. In addition, it was necessary to omit a boundary of 5 pixels (~30 µm) from the surface of *S* using the morphological erosion due to beam hardening at the sample edges.

The next step was to segment pores (*P*) from inside *S*. This was done in a single step by global thresholding. The threshold level was calculated for each sample using Otsu's method [147] applied to the 3D image. The histogram range was restricted to include only the greyscale values of pixels inside of *S* in order to prevent skewing of the calculated threshold level by the image background.

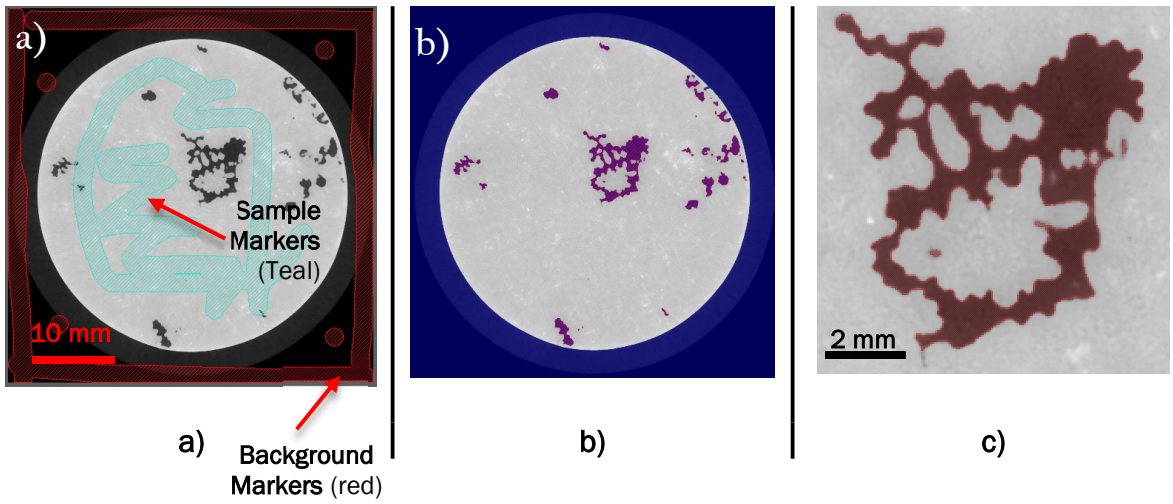

Figure 5.18 Examples of a) user defined markers for the MBWT used to segment *S* is Step 1, and b) & c) examples of *P* segmented during Step 2.

Analysis

The porosity and sample volumes were analysed using the same size-thresholds as the macro-CT procedure (described in Section 5.2.2). Because of the high degree of interconnectivity amongst the pores, and their contact with the edges of the sample and the image, it was found that the macro-CT measurements (**Table 5.3**) were rarely meaningful, and therefore were not used to characterise the micro-CT images. So instead, the interconnectivity of the pores in the entire sample volume was quantified. This was done using the Euler-Poincare characteristic, also known as the Euler number, which was calculated by Avizo's inbuilt *Global Analysis* algorithm. The Euler number represents the *multiconnectivity* of an object [176]; and it is increasingly positive as the interconnectivity of the pores decreases, while it is increasingly negative as the interconnectivity increases [177].

Chapter 6

Evaluation of Porosity Characterisation Methods

The metallographic and macro-CT image analysis methods described in the preceding chapter serve as the foundation for the analyses that are performed in this research work. To give an idea of their extent, metallography was used to analyse 21,405 pores in 81 RPT samples and macro-CT was used to analyse 60,753 pores in 31 samples in the analyses presented in this thesis.

This chapter therefore serves to give an overview of the abilities and nuances of the porosity analysis methods. Of course it will not be possible to cover every specific case, but instead here things will be generalised.

6.1 Metallographic Analysis of Porosity

It is important to emphasise that metallographic analysis measures 2D manifestation of pores inside the RPT samples, which, as is discussed in Section 3.2, is not always representative of their true structure, but can nevertheless serve as a useful measurement.

6.1.1 Some Characteristics of the Analysis Procedure

A typical metallographic cross-section of an RPT sample is given in **Figure 6.1** a) and shows that most of the gas pores are reliably detected by the analysis technique. Given the small pixel size of ~16 µm, very fine features can be resolved and measured, provided that the

pores are larger than the size threshold of 44 pixels (d_{eq}=120μm) otherwise they are not included.

Because of the way that the analysis is conducted, interconnected pores are not separated, which can result in erroneous measurements of the size and shape of these pores. Another result of the image segmentation procedure is that pores that are close to the surface of the RPT are omitted from the analysis. These aspects can be seen from **Figure 6.1** a).

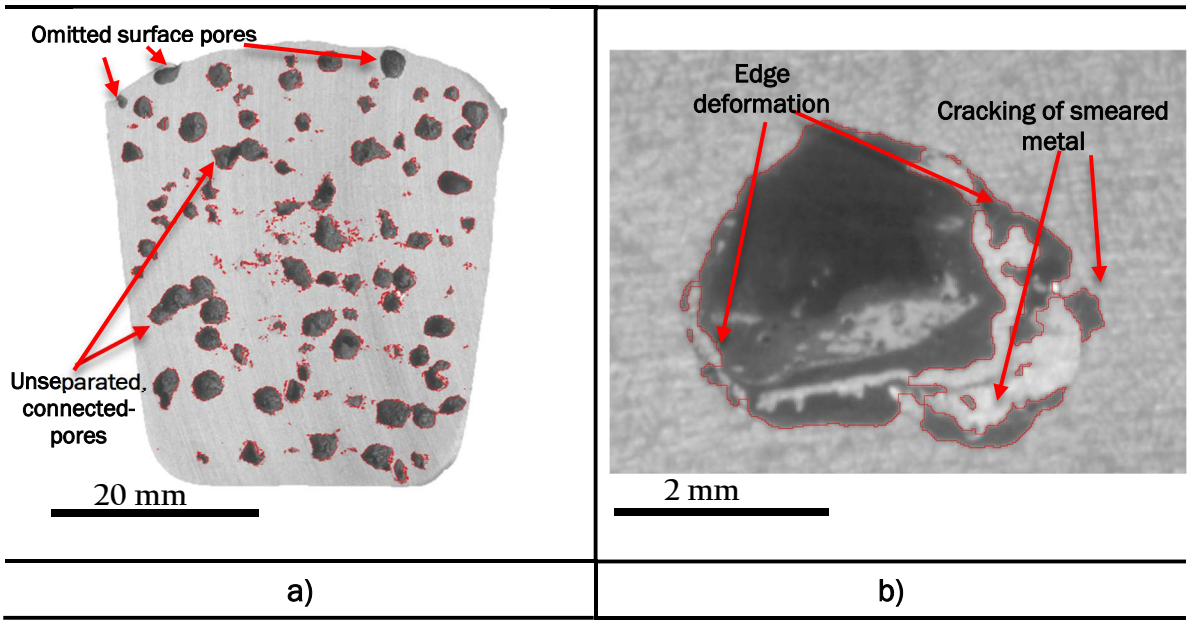

Figure 6.1 Metallographic porosity measurement on a) a typical RPT image, and b) a close-up of a pore showing cutting artefacts that are detected and measured in the analysis.

6.1.2 Preparation Artefacts & Shrinkage Pores

Sectioning by abrasive cutting and the subsequent grinding with SiC paper causes deformation of the metallic substrate around the edges of pores as shown in **Figure 6.1** b). This is termed here as a *Preparation Artefact*, and has the problematic effects of:

- Warping the cross-sectional morphology of pores, which in turn effects the shape and size measurement of the pores.
- Creating numerous cracks, which are subsequently detected and measured as pores in the analysis.
- Filling in small pores, by smearing metal over them, meaning that small pores may not be detected at all, though this tends to happen to shrinkage pores, which themselves are problematic.

Similar artefacts have been reported by others in various metallographic studies [173], [174].

Shrinkage pores that develop in the casting also heavily contribute towards misleading results from the metallographic analysis. This is because, due to their complex, irregular shape, when sectioned, they appear as multiple small pores, which may skew the measurements.

6.1.3 Estimation of 3D Pore Size Distributions and Number Density

Stereological relationships can be used to convert the 2D size distributions of pores into their approximate 3D size distributions. There exist a number of approaches for this [115], [116], though here, Saltikov's area method [178] has been used. This method was selected because, it is applicable to poly-dispersed systems, does not require the particles to be spherical, and could easily be applied using the measurements of area collected in the metallographic analyses.

Effectively, this technique can be thought of as reverse engineering the randomly intersected 2D sections of pores back into their 3D form – thus giving an estimate of the 'real' size distribution of pores. However, it does have the key limitations of [118], [178]:

- All pores need to be the same shape, differing only in size,
- Single pores can only be intersected once by the analysis plane.
- Pores must be randomly dispersed.

Henceforth, this can only be applied to gas pores – which are generally approximately spherical – but not to shrinkage pores, which invalidate these criteria, given their complex, non-uniform shape [1], [15] meaning that they are likely to be intersected by the analysis plane multiple times. In addition, preparation artefacts, which also occupy the size range of the shrinkage pores are falsely represented as multiple pores, and further complicate the analysis. A size cut-off is therefore imposed, with only pores with an equivalent circular diameter (d_{eq})›0.5 mm being considered to be gas pores and included in the analysis.

Another assumption of Saltikov's area method is that pores have a lognormal distribution. If it is assumed that the gas pores with d_{eq}›0.5 mm are all spherical and not connected – which

is not truly the case, but a reasonable estimate for gas pores – a lognormal distribution may be fitted to the minor peaks in the data as shown in **Figure 6.2** a). The 3D macro-CT size distribution in **Figure 6.2** b) confirms that gas pores roughly follow a lognormal distribution, and has also been shown to be the case in RPT samples by others [8]. It can be seen from **Figure 6.2** c) that there is a reasonable agreement between the Saltikov estimate and the macro-CT 3D size distributions.

Once Saltikov's estimate has been applied, the volumetric PND in the metallographic sample can be determined by simply summing up the normalised counts (volumetric number density) of pores in each class.

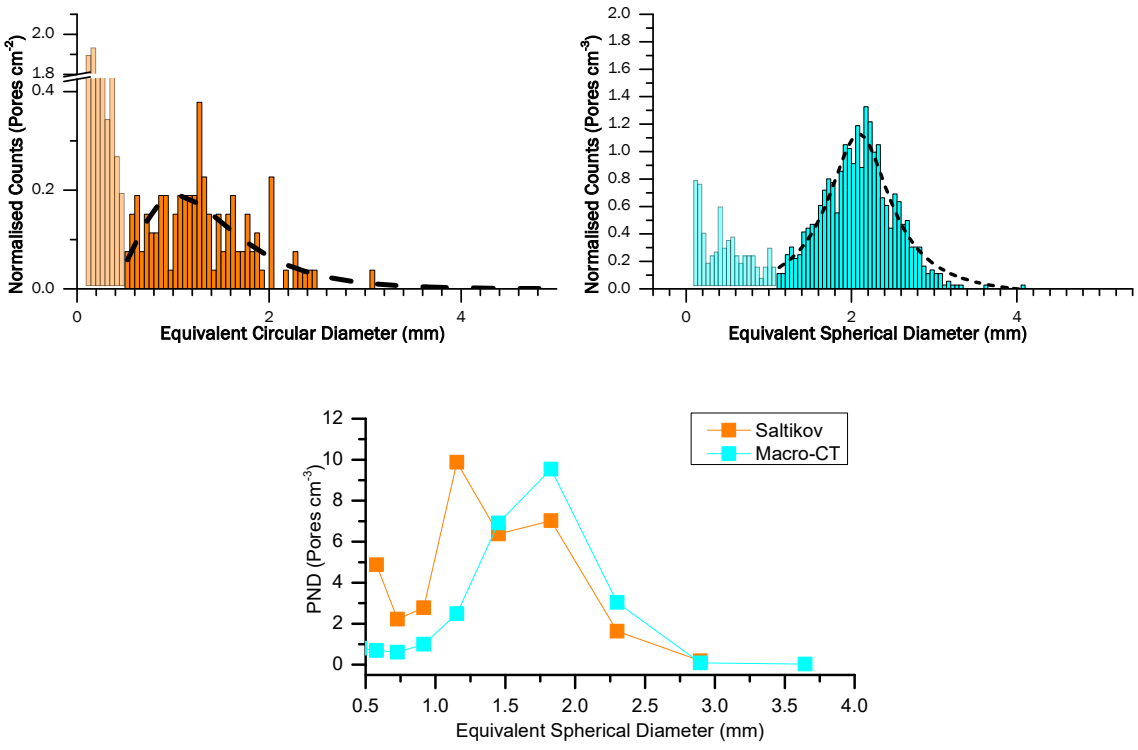

Figure 6.2 Pore size distributions in a sample with a volume fraction of porosity of 11.99%, showing a) the fitting of a lognormal distribution to pores with d_{eq}>0.5mm *in the metallographic analysis, b) Fitting of a lognormal distribution to the 3D macro-CT to gas pores, and c)* Result of the application of Saltikov's Area method to estimate the 3D size distribution of gas pores.

6.2 Porosity Analysis by Macro-CT

This section will give a brief overview of the macro-CT method used for the analysis of porosity in the RPT samples.

6.2.1 Characteristics of Porosity in Macro-CT Images

Figure **6.3** shows a typical 2D slice and 3D reconstruction of segmented macro-CT data. Compared to the metallographic cross-section (shown in **Figure 6.1**), smaller pores are more clearly observable, although the resolution of the technique is lower, which means that they are more blurry than how they would appear at higher resolutions – such as micro-CT.

As shown in Figure **6.3** b), pores can broadly be categorised into two families based on their intensity in the image, as either: 'strong' pores, which are mainly gas pores that are well defined; or as 'weak' pores, which are mainly interdendritic pores that are less well defined in the image. The definitions are quite loose because it can clearly be seen that weak pores are connected with strong pores throughout the image. It will be shown in Section 6.4 that the complexity of weak pores cannot truly be captured due to the large voxel size used during macro-CT.

The 3D reconstruction of the data shown in Figure **6.3** c) reveals the extensive 3D interconnectivity of the pores. This can quickly be judged from the size of the largest pore – shown in red in the image – which proliferates extensively within the sample. Clearly, this pore is made up of a number of gas pores – 392 to be precise, in this case. Although it is not represented in this image – for the sake of simplicity – the other pores in the RPT sample are also interconnected, though to a lesser extent.

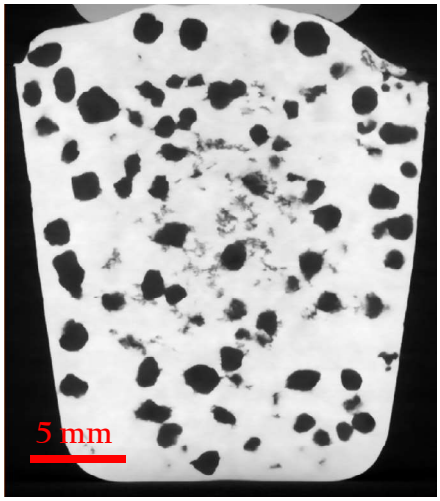

a)

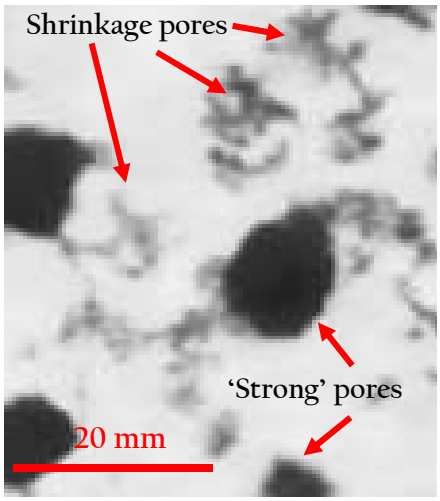

b)

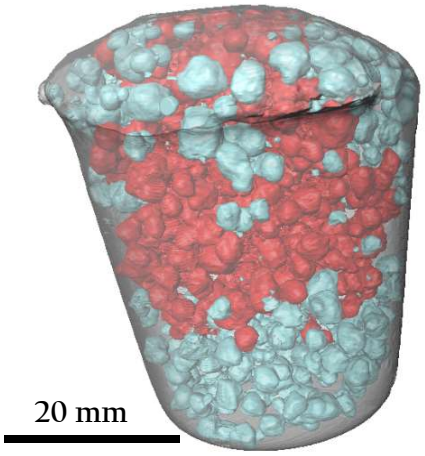

c)

Figure 6.3 a) *x*-z slice, b) close-up of the x-z slice with gas pores and shrinkage pores indicated, and c) reconstruction of the porosity inside an RPT sample with a pore volume fraction of 19.29%. The largest interconnected pore in the sample shown in red is made up of multiple individual gas pores.

6.2.2 Separation of Coalesced Pores

The extensive interconnectivity of pores in the RPT samples (Figure **6.3** c)) results from the application of vacuum, and is an artefact of the RPT – though this is not to say the gas pores themselves are, they are just bigger in size. It is therefore logical to separate the interconnected pores into their constituents prior to analysis.

The effect of separating the pores on various measurements is shown in **Figure 6.4** to 6.7. **Figure 6.4** shows, as expected, that the PND is larger after separation of the pores. **Figure 6.6** shows that separation splits the large interconnected agglomeration into a number of smaller ones, though it has negligible effect on the minor peak of the bimodal distribution. **Figure 6.5** shows that the splitting has the effect of revealing the 'true' morphology of the gas pores in the RPT sample.

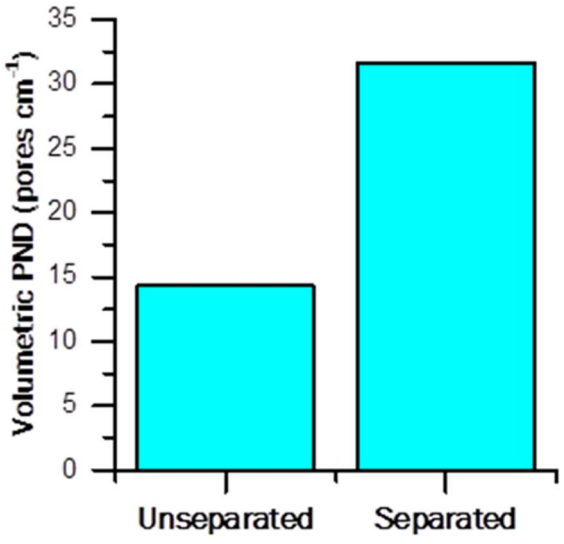

Figure 6.4 Effect of separating interconnected pores on the volumetric pore number density in the RPT sample shown in Figure **6.3** c).

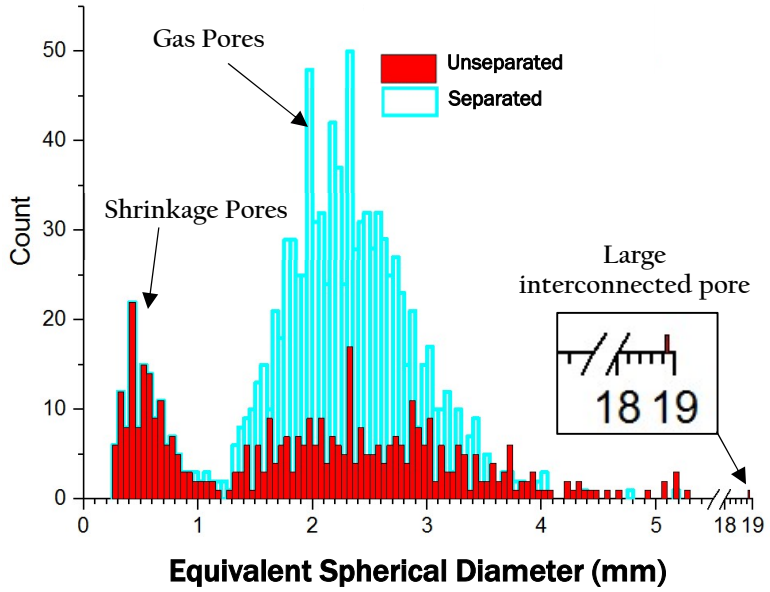

Figure 6.5 Comparison of the number of separated and unseparated pores in the sample shown in Figure 6.3 c).

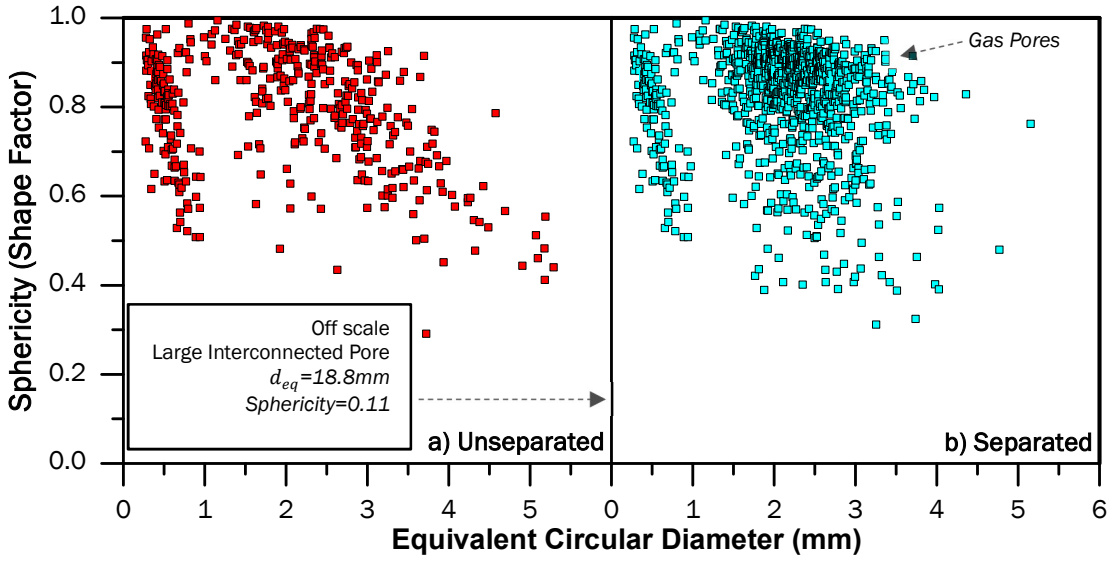

Figure 6.6 Comparison of the size-shape distributions of the pores inside the RPT sample shown in Figure **6.3** a) before separation, and b) after separation. It shows that a large number of individual gas pores are liberated from the separation process.

6.2.3 Reproducibility of the Watershed Segmentation

The macro-CT images were segmented using a marker based watershed transform (MBWT) algorithm, the result of which is governed by the location of the markers for each phase (pore, metal, etc.). In turn the result of the segmentation affects the result of the image analysis.

It was not straightforward to investigate the extent to which marker placement affected the results in this work, due to the methodical, multi-staged process that was used. It was decided that the most straightforward approach would be to vary the number of markers that were placed in the image using a black top-hat (BTH) transform. The BTH transform was used in the standard segmentation procedure of the macro-CT images to place markers in the shrinkage pores.

Markers were placed as outlined in Step 3 of the segmentation procedure described in Section 5.2. The input image was subjected to a BTH transform using a spherical structuring element of radius 1, though here, the threshold that was applied to the transformed image was varied in order to vary the selection of markers that were placed in the image. Decreasing the threshold value has the effect of placing more markers for pores throughout the image, while increasing the threshold has the opposite effect.

Figure 6.7 shows examples of marker placement and the resulting segmentation using this method. Notably when a threshold of 2 is applied, many markers are erroneously placed in regions that are clearly part of the metal substrate, which causes severe over-segmentation. However, in the other cases, there is very little variation from the standard procedure. More markers in the image (decreasing BTH threshold) tend to more thoroughly

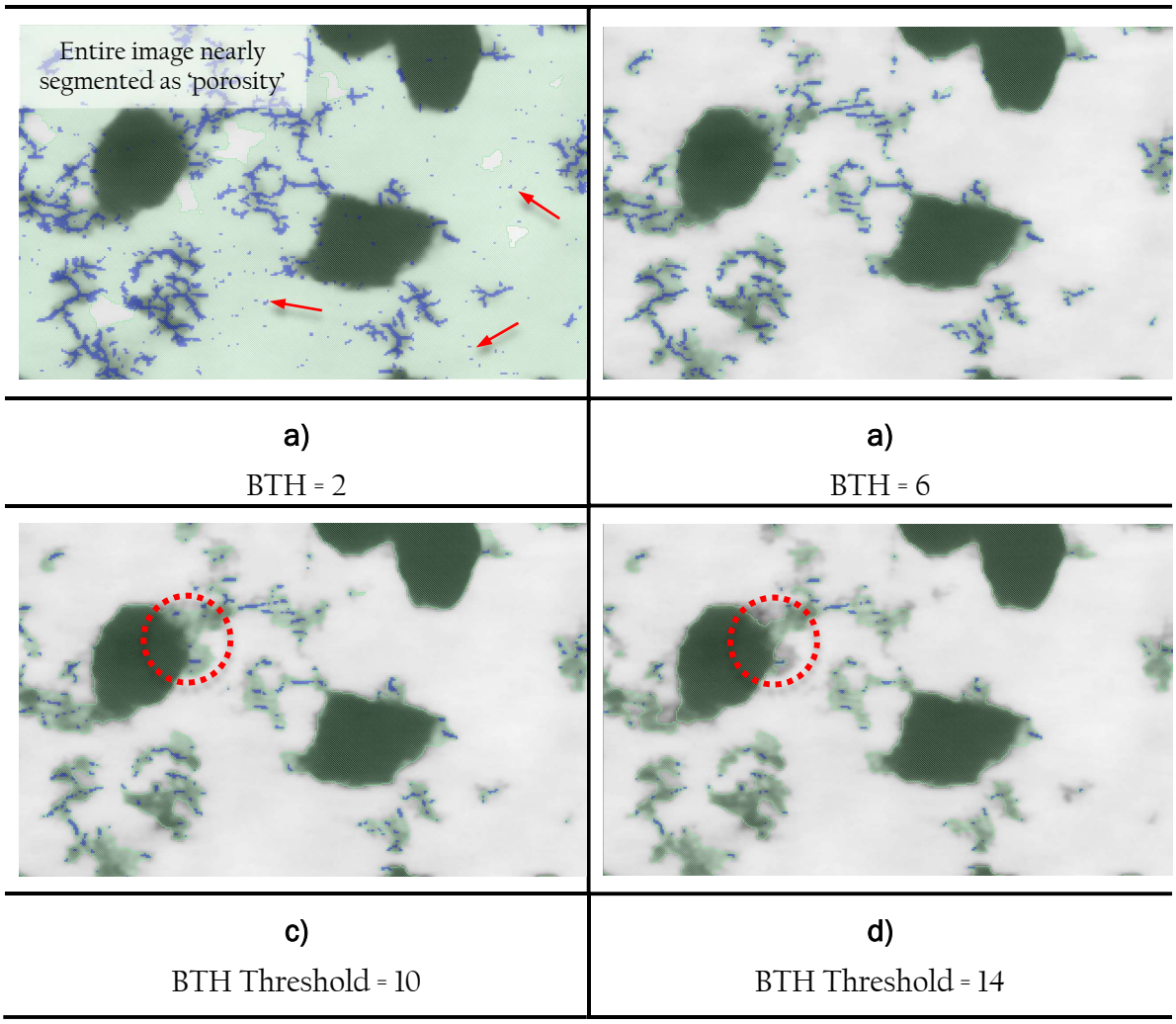

Figure 6.7 Segmentation results from varying marker placement for the MBWT algorithm. The markers used in the segmentation procedure are shown in dark-blue, while the resulting segmentation of the porosity is shown in light green. The red arrows on a) indicate some of the small markers that have erroneously been placed in the non-pore region of the image. The encircled regions on c) and d) can be used to compare differences in the amount of porosity that us segmented in with different thresholds applied to the BTH transformed image.

segment the shrinkage pores, whereas decreasing the number of markers results in a less thorough segmentation of shrinkage pores.

Figure 6.8 quantifies the effect of varying these parameters on various measurements. In general it shows there is minimal when reasonable markers are placed conservatively in the image, **Figure 6.9** shows that varying the BTH threshold has little effect on the gas pores

that compose the major peak of the bimodal distribution, but increasing the number of markers (decreasing the BTH threshold) increases the number of small pores that are segmented from the image, as is indicated on the plot.

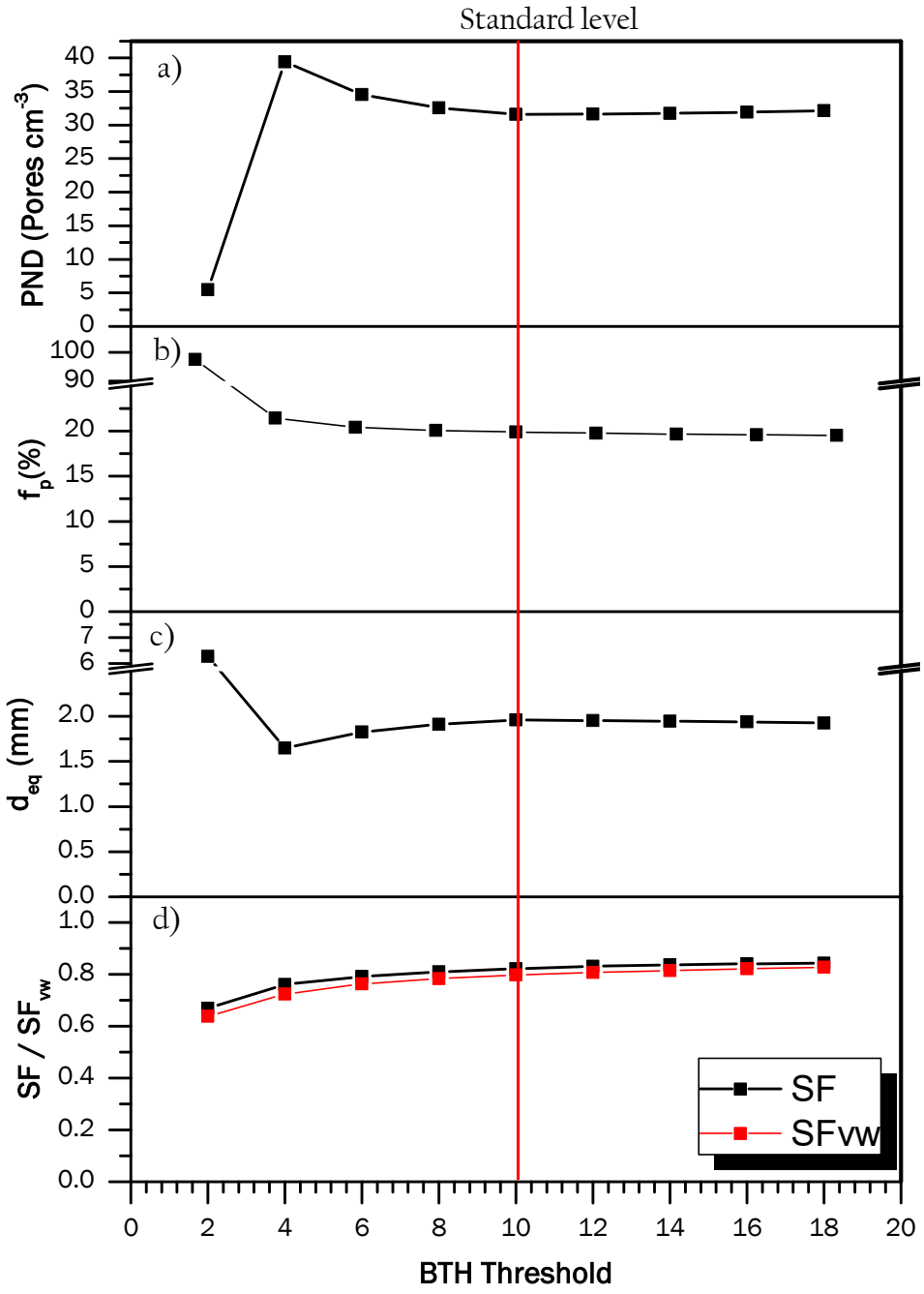

Figure 6.8 Effect of varying the number of markers for porosity in the MBWT on a) the pore number density, b) volume fraction of porosity, c) average equivalent diameter, and d) Shape factor (sphericity) and weighted shape factor. Note that a BTH threshold=2 is erroneous and represents excessive marker placement.

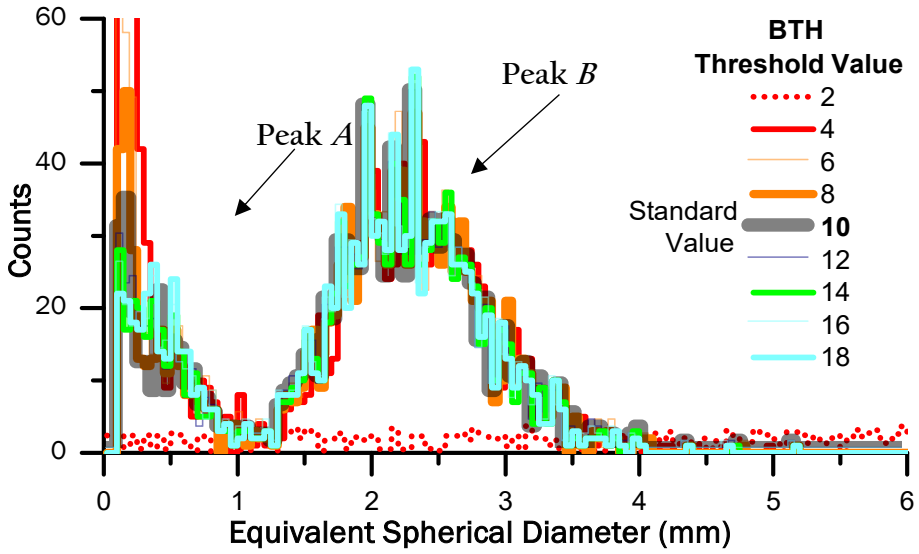

Figure 6.9 Effect of varying the BTH threshold used for marker placement in the MBWT on the size distribution of the segmented (and separated) pores. Note that a BTH threshold=2 is erroneous and represents excessive marker placement.

6.2.4 Influence of Input Parameters on the Separation of Pores

The separation of interconnected porosity into its constituents is governed by the parameters of the watershed-based *Separate Objects* algorithm, namely the user input *marker extent*. This parameter governs the degree to which the interconnected pores are split, and the number of constituents that are split from them, which increases with decreasing input value.

Figure 6.10 shows that the splitting parameter, if selected reasonably, has very little effect on the overall PND compared to the effect of not splitting them.

Figure 6.11 shows that splitting of the interconnected porosity effects only the major peak (gas pores) and not the minor peak (shrinkage pores) of the bimodal distribution when reasonable values of marker extent are selected – only the use of a marker extent input of 1, which is extreme, seems to erroneously split shrinkage pores. It can also shows that the

valley between the peaks remains at the same point before and after pores are split, and does not change with varying marker extent values (except when set to 1).

Based on these results, it can therefore be concluded that the marker extent value has only a minor effect on the overall result of the analysis, provided it is selected with reasonable parameters that do not produce erroneous over splitting of the pores. Nevertheless, it needs to be said that the result is highly subjective, and does not give a 'one size fits all' solution for pores of all shapes and sizes.

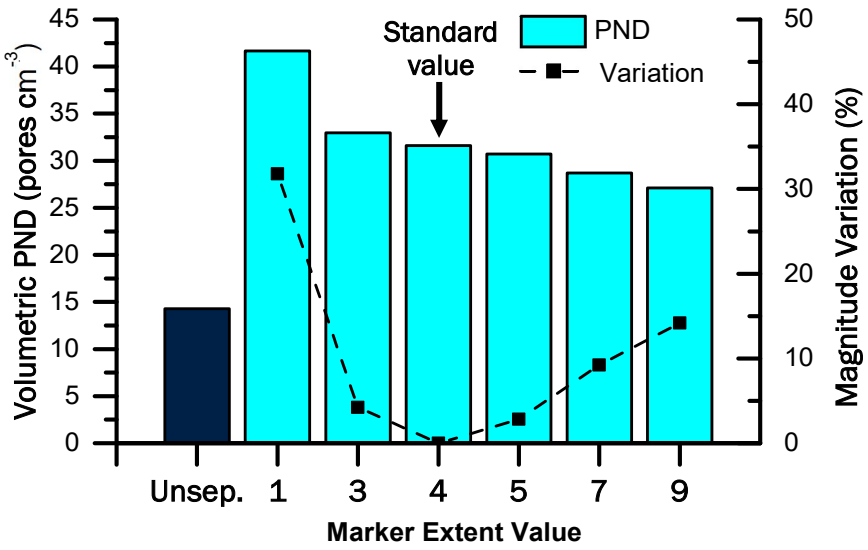

Figure 6.10 Effect of Marker Extent on the NED result & the magnitude of the variation of the result from the standard Marker Extent value of 4.

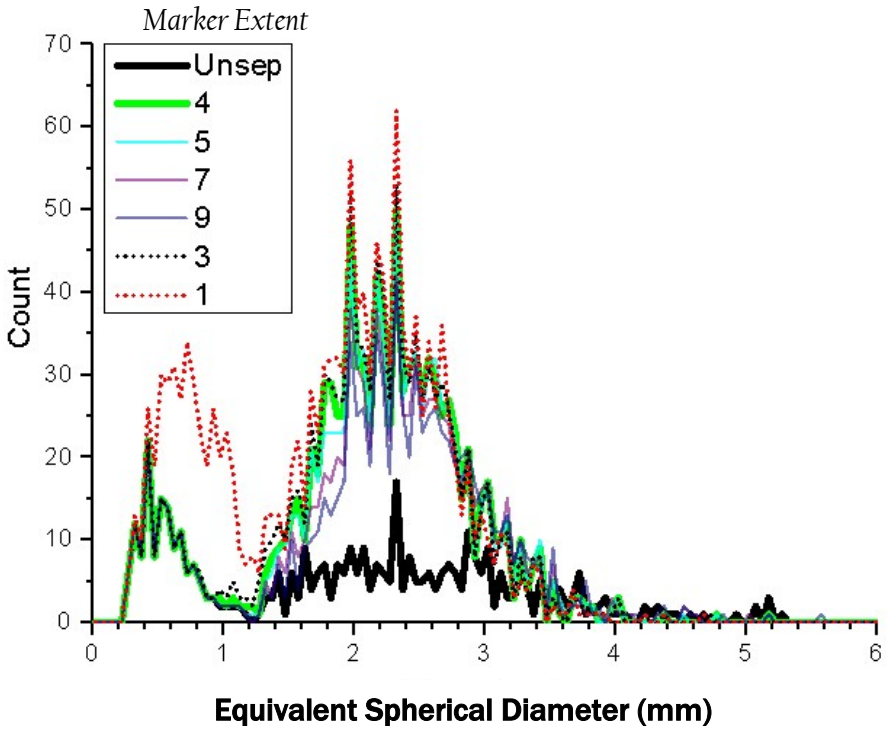

Figure 6.11 the effect of varying the value of 'marker extent' on the splitting of pores on the pore size distribution of pores in the sample. Note, for the unseparated sample interconnected pores with a d_{eq}>6mm are not shown, although a few are present.

6.3 Metallography vs Macro-CT

In this section, selected measures of the porosity 3 RPT samples made by metallography and macro-CT are compared to show their respective abilities and limitations.

Figure 6.12 shows a comparison of images of the samples acquired by each technique. The first observation that can be made is that although the spatial resolution of macro-CT is lower than that of metallography, at 44 µm as opposed to 16 µm, it is still able to detect smaller pores due to the absence of substrate deformation (Preparation Artefacts).

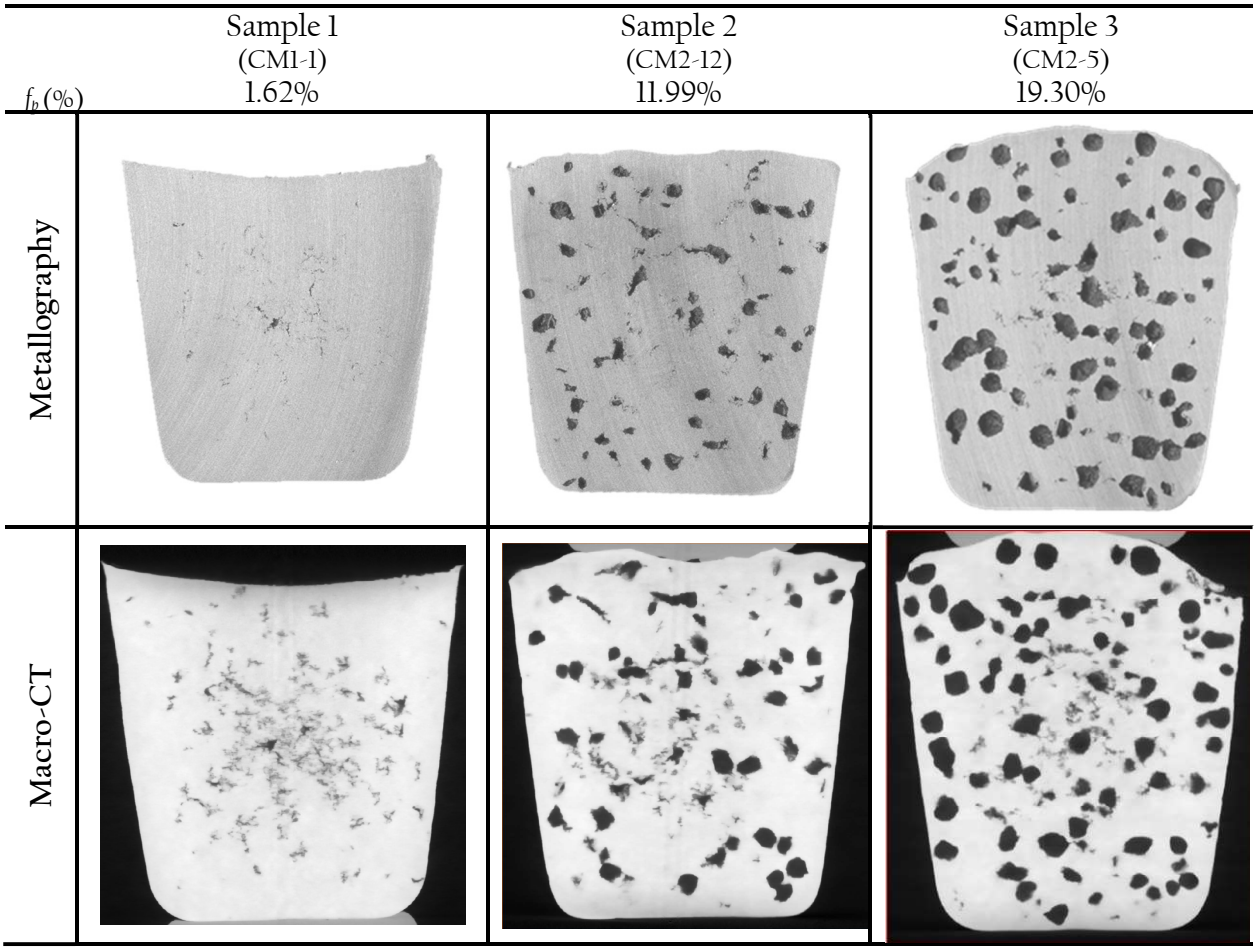

Figure 6.12 Comparison of metallographic and macro-CT images. Note that equivalent planes are not shown, though all are taken through the centre of the samples.

6.3.1 Volume Fraction of Porosity

Although not used for characterisation of experimental results in this work, the fraction of porosity in the RPT samples can be used to give a rough indication of the efficacy of each technique. The areal fraction of porosity can be related to the volumetric fraction of porosity by the Delesse-Rosiwal principle [116], [118], [179]:

$$f_p = \frac{\sum A_P}{A_T} = \frac{\sum V_P}{V_T} \tag{6.1}$$

The comparison of the f_p in the three RPT samples is given in **Figure 6.13**, which shows that metallographic measurements can miss-out on much of the porosity in the samples, especially when the $f_p$is low (Sample 1), whereas macro-CT tends to more closely measure the actual amount of porosity that is present in the sample. As the volume fraction of porosity increases, the relative error compared to the actual (Archimedes') porosity decreases sharply for both techniques. This is due to the increased size of pores that normally accompanies increases in the volume fraction. This is good news, because much of porosity analyses conducted in this work have been conducted on samples with a relatively high f_p.

This difference in the metallographic and macro-CT measurements, and their intrinsic scatter, can be further appreciated from **Figure 6.14**.

The difference in the detectability of the pores by the techniques can be appreciated by comparing the metallographic measurements in **Figures 6.13** and **6.14** with the '2D Macro-CT' measurements, which are a measure of the areal pore fraction on the central slice of CT data. Although both metallography and 2D Macro-CT measurements are performed on a central slice, it can be seen that there is an appreciable difference in the f_p between the two methods. This is due to the superior image clarity of macro-CT, which means that small

gas pores and shrinkage pores – which are concentrated at the sample centres – are better detected. This, combined with the coarse voxel size of macro-CT (which overestimates shrinkage pore volume, as will be shown in **Figure 6.22**), means that the areal f_p measured by macro-CT is higher than metallography. Additionally, when the f_p is low, 2D Macro-CT measures a higher area fraction than volume fraction due to the concentration of the pores at the centres of the samples.

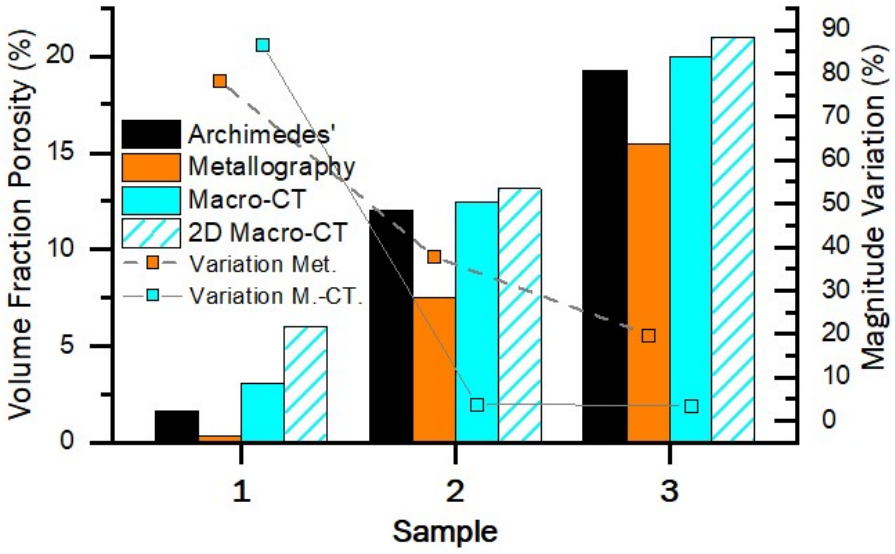

Figure 6.13 Comparison of the fraction of porosity measured in RPT samples by macro-CT and metallography, and the relative error compared to the actual porosity.

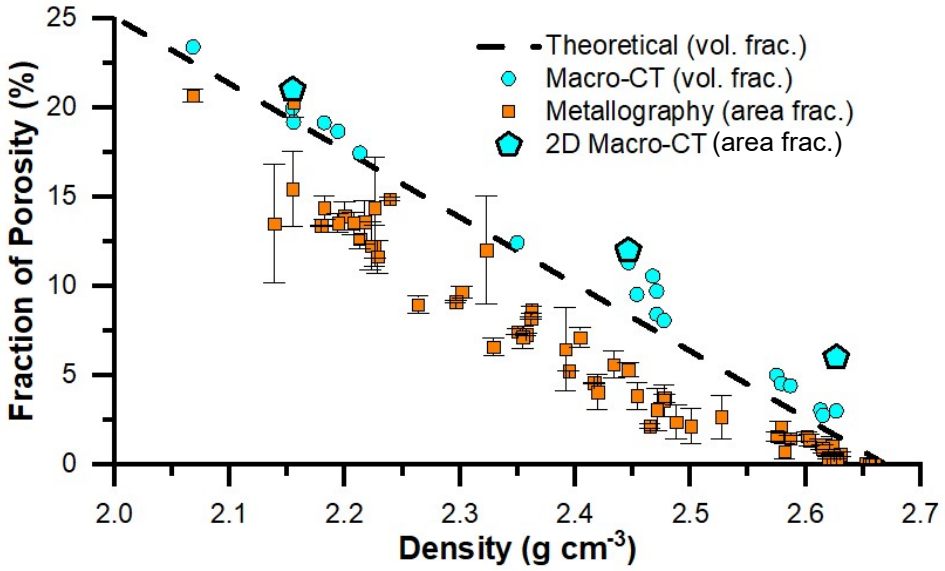

Figure 6.14 Density versus fraction of porosity in various RPT samples measured by macro-CT and metallography.

6.3.2 Pore Size-Shape Distribution

A comparison of the size-shape distribution of the pores measured by metallography and macro-CT is given in **Figure 6.15**, which shows that the two methods measure very different distributions - with the macro-CT distribution being far clearer than that from metallography.

The metallographic distribution shows a great deal of scattering, whereas macro-CT shows a more pronounced clustering of the data. This clustering can be broadly used to classify pores into shrinkage- and gas-pores as will be discussed later on in Chapter 7, though for now, the classes are indicated with arrows.

Some further observations that can be made, namely it can qualitatively be seen that macro--CT measures more pores, that are generally larger, and more spherical than what is

measured in the metallographic analysis. This would help explain the discrepancy in f_p which was shown above.

With regards to the shape of pores, it is difficult to say which method is more accurate as the pores in the metallographic measurements are subject to deformation during preparation, and interconnected gas pores are not separated (which gives them an artificially lower shape factor than what the individual pores have); but the macro-CT measurements are heavily limited by the coarse spatial resolution, which makes them appear more spherical as will be discussed later on.

Of particular note is Sample 1 (**Figure 6.15** a)), whose pores are a highly convoluted mix of shrinkage and gas pores – hence the low shape factor of the large pores. The metallographic analysis is difficult to interpret, because most of the difficulty in interpreting complexly shaped interconnected pores from a metallographic section.

A curious effect can clearly be seen from the macro-CT distribution of Sample 1 is that pores become increasingly spherical as they decrease in size. This arises due to the effects of the relatively low spatial resolution of macro-CT, and as pores become smaller in size, they are comprised of fewer and fewer voxels, which makes it increasingly difficult to attain an accurate measurement of their true morphology.

Nevertheless, macro-CT is still able to give a more comprehensive view of the porosity in the samples than the metallographic analysis, so it will therefore be used preferentially for pore size-shape distributions in the remainder of this work.

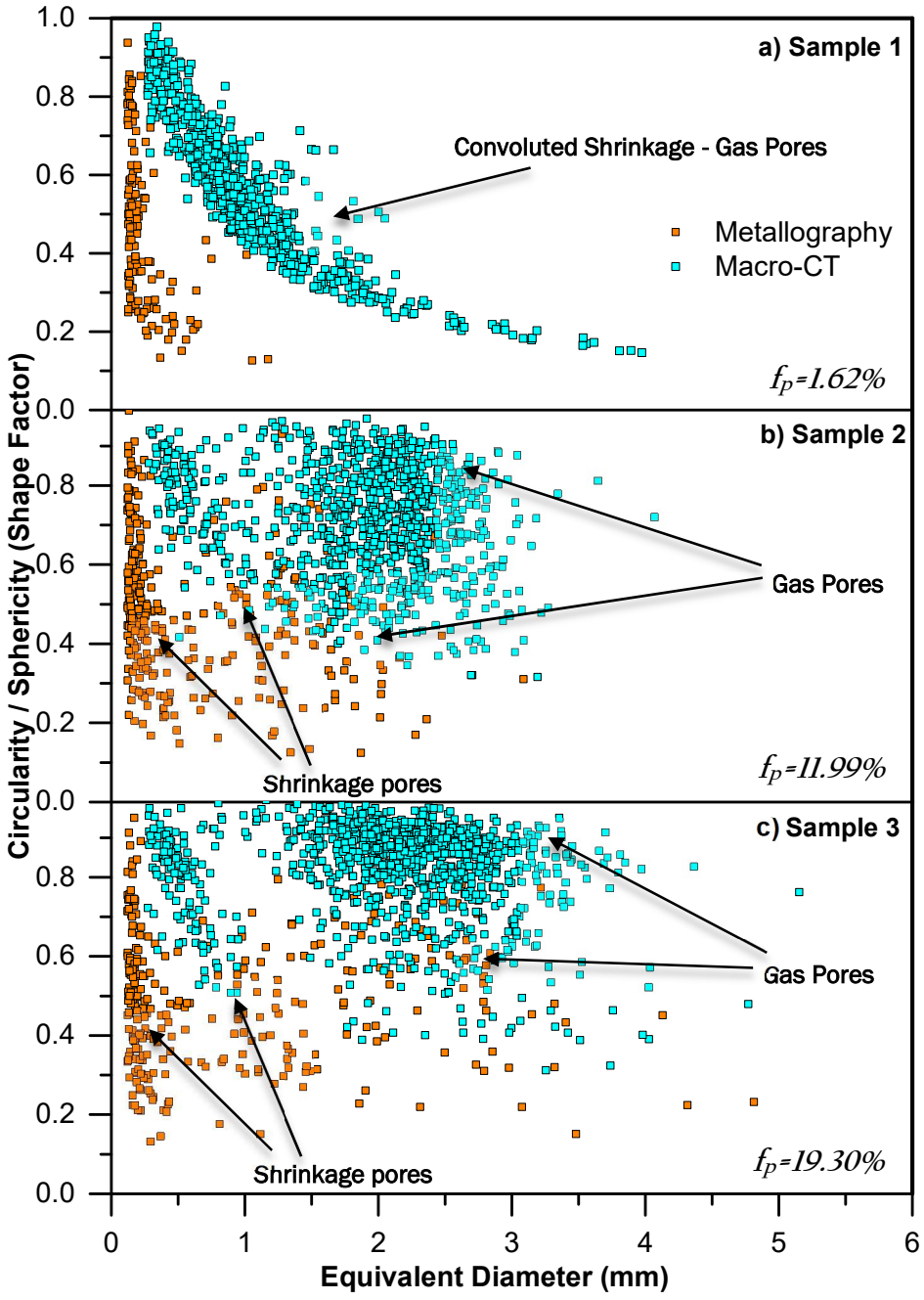

Figure 6.15 Comparison of the size-Shape distribution of pores measured by metallography and macro-CT in RPT samples a) 1, b) 2, and c) 3.

6.3.3 Pore Size Distribution

A comparison of the pore size distributions of the metallographic and macro-CT analyses is shown in **Figure 6.16**.

It can be seen that the metallographic distributions display a heavy right-skewedness. This arises mainly due to the combination of interdendritic shrinkage pores and preparation artefacts. The presence of these means that it is difficult to utilise sections of gas pores in this region.

In Samples 2 and 3, which contain higher fractions of porosity (f_p), the bimodal distribution of the data that is strongly evident in the macro-CT data can also be distinguished in the metallographic data, with Peak *B*, that comprised chiefly of gas pores, being visible in it, albeit very weakly. A division can be made at approximately d_{eq}=0.5mm between Peak *A*, the shrinkage pores, and Peak *B*, the gas pores, in the metallographic data, and is done so throughout this thesis. This gives the generalised and approximate distinction that pores with d_{eq}>0.5mm are gas pores. However, as can be seen in the distribution of Sample 1, this approximation breaks down as Peak *B* has largely disappeared. The results shown in Section 7.5 will demonstrate that this begins to occur for samples with a volume fraction of porosity (f_p) <10%.

In regards to the macro-CT data, there is a very strong bimodal distribution in the data, with Peak *B*, the gas pores, being very prominent even in Sample 1. It can qualitatively be seen here that Peak *B* moves as a function of hydrogen content, however, for simplicity of analysis,

a division will be made at a set value of d_{eq}=0.8mm between the peaks, with pores larger than this being considered as gas pores, and those smaller being considered as shrinkage pores.

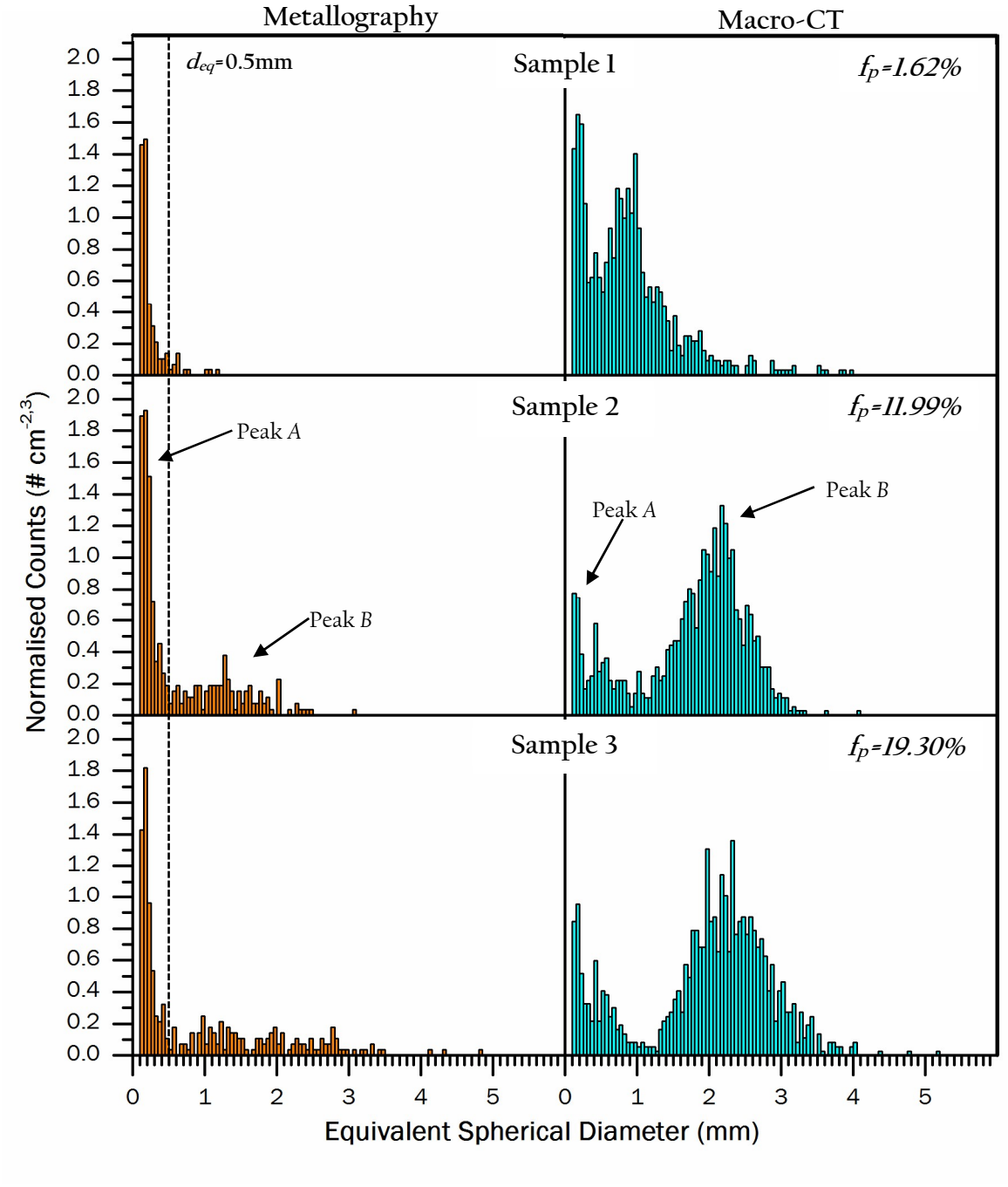

Figure 6.16 Size distribution of pores using equivalent diameter (d_{eq}) *in* RPT samples 1 (f_p=1.62%), 2, and 3.

Figure 6.17 shows that the stereological Saltikov estimate of the 3D size distribution of gas pores (d_{eq}>0.5 in the metallographic data), very roughly agrees with the macro-CT data, but tends to underestimate the size distribution. It can be seen that it does a satisfactory job at estimating the size distribution of the gas pores, despite a large number of pores being omitted due to their size being smaller than d_{eq}=0.5mm (as shown in **Figure 6.16**). The technique does however struggle to give an accurate distribution of pores in Sample 1 due to the small and complex pore size.

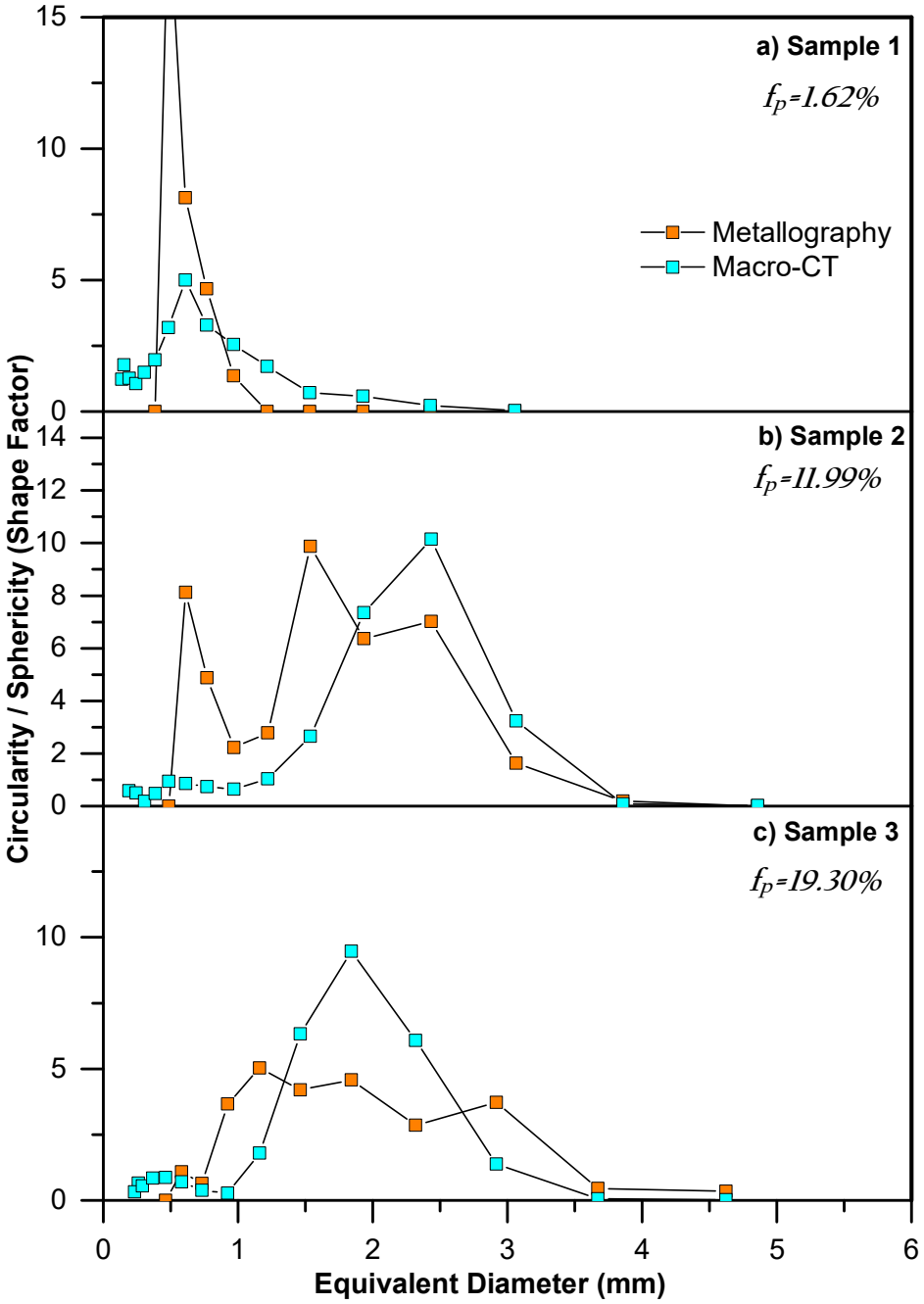

Figure 6.17 Saltikov area method of pores in the three RPT samples compared with macro-CT measurements. The data for each technique are binned at the same intervals.

6.3.4 Pore Number Density

A comparison of the pore number density (PND) is given in **Figure 6.18**. It shows that the areal PND measured by metallography does not agree with the volumetric PND from macro-CT. This arises because 2D measurements are not directly translatable to 3D [116], [118] – though this is not to say that the areal PND is not a useful measurement.

The Saltikov estimates a volumetric PND of gas pores (d_{eq}›0.5mm) shows a reasonable comparison with the macro-CT volumetric PND of gas pores (d_{eq}›0.8mm), though it is not perfect. Nevertheless, it serves as a useful independent method of estimating this quantity.

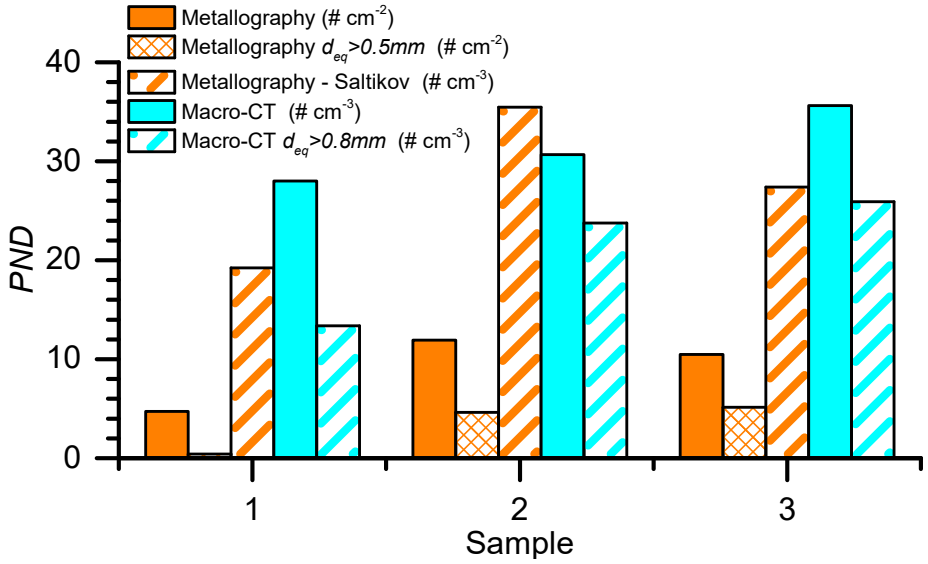

Figure 6.18 Comparison of the PND measured by metallography and macro-CT.

6.4 Evaluation of Macro-CT using Micro-CT

The effectiveness of macro-CT for porosity analysis was investigating by comparing its results with micro-CT.

6.4.1 Procedure

A comparison of the XCT methods required samples that contained pores that were large enough to be detected by macro-CT, but also required that the samples were sufficiently to fit the field of view (FOV) of micro-CT. This therefore necessitated a different approach to the standard analysis procedures outlined in Chapter 5, especially for the micro-CT.

Specimen Preparation

The specimens were taken from sectioned RPT samples as shown in **Figure 6.19** by turning with a metal lathe.

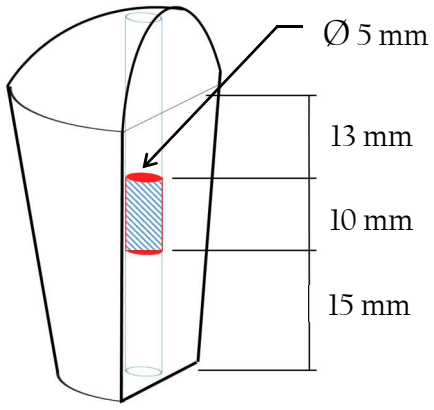

Figure 6.19 Position and dimensions of the specimens machined from RPT samples for the comparison of Macro-CT and Micro-CT.

Scan Acquisition

The specimens were scanned using the same macro-CT procedures and parameters as outlined above in Section 5.2.1. The micro-CT scans were performed using similar parameters to the standard micro-CT with the minor differences listed below in **Table 6.1**. The reason for this is that it was necessary to acquire and 'stitch' multiple scans that were over the height of the sample in order to cover the entire volume of the sample.

Table 6.1 Micro-CT scan parameters used for comparison with macro-CT. Parameters differ from those used in the standard micro-CT analysis are indicated in grey.

Parameters	Value
Scan Voltage	80 kV
Beam Power	7 W
Focal Spot Size	20 µm
Beam Filter*	LE4
Optical Lens†	4×
Exposure Time	2.5 s
Source-Sample Distance	41.70 mm
Sample-Detector Distance	10.35 mm
Binning	2
Number of Projections	1601
Nominal Voxel Size	~5.4 µm
Scan Type	Stitch
Number of Scans Stitched Together	3

* Zeiss proprietary materials. The number indicates the filter's attenuating strength, increasing in ascending order.

† This system includes an optical magnification lens as described in Section 3.4.2.

Image Processing & Analysis

The reconstructed macro- and micro-scan volumes were cropped into equivalent volumes to omit burs and open pores at their ends, which would otherwise prove problematic to subsequent segmentation operations. Cropping was done manually by the operator, using landmarks in the images to aid the selection of the equivalent volumes, though it should be noted that it was impossible to exactly align the slices as one macro-CT slice is as thick as approximately 8 micro-CT slices. The resulting analysis volumes are given in **Table 6.2**.

The macro-scans were processed, segmented & analysed using the procedure in Section 5.2.2.

The micro-CT images were processed and segmented as listed in Section 5.3.2, though, due to the very large pore size there were the slight differences in the procedure for segmenting the micro-CT images as follows. After segmentation of the sample volumes (S) from the background (using the MBWT), open pores at the surface of sample surface were closed by applying the following sequence of morphological operations:

- dilation (3D, 250 iterations),
- flood fill (3D),
- fitting of a convex hull (to smooth the dilated surface), and
- erosion (267 iterations).

It was necessary to omit a boundary of ~17 voxels at the edges of the samples using the final erosion operation in order to avert the incorporation of erroneous cracks at the edges of the samples into the analysis as artefacts.

A summary of the specimens and the analyses is given in **Table 6.2**.

Table 6.2 Summary of the specimens used for the comparison of macro-CT & micro-CT porosity analysis.

Specimen No.	Specimen f_P^* (%)	Analysis Volume (mm^3)	
		Macro-CT	Micro-CT
1	1.89	148.36	149.31
2	10.18	154.35	153.32
3	20.85	137.45	138.16

* Calculated from micro-CT analysis.

6.4.2 Macro-CT vs Micro-CT Image Clarity

A comparison of the equivalent *x-y* slices of the XCT data in **Figure 6.20** shows that there is a very strong difference in the types of features that are resolved by the two methods. In particular it can be seen that in the macro-CT scans individual pores are less well defined, with multiple pores often blurred together into a single entity. It also does not accurately pick up the surface roughness and other small features of the pores, giving the edges a smoothed effect. The effect of this on the 3D reconstruction of a typical pore with interdendritic features is shown in Figure **6.21**.

The reasons for these differences in measurement can be appreciated from **Figure 6.22**, which shows that when pores are viewed with relatively large voxels, like in macro-CT, their digitalised representation becomes increasingly contorted. In the case of the small dendritic pores, their shape is essentially completely lost. The accuracy of the digitalised representations becomes increasingly accurate as the voxel size decreases – as is the case with micro-CT.

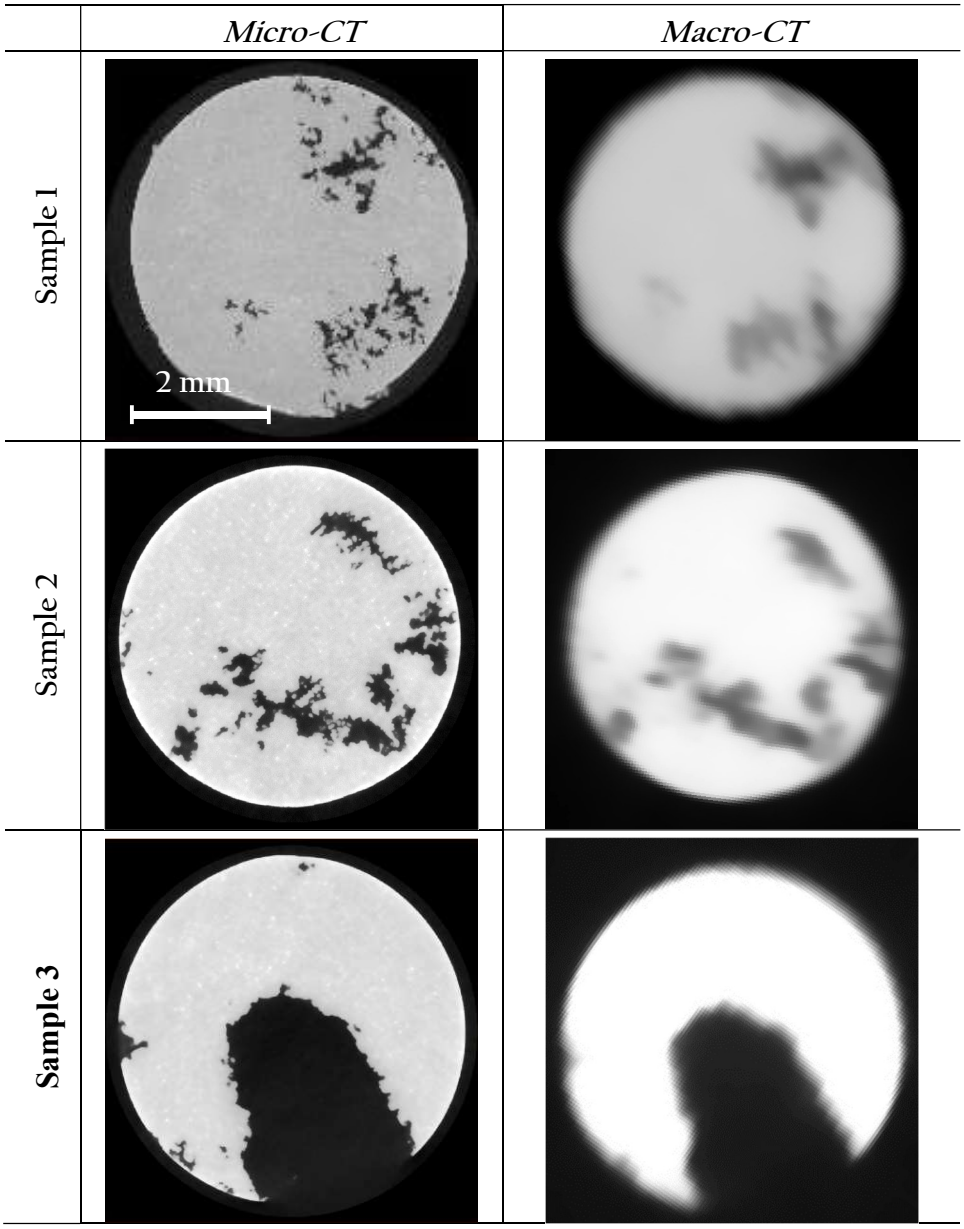

Figure 6.20 Comparison of almost equivalent micro-CT and macro-CT Slices

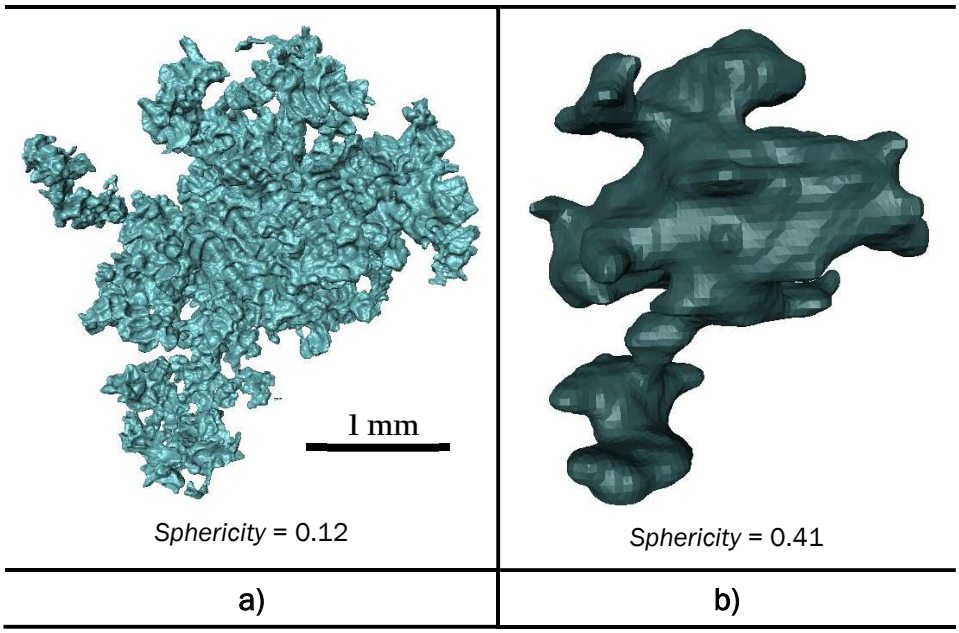

Figure 6.21 3D reconstructions of the same pore in sample 1 from the a) micro- and b) macro-CT scan images. It shows that the macro-CT data are heavily smoothed in comparison to the micro-CT and not all features of the pore are captured in the macro-CT image.

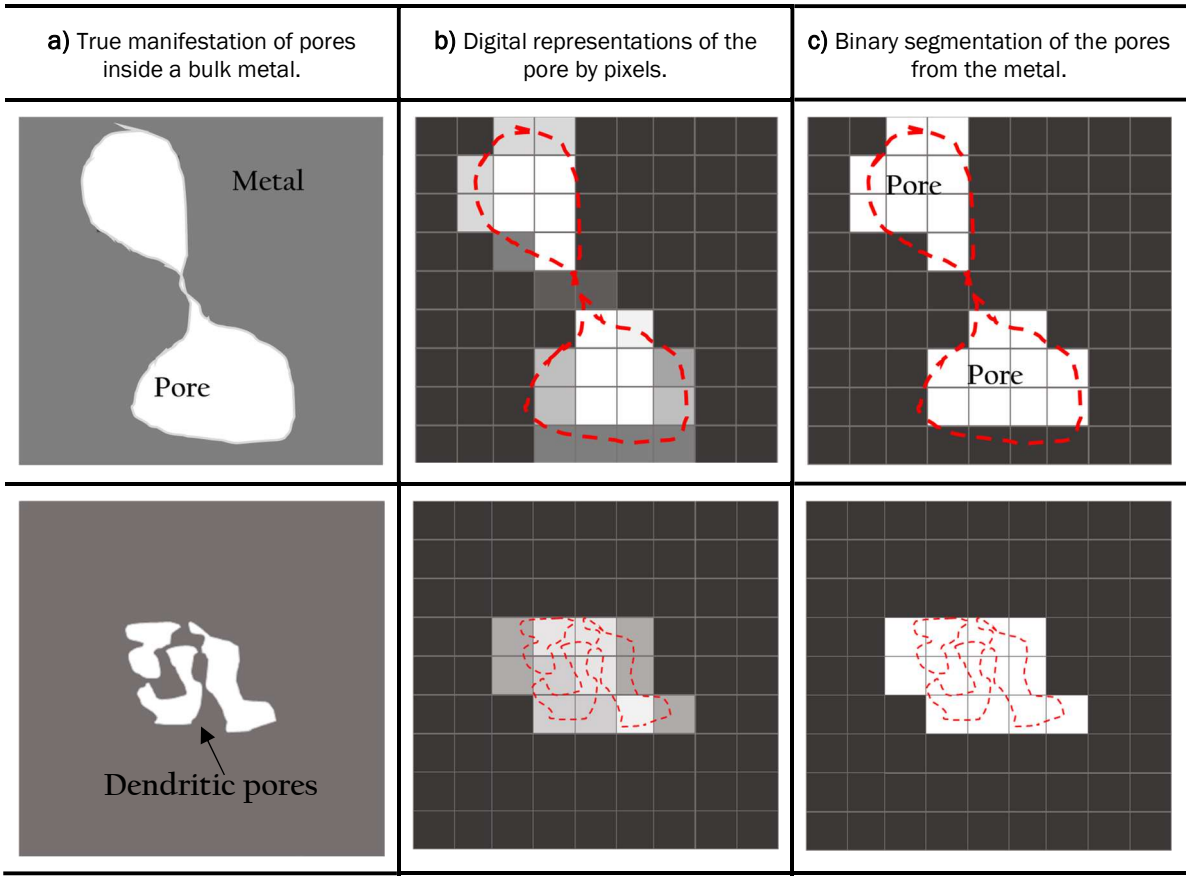

Figure 6.22 Example of a digital representation of a pore and the effect of sub-voxel features on the resultant segmentation.

6.4.3 Volume Fraction of Porosity

The volume fraction of porosity (f_p) serves a good first quantitative comparison of the methods, and is given in **Figure 6.23**. It shows that there is a good agreement between the two methods, with the relative difference between them sharply decreasing with increasing fractions of porosity. This is likely due to the pores increasing in size as the overall volume fraction increases, which makes them easier for macro-CT to resolve and measure.

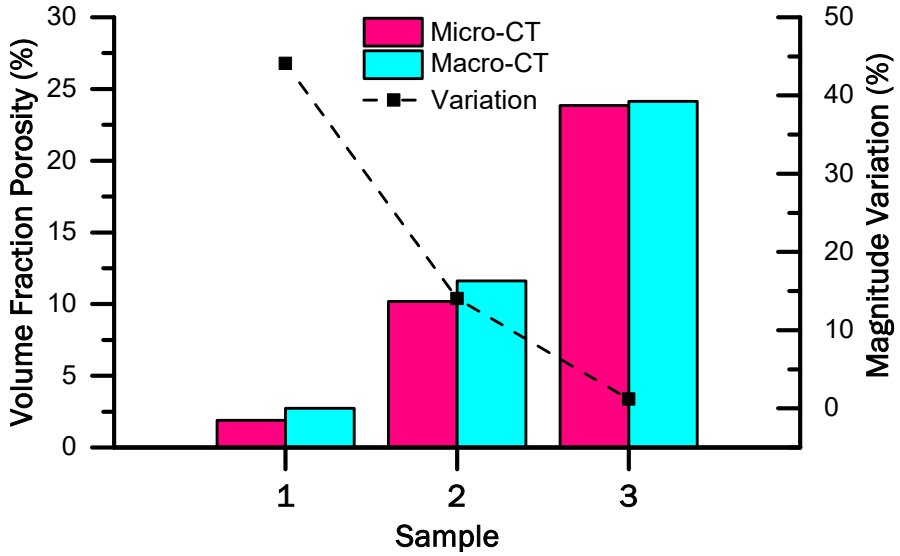

Figure 6.23 Volume Fraction of Porosity measured in the three specimens by macro- and micro-CT analysis.

6.4.4 Pore Size-Shape Distributions

The pore size-shape distributions measured by micro-CT and macro-CT in the three samples is given in 6.24. Again as in **Figure 6.25**, it can be seen that many smaller pores are detected by micro-CT than by macro-CT, though in both cases only pores comprising of 125 voxels or more are included in the data for morphological analysis. When measuring the larger pores, the macro-CT seems to measure the size of pores to be very similar to the micro-CT analysis, though the shape factor is substantially higher. This is a key factor that needs to be kept in mind when interpreting the results of macro-CT, and is the result of the relatively course spatial resolution of the technique. This can be appreciated by comparing the equivalent slices from each scan in Figure **6.20**, where it can be seen that this is particularly detrimental to the clarity of interdendritic shrinkage pores.

As the number of voxels within an object decreases, its apparent sphericity increases; which is why the shape factor tends toward a value of 1 as the pore size decreases. A good example of this can be seen in Sample 3 (**Figure 6.24**c)).

What should be taken away from this is that macro-CT measures the size of pores quite accurately, but the shape is artificially high.

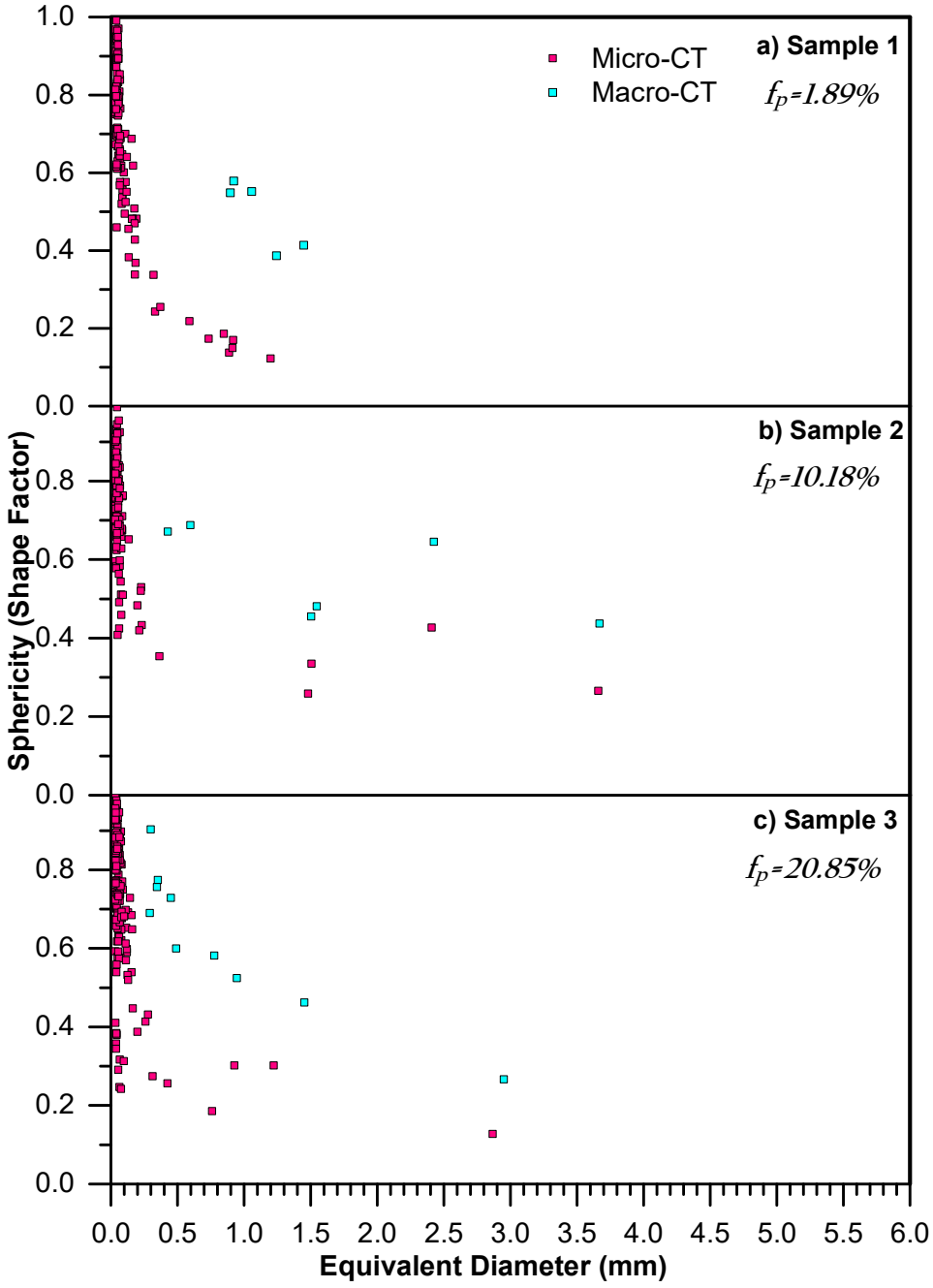

Figure 6.24 Size-shape distribution of pores in the three specimens used for the comparison of macro-CT with micro-CT.

6.4.5 Pore Size Distributions

The pore size distributions measured inside the samples are shown in **Figure 6.25**. It shows a significant difference in the pores measured by each technique, with micro-CT measuring a higher number of smaller pores, especially pores d_{eq}‹0.3 mm. This is expected due to the minimum size limit of pores in macro-CT is d_{eq}‹0.12 mm, moreover, as pores get smaller, they cannot be expected to reliably be detected by macro-CT. The reason for this discrepancy can easily be understood by comparing the images in **Figure 6.20**, which shows that macro-CT images, may simply not resolve small pores at all, or adjacent individual small pores may appear as a single larger pore.

That being said, there may be minor amounts of noise or artefacts in the micro-CT analyses, but nevertheless, the results still illustrate that macro-CT overlooks a large population of small pores in the samples. Both techniques measure a similar number of larger pores, d_{eq}›0.5 mm. This is good news, because, as will be shown in the coming work, the pores of most importance to this work are generally larger than this.

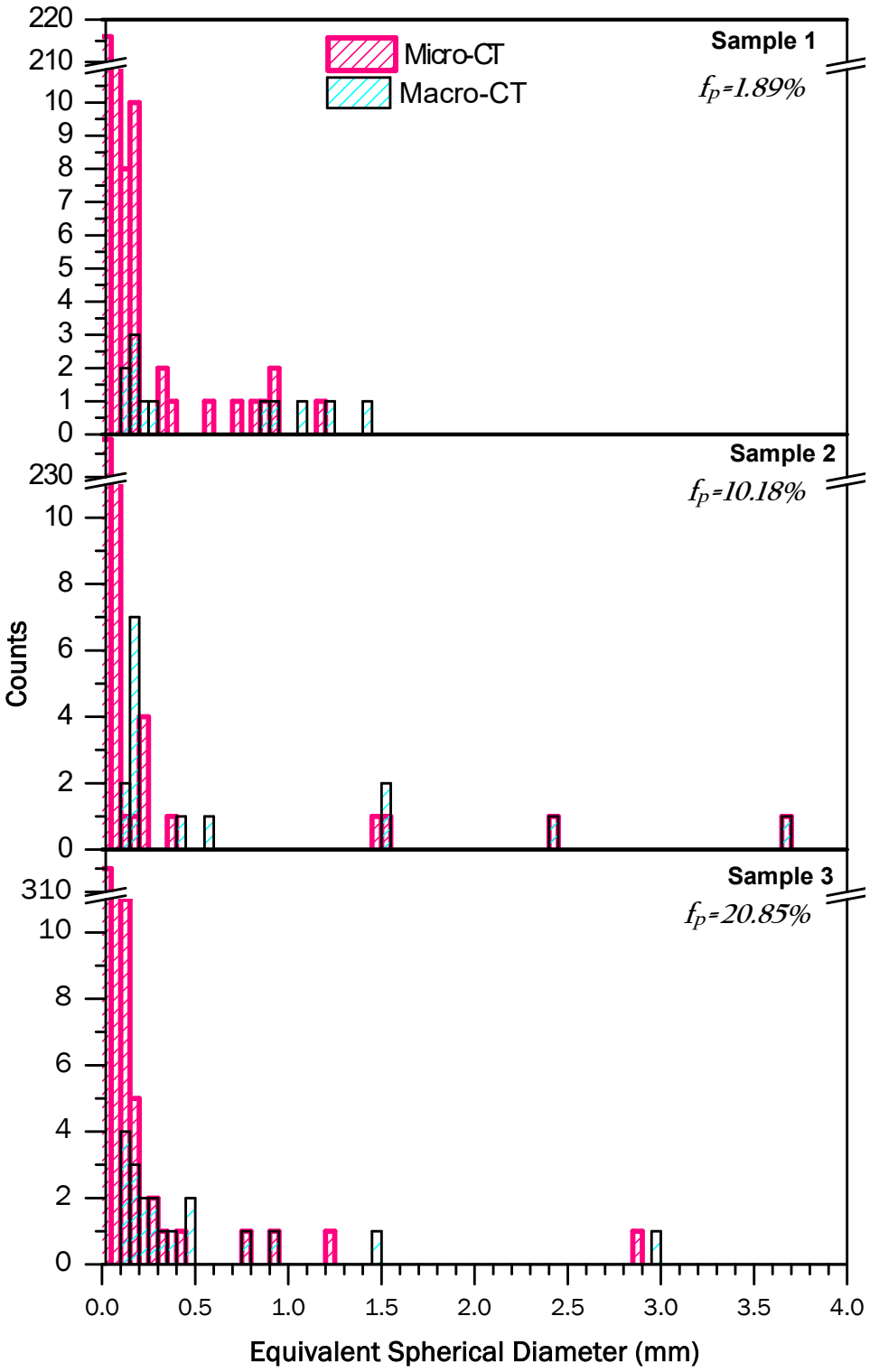

Figure 6.25 Pore size distribution in the three specimens measured by macro-CT and micro-CT.

6.4.6 Pore Number Density

Due to the open nature of pores in the specimens that were used in this area of work, the *Separate Objects* module that was normally used to split interconnected pores proved ineffective using the standard parameters. Moreover, the efficacy of the module would have been different for the micro-CT scans. Therefore, for a straightforward comparison of the number of pores that each technique sees, the unseparated PND was compared.

Figure 6.26 shows a comparison of the (unseparated) pore number density (PND) measured in the samples by each of the techniques. It shows that there is a very poor agreement between the PND measured by micro- and macro-CT, with the former measuring a significantly higher PND than the latter, and there does not seem to be a decrease in the difference between the techniques as the fraction of porosity in the samples increases.

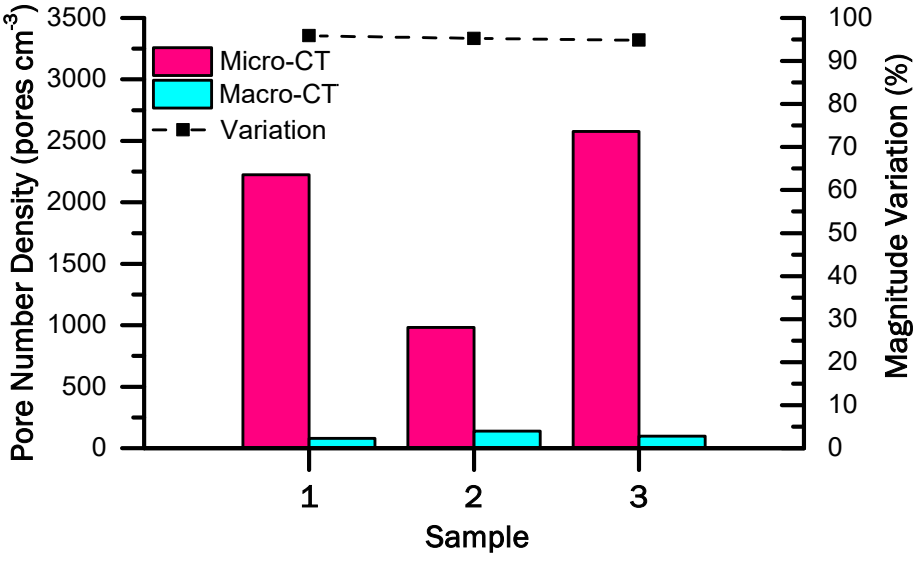

Figure 6.26 Comparison of the volumetric pore number density (PND) measured by macro-CT and micro-CT analysis.

The PND is of the order of thousands in the micro-CT analysis because of the small sample size, and the large number of small pores in the small sample. The large number of small pores are probably regions of shrinkage, as gas pores are induced to grow to a large size during the RPT, at least when the hydrogen content and f_p are high, like in the case of Samples 2 & 3.

6.5 Micro-CT Analysis of Porosity

The extensive interconnectivity of pores with each other, and with the edges of the sample and the image (**Figure 6.27**), meant that it was not feasible to disregard pores at the edge of the image from the micro-CT analyses, as is usually the standard protocol in this sort of analysis – due to difficulties in properly defining the morphology of such pores. Otherwise, this would have resulted in a significant proportion of the porosity in the samples being omitted – especially in the samples where the interconnectivity was very high (**Figure 6.27** b)) – which would have made sample comparison difficult. This is therefore one of the key potential sources of error in this analysis, which must be laid out.

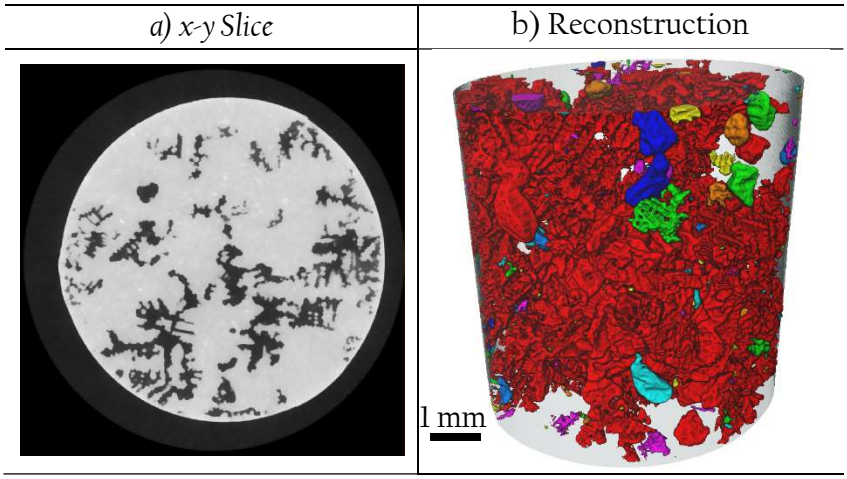

Figure 6.27 Micro-CT a) *x-y* slice and b) 3D reconstruction. The colours in the 3D reconstruction represent individual pores. The large red pore is a single large pore

Part III
Main Results

Chapter 7

Melt Quality Experiments

This chapter presents the results of the first phase of experimental work, where the effects of the melt hydrogen and oxide film content on porosity were investigated. Details on the experimental procedure for this work have been described in Section 4.5, and a discussion of these results will be given in Chapter 9.

7.1 Summary of Experiments & Melt Compositions

A summary of the melt treatments performed in each of the four experiments is reproduced below in **Table 7.1**, and the initial compositions of the melts are listed below in **Table 7.2**.

Table 7.1 Experiments & melt treatments performed (reproduced from Section 4.5).

ID	Melt Treatment
CM1	**Clean Metal** Self-cleaned (holding) & upgassed.
CM2	**Clean Metal** Fluxing & upgassing.
DM	**Dirty Metal** Swarf chips added.
RD	**Degassed Metal** Rotary treatment.

Table 7.2 Initial melt compositions.

Exp.	Elemental Content (wt.%)								
	Si	Fe	Cu	Mg	Zn	Ti	V	Al	Others
CM1	6.96	0.21	0.001	-	0.018	0.006	0.006	92.77	0.02
CM2*	7.18	0.24	0.033	0.011	0.008	0.006	0.005	92.48	0.04
DM0†	7.43	0.22	0.002	0.005	0.005	0.006	0.006	92.31	0.04
RD	7.38	0.23	0.012	0.005	0.006	0.003	0.003	92.33	0.02

* After flux addition.
† After swarf addition.

7.2 Melt Quality Change in Response to Melt Treatments

The change in the volume fraction of porosity (f_p) in the RPT samples measured using Archimedes' method, and the melt hydrogen content over the course of the experiments, is shown in **Figure 7.1** to **Figure 7.4**; the points at which the Prefil samples were taken are also indicated on them. As has been discussed in Section 2.6, f_p in the RPT samples can loosely be taken as a measure of melt quality.

The figures show that in all experiments f_p closely mirrors the same trend as the melt hydrogen content. As expected, the upgassing process increased the hydrogen content of the melt and f_p. When upgassing was ceased, leaving the melt with an initially high hydrogen level, the hydrogen content and f_p can be seen to then decrease over time as the melt naturally *off-gasses* toward its equilibrium value with the environment. A good example of this is given in **Figure 7.2**, which displays a smooth curve due to the constant skimming of the melt aiding off-gassing.

In DM (**Figure 7.3**), the melt was initially upgassed to a high hydrogen level prior to starting the experiment, however, when the swarf was added at the beginning of the experiment, the hydrogen content further increased. It was only after the skimming-off of some of the dross layer that the hydrogen began to decrease. This suggests that the swarf chips introduced some hydrogenous substance, perhaps residual machining lubricant, which *up-gassed* the melt; it also underscores the impediment to hydrogen diffusion that the dross layer poses. Notably, it can be seen that there was a perturbation in f_p in the immediate RPT sample taken immediately after partial skimming of the dross – this was probably due to a lower fraction of dross captured at this surface. As can be seen from the RPT sample cross-sections, the dross had a propensity to balloon during the RPT. It can also be seen that after some of the dross layer was skimmed from the surface of the melt that the melt hydrogen content begins to decrease, albeit slowly.

Finally, **Figure 7.4** shows that in RD a low melt hydrogen content and f_p was achieved following rotary degassing. However, after this the hydrogen content immediately began to increase towards equilibrium with the environment, and f_p followed concomitantly.

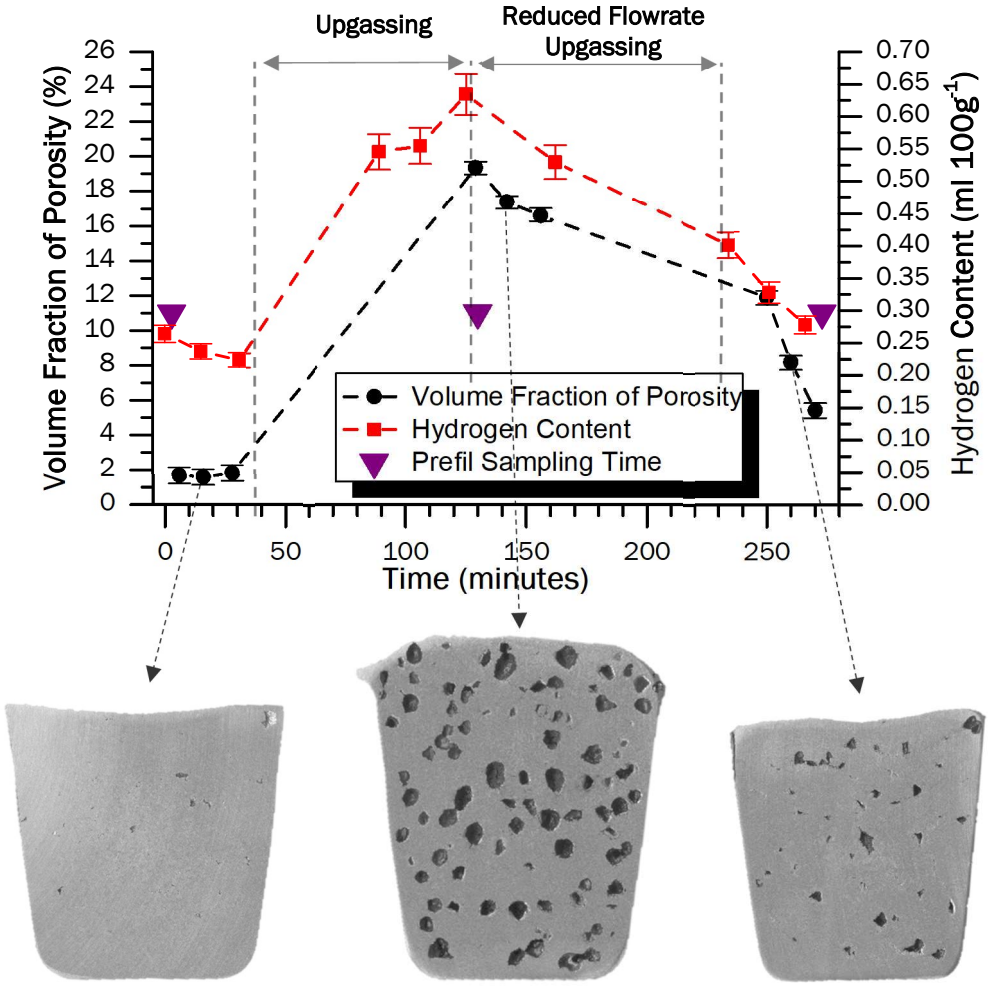

Figure 7.1 CM1 f_p measured by Archimedes' principle and melt hydrogen content versus time, and selected of metallographic cross-sections of RPT samples.

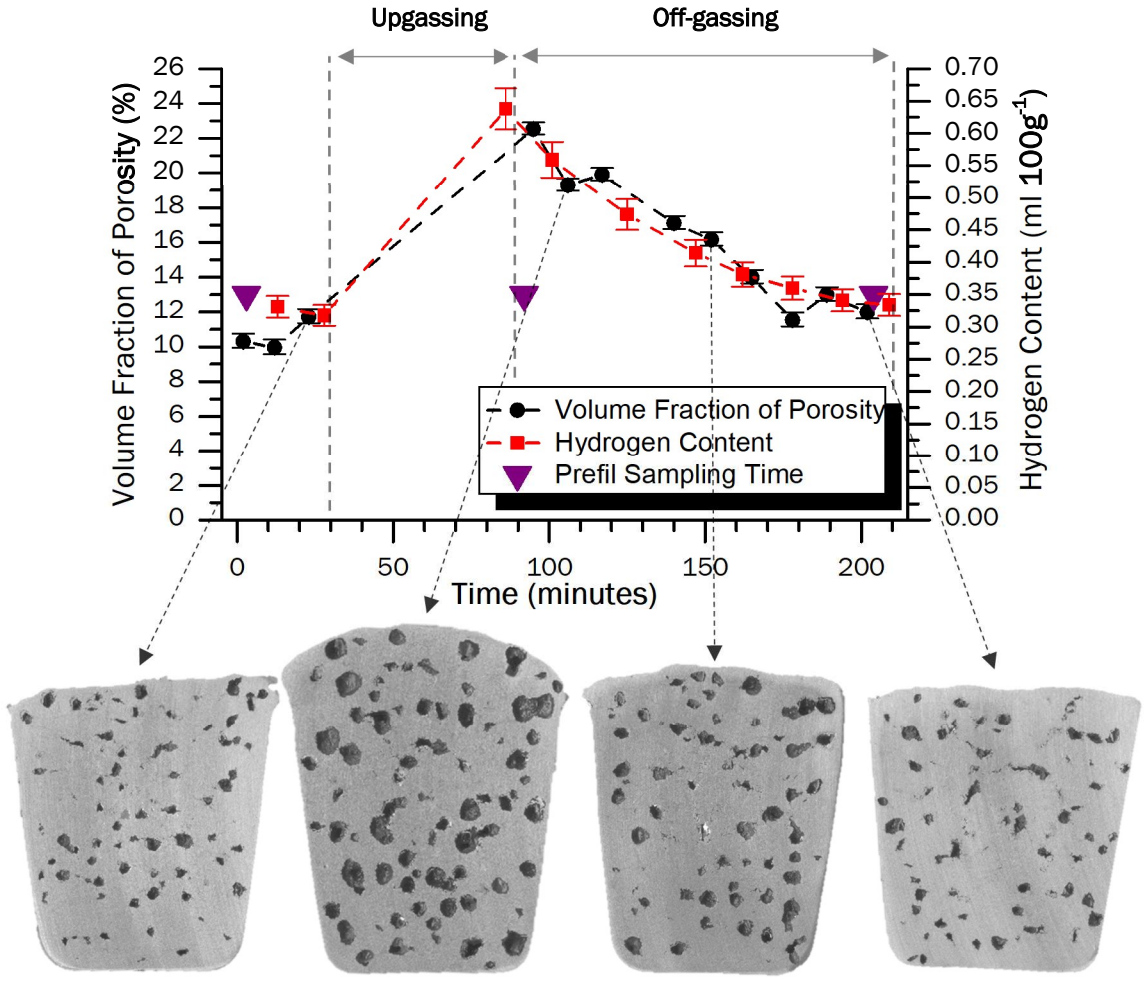

Figure 7.2 CM2 f_p measured by Archimedes' principle and melt hydrogen content versus time, and selected of metallographic cross-sections of RPT samples.

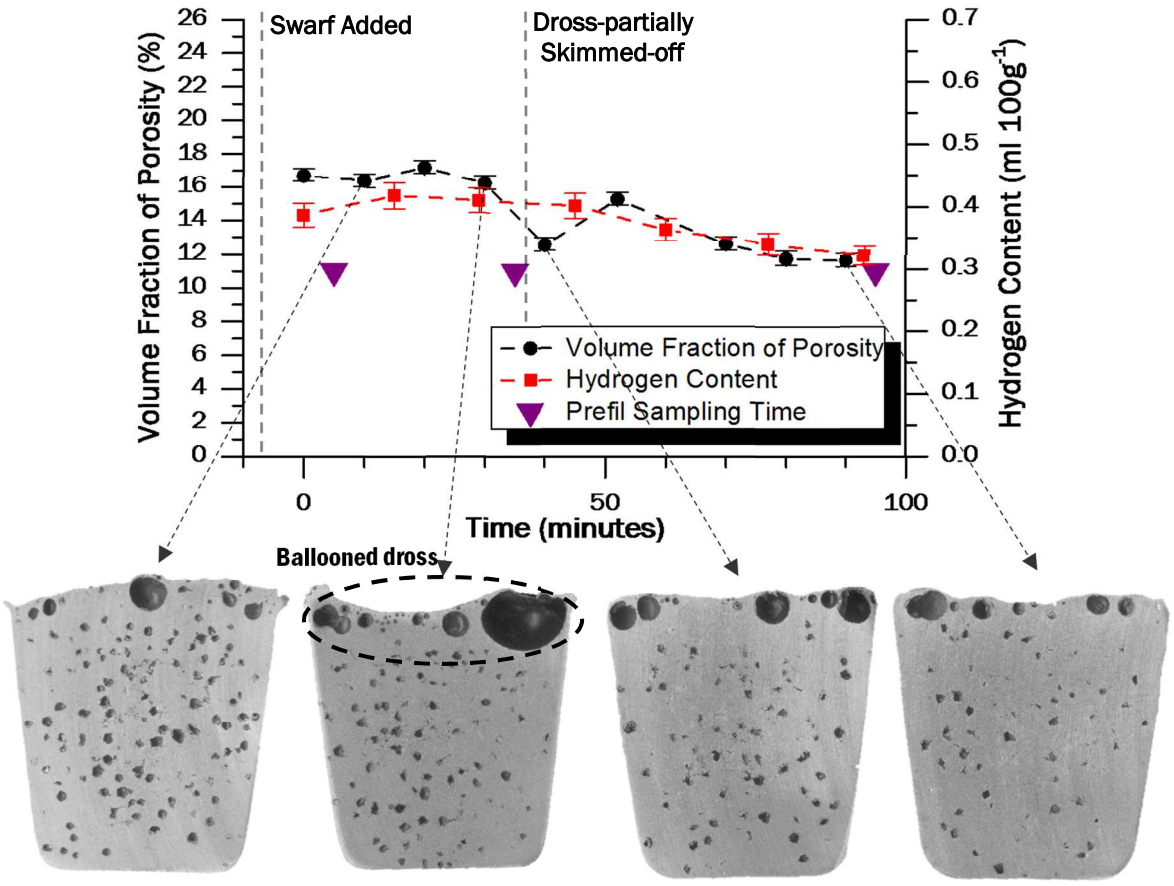

Figure 7.3 DM f_p measured by Archimedes' principle and melt hydrogen content versus time, and selected of metallographic cross-sections of RPT samples.

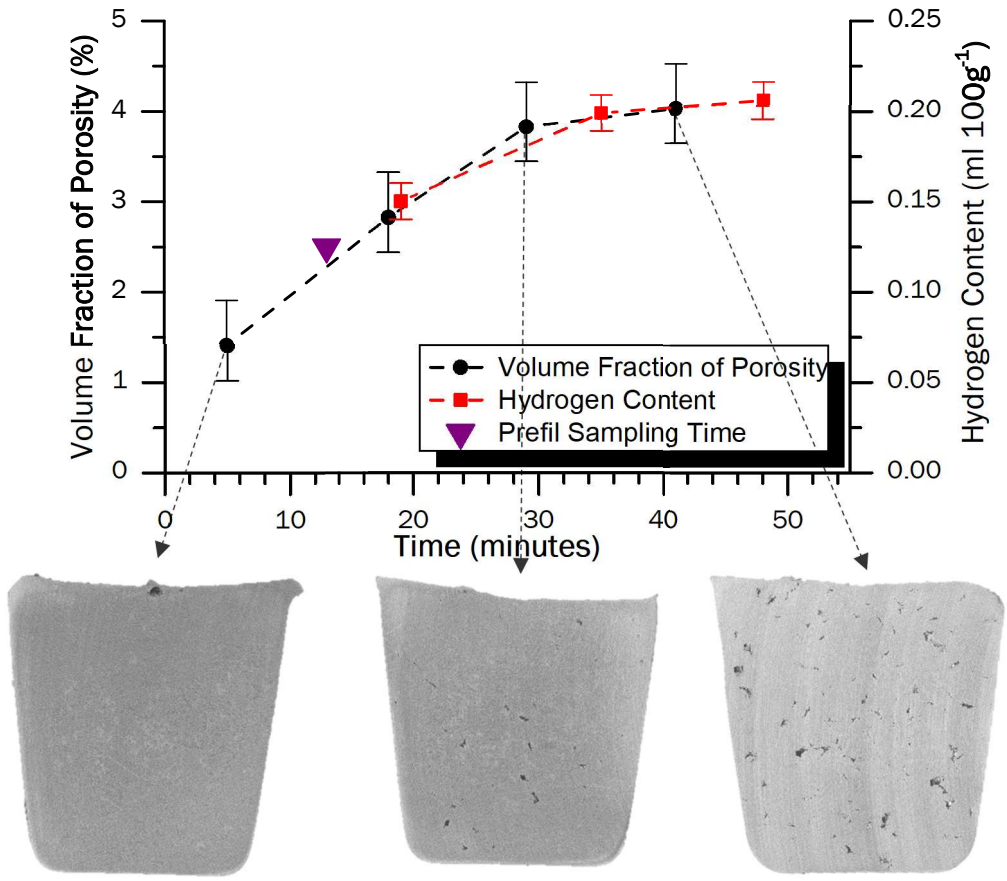

Figure 7.4 RD f_p measured by Archimedes' principle and melt hydrogen content versus time, and selected of metallographic cross-sections of RPT samples.

7.3 Melt Cleanliness Change in Response to Melt Treatments

The oxide and inclusion content in the melt over the course of the experiments was measured using Prefil samples that were taken at intervals over the course of the experiments. The time at which the samples were taken is indicated on **Figure 7.1** to **Figure 7.4**, above.

7.3.1 Premetz & PoDFA Analysis

The Premetz MC values and the complete results of the PoDFA analyses of the Prefil filter residues are given in **Table 7.3.**

Premetz

Figure 7.5 shows that there is great variability in the MC values of the melt over the course of each experiment, and because of this, does not show any consistent trend between the nominally clean melts (CM1 & CM2), and the nominally dirty melt (DM). Hence it is difficult to draw conclusions about the oxide or inclusion populations in these experiments. Notably however, the rotary treated metal (RD) has a high MC value.

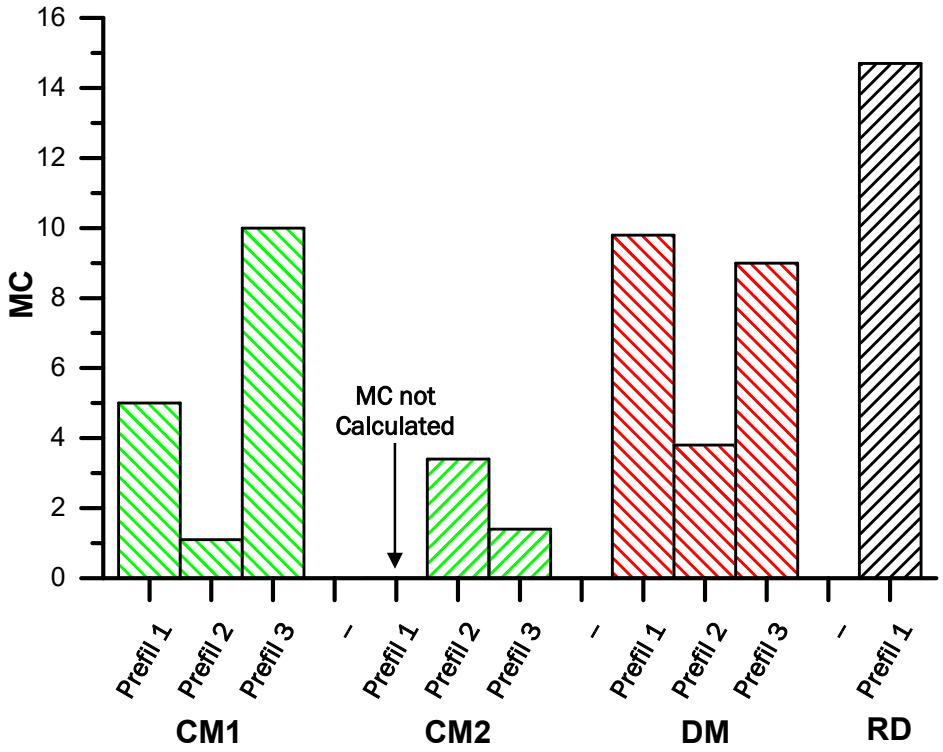

Figure 7.5 Premetz MC values from the melt quality experiments. The MC value for Prefil 1 of CM2 was not calculated as the filtration curve was not saved due to premature termination of the Prefil test due to failure of the apparatus' pressure valve.

Table 7.3 Premetz MC and complete PoDFA analysis results from the melt quality experiments.

Exp.	Sample #	Relative Sampling Time (min)	MC	PoDFA								
				Oxide Films (#/kg)	Refractory		Crucible Fragments (mm^2/kg)	α-Al_2O_3 (mm^2/kg)	Borides (mm^2/kg)	Particle Cluster ($mm^2\,kg^{-1}$)	Total Inclusion Count (mm^2/kg)
					Reacted (mm^2/kg)	Unreacted (mm^2/kg)					
CM1	1	3	5	11		0.0005	0.003		0.007	0.007	0.021
	2	132	1.1	13	Trace	0.005			Trace	Trace	0.008
	3	261	10	27		Trace	Trace		0.009	0.018	0.027
CM2	1	3	-*	23	0.001	0.008	0.015	0.007	0.036		0.066
	2	92	3.4	20	0.0004	0.003	0.003	0.002	0.007		0.016
	3	204	1.4	11	0	0.004	Trace	0.003	Trace		0.007
DM	1	5	9.8	20	Trace	0.013	0.006	0.003	0.003		0.023
	2	35	3.8	25	0.015	0.023	0.007	0.001	0.001		0.047
	3	94	9	47	Trace	0.001	0.011	0.001	0.001		0.012
RD	1	13	14.7	25	0.007	0.004	0.004	0.005	Trace		0.020

Blank cells indicate that no amount of the given inclusion species were measured, while 'trace' indicates that trace amounts of the inclusion species were observed, though not in measurable amounts.

* MC not measurable as the filtration curve was not saved due to premature termination of the Prefil test due to failure of the apparatus' pressure valve.

PoDFA Analysis: Oxide Film Content

It is difficult to determine if there is any appreciable difference in the oxide film content of the melts based solely on these results as both show scattered and inconsistent results in all experiments. For example, **Figure 7.6** shows that Prefil 1 from DM (swarf loaded), and Prefil 3 from CM1 and Prefil 2 from CM2 have similar levels of oxides. However, the other Prefil samples from these experiments do show a difference in the number of oxides in the material, though this is not very significant, given that PoDFA should be considered to give an order of magnitude estimate [92]. This is interesting as PoDFA analysis would be expected to be able to resolve large oxides which would be expected to be much more numerous in the DM samples, especially in Prefil 1, which was taken just after swarf addition. Finally, it is also important to point out that the rotary treated metal (RD) has a similar count of oxides to the aforementioned samples.

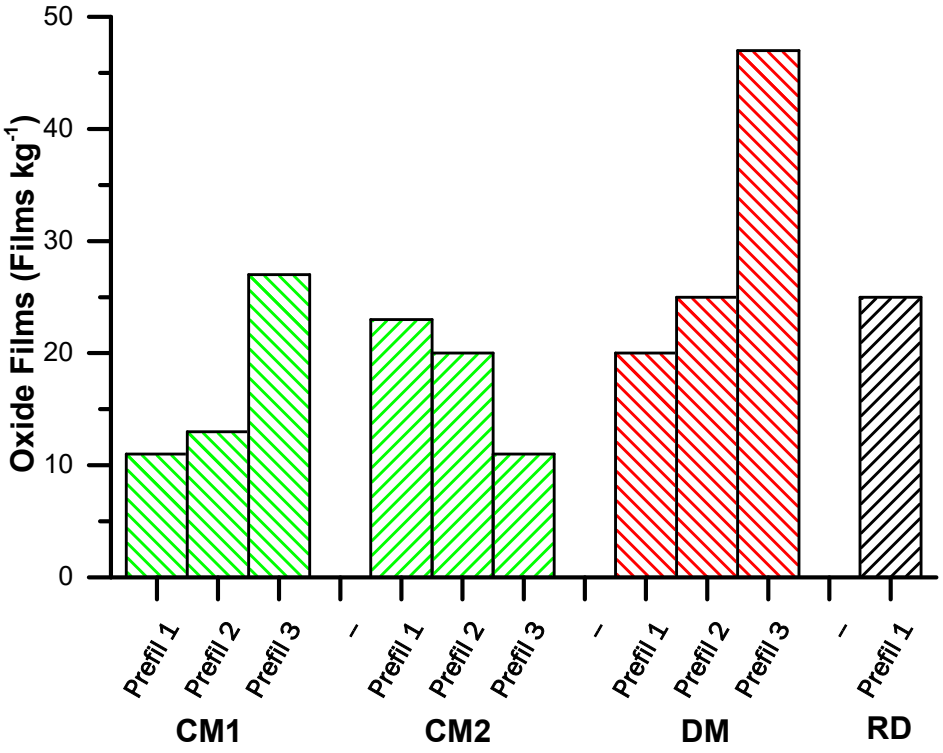

Figure 7.6 PoDFA count of oxide films per kilogram in each Prefil sample.

PoDFA Analysis: Other Inclusions

Table 7.3 and **Figure 7.7** show that there are a number of other inclusion species present in the melts. A few notable observations can be made:

- Borides are omnipresent in all of the melts, even though no grain refiner was added to the material. An investigation into these particles was conducted and will be presented in Section 8.2.
- Spalled crucible fragments are a common inclusion, and probably originate from the bottom of the furnace, which became noticeably damaged when removing the 'heel'.

- There is an unknown species of 'Particle Cluster' inclusions in CM1. EDX analysis (Appendix III.2) determined that these particles were rich in copper. It is unclear where these inclusions originate from – perhaps some contaminants on the foundry tools.
- CM2 Prefil 1 has the highest inclusion content of all of the samples across the experiments. It is not clear why this is the case. A possible explanation is that the vigorous stirring during flux addition suspended a large number of small inclusions that did not settle out during holding.
- DM has the highest fraction of unreacted refractory. This might originate from the refractory particles having a tendency to float out of the melt into the dross layer, which in this experiment, was stirred back by top-stirring the melt.
- RD has a very low total inclusion content. This may be the result of the cleaning of the metal during the rotary degassing process.

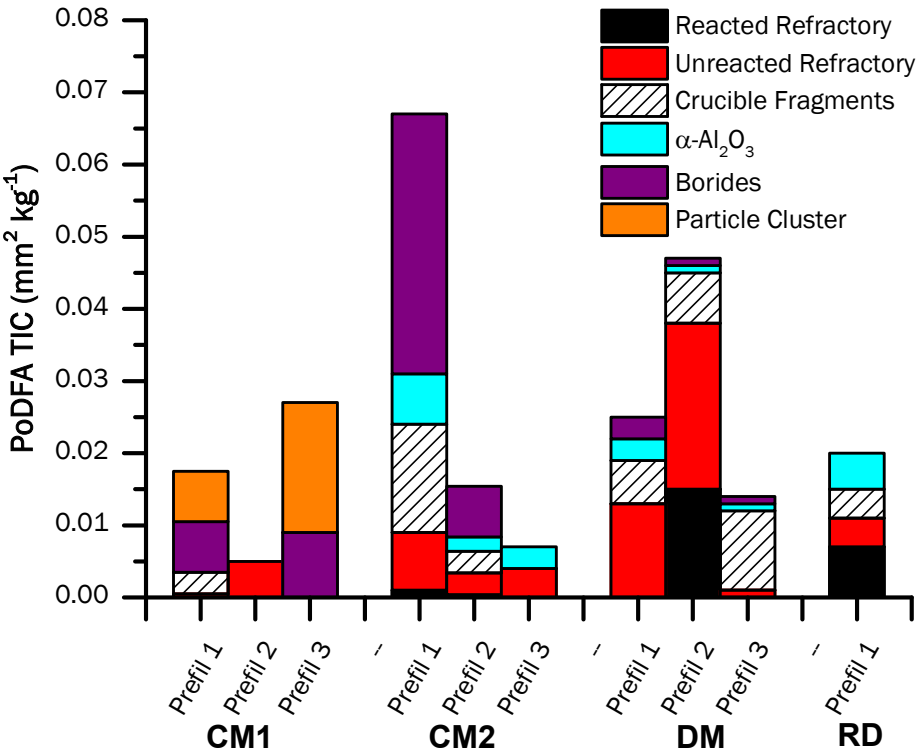

Figure 7.7 Graphical representation of the PoDFA TIC in the melt quality experiments.

7.3.2 SEM Microanalysis of Prefil Samples

Typical Back Scattered Electron (BSE) micrographs from SEM examination of the inclusion band of Prefil samples are presented in **Figure 7.8** to **Figure 7.12** below. The two main observations that can be made are, firstly, the samples from CM1 and CM2 have a relatively low oxide film content compared to the samples from DM and RD – which contrasts heavily with the results of the PoDFA analysis – and secondly, these oxide films are concentrated in the interdendritic regions of the samples, amongst the eutectic. Some of the oxide films, though not all, can be seen to exhibit a complex crack-like shapes, a characteristic that is often attributed to bifilms.

Table 7.4 provides a qualitative estimate of the oxide film content of each of the samples, by assigning them a '*Cleanliness Rating*' on a scale of 1 to 10. This was qualitatively determined

by the operator based on the number of oxide films that were seen over the inclusion bands of the Prefil samples, and is dimensionless. It should be used to give a 'ballpark' indication of the relative number of oxide films in each of the experiments.

A summary of some of the key observations that were made from the examinations of the samples is as follows.

Table 7.4 The 'Cleanliness Rating' of each Prefil Sample from SEM (BSE) micro-analysis. The Cleanliness Rating givens a qualitative estimate of the number of oxide films in the material made by the SEM user based on the observations that were made during the analysis. A value of 1 represents a clean metal, with a very low oxide content, whilst a value of 10 represents a dirty metal, with a high oxide film content. This should be taken only as a ballpark estimate of the relative oxide contents between the experiments.

Exp.	Prefil No.	Cleanliness Rating (1 – 10)
CM1	1	1
	2	1
	3	3
CM2	1	3
	2	2
	3	2
DM	1	7
	2	10
	3	6
RD	1	10

CM1 Prefil Samples

The overall oxide film content was relatively low in all of these samples. In general, the films tended to be thin and small in size, though some larger films were also sparsely present, which were probably entrained from the surface of the melt during sampling and pouring. Because these oxides are thin, this suggests that they are probably young-oxides. An oxide film with a complex bifilm morphology can be seen in **Figure 7.8** d).

There were slightly higher fractions of thin oxide films in localised areas of the inclusion band of Prefil 3 (**Figure 7.8** d)). These oxides were probably entrained during the hasty removal of the lance and skimming-off of the dross layer.

In addition, some of the copper-rich '*particle clusters*' can also be seen as indicated in **Figure 7.8** (further details are given in Appendix III.3).

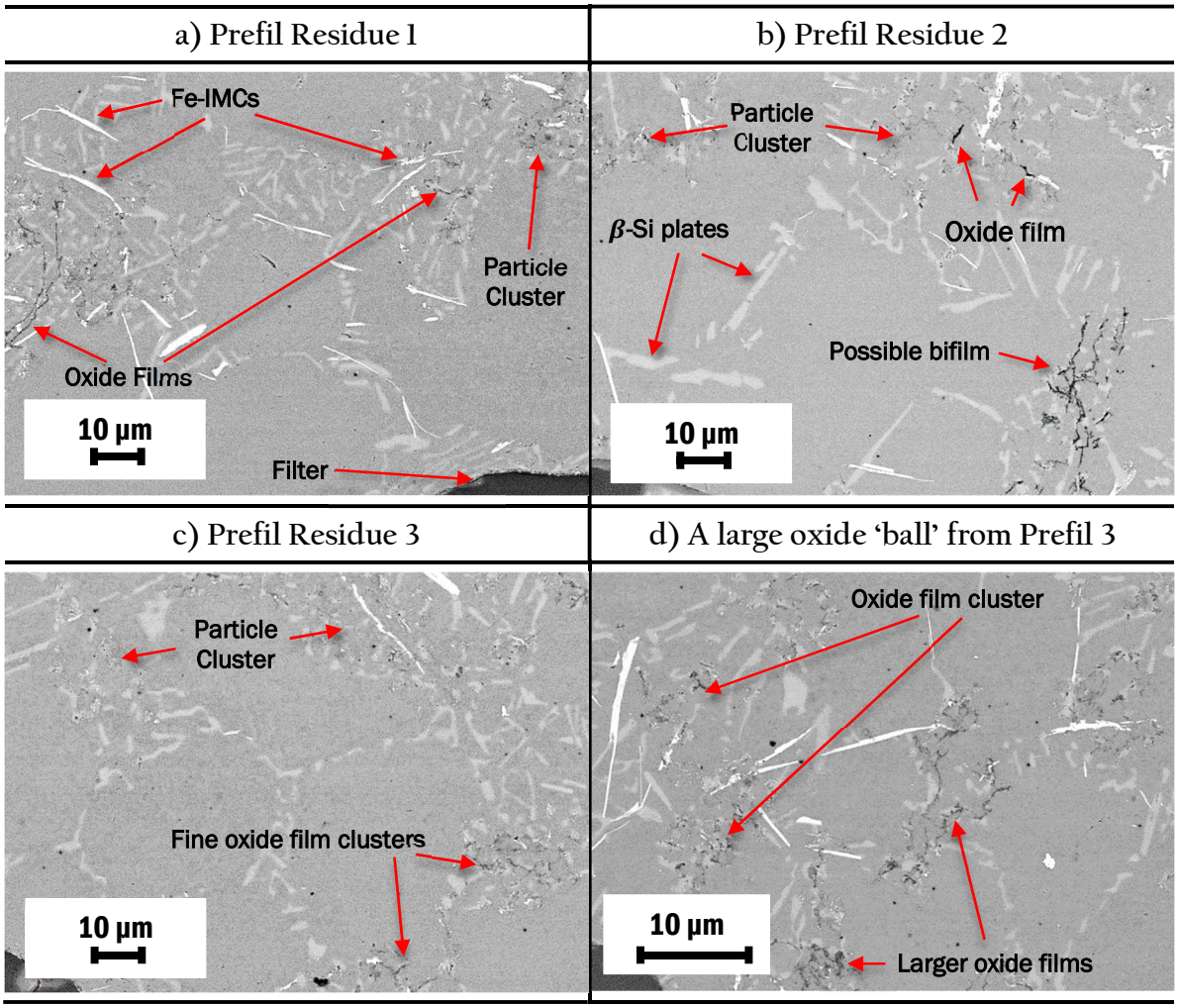

Figure 7.8 BSE micrographs from CM1 Prefil samples, showing a), b), and c) typical microstructures from Prefil samples 1, 2, and 3, respectively; and d) an example of a region in the inclusion band from Prefil sample 3 that contained larger oxides. Note that the *Particle Cluster* inclusions have quite low contrast in the BSE images.

CM2 Prefil Samples

The overall oxide film content was generally relatively low in all of these samples - similar to those found in CM1. There were a higher number of small thin oxides and some thick and large oxide films in localised areas of the inclusion band of Prefil 1 (**Figure 7.9** d)), which probably originate from the stirring in of the flux, but not broken down by the flux. The thin oxides were probably entrained during the stirring process, while the thicker oxides were probably freed from the scrap on the crucible wall from the stirring. The thick nature of the latter suggests that they are old oxides, probably the α-Al_2O_3 that was observed during PoDFA. The oxide film content in Prefil samples 2 & 3 was lower. Upgassing may have contributed to cleaning the melt.

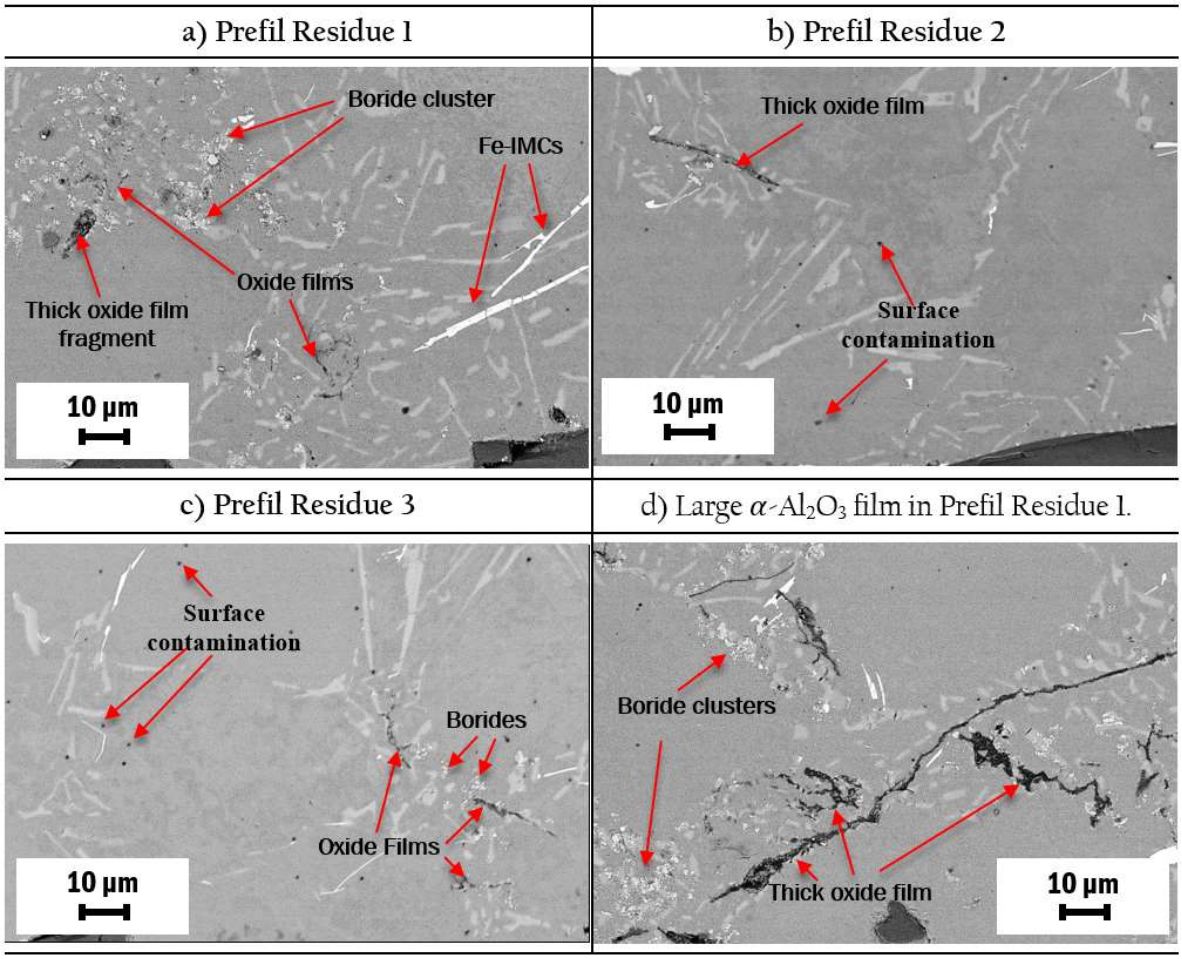

Figure 7.9 BSE micrographs from CM2 Prefil samples, showing a), b), and c) typical microstructures from Prefil samples 1, 2, and 3, respectively; and d) an example of a large old oxide film found in Prefil 1.

DM Prefil Samples

The overall oxide film content was very high oxide film content over the entire duration of the experiment, but highly variable, as can be seen from the micrographs. This was probably due to a combination of the propensity of oxide films to float from the metal over the course of the experiment, the continual top-stirring of the melt that was performed to attempt to reincorporate the floated films, and the partial skimming of the melt midway through the experiment. The oxide films in this melt could therefore either be exogenous, originating from the swarf chips, or endogenous, generated during stirring of the melt.

The oxide films were generally thin, though their size varied substantially. Notably, there were many small oxides in the metal. The EDX analysis in **Figure 7.10** e) confirms that these young oxides are in fact oxide films, with almost nominal Al_2O_3 stoichiometry. Again, some of the oxide films were observed to exhibit complex crack like morphologies. Oxide 'pockets' were also observed, as indicated on a) and b), which may be formed from the entrapment of air bubbles - or the hydrogenous substance on the swarf that caused the melt hydrogen to rise (**Figure 7.3**) – in the oxide during melt stirring.

It is difficult to determine the extent to which the oxide films are connected in 3D based solely on their 2D appearance; however the EDX oxygen map in **Figure 7.11** shows that they can be very large in size, despite their 2D appearance. From the oxygen map, it can be seen that parts of the oxide films are twisted and contorted as if folded.

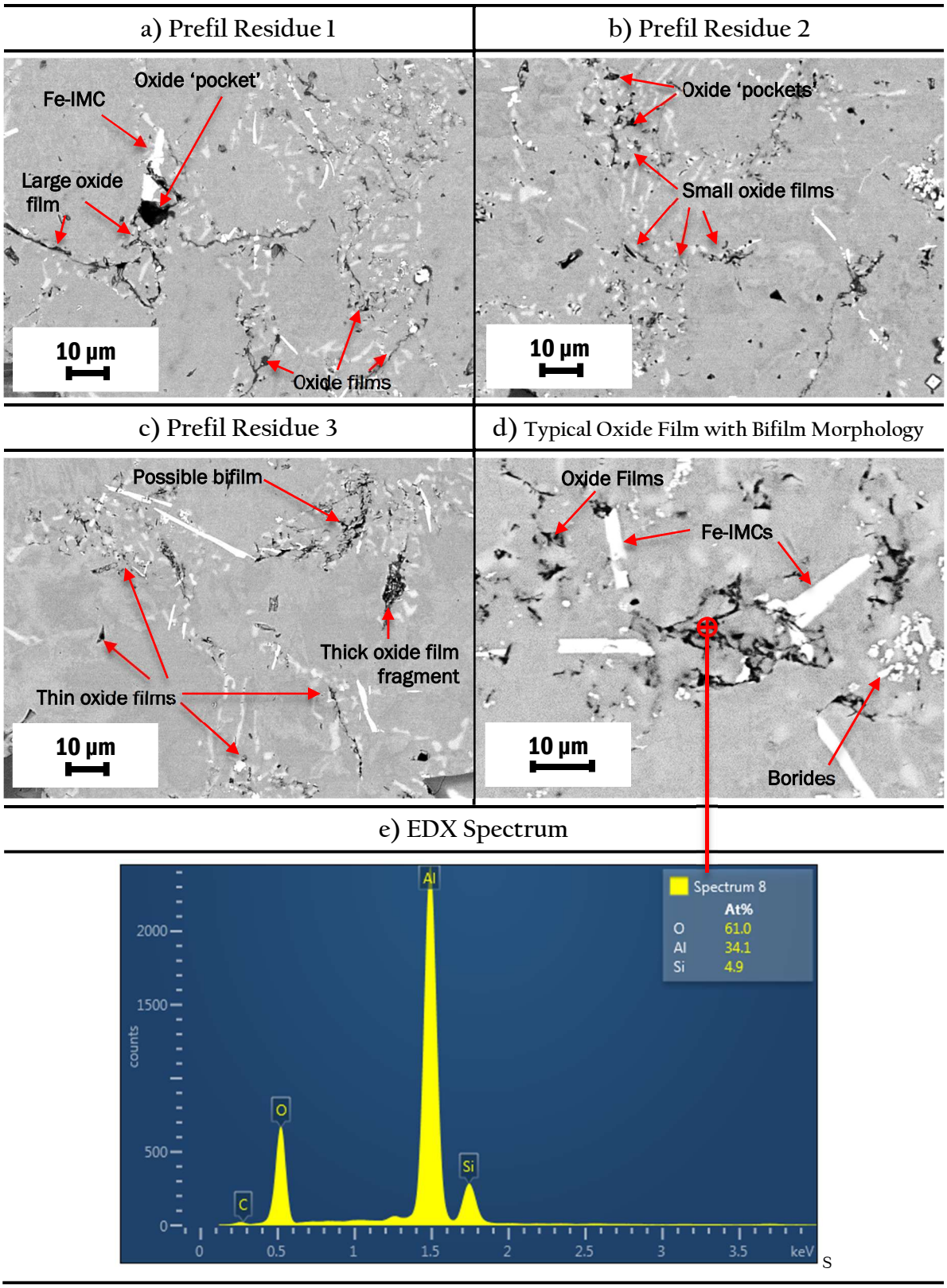

Figure 7.10 BSE micrographs from DM Prefil samples, showing a), b), and c) typical microstructures from Prefil samples 1, 2, and 3, respectively; d) a close up of an oxide film with a complex, bifilm morphology from Prefil Sample 2 and e) and EDX spectrum of the oxide film in d).

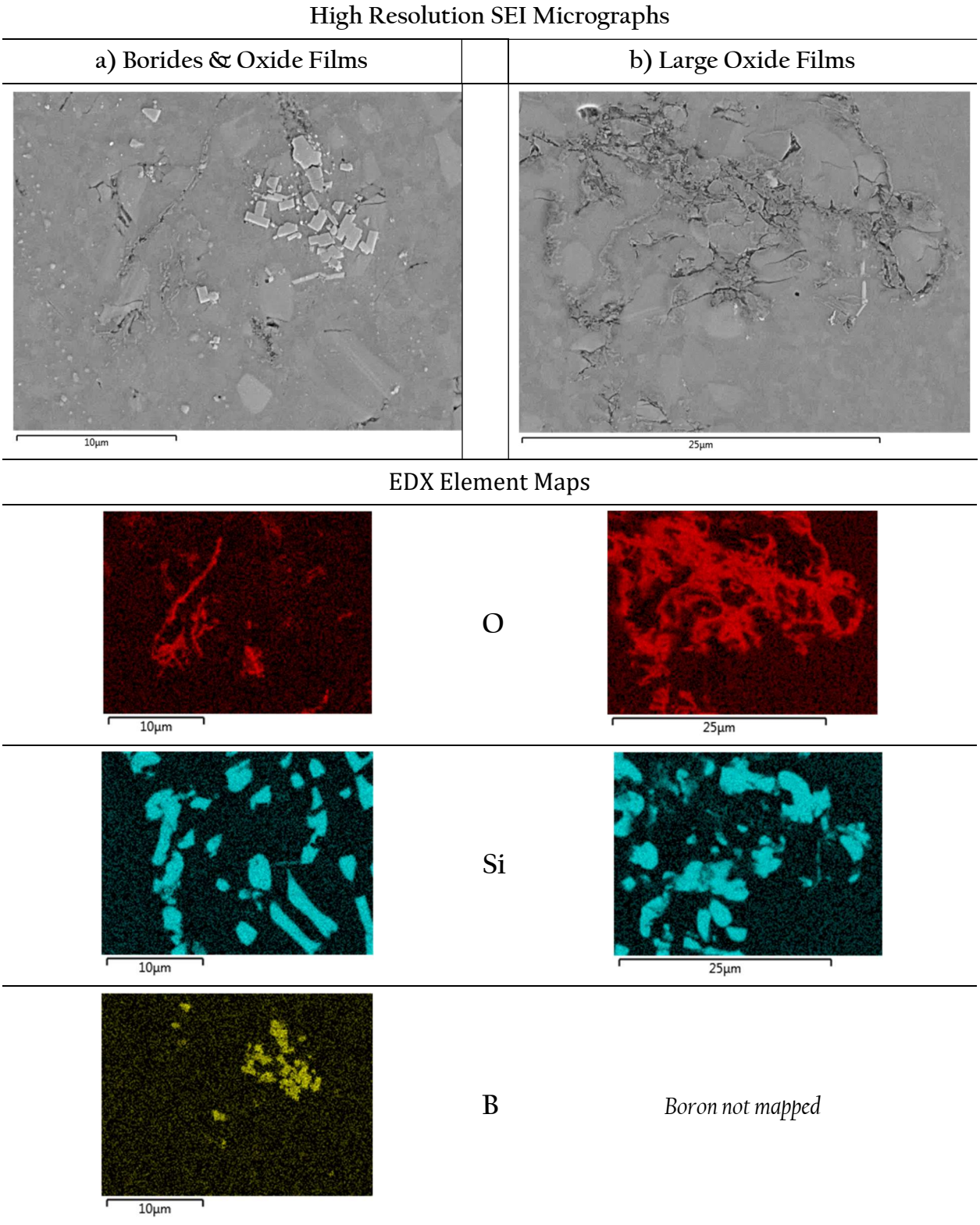

Figure 7.11 High resolution secondary electron micrographs and EDX maps taken from DM Prefil 2 using a Zeiss Merlin SEM, which shows a) oxide films and boride particles, and b) a large oxide film.

RD Prefil Samples

Figure 7.12 shows that the rotary degassed material is riddled with a numerous oxide films. Most of these films are thin in nature, indicating that they are young oxide films, incorporated from the surface during the mechanical stirring. A few apparently thicker, but small oxide fragments were observed, which may be α-Al_2O_3 (an old oxide) that was freed from the crucible walls and sheared up during the stirring process.

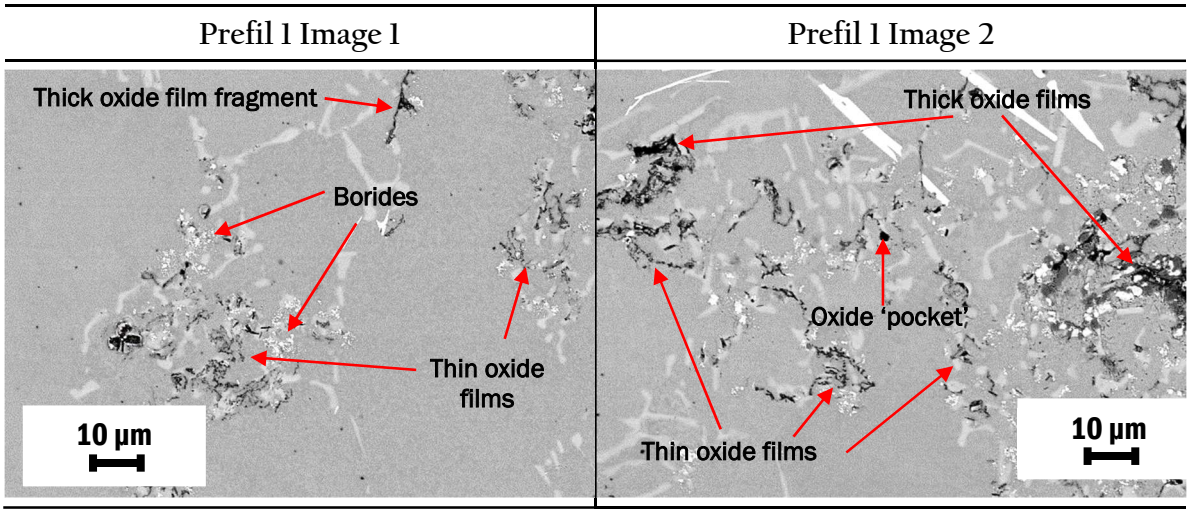

Figure 7.12 Typical BSE micrographs from the RD Prefil samples.

7.4 Sample Classification

7.4.1 Melt Cleanliness

To aid further analysis each melt has been explicitly classified in **Table 7.5** as either *clean* or *dirty* based on the level of oxides that were observed in the metals during the SEM examination in the preceding section.

Additional Data: Experiment DMX

Here it is necessary to introduce another set of samples from a less successful experiment that was performed, *DMX*, as some of the results from this work can be used to assist in the interpretation of the meta-analyses of the experimental results presented in Section 7.8. The methodology, and results of DMX are outlined in Appendix III.1. The oxide film content in the melt changed over the course of the experiment, though here only the data from the dirty melt condition will be shown.

Table 7.5 Melt cleanliness classification used in the meta-analysis.

	Experiment ID	
Clean Metal	CM1	CM2
Dirty Metal	DM	RD
Dirty Metal (Additional Data)	DMX	

7.4.2 Approximation of RPT Hydrogen Content

Because the AlScan's melt hydrogen measurements were taken intermittently at 15 minute intervals, measurements did not always coincide with the casting of RPT samples. It was therefore necessary to approximate the melt hydrogen content at the time of taking each RPT sample as shown in **Figure 7.13**. This was done by interpolating between the AlScan's melt hydrogen content measurements.

When the melt hydrogen content was following a diffusion controlled trend (such as during off-gassing, as shown in **Figure 7.13**), the hydrogen content was approximated by fitting an exponential function between 3 or more data points of the hydrogen versus time data using Origin (9.1) software:

$$H = H_0 + A \exp\left(-\frac{t - t_0}{k_1}\right) \tag{7.1}$$

Where H_0, A, and k are constants and t is the time at which the sample was taken. As **Figure 7.13** shows, the curve fits the measured data quite closely, and is well within the projected measurement uncertainty.

When the measured hydrogen content was moving in a less predictable manner or when only 2 data points were present, and there was only about a 15 minutes time difference between them, a linear fit was used to approximate the hydrogen content of the sample:

$$H = H_0 + Bt \tag{7.2}$$

Where B is a constant.

Figure 7.13 shows that there is very little difference between the exponential and linear fits, both of which are well within the projected measurement uncertainty range. Hence it is

very likely that both methods provide a reasonable approximation of the melt hydrogen content at the time of sampling.

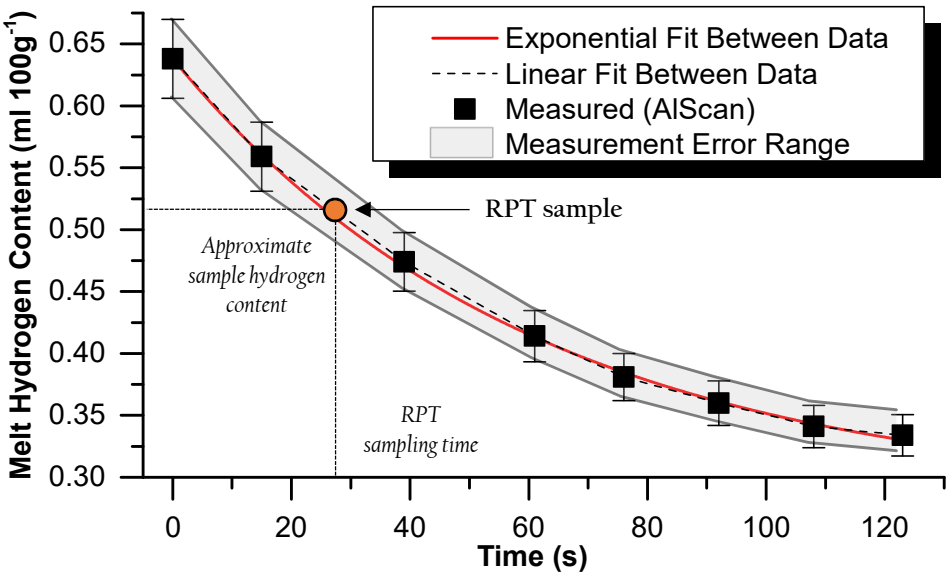

Figure 7.13 An example of fitting of curves to the measured hydrogen data from CM2 for to approximate the hydrogen content of the RPT samples between measurement intervals.

7.5 Volume Fraction of Porosity

The effects of changes in hydrogen content and melt cleanliness on the volume fraction of porosity in the RPT samples, calculated using Archimedes' principle, is shown in **Figure 7.14**. As expected, the data in both plots shows that that the volume fraction of porosity in the samples increases with increasing the melt hydrogen content.

It is interesting to note that as the hydrogen content in the metal decreases, the amount of porosity that is formed in clean metals compared to dirty metals also decreases. A good example of this can be seen by comparing the encircled data labelled I. and II. At high hydrogen contents there does not seem to be a significant difference between the f_p of clean and the dirty metals, and instead is appears to be a function of the hydrogen content. The point hydrogen level at which parity between the clean and dirty metals appears to be very approximately ~0.3 ml 100g^{-1}, though this is very difficult to ascertain because of scatter and gaps in the data.

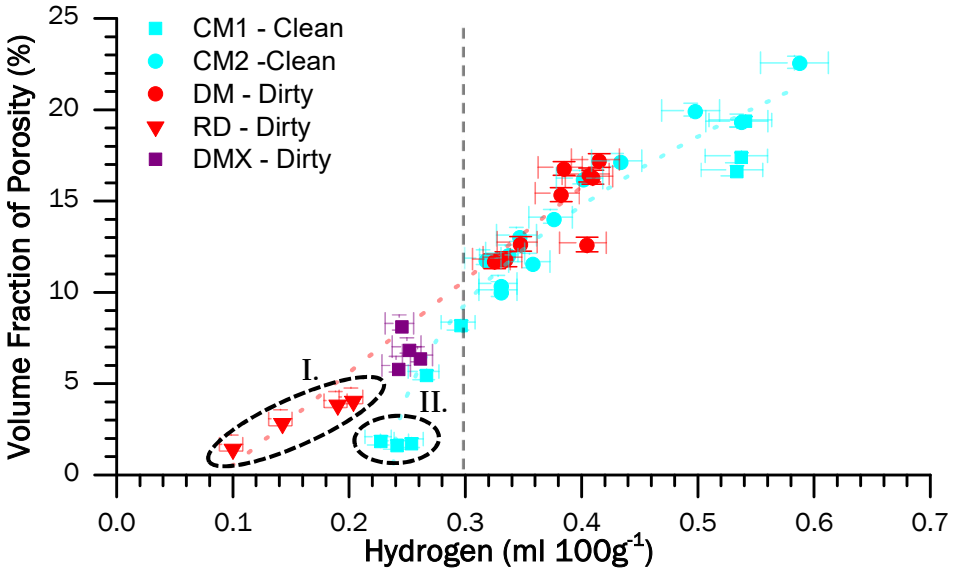

Figure 7.14 Volume fraction of porosity (f_p) versus hydrogen content in the RPT samples. The encircled data points indicate clean samples that have developed a lower fraction of porosity than dirty samples with similar hydrogen contents.

7.6 Changes in Pore Structure with Hydrogen Content

In order to understand the individual effects that hydrogen and the oxide film content have on porosity formation, they must each be individually examined. Here, the effect of the melt's hydrogen content is investigated by assessing the structure of porosity that was formed in selected RPT samples cast from the clean melts (CM1 and CM2). **Figure 7.15** shows macro-CT slices of the porosity in these samples. Qualitatively, it can be seen that as the hydrogen level decreases pores become increasingly irregular and interdendritic in shape. Pore morphology is governed by the fraction of solid present while the pores are forming.

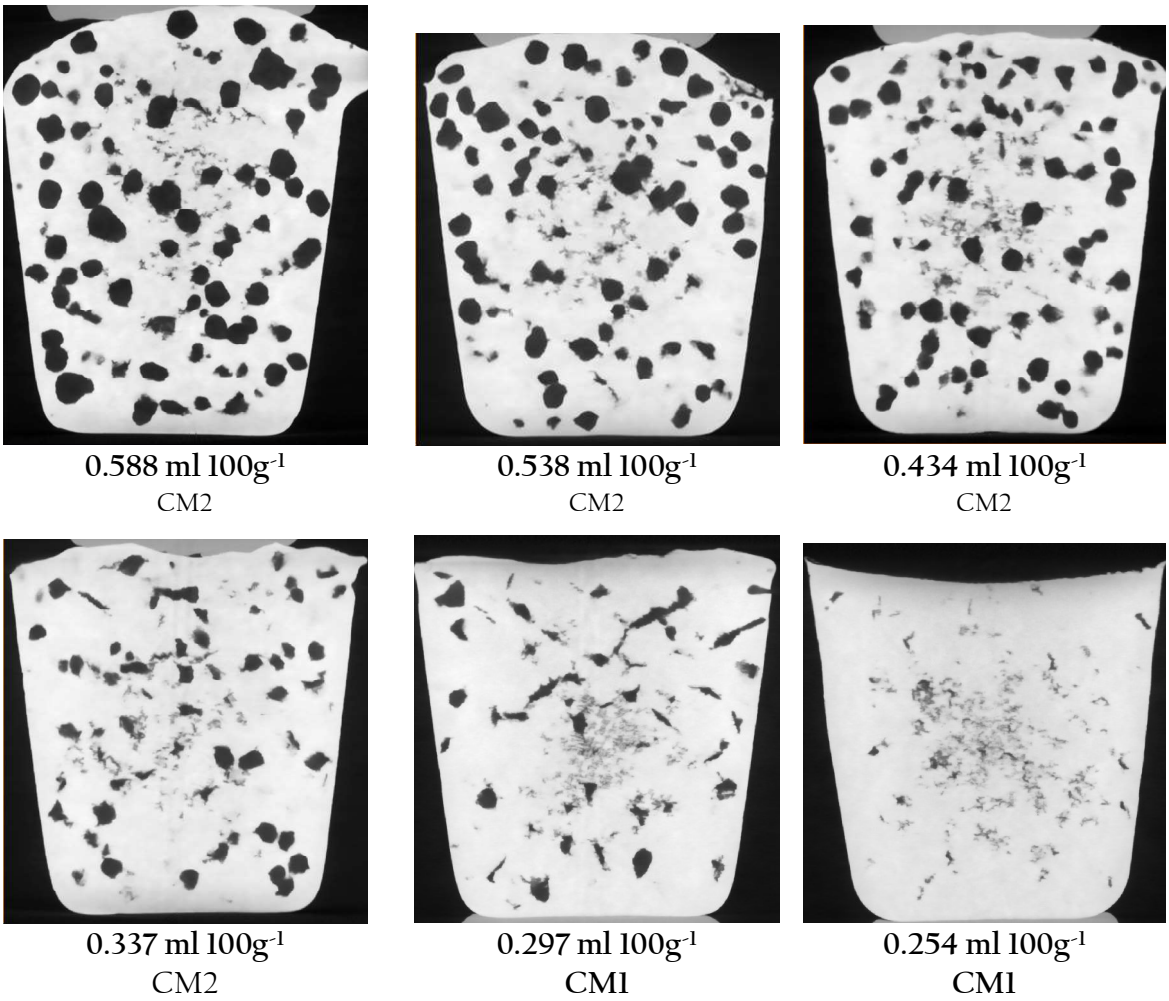

Figure 7.15 Macro-CT slices of RPT samples cast from clean melts (CM1 &CM2)

7.6.1 Pore Size–Shape Distribution

To gain an overall appreciation of the change in the structure of porosity with melt hydrogen content, the size-shape distributions of the pores serves as a good 'first port of call'.

The macro-CT size-shape distribution is given in **Figure 7.16**. The key observation that can be made is that the mean size and sphericity of pores increases with hydrogen content. This is because as the hydrogen level in the samples decreases, shrinkage increasingly influences the shape of the pores. This makes them making them an increasingly convoluted combination of shrinkage and gas pores. When the hydrogen level decreases to the point of 0.250 ml $100g^{-1}$, the gas pores become a nearly inseparable combination of gas and shrinkage pores, as can be seem from the low shape factors of large pores. The classes of shrinkage pores and gas pores will briefly be discussed in the following section.

The metallographic size-shape distribution may be found in Appendix III.3.1.

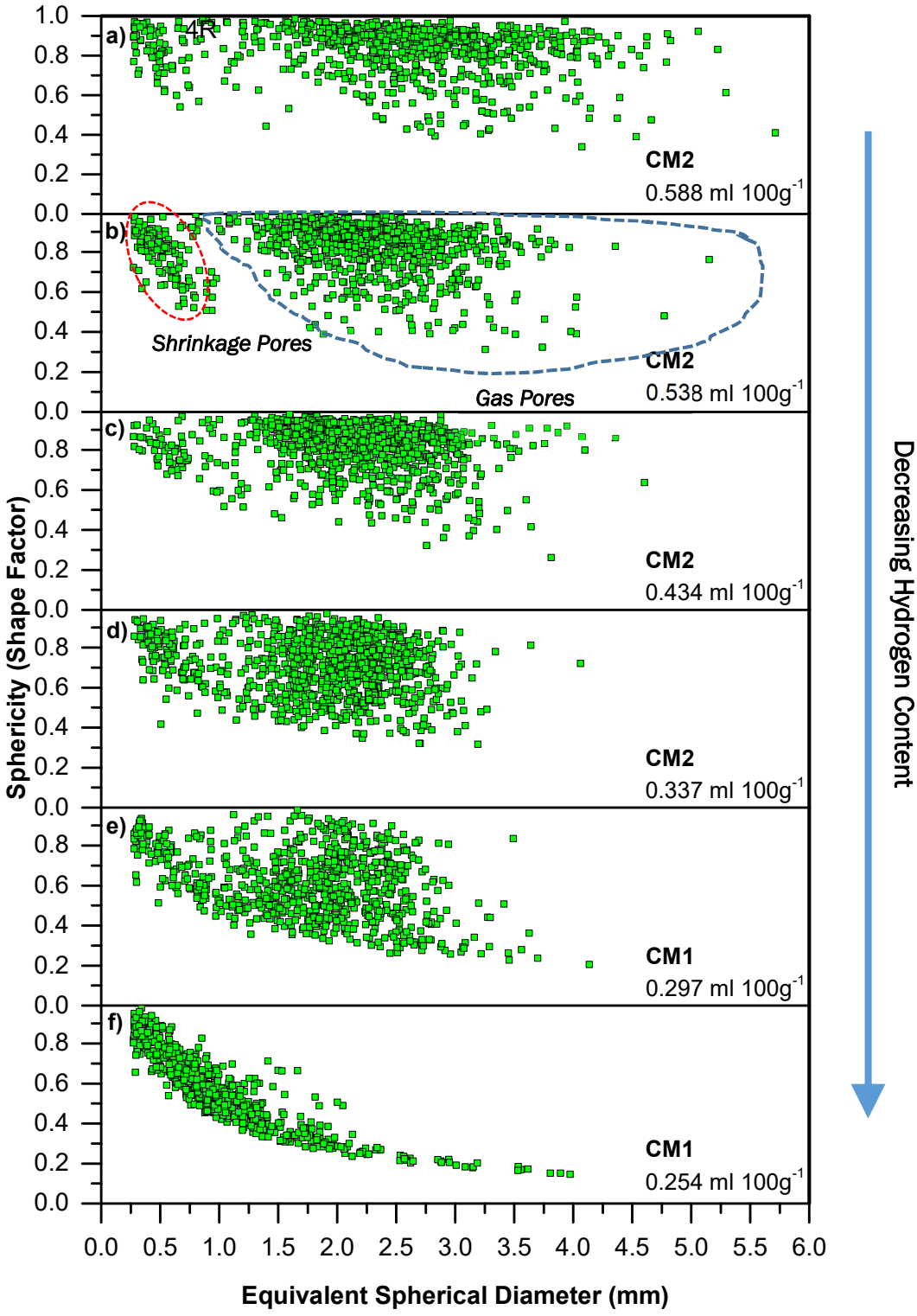

Figure 7.16 3D Pore size-shape distributions in RPT samples (>125 voxels in size) from experiment CM1 & CM2 measured by macro-CT analysis.

7.6.2 Classes of Pores

The clustering of the data in the macro-CT size-shape distributions in **Figure 7.16** broadly represents the two classes of pores in the samples: *shrinkage pores* and *gas pores*, though these classes are not mutually exclusive.

Shrinkage Pores

Shrinkage pores nominally occupy the low shape-factor region of the size-shape graph, however, given resolution limits of the technique, as the pores decrease in size, they are measured to be increasingly spherical in shape (as has been described in Section 6.4), which is a key artefact of XCT analysis.

Gas Pores

Gas Pores nominally occupy the high shape-factor region of the of the size-shape graph, and tend to grow to a much larger size than the shrinkage pores in the RPT samples.

Combined Gas & Shrinkage Pores

Shrinkage pores tend to be associated with gas pores, especially those at the centre of the sample, which lowers their overall sphericity compared to 'pure' gas pores. A comparison of an almost 'pure' gas pore and a combined gas and shrinkage pore is given in **Figure 7.17**.

It should be noted that the separate objects algorithm that is used to separate interconnected pores (detailed in Section 6.2.4) only separates gas pores, and is incapable of splitting shrinkage pores from gas pores using the parameters here.

Finally, as the hydrogen level decreases, classifying the pores based on their size and shape becomes increasingly difficult. This is because gas pores become increasingly interdendritic in shape (**Figure 7.16** f)). This makes it difficult to separate individual gas pores.

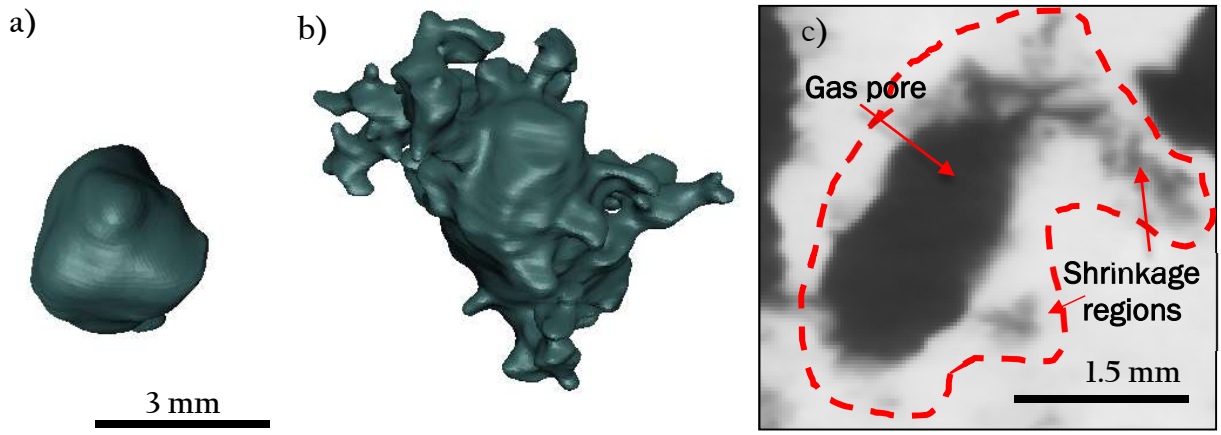

Figure 7.17 Comparison of a a) gas pore, and b) a gas pore combined with a shrinkage pore. A close-up 2D slice of the macro-CT data is given in c), which shows the pore of b) in the encircled red region.

7.6.3 Size Distribution

To further quantify changes in the size of porosity in response to changing hydrogen content, the size distribution of the pores shall be examined.

The size distribution of pores measured by metallography and macro-CT are given in **Figure 7.18** and **Figure 7.19**, respectively. Some of the key observations that can be made are; firstly, the macro-CT distribution shows a very strong bimodal distribution, with Peak *A* consisting of shrinkage pores, and Peak *B* consisting mainly of gas pores (though the gas pores may be combined with shrinkage). This can be inferred from the size-shape distributions of the pores that have been given in **Figure 7.16** from the clustering of the data. Because of the application of reduced pressure in the RPT, the gas pores are able to expand, and become very distinct in size from the pure shrinkage pores. This bimodal distribution is non-existent in the metallographic data, because the shrinkage pores greatly outnumber the number of gas pores. However, application of Saltikov analysis draws out the gas pore peak better.

The second key observation that can be made from both the metallographic (especially the 3D Saltikov analysis) and macro-CT analyses is that the gas pores, Peak *B*, increase their mean size with increasing melt hydrogen content. In other words, gas pores get bigger as the hydrogen content increases. The difference in the number of counts in the Saltikov analysis of the metallographic data and the macro-CT data simply arises due to differences in the binning of the data.

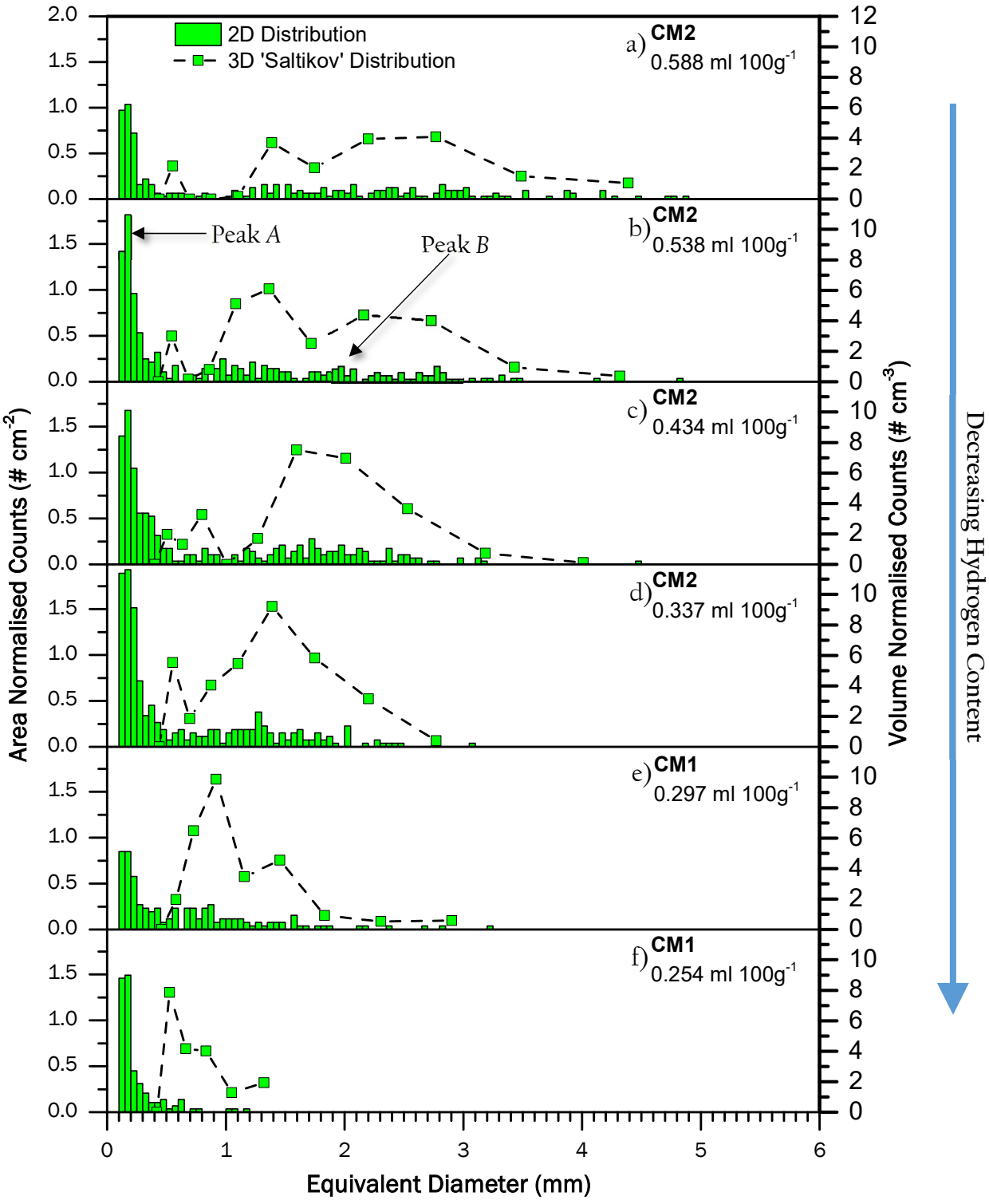

Figure 7.18 2D & 3D ' Saltikov' size distributions of pores in RPT samples cast from CM1 & CM2 with variable hydrogen contents, measured using metallography.

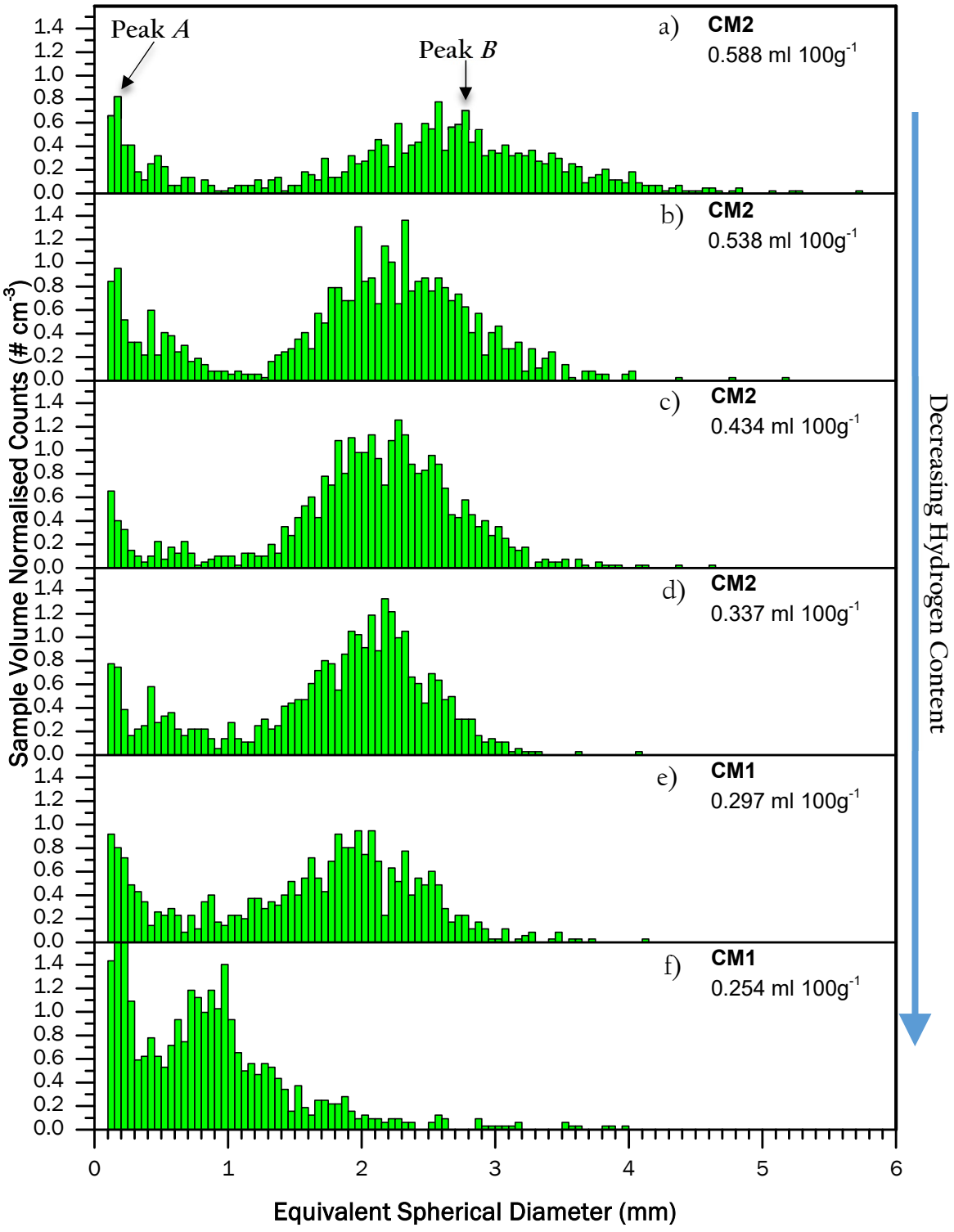

Figure 7.19 3D size distribution of pores in RPT samples cast from CM1 & CM2 with variable hydrogen contents, measured using macro-CT.

The division point between the peaks can be made very roughly at d_{eq}≈0.5 mm in the metallographic data, and in the macro-CT data it can be qualitatively seen to increase with the hydrogen content. Given that the peaks represent classes of pores, Otsu's method [147] was employed to estimate the division point between these classes – this means that the division point represents the point at which the variance in the pore size of each class is minimised. From the macro-CT data, **Figure 7.20** a) and b), respectively show that the division point and the mean size of pores increases with hydrogen content. This effect can be appreciated based on the illustration in **Figure 7.20** c), which shows that the (lognormal) distribution of gas pores in *Peak B* is shifted right as the melt hydrogen content increases.

For simplicity during further analysis, a set value of d_{eq}=0.8mm is used as the division point between the peaks in the macro-CT analysis. This value was selected as it gave a reasonably conservative division of pores, with most larger than this value are considered gas pores

Meanwhile, Peak *A* only grows and widens when the melt hydrogen content is low and when gas pores become highly convoluted with shrinkage pores.

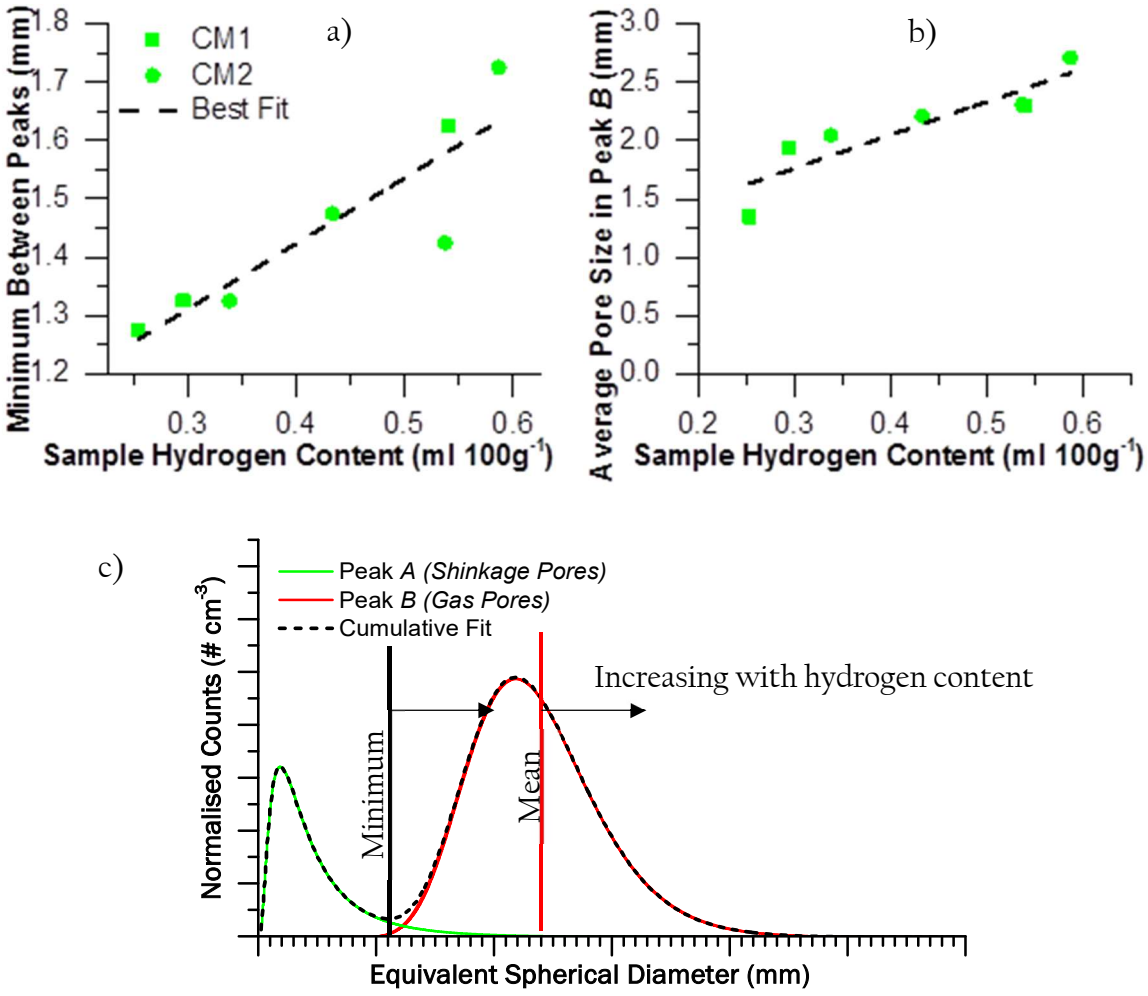

Figure 7.20 a) the change in the position of the minima between the two peaks with increasing hydrogen content, b) the change in the mean size of gas pores (Peak *B*) with increasing hydrogen content, and c) a diagram demonstrating that these latter two effects arise because of the shifting of the mean of Peak *B* with increasing hydrogen content.

7.7 Comparative Analysis of Porosity in Clean & Dirty Metal

This section presents a comparative analysis of the porosity in 3 pairs of RPT samples in order to elucidate the effect of oxides on porosity. **Table 7.6** summarises the melt hydrogen content and the approximate inclusion content in each of the RPT samples. Each pair of samples contain a similar hydrogen content (though the difference is larger in Pair 1 than the others), but differ in their oxide content. Differences in oxide film content are difficult to appreciate based on the PoDFA data, and the *Cleanliness Rating* from the SEM analysis should instead be used.

Table 7.6 Summary of hydrogen and the approximate melt cleanliness of each RPT sample used in the comparative analysis.

Pair	Exp.	RPT Sample No.	Approx. Hydrogen Content (ml 100g^{-1})	*Approximate Melt Cleanliness**				
				Prefil no.	MC	PoDFA Oxide Films (#/kg)	PoDFA TIC (mm^2/kg)	Cleanliness Rating (from Table 7.4)
1	CM1	1	0.250	1	-	11	0.021	1
	RD	4	0.204	1	14.7	27	0.935	10
2	CM2	12	0.337	3	1.4	11	0.007	2
	DM	9	0.325	3	9	47	0.012	6
3	CM2	7	0.433	-†	1.4 – 3.4	11 – 20	0.007 – 0.016	2
	DM	5	0.404	2	3.8	25	0.047	10

*Melt cleanliness is approximate, based on analysis of the nearest Prefil sample.

† No Prefil sample was taken close to the time of this RPT sample. The values presented are an average of the results from Prefil samples 2 & 3, which were taken either side of this sample.

From **Figure 7.21** it can immediately be seen that the dirty metals develop more pores that are smaller in size than those developed in the clean metals at a given hydrogen content. Also of note is that in Pair 1, when the hydrogen content is low, the pores in the clean metal are concentrated mainly at the centre of the sample, whereas pores in the dirty metal are more numerous and uniformly distributed throughout the sample.

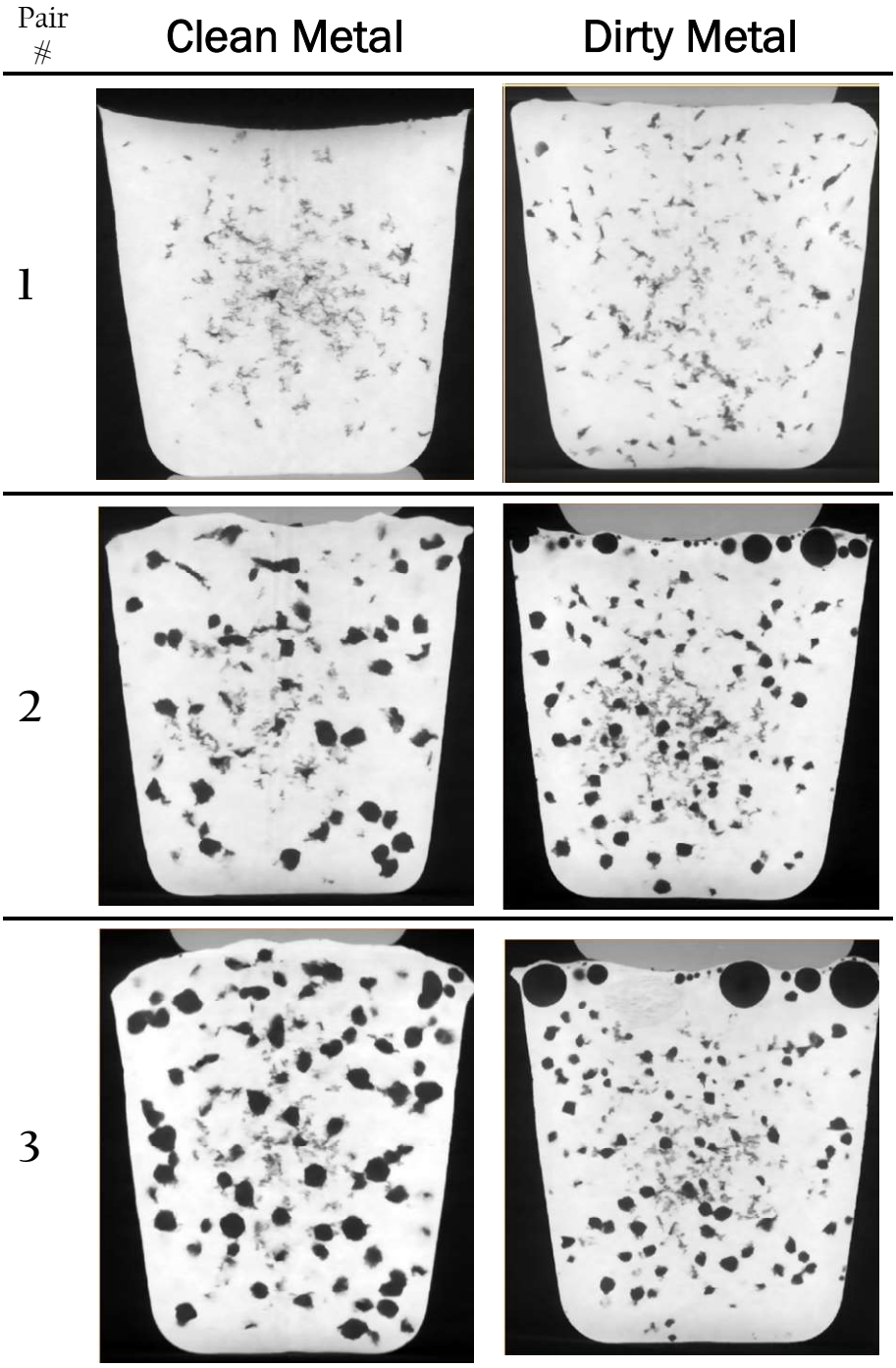

Figure 7.21 Macro-CT images of the RPT samples used in the comparative analysis between clean and dirty RPT samples.

7.7.1 Pore Size-Shape Distribution

The comparison of the size-shape distribution of pores in RPT samples cast from clean and dirty metals using macro-CT is given in **Figure 7.22**. It qualitatively shows that in general, the RPTs cast from the dirty metal develop more pores, and that the bimodal clustering of pores is less prominent. The gas pores in are also smaller in size and less spherical. There also appears to be more shrinkage pores in the samples, though due to the low spatial resolution of the macro-CT (which makes shape analysis of small objects difficult), it is difficult to determine whether the number of shrinkage pores in the samples has increased, or if there are a higher number of small gas pores.

The effect of the ballooning of dross that was picked up on the surface of the RPT samples from DM can be appreciated from the dirty metal samples of Pairs 2 & 3.

Pair 1 represent an interesting case, because the melt hydrogen level was relatively low. It again shows that the distinction between gas pores and shrinkage pores is difficult to make, with the pores tending to be a combination of both. As is indicated on the figure, it can be seen that there is a more pronounced 'belly' in the dirty metal. This arises because of increased expansion of pores by hydrogen, which causes them to take on a more spherical shape – this effect can be appreciated from **Figure 7.21**. Increased expansion of the gas pores would explain the higher f_p developed in the dirty metals (labelled I.) than the clean metals (labelled II.) at low hydrogen contents shown in **Figure 7.14**.

The size-shape distributions measured by metallography measurements can be found in Appendix III.3.1.

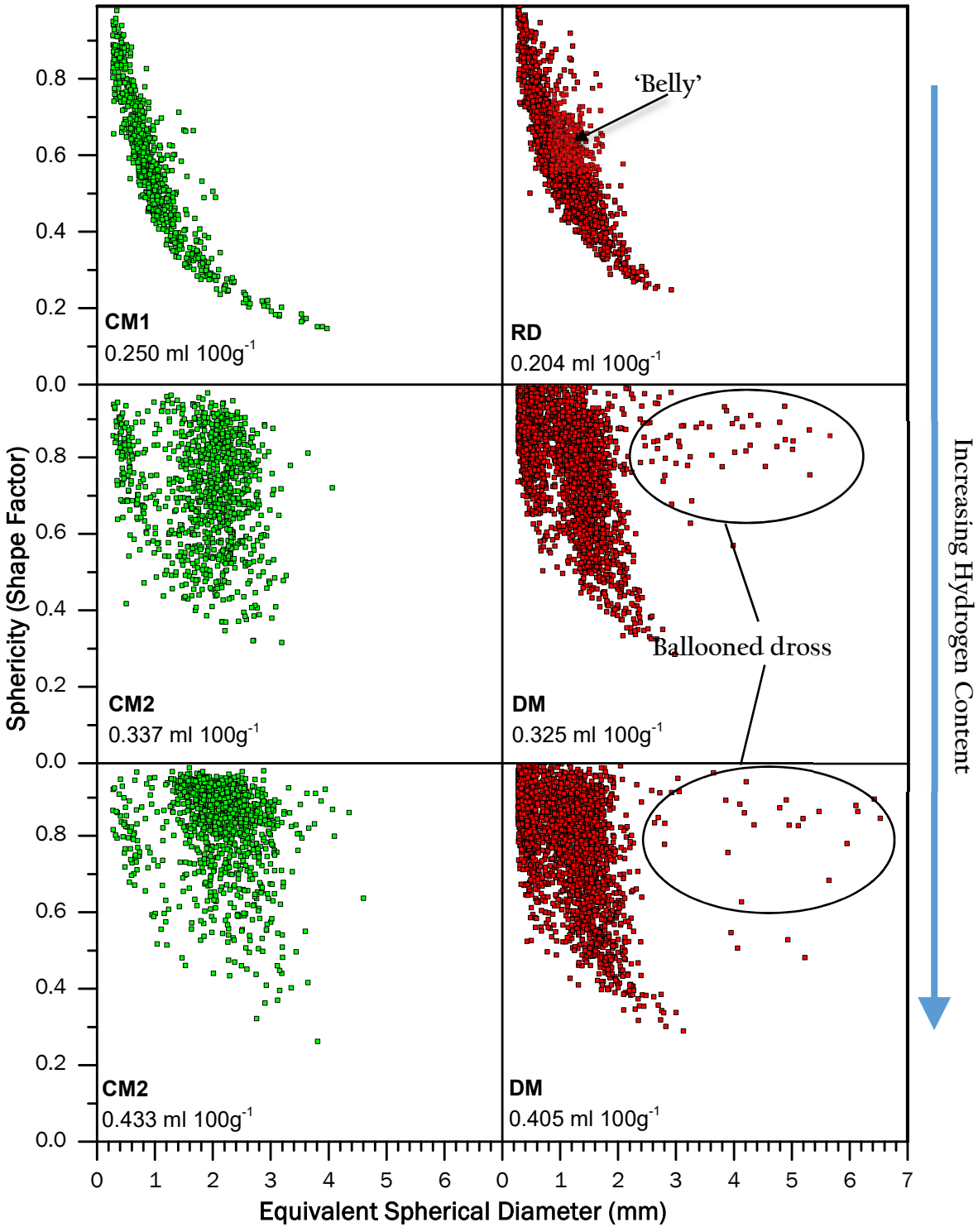

Figure 7.22 3D size-shape distribution of pores (>125 voxels in size) measured by macro-CT analysis.

7.7.2 Pore Size Distribution

A comparison of the size distribution of the pores in each pair of RPT samples measured by metallography and macro-CT are given in **Figure 7.23** and **Figure 7.24**, respectively.

The key observations that can be drawn are; firstly, the macro-CT data show in Pairs 2 and 3, that significantly more shrinkage pores (Peak *A*) and gas pores (Peak *B*) are developed in the dirty metals compared to the clean metals. This indicates that the dirty metals are more prone to shrinkage porosity, but also nucleate more bubbles during solidification. In Pair 1, there are again more pores (which is apparent in the metallographic analysis), though it is difficult to distinguish between gas pores and shrinkage pores as there is not a strong bimodal distribution, due to the heavy convolution between gas and shrinkage pores.

The second key observation, which can be made from both the metallographic (namely the 3D Saltikov distribution) and macro-CT distributions, is that in Pairs 2 and 3, the mean of the gas pores (Peak *B*), is centred at a lower d_{eq} compared to the clean metal, and on average have less of a spread than the clean metals (although there are some outliers). The latter point would suggest that the spread in the sizes of gas pores is determined by the oxide film content. In Pair 1 it is difficult to determine changes in the position of Peak *B*, but it does not appear to have moved.

Finally, a number of large outlier pores from Peak *B* can be seen in the metallographic and macro-CT distributions of the dirty metals in pairs 2 & 3. These pores have formed due to the ballooning of dross during the RPT, which have expanded to a very large size.

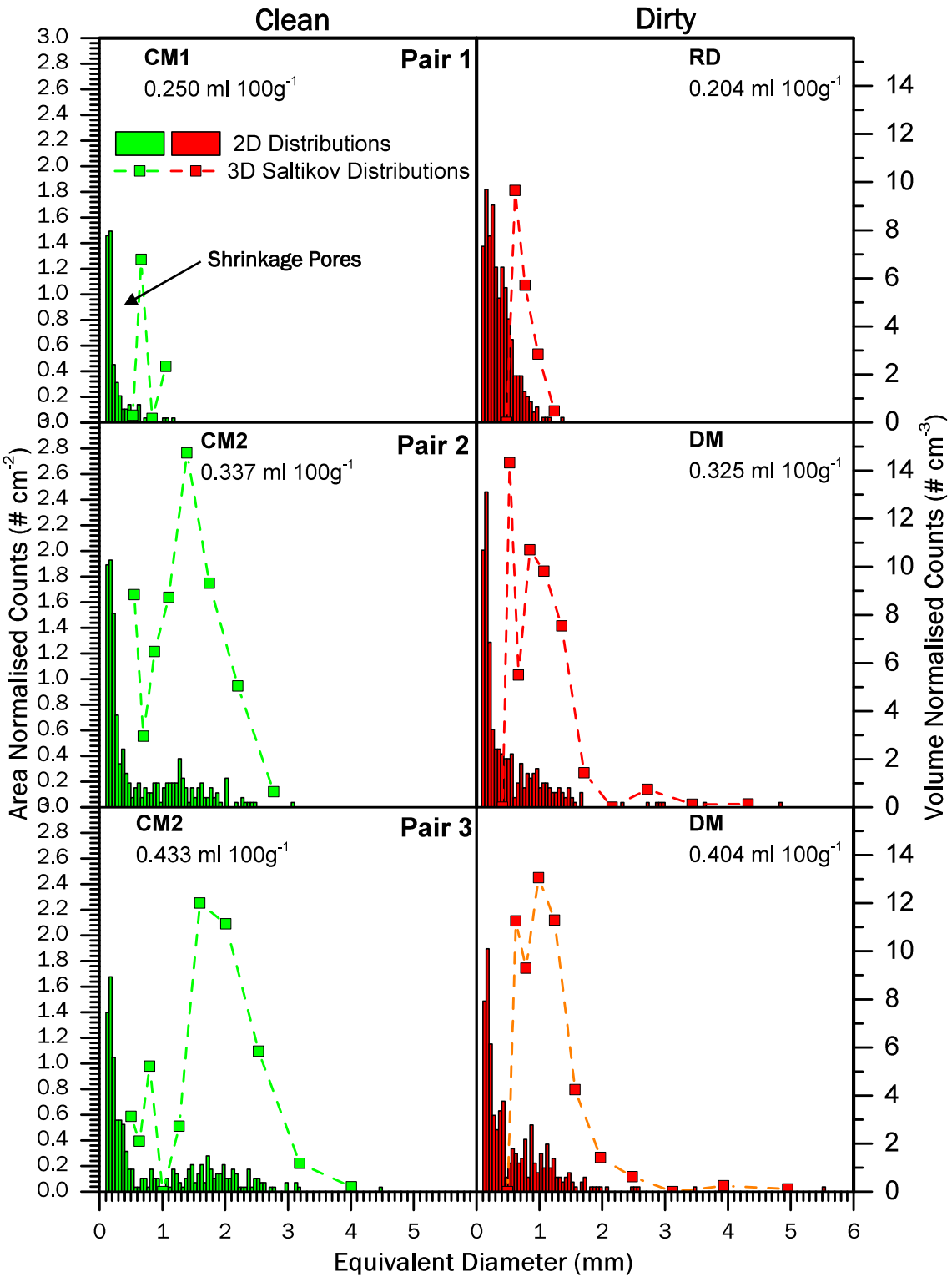

Figure 7.23 Comparison of the metallographic pores size distributions in clean and dirty metals, showing both the 2D and 3D size distributions.

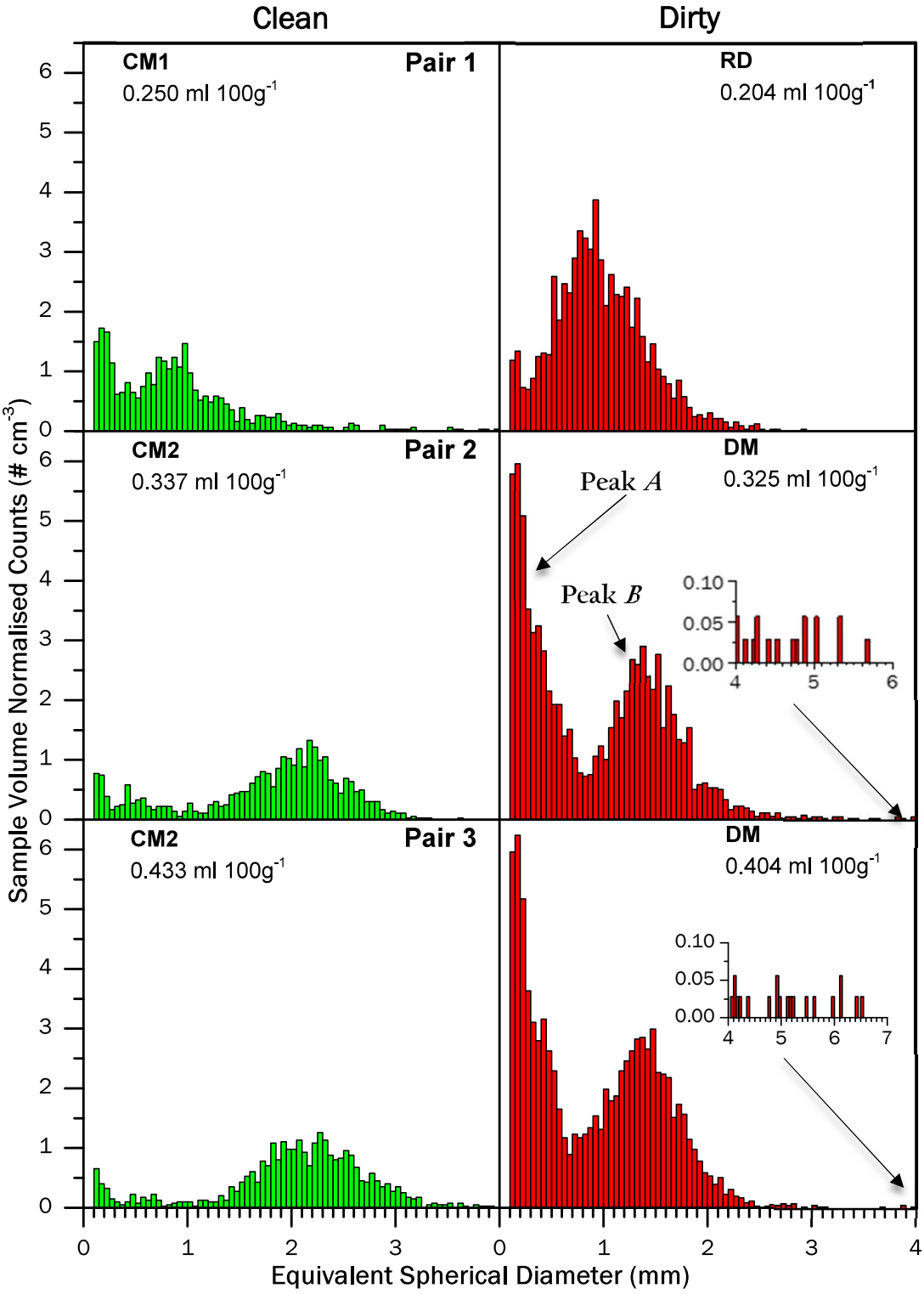

Figure 7.24 The size distribution of pores (>8 voxels) measured by macro-CT in 3 pairs of RPT samples cast from clean and dirty melts.

7.7.3 Influence of the Dross-Layer on Macro-CT Analyses

The dirty RPT samples cast during DM (pairs 2 and 3) had a layer of dross on their surface which, as can be seen in **Figure 7.25** a) & b) (and also in **Figure 7.21** above), had a tendency to 'balloon' under the vacuum of the RPT. It may therefore be considered to have formed on top of the samples rather than inside them.

In order to determine if the presence of the dross layer had a significant influence on the results of the macro-CT analysis, the volume of the RPT samples was cropped to omit the dross layer (as shown in **Figure 7.25** c), and selected analyses were performed again.

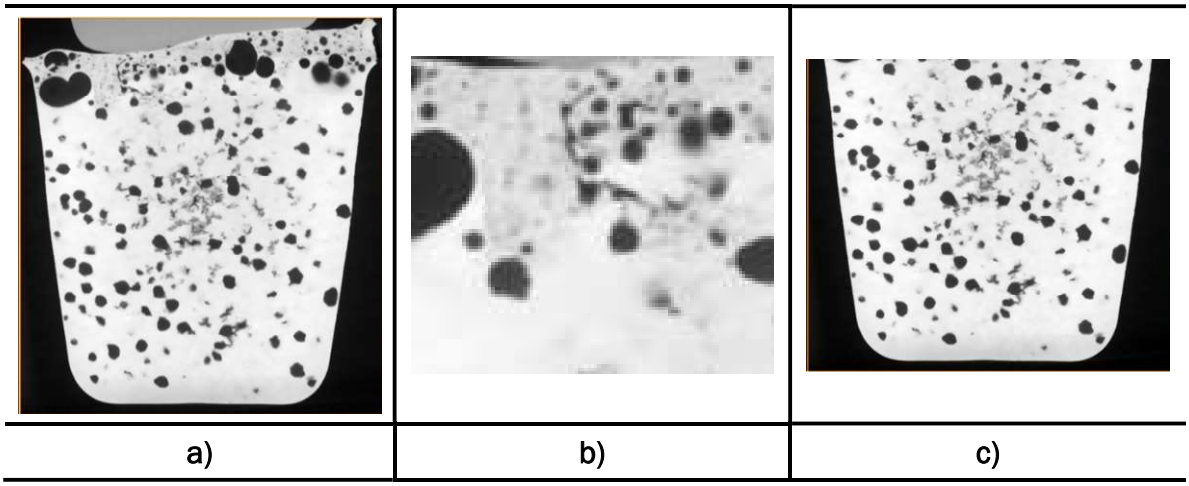

Figure 7.25 a) An example of the pickup and ballooning of dross picked up on the surface of an RPT sample from experiment DM, b) a close-up of pores inside this layer, and c) an example of how the samples were cropped in some of these analyses.

Volume Fraction of Porosity

The effect of cropping on the volume fraction of porosity (f_p) calculated from the macro-CT data is given in **Figure 7.26**. It shows that cropping reduces the f_p in the dirty metals, though it remains almost constant in the clean metal. This indicates that the dross layer in the dirty metal contains a larger proportion of porosity than the bulk sample.

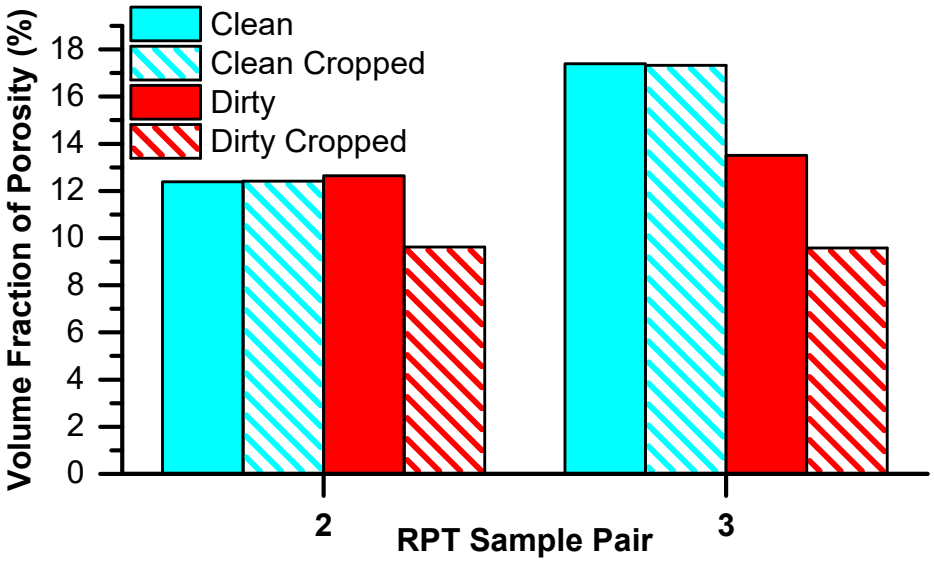

Figure 7.26 Comparison of the volume fraction calculated using macro-CT, when the dross-layer is cropped from the surface of RPT samples.

Pore Number Density

The effect of cropping on the volumetric PND can be seen from the plot given in **Figure 7.27**, which shows that cropping the macro-CT data has little effect on the overall PND inside the clean metals, but has different mixed effects in each of the samples cast from the dirty metal. It is not known why this occurs, but may be due to differences in dross pickup on their tops. Nevertheless, an important observation to make is that the dirty melts still

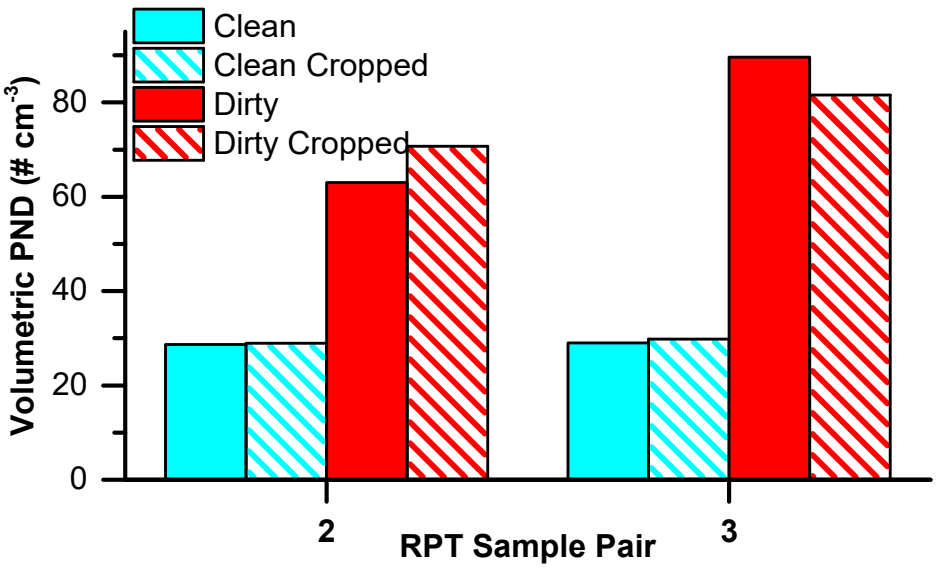

Figure 7.27 Comparison of the PND inside whole and cropped RPT samples from Pairs 2 and 3.

have a significantly higher PND than the clean metals, regardless of the presence of the dross layer.

Size Distribution

The size distribution of nucleation events in the cropped RPT sample volumes is shown in **Figure 7.28**. By comparison with **Figure 7.24**, it can be seen that the density number of small pores (d_{eq}<0.8mm) in the sample is decreased, and secondly, the very large pores are eliminated. There does not seems to be any appreciable change in the size distribution of the clean metal. These observations are to be expected based on the numerous small pores and the large pores that can be seen to inhabit the dross layer in **Figure 7.21**.

Overall, this has very little effect on the order of magnitude differences in the number of pores between the clean and dirty metals – though it should still be considered to influence the results a little.

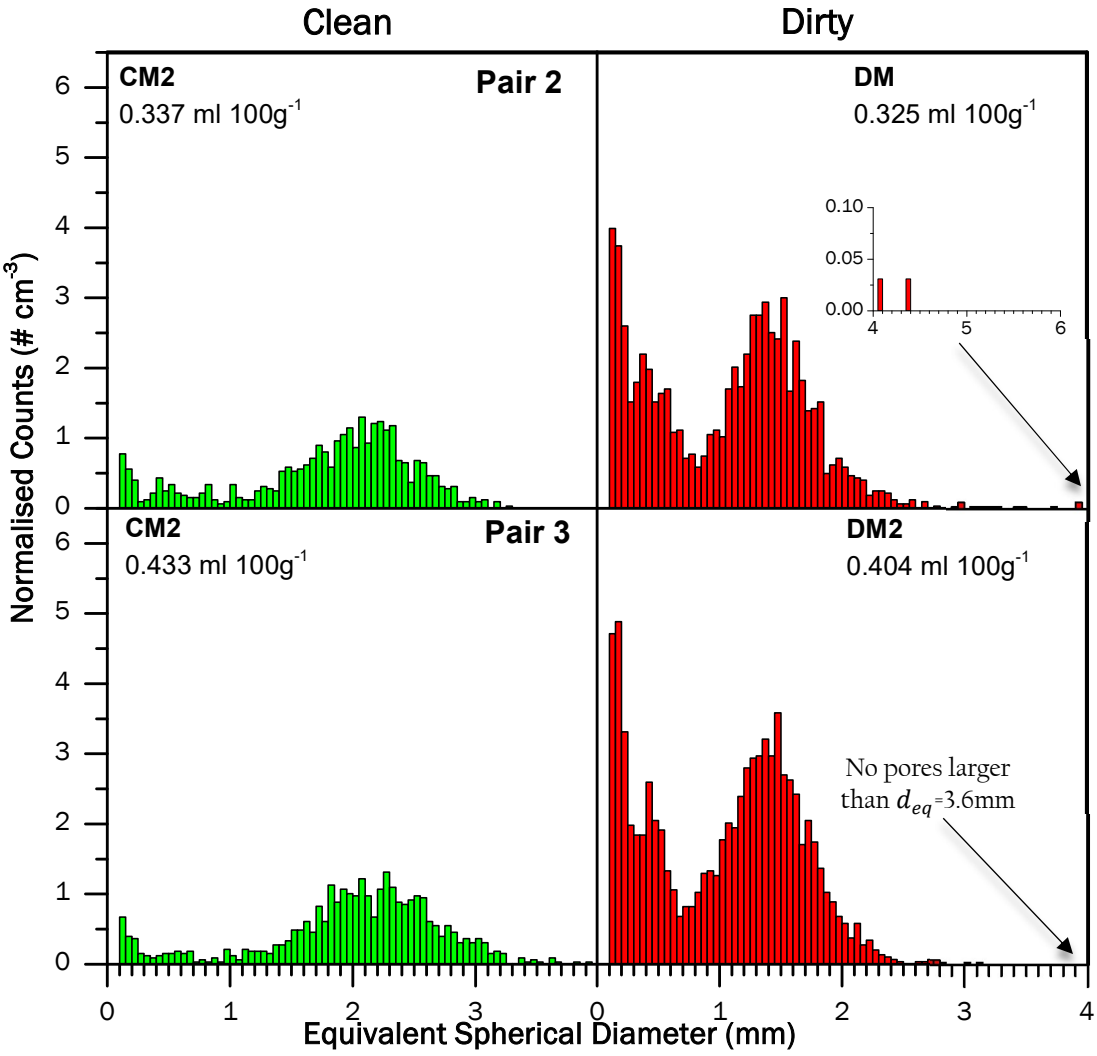

Figure 7.28 3D size distribution of pores in the cropped RPT samples from pairs 2 and 3.

7.8 Meta-Analysis of the Porosity in the RPT Samples

The use of pore size and size-shape distributions, although insightful, proves unwieldy when investigating more than just a few samples. Hence, for the comparison of a larger group of samples it is beneficial to characterise them using a single quantified value, which greatly simplifies the comparison process.

In this section, the results of the four experiments presented in the body of this work, along with selected results from experiment DMX (as described in Section 7.4) will be presented collectively as a 'meta-analysis' to further investigate the effects of hydrogen and oxide films on porosity formation. Based on the results from the preceding two sections, it can be concluded that the following metrics may prove useful in discriminating between clean and dirty melts:

1. the pore number density (PND),
2. the mean circular or spherical diameter of pores (d_{eq}), and
3. The mean shape factor of pores.

7.8.1 Pore Number Density

The metallographic analysis that includes all pores (**Figure 7.29** a)) only weakly shows a difference in the areal PND between clean and dirty metals, though the large scatter in the data make it difficult to determine this with certainty. This arises mainly due to the inundation of the measurement by sections of shrinkage pores (as indicated on **Figure 7.23**). The metallographic analysis of gas pores (d_{eq}>0.5mm) **Figure 7.29** b) shows reduced scatter compared to a) and that the dirty metals in DM develop has higher areal PND than the clean metal, but still shows some scatter with some of the DM samples having a similar PND to

the clean samples. However, because the number of pores with a d_{eq}>0.5mm in the samples are reduced with decreasing hydrogen content (as is shown in **Figure 7.19**), this method becomes increasingly unreliable for analysing porosity in samples with less than ~0.3 ml $100g^{-1}$ of hydrogen. This can be seen from the PND gradient in the graph. It therefore does not reveal differences in the PND of the RD sample (which are evident in **Figure 7.30**).

Applying Saltikov's area method (fitting of a lognormal distribution) to the measured gas pores (d_{eq}>0.5 mm), more clearly draws out differences in the PND between clean and dirty metal as shown in **Figure 7.29** c). Again, it is difficult to draw any conclusions from the data of about 0.3 ml $100g^{-1}$ because only larger pores are considered in the analysis.

The volumetric PND measured by macro-CT given in **Figure 7.30** a) shows a significant difference in the PND of the samples from the clean and dirty metals. Interestingly, it shows that the PND is essentially constant in the clean metals, and higher, albeit scattered, in the dirty metals. **Figure 7.30** b) shows that this is also the case for 'gas pores' (d_{eq}>0.8 mm). This indicates that oxide film content of the melt influences the number of pores that are formed. It should be emphasised that in b), the PND may be reduced, as pores d_{eq}<0.8 mm are cut from the analysis. From **Figure 7.24** it can be seen that some of the gas pores and combined gas and shrinkage pores are omitted by this simplification. Even so, the RD RPT samples have clearly higher PND of gas pores.

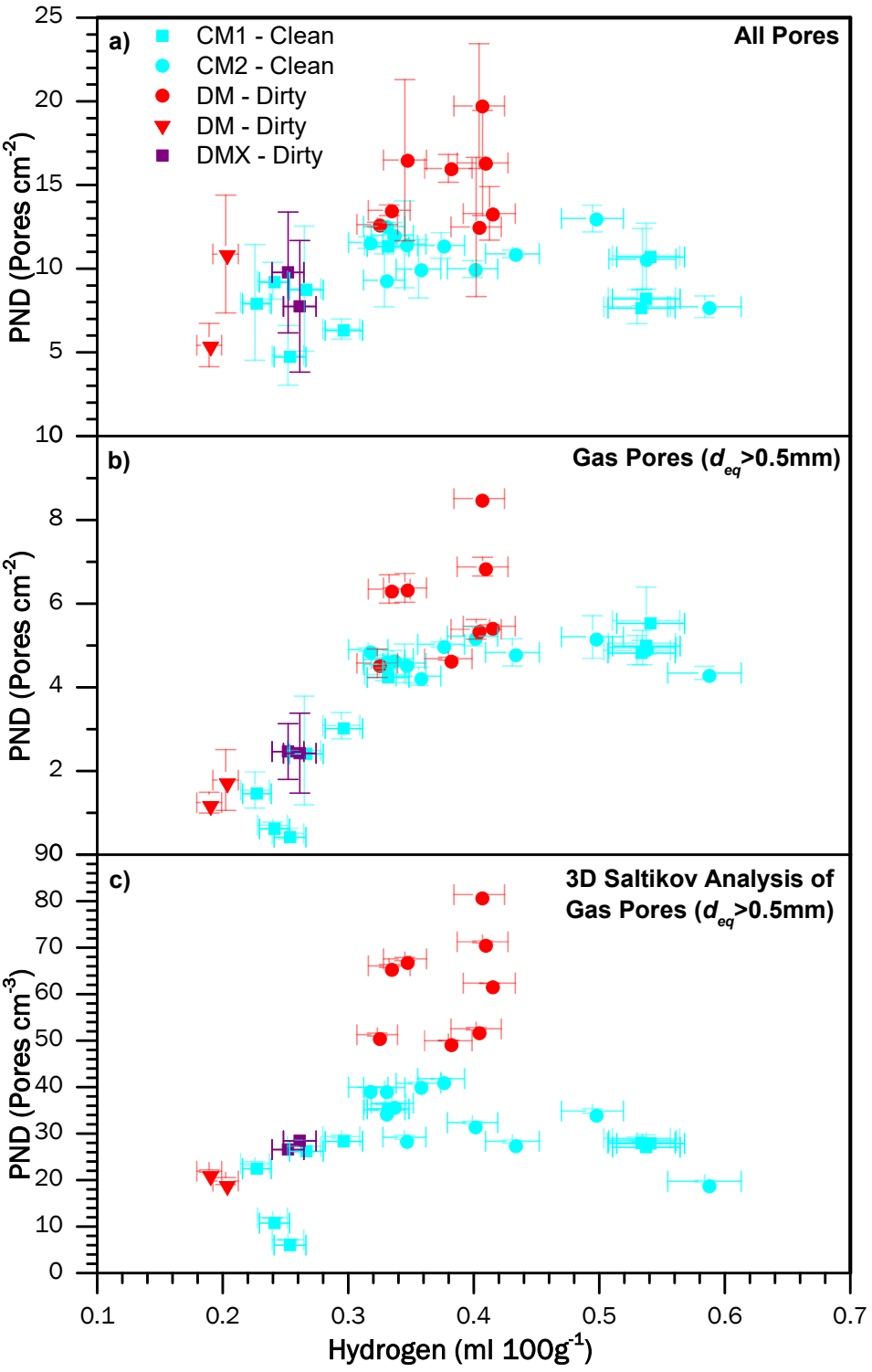

Figure 7.29 a) areal Pore Number Density (PND) all pores and b) areal PND of gas pores (d_{eq}>0.5mm) measured by metallographic analysis, and c) volumetric PND estimated from Saltikov's area method.

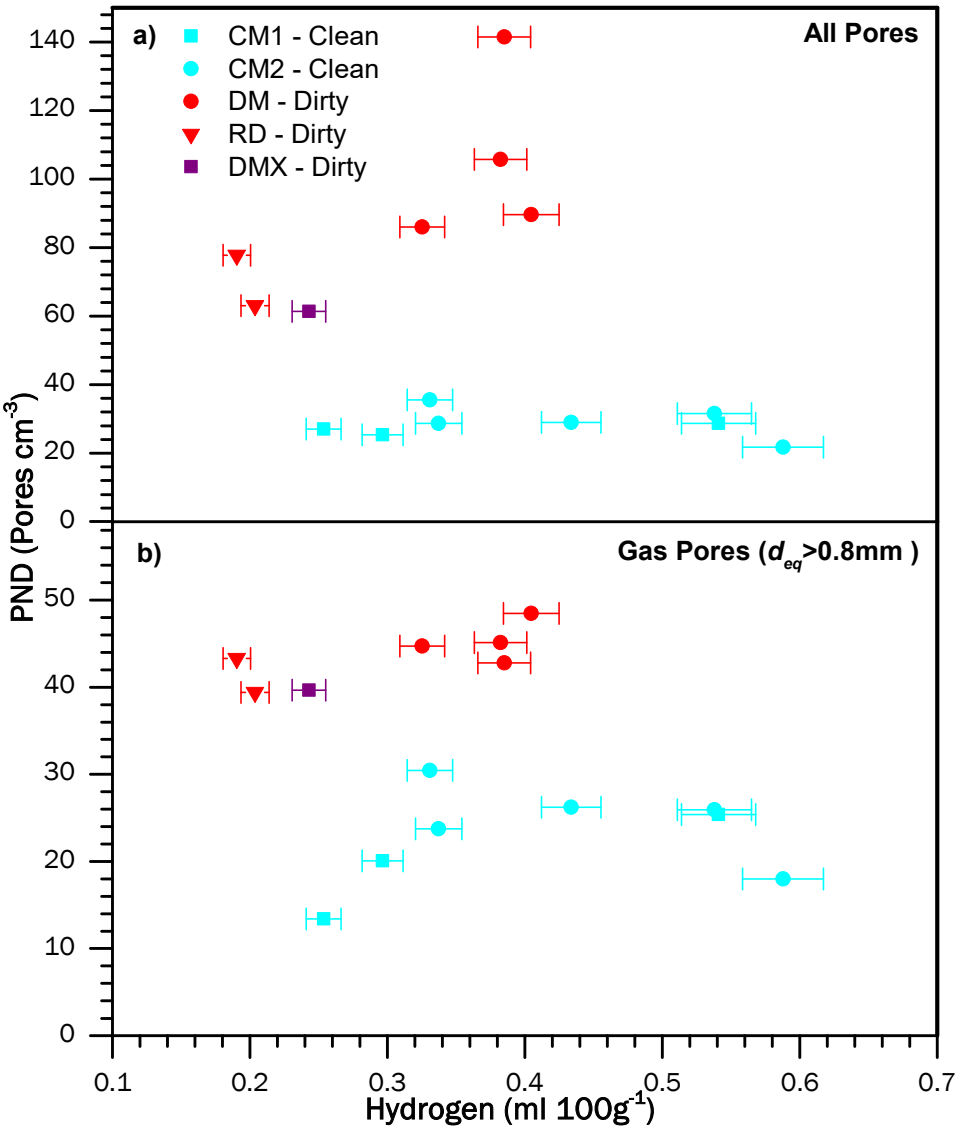

Figure 7.30 Volumetric PND of a) all pores, and b) gas pores (d_{eq}>0.8mm) measured by macro-CT analysis.

7.8.2 Average Pore Size

The mean equivalent circular diameters (d_{eq}) of the pores in the RPT samples measured by metallography is shown in **Figure 7.31**. Analysis of all pores (›44 pixels in size) in a) shows that the mean d_{eq} increases with hydrogen content, though it is difficult to confidently determine if there is any difference between clean and dirty metals. Analysis of only gas pores (d_{eq}›0.5 mm) shows that the mean d_{eq} of gas pores is smaller in the dirty metals, albeit not substantially. The result is the same for the volumetric estimate of the equivalent spherical diameter using Saltikov analysis, which is shown in c).

The macro-CT analysis of the mean equivalent spherical diameter (d_{eq}) of pores in selected RPT samples is shown in **Figure 7.32**. The analysis of all pores, shown in a), and the analysis of only gas pores (d_{eq}›0.8mm) both show that the mean d_{eq} is smaller for dirty metals than it is for clean metals. However, at low hydrogen contents, this may not be the case. However, it is important to recall that pores become increasingly interdendritic in structure as the hydrogen content decreases, which makes it increasingly difficult to distinguish and measure individual pores.

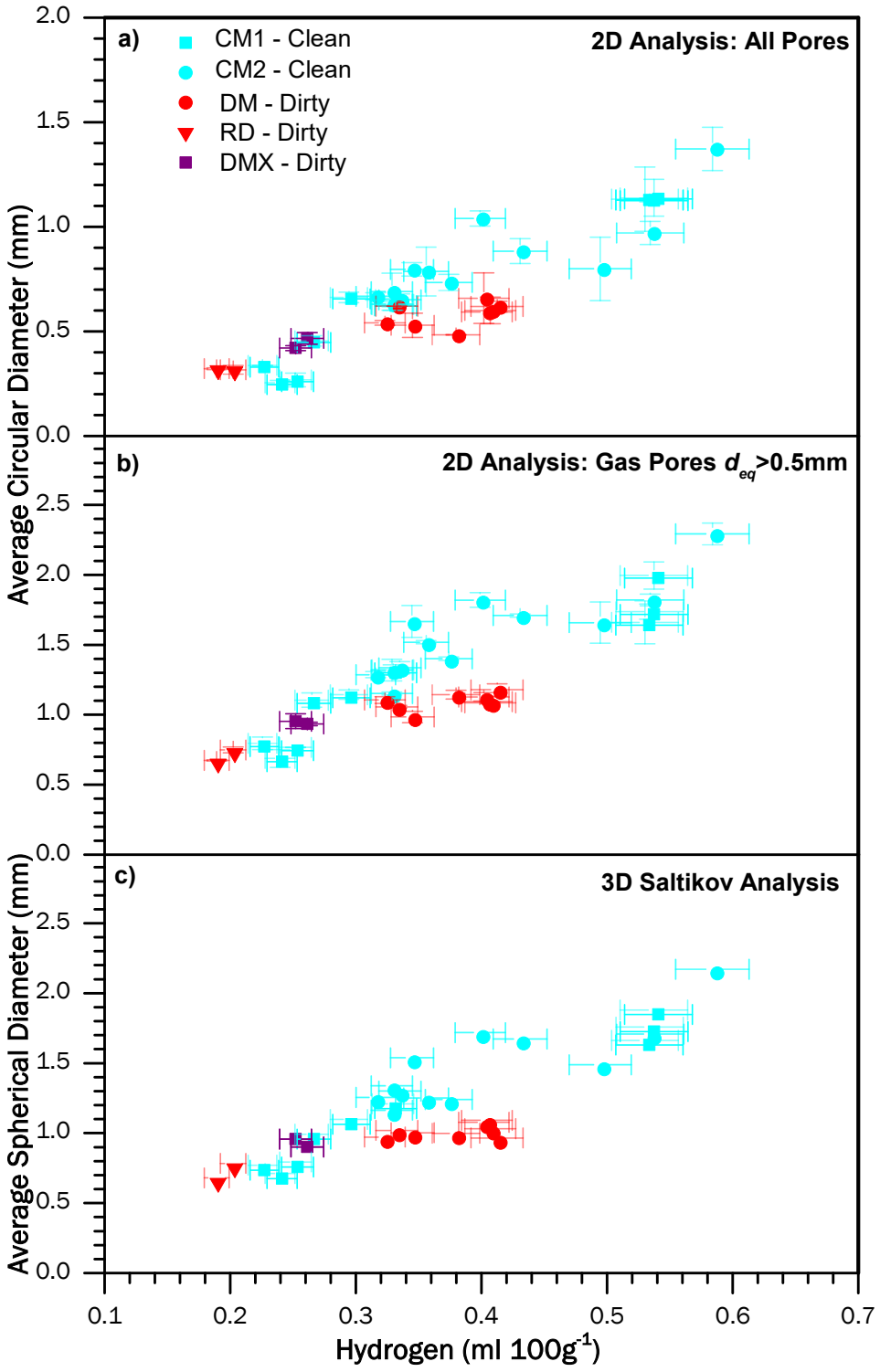

Figure 7.31 The mean equivalent circular diameter of a) all pores, and b) gas pores measured by metallographic analysis; and c) the 3D, equivalent spherical diameter, estimated by Saltikov's area method.

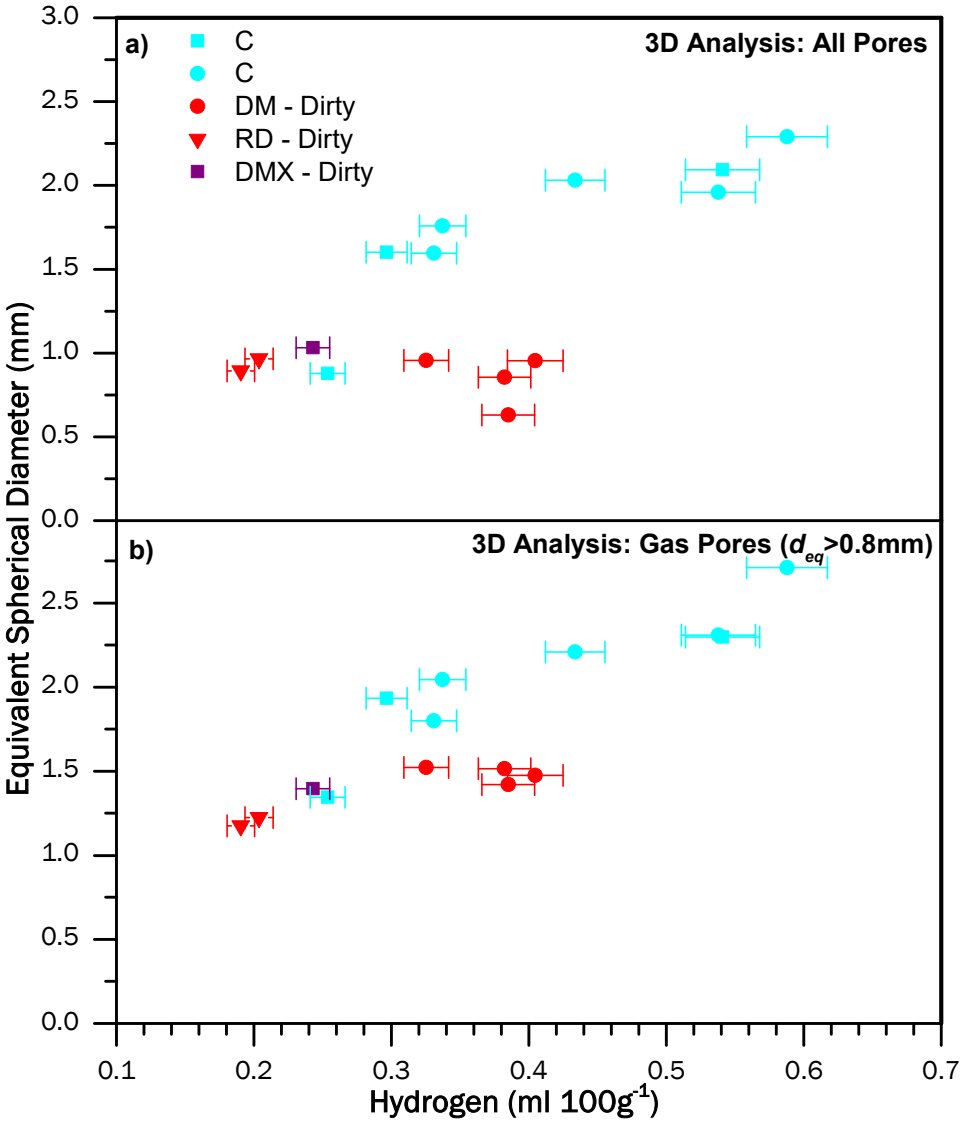

Figure 7.32 Mean equivalent spherical diameter (d_{eq}) of a) all pores, and b) gas pores in RPT samples measured by macro-CT analysis.

7.8.3 Pore Morphology

The mean circularity (the 2D Shape Factor, *SF*) measured by metallography is given in **Figure 7.33**. The analysis of all pores in a) shows that there is no significant change in the mean *SF* in the RPT samples with hydrogen content or melt cleanliness, making it somewhat of a useless measurement. This was also found to be the case by Dispinar [65], who attributed it to the errors in measurement of perimeter, however this is probably not the case, because Crofton's method was used [172]. Instead, it is again probably a result of the inundation of the measurement by the shrinkage pores in the section. Analysis of the gas pores (d_{eq}>0.5mm) in b) indicates that the pores develop a higher mean *SF* as the melt hydrogen increases, and the result of the area weighted mean circularity of pores in c) shows a similar result. The higher area weighted circularity of the DM samples should be taken cautiously, as the highly spherical pores in the dross layer on their tops would heavily skew the measurement due to their large size.

The mean sphericity (the 3D shape factor, SF) measured by macro-CT is given in **Figure 7.34**. Analysis of all pores in a) show that at low hydrogen contents pores are more spherical in the dirty metals than the clean metals. However, this must be taken cautiously, due to the decreased accuracy of macro-CT for analysing the shape of small pores. Analysis of only the gas pores (d_{eq}>0.8mm) in b) and the volume weighted mean sphericity in c), both show the trend that dirty metals develop more spherical pores than clean metals at lower hydrogen content.

Overall, the mean shape of pores seems to be indicative of hydrogen content, though it is difficult to draw many conclusions about the effect of oxide films. This is the use of averages can be quite misleading. It can be seen from the size-shape distribution in **Figure 7.22** that

the dirty metals developed a higher number of combined shrinkage and gas pores; but at the same time, the higher number of spherical pores skews off-sets this in the average.

It is difficult to confidently say which technique is most reliable in this case, as the pores are deformed in the metallographic analyses, and macro-CT does not fully capture the true shape of pores due to spatial resolution limitations. The macro-CT analysis of gas pores in **Figure 7.34** b) probably gives a satisfactory indication, as the measured pores are very large and the accuracy of the measurement improves with the size of the object.

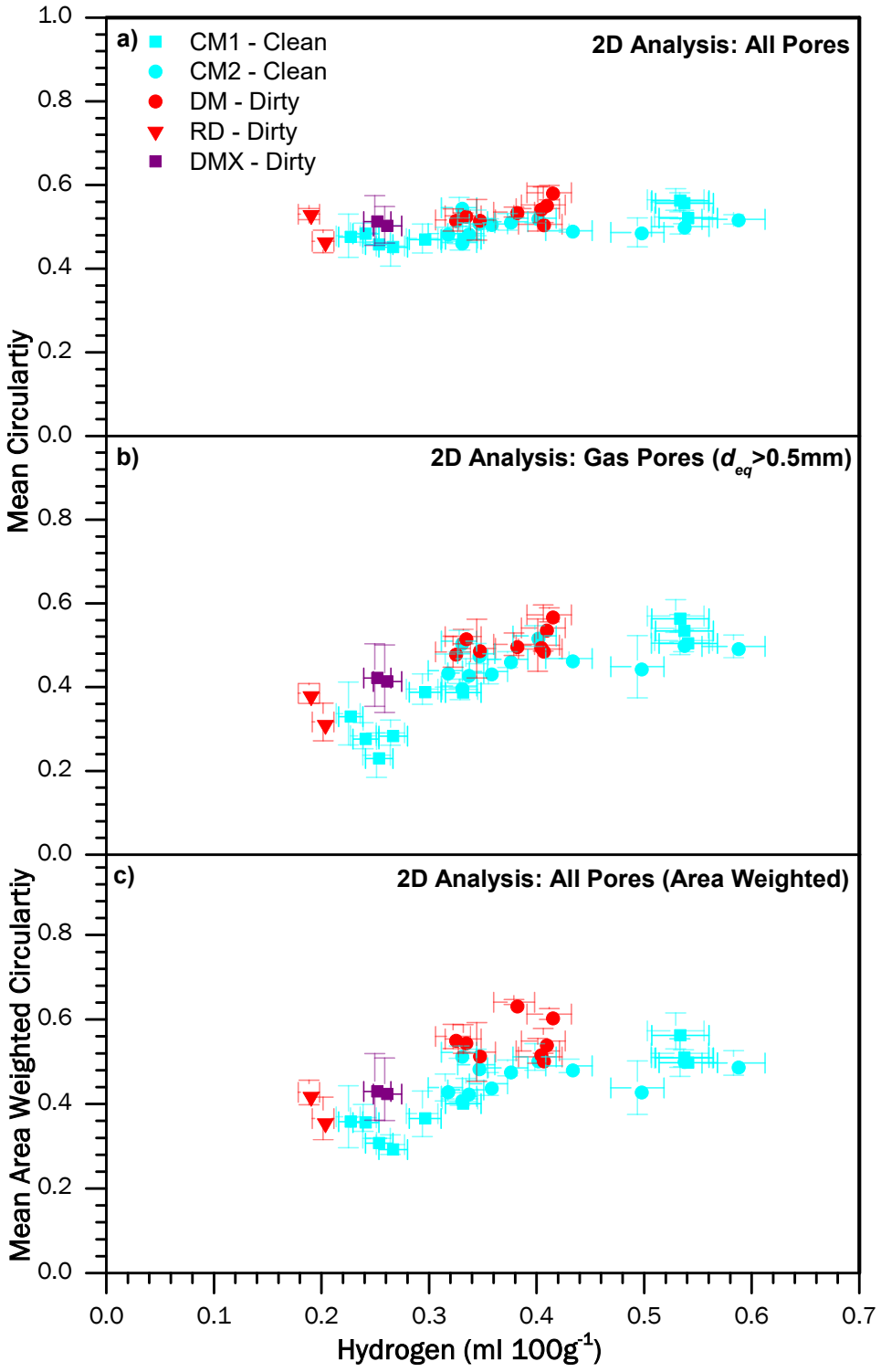

Figure 7.33 Mean circularity of a) all pores, and b) gas pores; and the c) area weighted circularity of all pores measured by metallographic analysis.

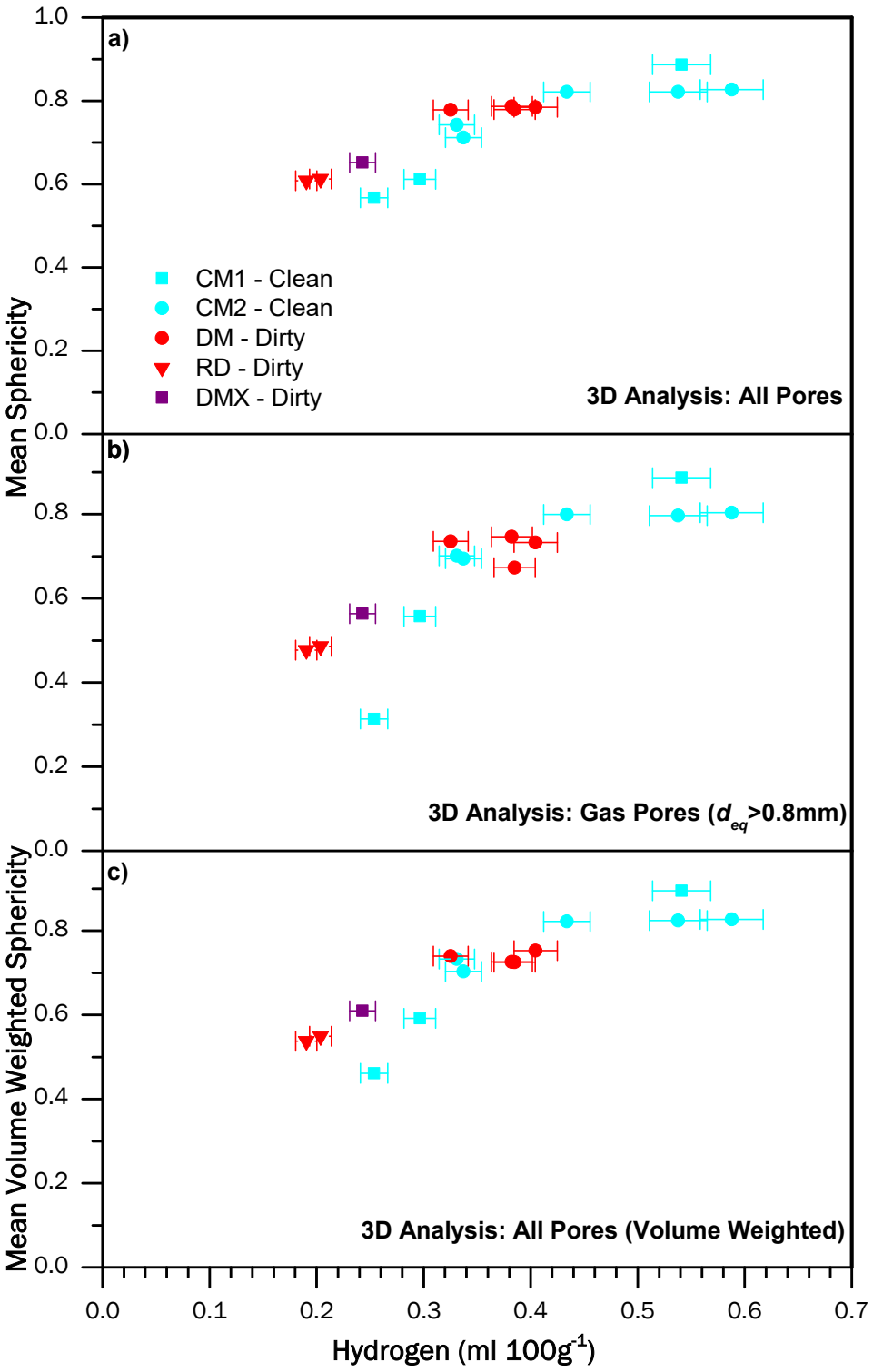

Figure 7.34 Mean sphericity of a) all pores, and b) gas pores d_{eq}>0.8mm; and c) the volume weighted mean sphericity of all pores measured by macro-CT analysis.

7.8.4 Bifilm Index

The Bifilm Index (*BI*) [65], [77] of each of the RPT samples was calculated to determine if it could be used to discern any difference in melt cleanliness. **Figure 7.35** a) shows that there is not an appreciable difference in the *BI* between clean and dirty melts, and simply showed that the *BI* varies in both cases. This suggests that it is more of a measure of the volume fraction of porosity than bifilms in the melt, as shown by **Figure 7.35** b).

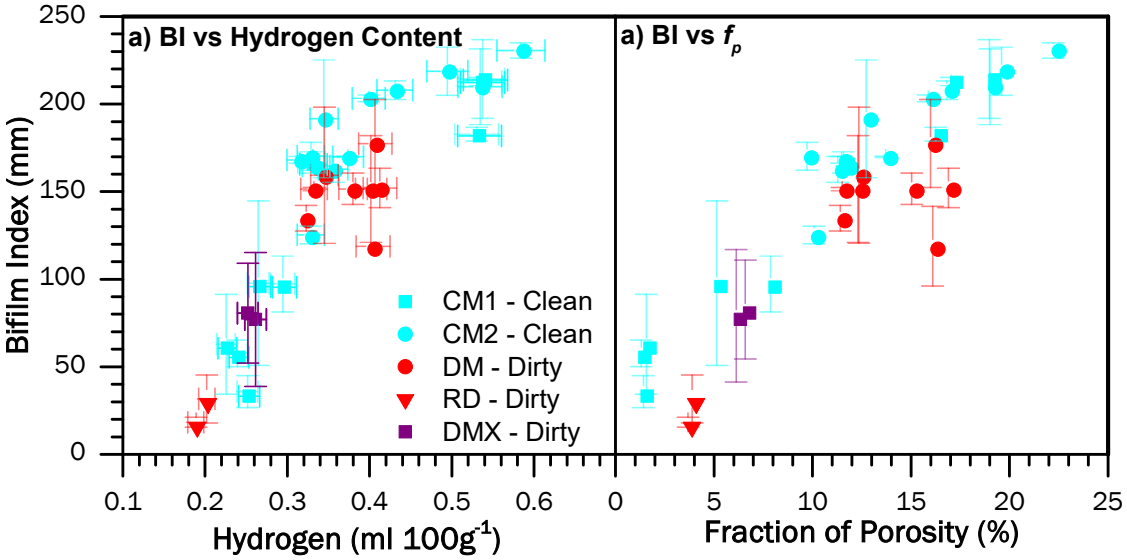

Figure 7.35 Bifilm Index of the RPT samples measured by metallographic analyses versus a) melt hydrogen content, and b) fraction of porosity (measured by Archimedes' method).

7.9 Micro-CT Analysis of Porosity in APT Samples

The results presented up until this point have focused on evaluating porosity in RPT samples, here the results of the micro-CT studies of the structure of porosity in specimens machined from APT samples will be presented.

7.9.1 Volume Fraction of Porosity

Figure 7.36 shows that the micro-CT samples of dirty metal tend to have a higher volume fraction of porosity than the clean metals. Interestingly, this is especially the case for the degassed metal.

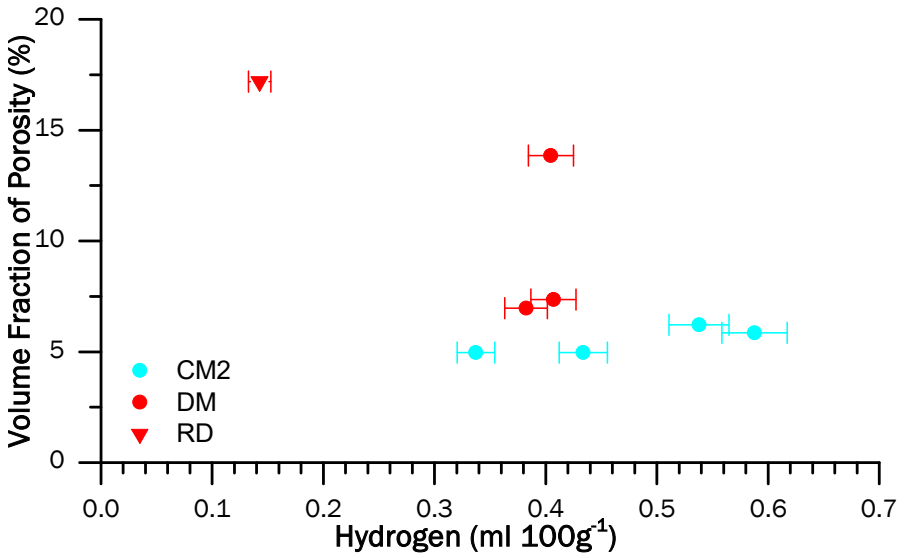

Figure 7.36 Volume fraction of porosity in the Micro-CT samples versus hydrogen content.

7.9.2 Pore Interconnectivity

The overall interconnectivity of the porosity in the samples, represented by the Euler number, is plotted in **Figure 7.37**. It shows that clean metals tended to have a less interconnected pore structure (given their positive Euler numbers), whereas the dirty metals tended to have a highly interconnected pore structure (given their negative Euler numbers), but had significant variability by an order of magnitude. Differences in the interconnectivity of the pore structures can be appreciated from the micro-CT slices shown in the figure.

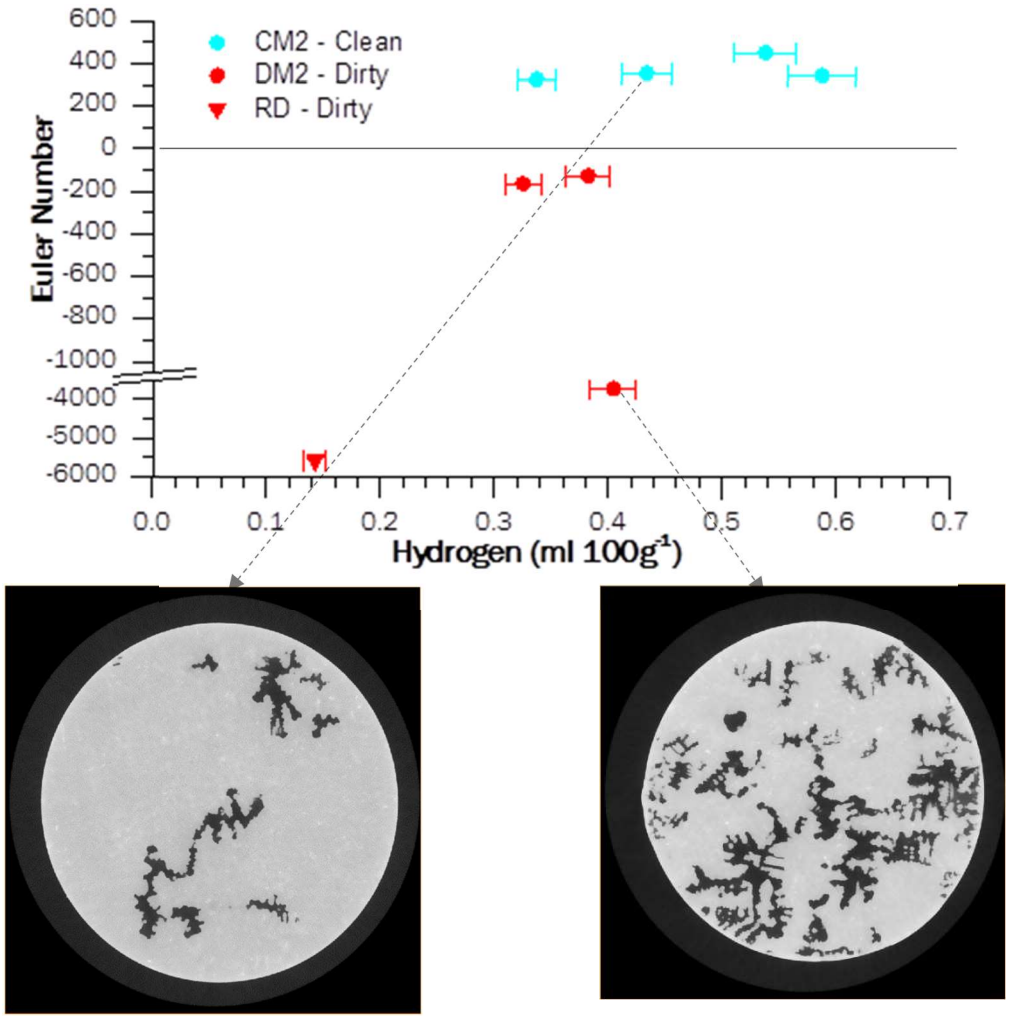

Figure 7.37 Euler number of the pores in the micro-CT samples, which represents the overall interconnectivity.

7.10 Summary of Results

There are four key findings of this study

1. The melt quality was manipulated in various ways through the application of various melt treatments. Upgassing had the effect of increasing the hydrogen contents, the addition of exogenous swarf-chips increased the oxide content, and rotary degassing had the dual effects of decreasing the hydrogen content of the melt, but increasing its oxide films content.
2. Premetz and PoDFA analysis did not consistently show a consistent or significant difference in the oxide film contents of the melts in the four experiments, though SEM analysis of the Prefil samples showed large differences.
3. Hydrogen and oxide films have the individual effects that listed in **Table 7.7** on the formation of porosity in RPT samples.
4. The higher PND of dirty metals may be a good measure of the number of oxide films in the metal. Pore size and shape do not always show strong differences.

Table 7.7 Summary of the effects of hydrogen and oxide film content on porosity formation.

	Vol. Frac. Porosity (f_p) (%)	Areal & Volumetric Pore No. Density (PND) (pores cm$^{-2,3}$)	Eq. Circ. & Spher. Diam. (d_{eq}) (mm)	Circ. & Spher. (Shape Factor)
Hydrogen	↑↑	-	↑	↑
Oxide Films	↑	↑↑	↓	↓

Chapter 8

Grain Refiner Addition Experiments

This chapter presents the results of the third area of experimental work, where the effect of grain refiner addition on the formation of porosity was investigated.

8.1 Summary of Experiments & Melt Compositions

A summary of the melt treatments is reproduced below in **Table 8.1**, and the initial melt compositions are listed in **Table 8.2**. Though both experiments are shown, GR2 will serve as the foundation for most of the investigation presented here, given its more constant hydrogen content.

Table 8.1 Summary of Grain Refiner Experiments

ID	Details
GR1	**TiB_2 Addition, Forerunner to GR2.** Al-3Ti-1B added to give a concentration of 20 ppm of B.
GR2	**TiB_2 Addition, Improvement on GR1** Al-5Ti-1B added to give a concentration of 40 ppm of B.

Table 8.2 Initial melt compositions prior to the addition of grain refiner.

Exp.	Elemental Content (wt.%)								
	Si	Fe	Cu	Mg	Zn	Ti	V	Al	Others
GR1	6.7	0.22	0.001	0.006	0.005	0.006	0.005	93.01	0.04
GR2	7.4	0.21	0.001	0.005	0.005	0.006	0.006	92.30	**0.03**

8.2 Melt Grain Refiner & Inclusion Population Assessment

The grain refiner and inclusion content in the melt, over the course of the experiments, was measured using Prefil samples taken at the start of sampling in each melt state.

Premetz, PoDFA analyses (GR2 samples only), and compositional analyses (OES) were used to track changes in the grain refiner and inclusion content over the course of the experiments. SEM examination was performed for closer examination of the boride population of the melts and of the Al-5Ti-1B master alloy used in GR2.

8.2.1 Grain Refiner Content

In these experiments, Premetz analysis could not be used to calculate an MC value for all of the Prefil filtration curves because of the significant effect that the grain refiner has on the flow rate, which prevented the fitting of filter permeability-normalisation curves [180]. The raw (not normalised) Prefil filtration curves in **Figure 8.1** can instead be used to show, albeit roughly, any changes in the melt cleanliness. The figure shows that in both experiments there are the significant changes in the inclusion content that occurs with grain refiner addition. In the *Grain Refined* and *Restirred* metal the curve is significantly 'flattened-out' compared to the *Baseline* or *Settled* (GR2 only) metal. The steep gradient in the *Settled* metal indicates that the metal has a very low content of particulates, and that both TiB_2 grain refiner particles and the other inclusions were sedimented out of the melt during the two hours of holding. This can be further underscored by the low MC value of 1.4 that Premetz was able to calculate for the *Settled* melt, meaning that it is largely free of inclusions – especially fine particulates which have the strongest effect on the MC [46], [89]. Restirring of the melt

causes the Prefil curve to flatten out again (and prevents the MC from being calculated), which indicates the resuspension of the sedimented particles.

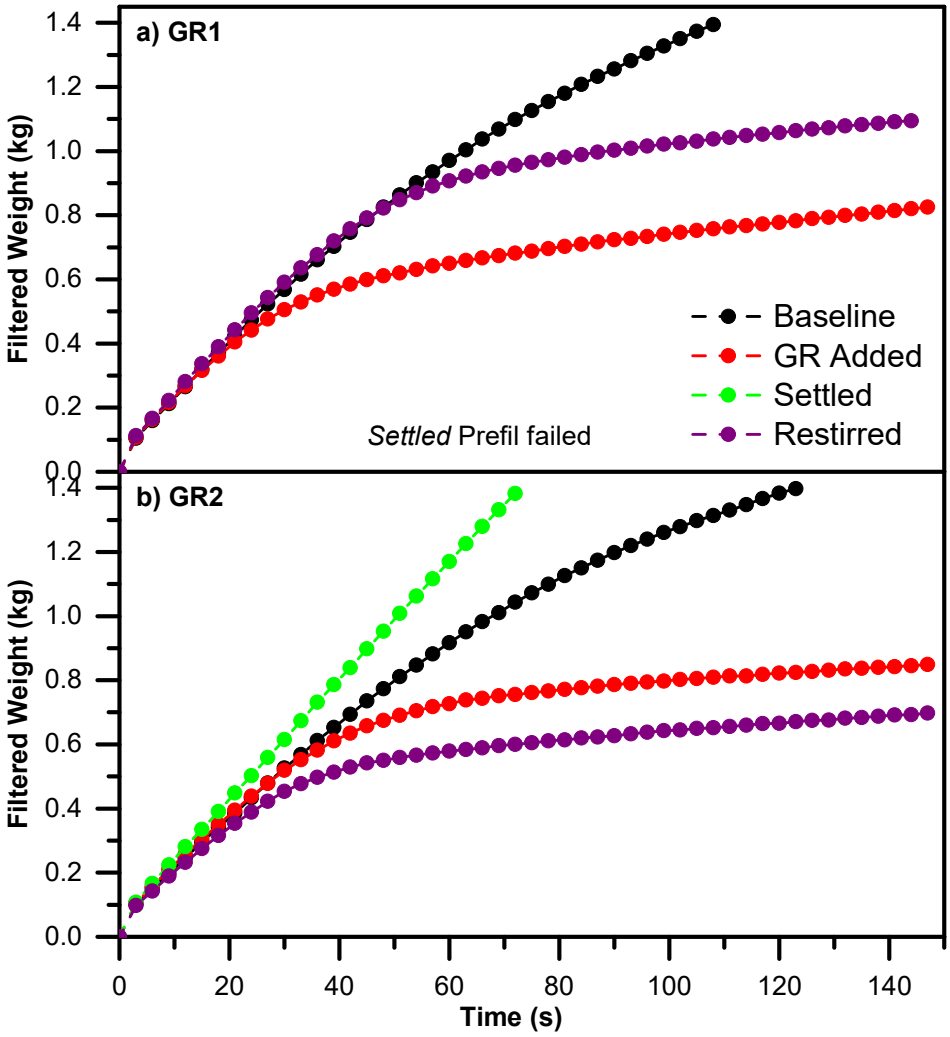

Figure 8.1 Raw (un- normalised) Prefil filtration curves from a) GR1 and b) GR2.

The results of the PoDFA analyses for GR2 are listed in **Table 8.3** and plotted in **Figure 8.2**. They again show that there are boride inclusions present in the *Baseline* material, which explains the high MC value of 50.3. As expected, there is a large increase in the boride content of the melt when grain refiner is added to the melt – it should be noted that it is not

possible to distinguish the difference between the endogenous borides and the grain refiner particles during PoDFA analysis because of their similar appearance, so they are both classified together simply as 'borides'. In the *Settled* metal, the boride content in the metal significantly decreases, again indicating that most of the borides were sedimented out. With restirring, the boride content increases due to their resuspension, but to a higher content, which probably the result of two factors:

- Removal of clean metal from the top of the melt during the sampling in the *Settled* condition, which reduces the total volume of (clean) metal in the crucible, resulting inclusion concentration in the remaining metal when restirred.
- The precipitation of additional endogenous TiB_2 particles as a result of the addition of more free titanium being introduced into to the melt by the grain refiner.

Moreover, PoDFA analysis can be particularly prone to measurement errors when analysing small particulates like borides. This is because of the use of the 20 micron rule, which calls for particles that are closer together than 20 µm to be estimated as a solid single particle [46]. This may result in significant differences from metallographic analysis plane to plane.

Finally, this change in the boride content over the course of the experiment is reflected in in **Figure 8.3**. Another key factor is that even after settling, when there are very few TiB_2 particles suspended, the melt titanium content is still much higher than the *Baseline* level, due to the excess titanium from the Al-Ti-B master alloys. The titanium content in GR1 is lower than in GR2 because Al-3Ti-1B rod was added to give a concentration of 20 ppm B, whereas in GR2 an Al-5Ti-1B rod was added to give a concentration of 40 ppm B.

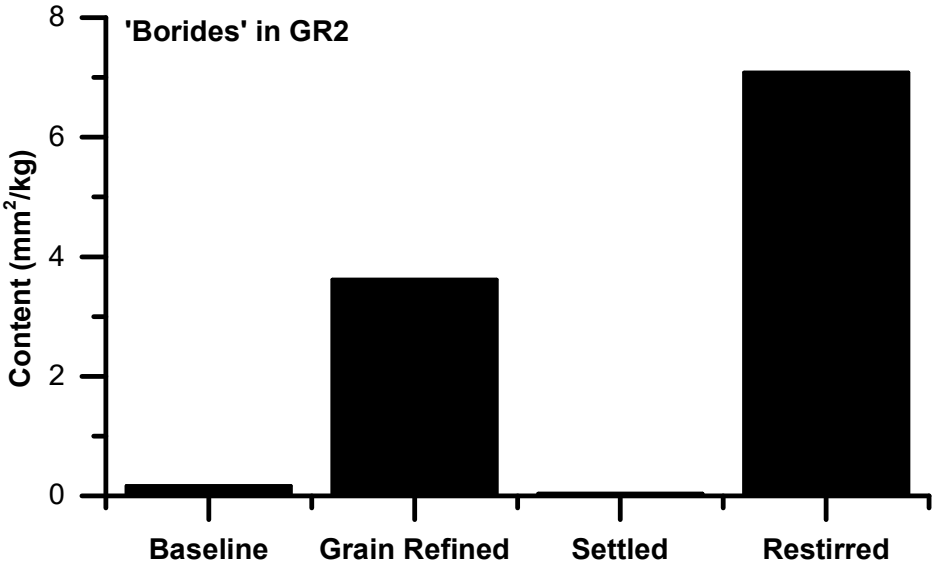

Figure 8.2 Boride content from the PoDFA analysis of GR2 Prefil samples.

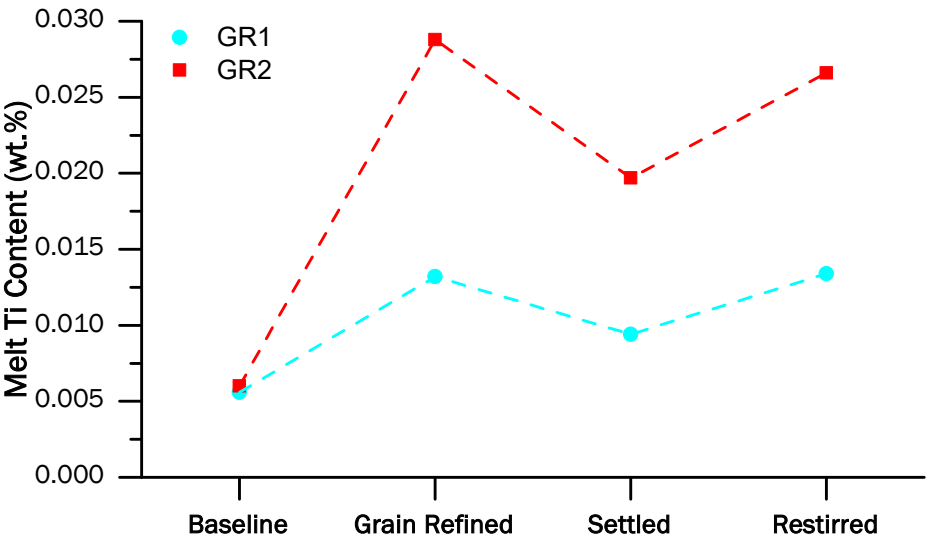

Figure 8.3 Variation in melt titanium content in GR1 and GR2 measured from disk-mould castings using OES.

Table 8.3 Premetz MC values and complete results of the PoDFA analyses of the Prefil samples from GR2

Exp.	Condition	MC	PoDFA							
			Oxides (#/kg)	Refractory		Crucible Fragments (mm^2/kg)	α-Al_2O_3 (mm^2/kg)	Borides (mm^2/kg)	Total Inclusion Count (TIC) (mm^2/kg)	TIC excl. Borides (mm^2/kg)
				Reacted (mm^2/kg)	Unreacted (mm^2/kg)					
GR2	*Baseline*	50.3	27		0.001	0.033	0.0004	0.168	0.202	0.034
	GR Added	-*	35		0.002	0.032	0.009	3.620	3.663	0.043
	Settled	1.4	24		Trace	0.007	0.002	0.043	0.053	0.010
	Restirred	-*	36	Trace	0.036	0.030	0.005	7.084	7.155	0.071

* MC indeterminate due to the very low (flat) gradient of Prefil filtration curve.

8.2.2 Endogenous Borides

As for the melt quality experiments in the preceding chapter, PoDFA analysis of Prefil samples taken from GR2 revealed that borides were a prominent inclusion in the *Baseline* melt.

A small side experiment was conducted in order to determine the origin of these borides, to see whether they were introduced from the alloy components (CP Al and Al-50Si master alloy) that were used to make the Al-7Si alloy, or if they were formed *in situ* during the experiment. In this experiment a small batch of ~4 kg of Al-7Si alloy was produced using an induction furnace and a well coated non-reactive crucible, with a Prefil being taken of the melted CP Al prior to Al-50Si waffle addition, and another after its addition. The Premetz-normalised flowrate curves and MC values in **Figure 8.4** show that neither the commercially pure aluminium base nor the alloy after alloying with the Al-50Si waffle contained any appreciable amount of fine particulates in the metal compared to the Al-7Si alloy that was produced and cast by the usual practice in this work. Thus it was concluded that these borides form *in situ* during the main experiments from reactions with the crucible and transition metals, titanium and vanadium, that are present in trace amounts in the alloy.

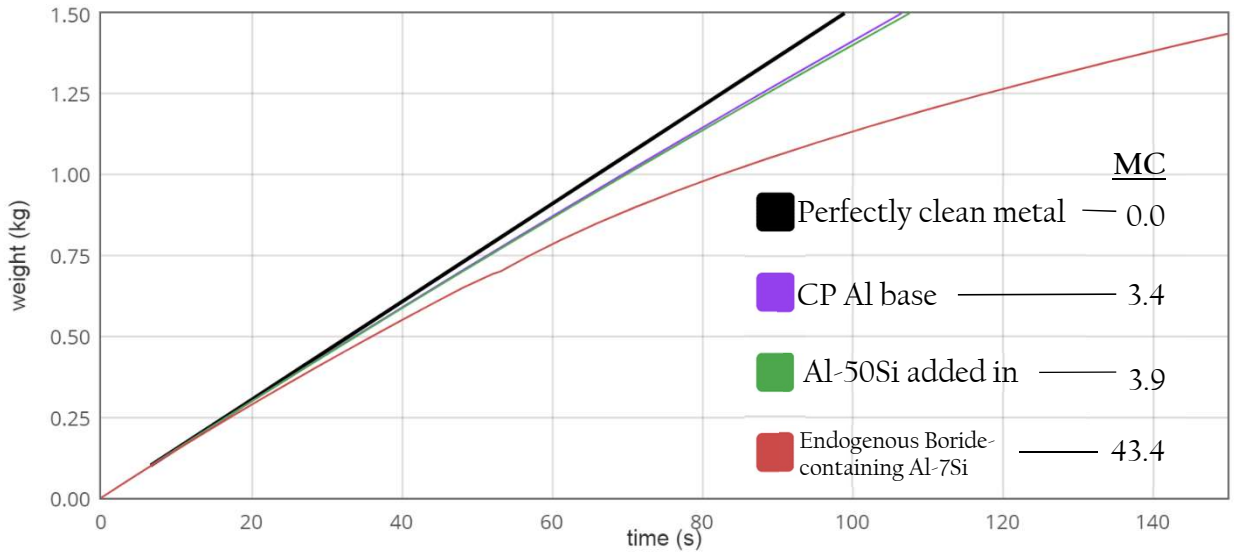

Figure 8.4 Premetz-normalised mass Prefil flowrate curves from small melt experiments showing the absence of small particulates in the material.

8.2.3 Non-Boride Inclusion Species

In addition to boride inclusions the PoDFA analyses of the GR2 samples show that there are other types of inclusions present in the material, similar to those found in the previous chapter of work, which includes oxide films, refractory material, spalled fragments of the crucible, and α-Al_2O_3. **Figure 8.5** shows a plot of the total content of these inclusions at each stage of the experiments.

The increase in the TIC with grain refiner addition is negligible, though the increase in oxide film content and α-Al_2O_3 might be due to melt handling time. The decrease in inclusions in the *Settled* metal can be explained by their sedimentation out of the melt. The increased inclusion content in the *Restirred* metal can be explained by the reduction in the volume of inclusion free metal due to sampling of the settled metal, which concentrates the inclusions in the melt after restirring – as mentioned in Section 8.2.1.

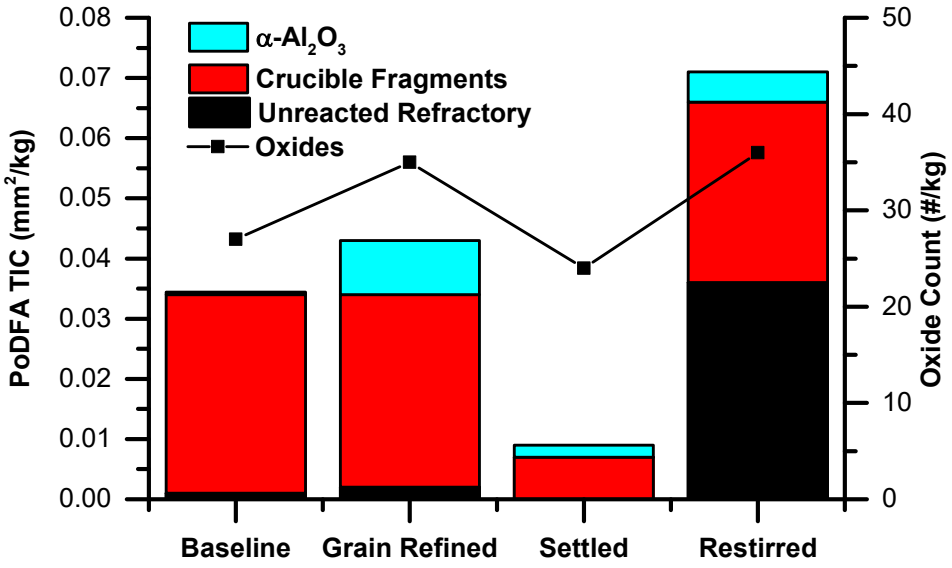

Figure 8.5 PoDFA analysis total inclusion content (exc. Borides) in GR2.

8.2.4 SEM Analysis of Boride Particles

Prefil Residue Analysis

The initial SEM analysis of exogenous boride particles that was conducted on our behalf by N-Tec Ltd on a un-grain refined Prefil filter residue revealed that the particles were rich in both Ti and V (**Figure 8.6**), which is what first suggested that they were borides.

Subsequent analysis of the Prefil samples taken from GR2 with high resolution SEM (**Figure 8.7**) showed that these particles were boron rich, confirming that they were borides. The high resolution imaging showed that endogenous borides in the *Baseline* were generally (but not always) highly polygonal and at times could be large in size. The borides in the *Grain Refined* samples were a combination of grain refiner (TiB_2) and endogenous borides. The borides in this material were generally smaller in size, and a number of them were observed

to be cracked borides. These cracked borides are probably the exogenous TiB_2 particles, which could have been cracked during the rolling process of the master alloy rod.

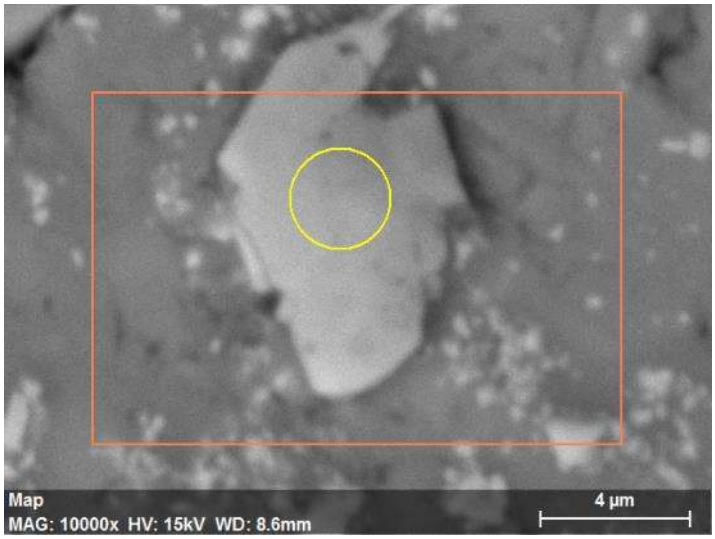

Element	AN	Series	Net	unn. C [wt.%]	norm. C [wt.%]	Atom. C [at.%]	Error [%]
Boron	5	K-series	1551	35.57	35.47	70.14	5.4
Titanium	22	K-series	28958	33.66	33.57	14.99	1.0
Vanadium	23	K-series	19758	25.97	25.90	10.87	0.8
Aluminium	13	K-series	9533	5.07	5.05	4.00	0.3
			Total:	100.26	100.00	100.00	

Figure 8.6 SEM secondary electron micrograph and the results of an EDX spot analysis, performed by N-Tec on a Prefil sample taken from a non-grain refined melt.

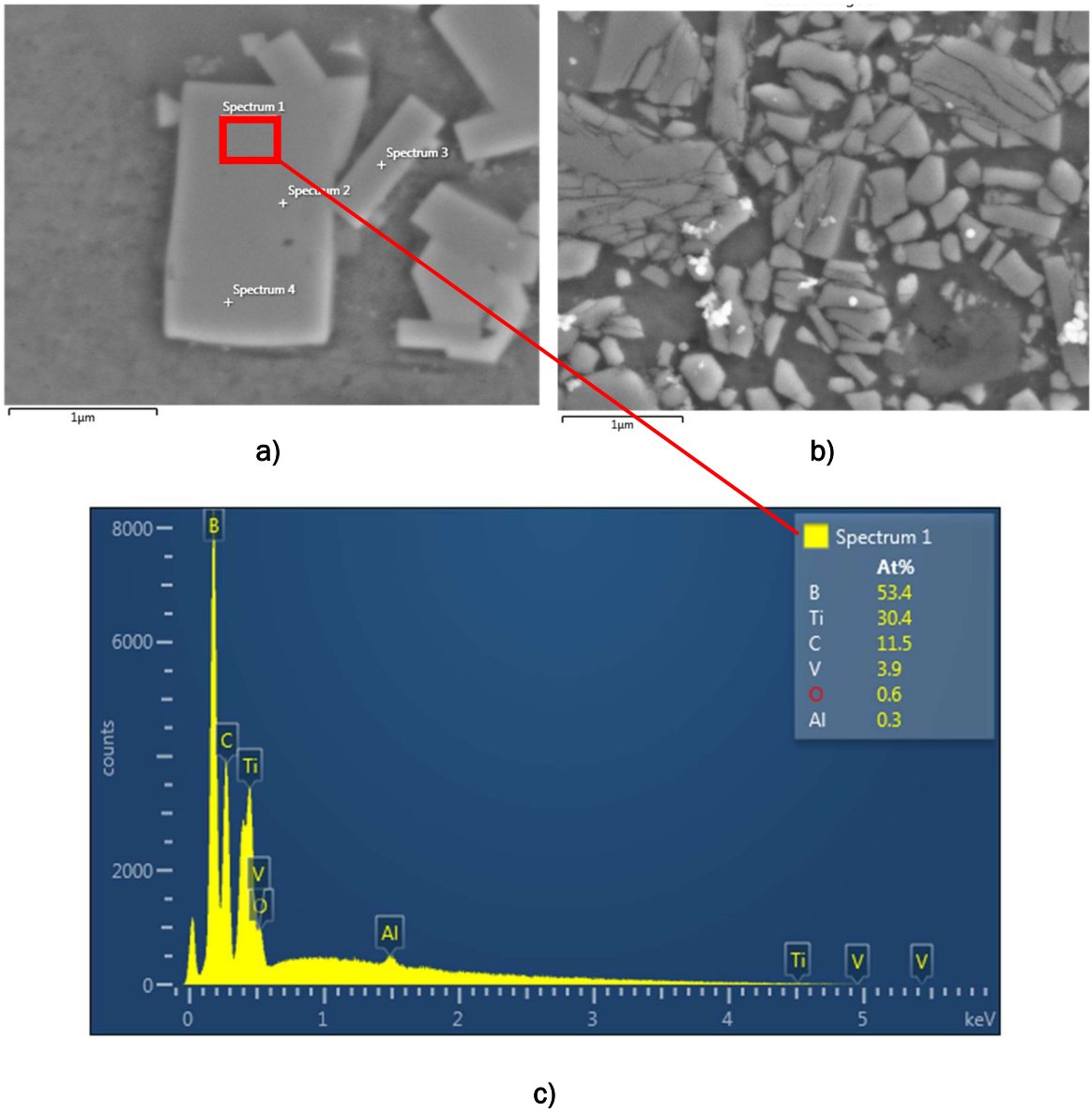

Figure 8.7 High resolution SEI micrographs and EDX analysis of Prefil samples from GR2. Showing a) endogenous borides in the *Baseline* metal, b) a combination of grain refiner and endogenous boride particles in the *Grain Refined* metal; and c), a low voltage EDX spectrum of the endogenous boride particle in a).

Al-5Ti-1B Grain Refiner Rod Analysis

SEM microanalysis was performed on transverse cross-section of the Al-5Ti-1B master alloy rod that was used in GR2. **Figure 8.8** a) shows that the master alloy contains numerous TiB_2 clusters. EDX spot analyses of these clusters showed that they often contain traces

oxygen, potentially originating from oxide films, an example of this is shown in **Figure 8.8** b). The number of oxygen peak counts in the EDX spectrum that is shown is very low, so it is not possible to rule this out as surface contamination. That being said, EDX analysis of other regions of the sample did not contain this oxygen trace, which suggests it might not be contamination.

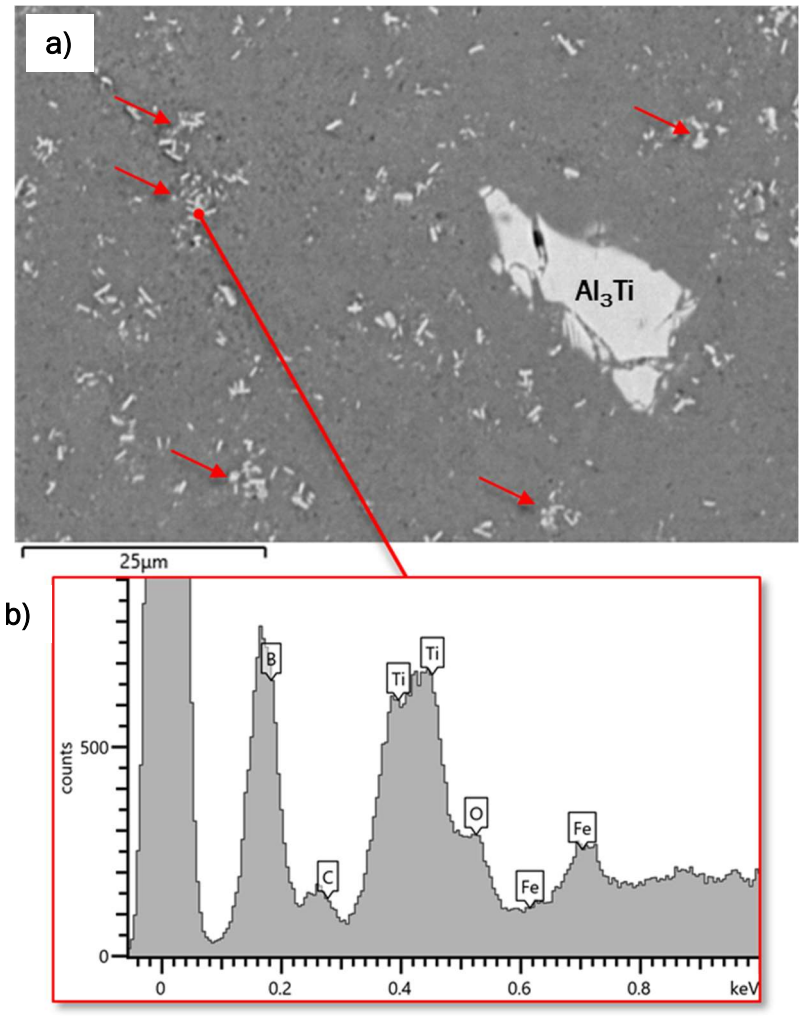

Figure 8.8 a) A BSE image of the Al-5Ti-1B master alloy rod, sectioned transversely, showing the presence of numerous TiB_2 clusters, indicated by the red arrows; and b) an EDX spectrum of a TiB_2 particle cluster

8.3 Change in Grain Structure

The etched grain structures of selected RPT samples from GR1 and GR2 are shown in **Figure 8.9** and **Figure 8.10**, respectively. Both show that the addition of grain refiner reduces the grainsize of the samples taken thereafter. Interestingly, after settling, the grain structure remains highly refined, with no qualitative difference compared the *Grain Refined* sample, nor does there seem to be one after restirring. Finally, an important observation that can be made, which has relevance to the work in this whole thesis, is that the grain structure in the RPTs (cast in the manner that they were in this work) is equiaxed, and not columnar.

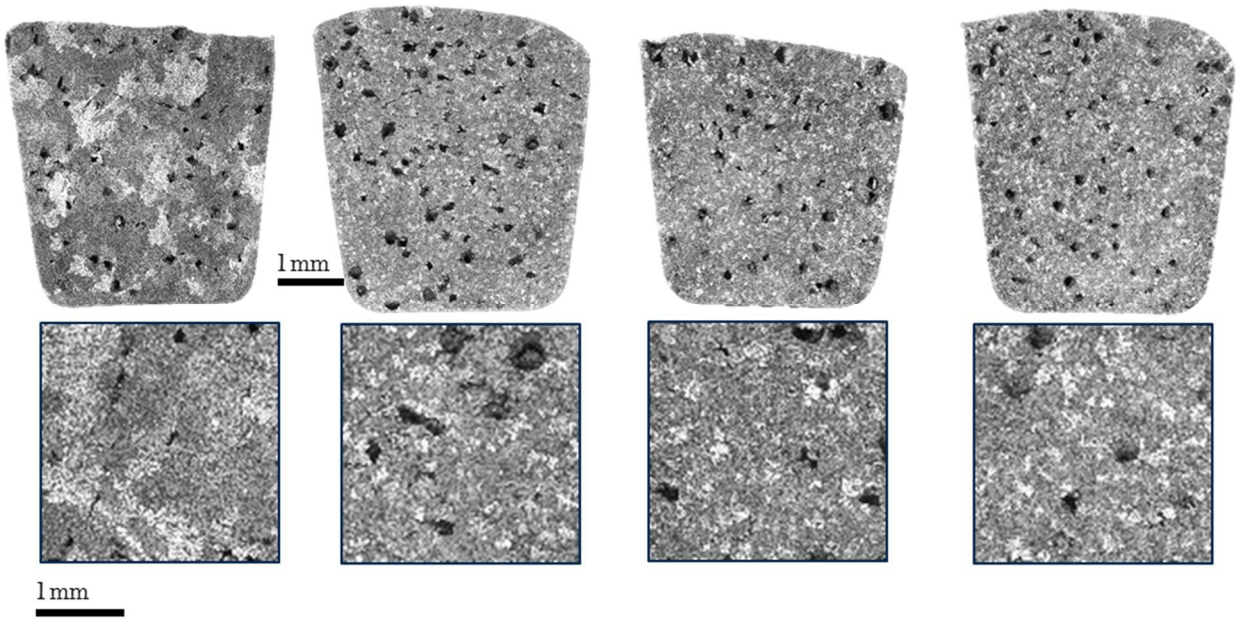

Figure 8.9 Macro-etched RPT sample sections from GR1.

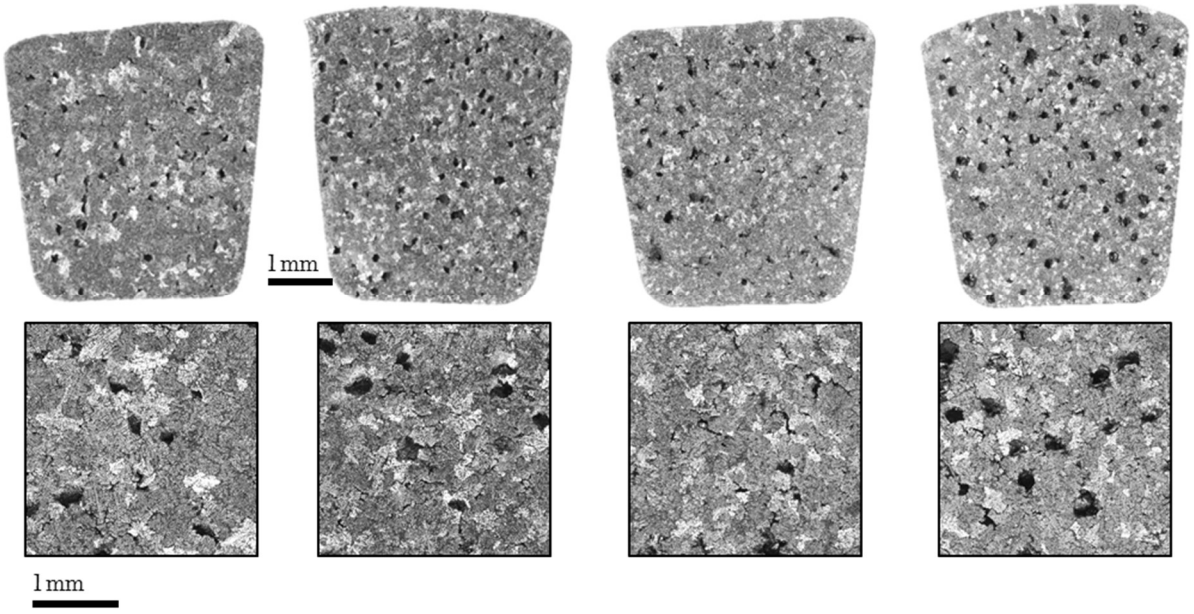

Figure 8.10 Macro-etched RPT sample sections from GR2.

8.4 Volume Fraction of Porosity

Figure 8.11 and **Figure 8.12** show the change in the volume of porosity (f_p) in the RPT samples and the melt hydrogen content over the course of the experiments. Although measurements of f_p (or the Density Index) from the RPT are often considered to measure the melt quality, it is difficult to say for this case, as grain refiner is not normally considered to deteriorate the melt quality. Something that is important to note is that the hydrogen content in GR1 was measured using LECO, and should serve as an approximation of the melt hydrogen content. Details on this technique are given in Appendix II.1.

The figures show that in both experiments the addition of TiB_2 results in a marked increase f_p of the *Grain Refined* melt compared to the *Baseline* melt. It can qualitatively be seen from the metallographic RPT cross-section that there is a concomitant increase in the number of pores, though it is difficult to qualitatively determine whether they are also larger. When the grain refiner was sedimented out in the *Settled* melt, f_p decreases to a level similar to the *Baseline* melt; and when the melt is *Restirred*, the f_p increases to a level similar to the *Grain Refined* metal.

From the results of GR2 (**Figure 8.12**) where the hydrogen content was more uniform over the experiment, it can more clearly be seen f_p in the *Settled* metal decreases to below the *Baseline* level. This is likely due to a reduction in the number of pores forming on inclusions (namely oxides) in the material. Restirring and resuspension of inclusions in the melt sees an increase in f_p, to a higher level than when the grain refiner was originally added, which can probably be attributed the resuspension of oxides and other pore forming inclusions in the metal. The slightly increased hydrogen content might also play as a factor in this.

The same trends are also in the f_p of the APT samples, shown in **Figure 8.13**.

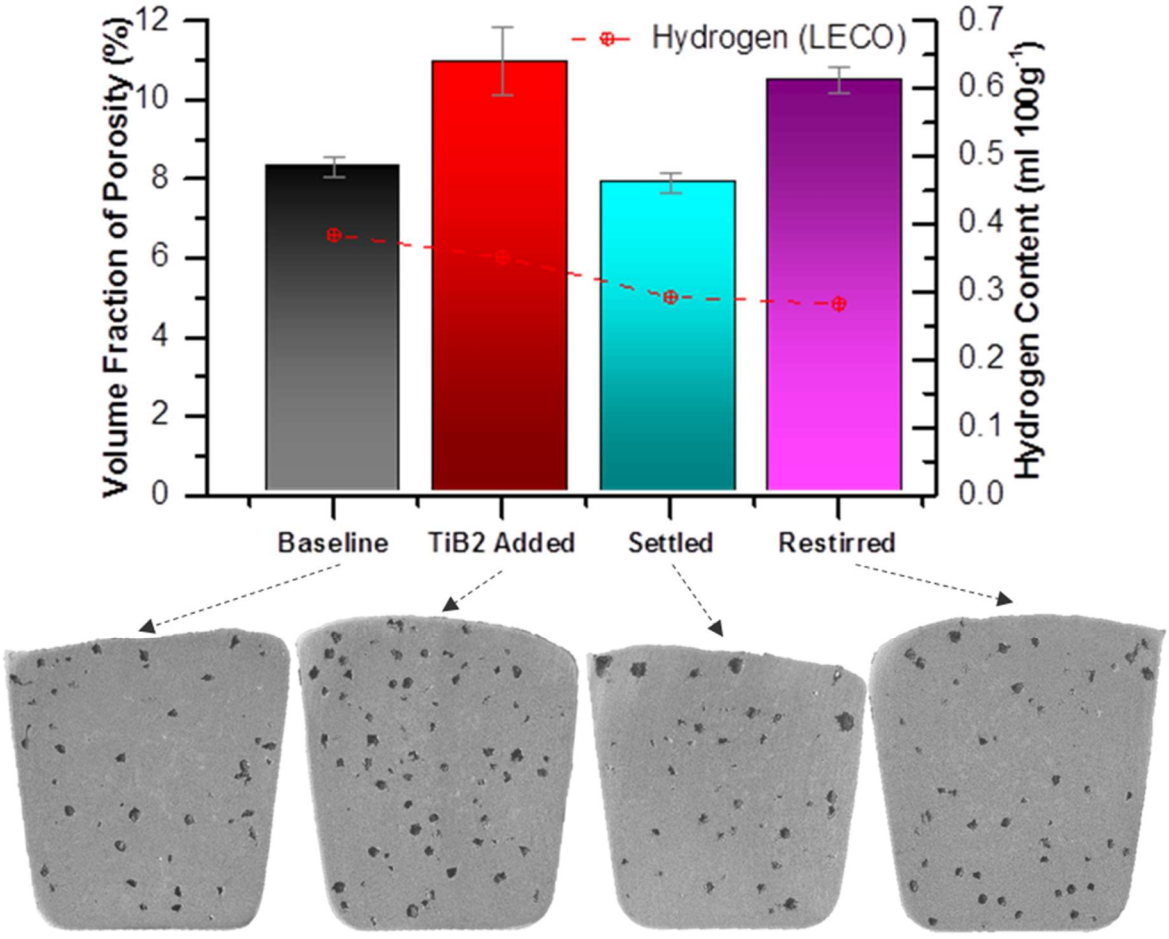

Figure 8.11 f_p measured by Archimedes' principle and melt hydrogen content at each melt condition in GR1, calculated from the average 2 RPT samples. The error bars on the f_p measurements represent the propagation of measurement error.

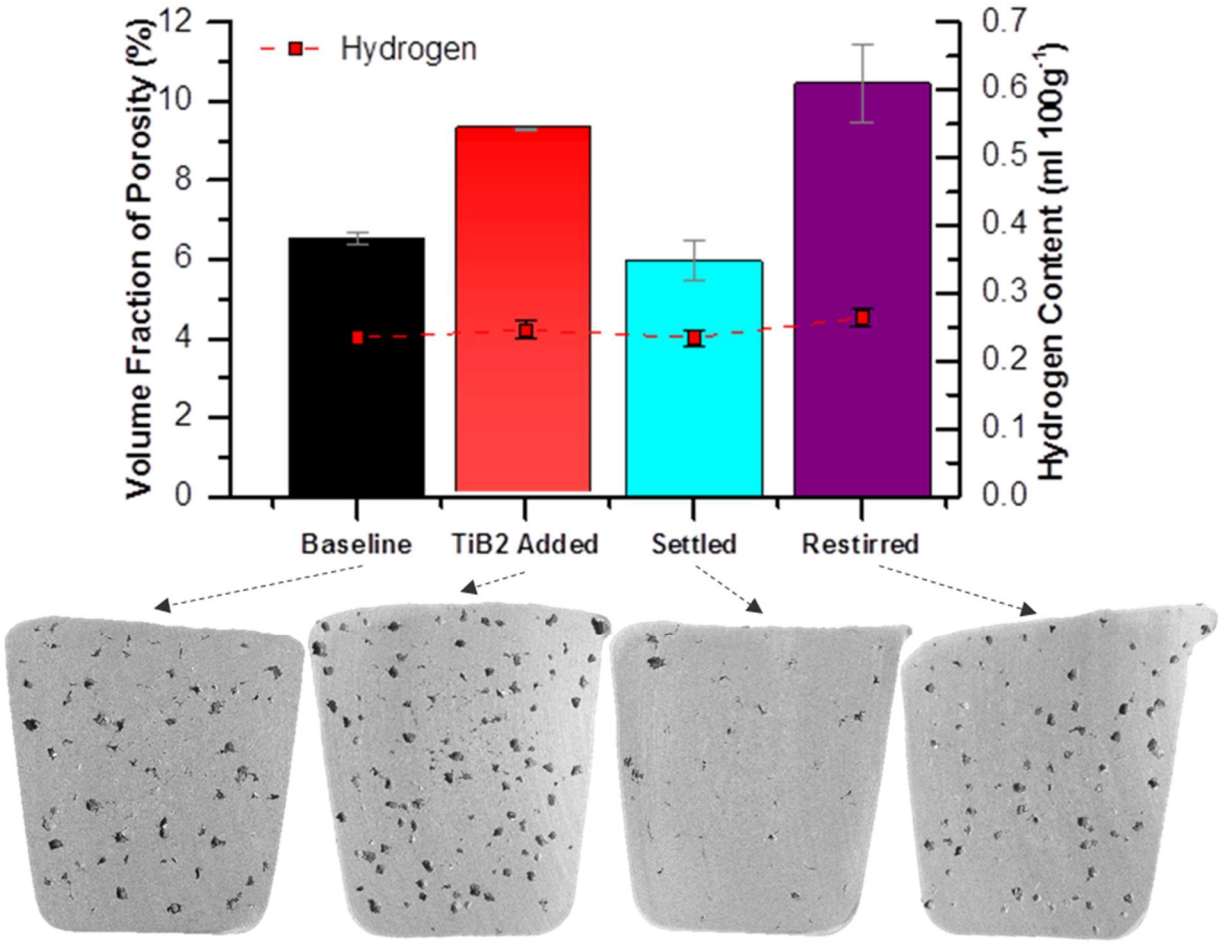

Figure 8.12 f_p measured by Archimedes' principle and melt hydrogen content at each melt condition in GR2, calculated from the average 3 RPT samples. The error bars on the f_p measurements represent the propagation of measurement error.

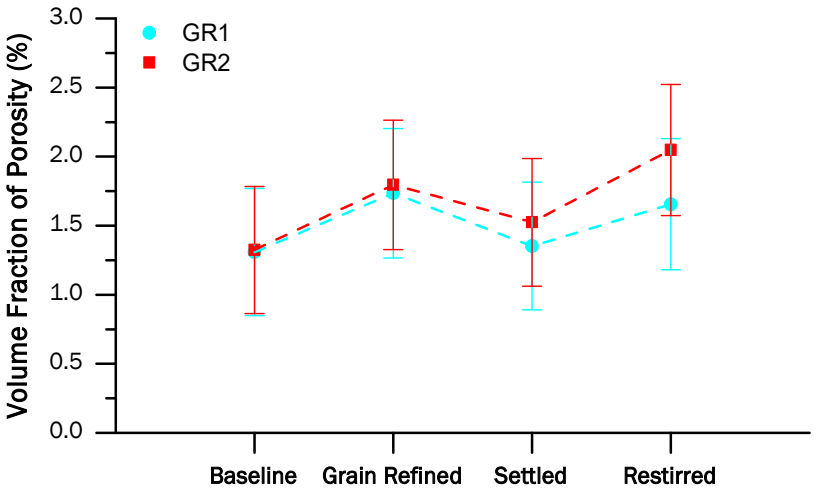

Figure 8.13 f_p of APT samples taken during GR1 and GR2, measured by Archimedes' principle. The error bars represent the measurement error.

8.5 Changes in the Structure of Pores

The structure of the porosity in the RPT samples was analysed using metallography and macro-CT in order to quantify the changes in the structure of pores that form in each condition. Metallographic analysis was only performed on selected RPT samples from GR1 as it was considered macro-CT gave a more thorough analysis.

Macro-CT slices of some RPT samples from GR2 are presented in **Figure 8.14**. Qualitatively, it can be seen that there are more pores in the *Grain Refined* and *Restirred* metals than the *Baseline* and *Settled* metals. The addition of grain refiner does not seem to have reduced shrinkage porosity, as it seems that all samples contain roughly the same quantity of it.

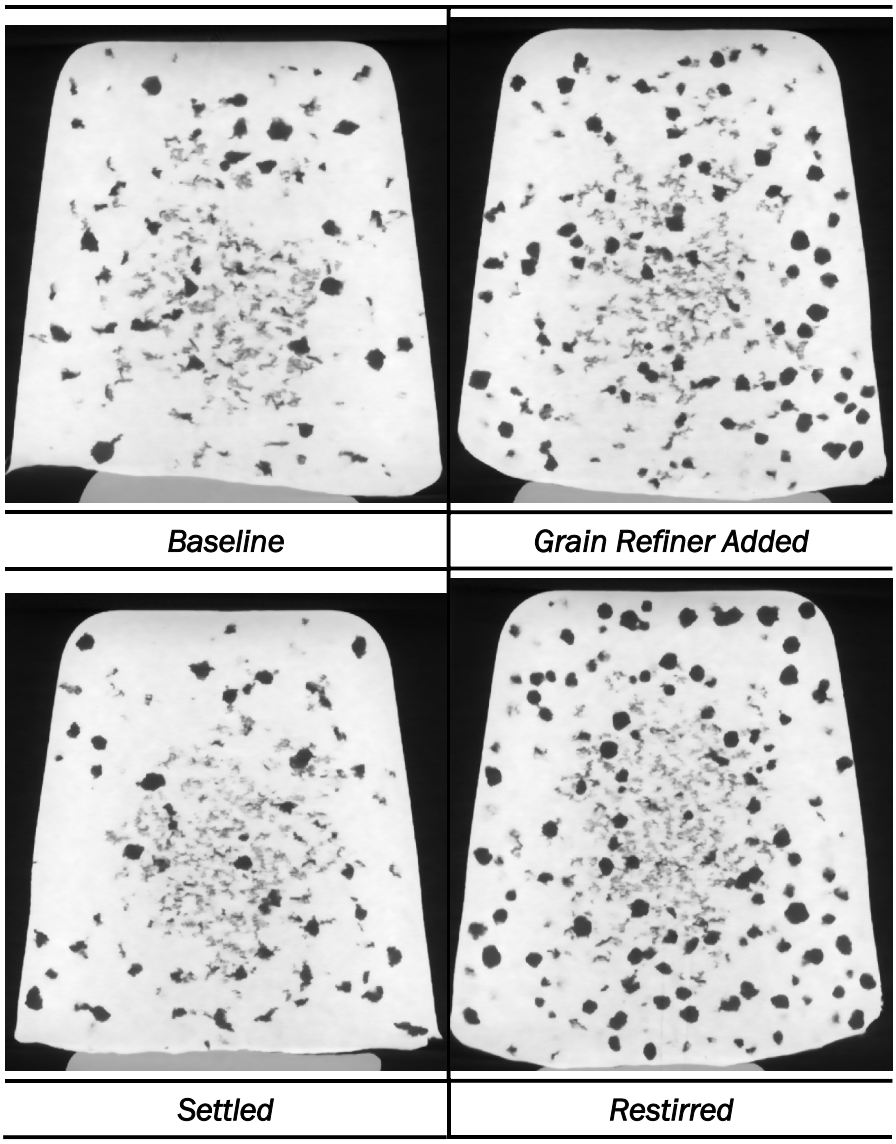

Figure 8.14 Macro-CT slices of RPT samples from GR2.

8.5.1 Pore Size-Shape Distribution

Again, the macro-CT size-shape distributions can be used to give a qualitative overall view of the structure of the pores that are formed at each melt condition, and are given in **Figure 8.15**.

In both experiments it can be seen that the addition of grain refiner increases the number of gas pores that are formed in the material, which are also more spherical in shape. This effect disappears in the *Settled* metal, and then returns in the *Restirred* metal. There seems to be very little difference

It is difficult to determine its effect on the shrinkage pores based on these distributions as many of the shrinkage pores are combined with the gas pores in the centre of the sample.

The size-shape distribution of pores in GR1 is given in Appendix III.3.2.

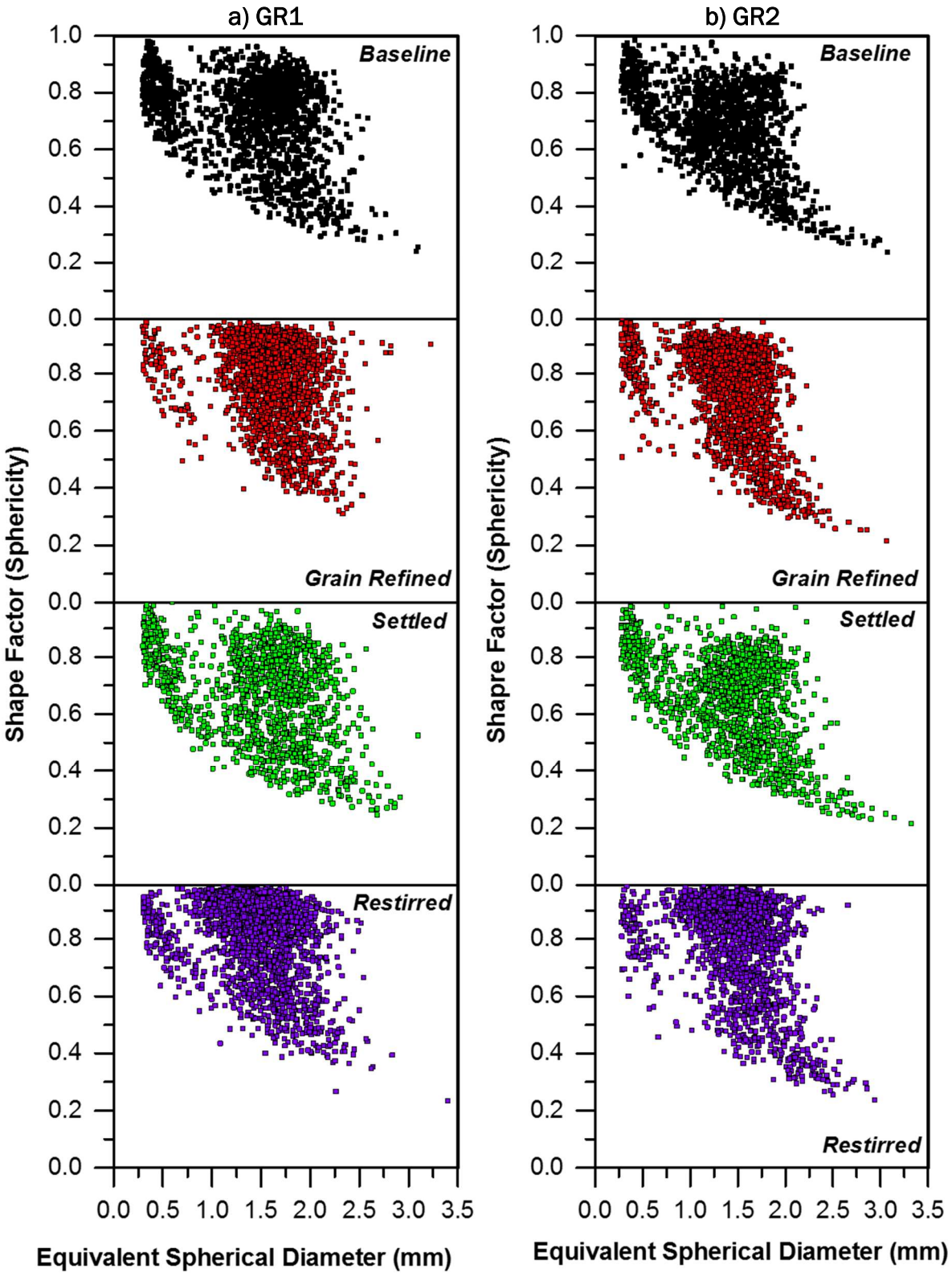

Figure 8.15 Macro-CT size-shape distribution of pores in RPT samples from a) GR1 and b) GR2

8.5.2 Quantification of Pore Size

The macro-CT pore size distribution in the RPT samples from GR1 and GR2 are presented in **Figure 8.17** a) and b), respectively.

Like the results presented in the previous chapter, they show a bimodal distribution of pore sizes in all the samples with the division between the peaks again being roughly at d_{eq}=0.8mm. Again, the peaks broadly represent gas pores and shrinkage pores. The slight shift in the peaks that occurs in GR1 is due to the decreasing hydrogen content over the course of the experiment. The presence of grain refiner in the melt in the *Grain Refined* and *Restirred* samples increases the number of gas pores relative to the *Baseline* and the *settled* samples; and when the melt is settled, the pores size distribution reassumes close to that of the baseline. **Figure 8.17** shows that there is very little change in the mean equivalent spherical diameter (d_{eq}) of gas pores across the melt conditions, and the slight decrease in GR1 in the restirred metal likely arises because of its lower hydrogen content. It can also qualitatively be seen from **Figure 8.17** that there is very little change in the width of the distributions. It is likely that the slightly increased width of the gas pore peak in the settled metal is due to the reduction in the number of oxides in the material, as the results of the previous chapter have demonstrated. The metallographic analysis (not shown) also showed that there was not a significant change in the d_{eq} of the gas pores.

The metallographic pore size distribution of pores in the GR1 RPT samples is shown in Appendix III.3.2.

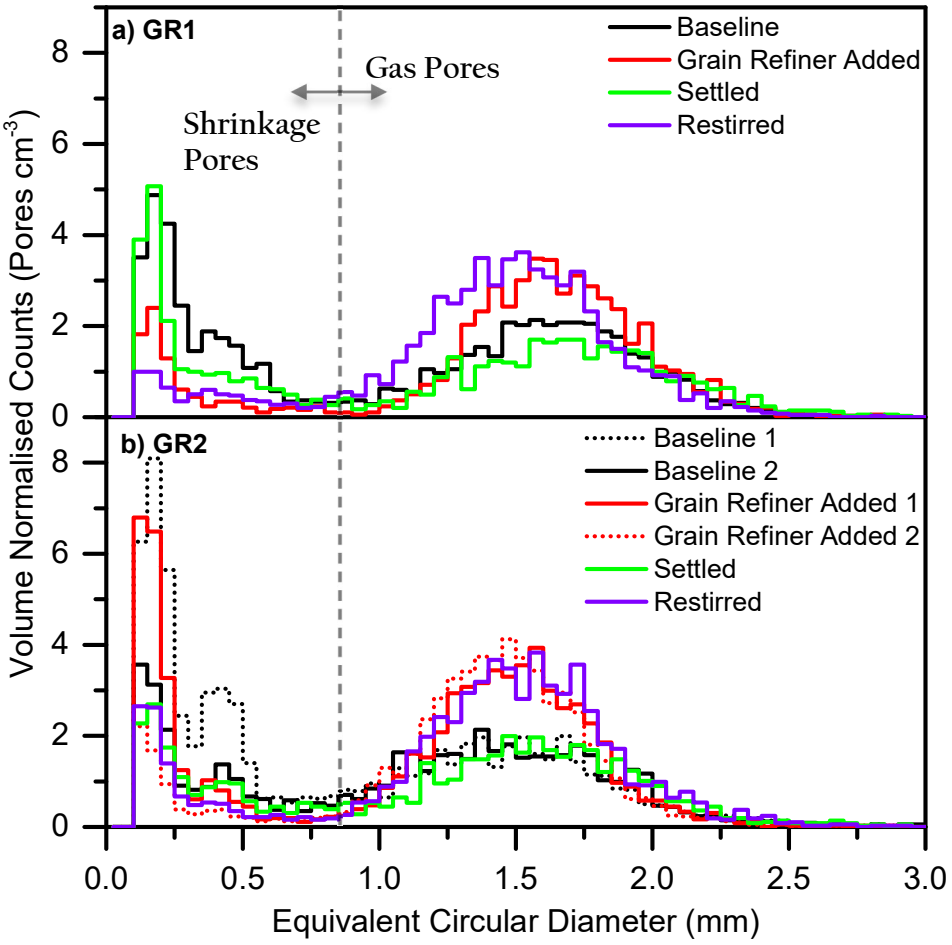

Figure 8.16 Macro-CT size distribution of pores in RPT samples cast from a) GR1 and b) GR2 measured by macro-CT.

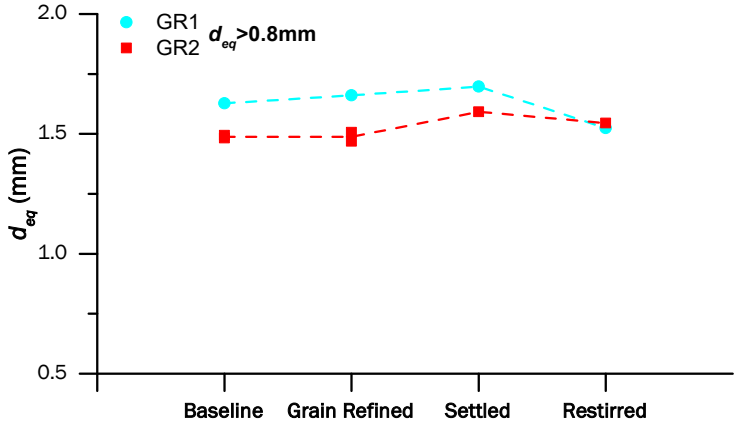

Figure 8.17 Mean equivalent spherical diameter (d_{eq}) of gas pores in RPT samples at each melt condition in GR2 measured by macro-CT

8.5.3 Quantification of Gas Pore Morphology

The shape distribution of gas pores in the GR2 samples is given in **Figure 8.18** a), and shows that there is a greatly increased number of spherical pores in the RPT samples cast from the *Grain Refined* and *Restirred* metal compared to the *Baseline* and *Settled* metal. This is further reflected in the plot of the mean sphericity in **Figure 8.18** b). There is a slight indication that the pores are slightly more spherical after restirring of the melt.

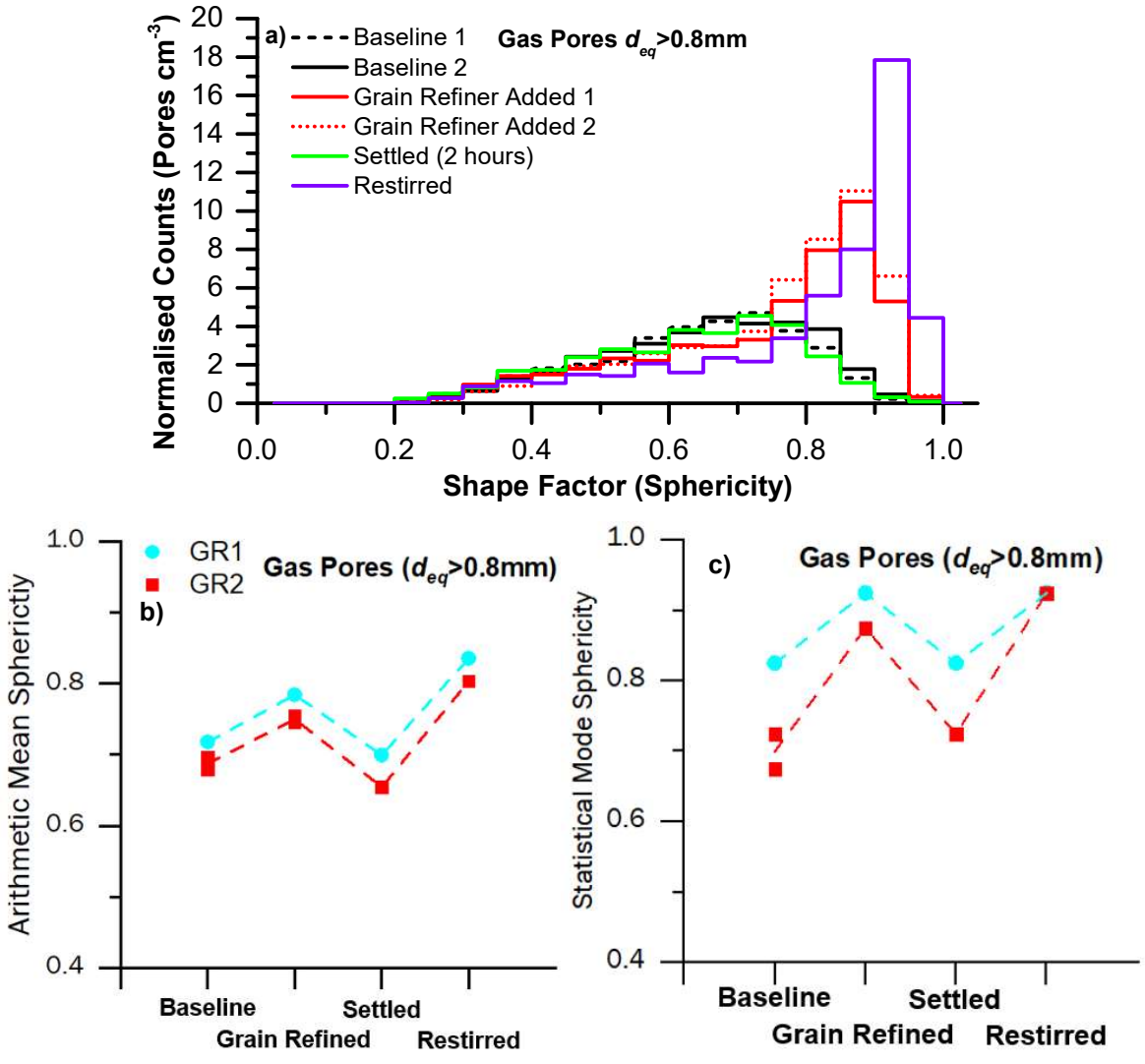

Figure 8.18 Macro-CT a) pore shape distribution of pores in GR2, b) the arithmetic mean pore shape, and c) the statistical mode of the pore shape distribution in RPT samples from GR1 and GR2.

Figure 8.19 shows that the metallographic analysis of the mean shape of gas pores in some of the RPT samples from GR1 displays the same trend as the macro-CT analysis.

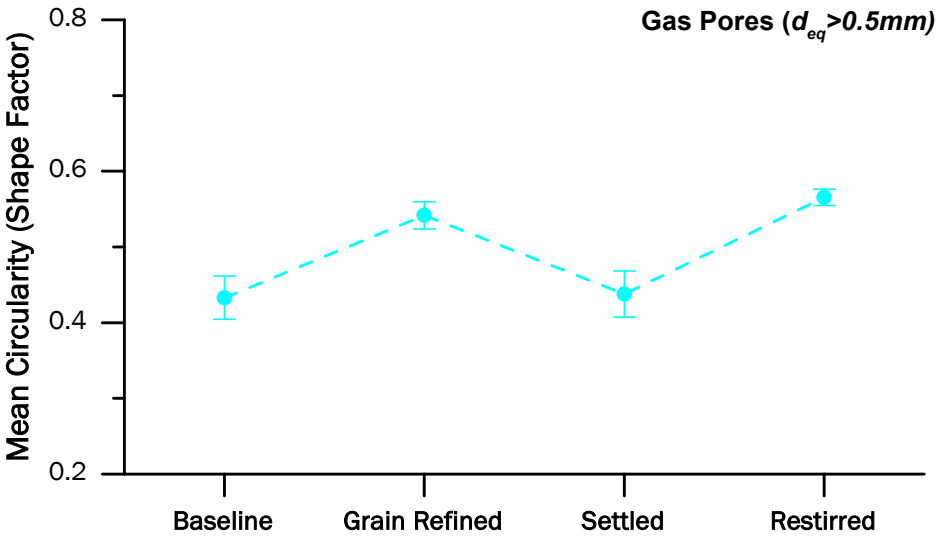

Figure 8.19 Mean circularity gas pores measured by metallographic analysis. The error bars represent the range in the measurements from each half of the RPT sample.

8.5.4 Pore Number Density of Gas Pores

The volumetric PND of gas pores (d_{eq}>0.8mm) from macro-CT analysis in **Figure 8.20** shows that there is a clear increase in the number of gas pores in the material when grain refiner is present, with the number of gas pores in the *Grain Refined* and *Restirred* metal increasing by approximaytely one third compared to the baseline and settled melts.

A similar trend can be seen from the areal PND of gas pores (d_{eq}>0.5mm), and the volumetric PND estimated using Saltikov's area method, from the metallographic analysis. in **Figure 8.21**.

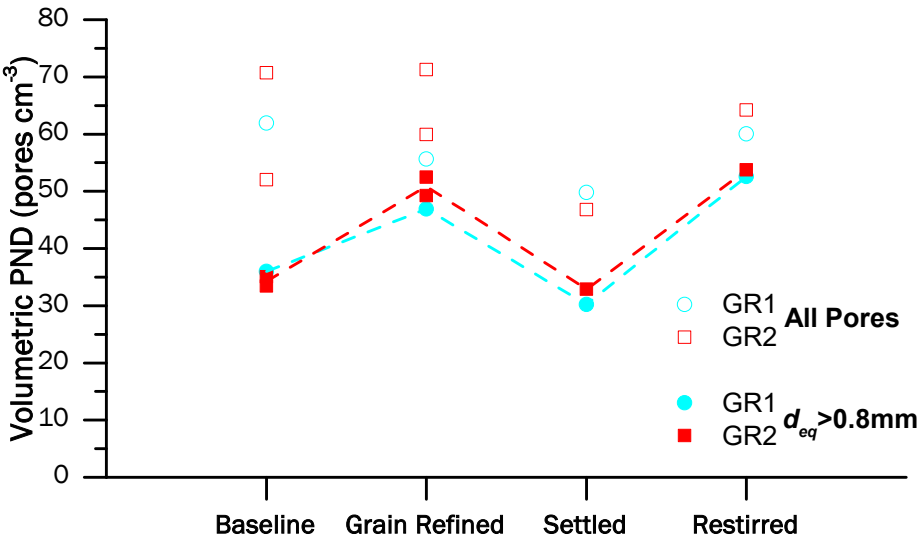

Figure 8.20 Macro-CT volumetric PND of all pores and only gas pores (d_{eq}>0.8mm) in selected RPT samples taken from GR1 and GR2.

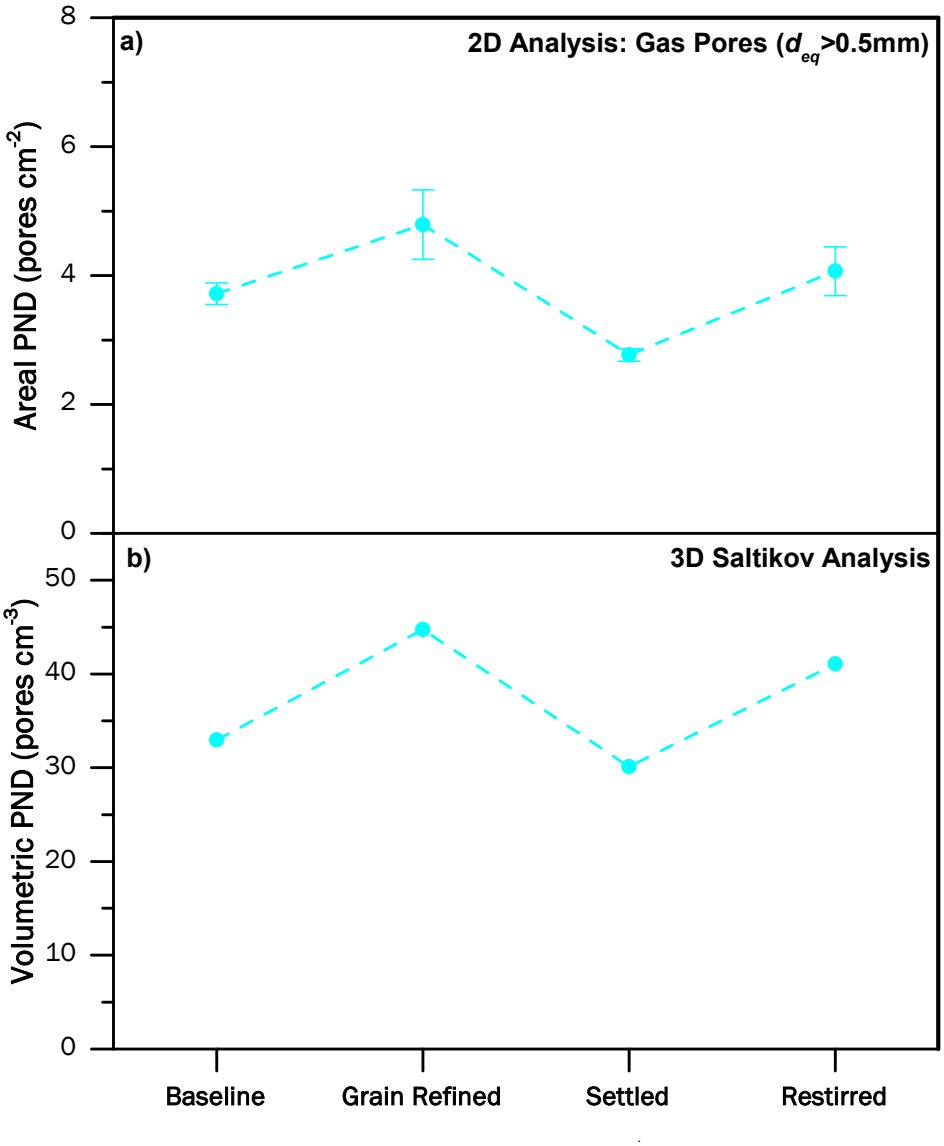

Figure 8.21 Macro-CT volumetric PND of all pores and only gas pores (d_{eq}>0.8mm) in selected RPT samples taken from GR1 and GR2. The error bars represent the range in the measurements from each half of the RPT sample.

8.6 Micro-CT Analysis of Atmospheric Porosity

Micro-CT analysis of the porosity specimens cut from the centres of *APT* samples that were each melt condition in GR1 and GR2.

8.6.1 Volume Fraction of Porosity

Figure 8.13 showed that the presence of grain refiner suspended in the melt increased the overall volume fraction of porosity (f_p) the whole APT samples. However, as **Figure 8.22** shows, the trend of the f_p (measured by micro-CT) in the micro-CT specimens - (taken from the centres of the APT samples – follows the opposite trend, with the f_p decreasing when grain refiner is suspended in the melt. This suggests that the presence of grain refiner in the melt redistributes the porosity throughout the APT samples.

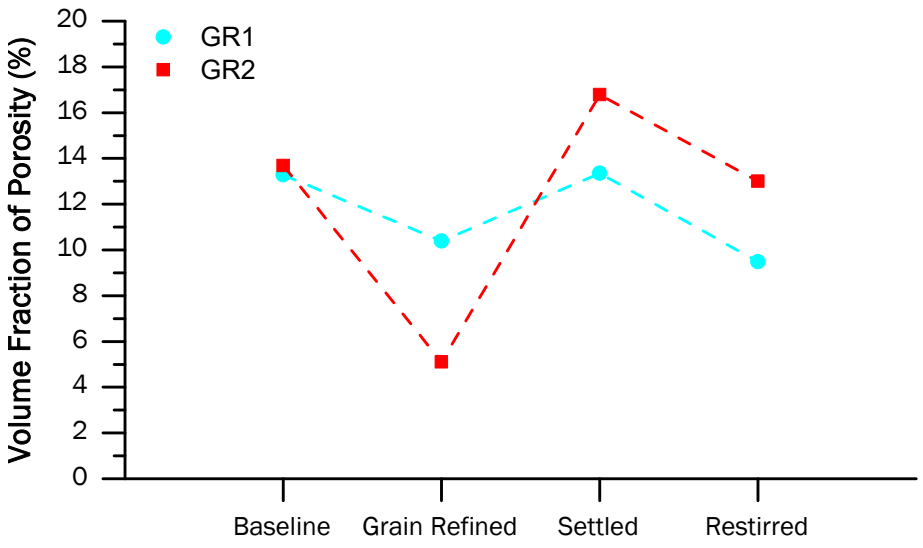

Figure 8.22 Volume fraction of porosity measured in the micro-CT samples, measured by micro-CT.

8.6.2 Pore Interconnectivity

The interconnectivity of the pores, measured by the Euler-number, is given in **Figure 8.23**. The more negative the Euler number, the higher the degree of interconnectivity. The results show that in both experiments the pore interconnectivity decreases with grain refiner addition. This indicates that the porosity at the centres of the samples becomes decreasingly interdendritic with in grain refined metal.

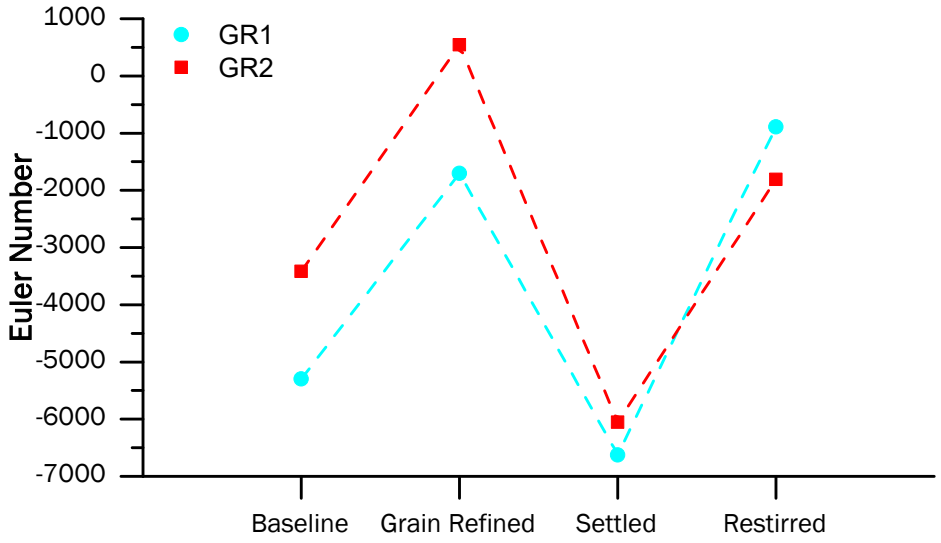

Figure 8.23 Variation in the Euler number in the micro-CT APT samples from GR1 and GR2.

8.7 Summary of Results

There are 4 notable findings from this study:

1. The addition of grain refiner into the melt refines the grain structure, however, even when the TiB_2 particles are settled from the melt the grain structure is still refined.
2. The presence of grain refiner particles suspended in the melt increases the overall f_p in RPT and APT samples. There was no measureable difference between the effects of the freshly added and restirred metal.
3. The presence of grain refiner particles suspended in the melt (in the *Grain Refined* and *Restirred* melt conditions) increases the number of gas pores in the material, which are on average more spherical than in non-grain refined metal. A summary of the effects are listed in **Table 8.4**.
4. Micro-CT analysis of the atmospheric porosity could only reveal that the presence of grain refiner particles suspended in the metal decreases the interconnectivity of pores and the f_p in the centre of the *APT* samples. This indicates that the porosity may be redistributed in the material.

Table 8.4 Summary of the effects of Al-Ti-B grain refiner addition on porosity formation.

	Vol. Frac. Porosity (f_p) (%)	**Areal & Volumetric Pore No. Density** (PND) (pores $cm^{-2,3}$)	**Eq. Circ. & Spher. Diam.** (d_{eq}) (mm)	**Circ. & Spher.** (Shape Factor)
Grain Refiner	↑	↑	↑	↑

Part IV
Discussion

Chapter 9

The Effect of Melt Quality on Porosity Formation

The roles of melt hydrogen and melt oxide content on porosity formation will be discussed in this chapter based on the results of the Melt Quality experiments in Chapter 7.

9.1 The Efficacy of the Melt Treatments in Manipulating Melt Quality

The effects and reproducibility of some of the melt treatments will be discussed here. The melt *Self-Cleaning* or fluxing processes are not discussed, as they did not prove particularly insightful – though they were successful in cleaning the melt up by their mechanisms that have been discussed in Section 2.7.

9.1.1 Upgassing: Experiments CM1 & CM2

Bubbling of an Ar-15H gas mixture through the melts using a submerged diffuser was shown to successfully increase their hydrogen contents (**Figure 7.1** and **Figure 7.2**). Similar results have been reported others who have used various mixtures argon and hydrogenous gases [9], [59], [173]. The process can therefore be considered reproducible in this regard, though the hydrogen content in the melt that is achieved is dependent on many factors, such as the rate of hydrogen loss from the top of the melt, the ambient humidity of the

surroundings, the hydrogen content of the gas mixture, the upgassing duration, and the bubble size.

Upgassing was also found to have had the equally important secondary effect of removing inclusions – particularly oxides in the melt – though this is discussed in Appendix III.1.3 as it was noted as a result of the experimental work presented there.

9.1.2 Swarf-Chip Addition: Experiment DM

The SEM micrographs (**Figure 7.10**) showed numerous oxides were present in the melt over the duration of experiment *DM*. It is difficult to say with certainty whether these oxides are exogenous, originating from the outsides of swarf chips, or endogenous, incorporated during melt stirring – through direct entrainment from the surface, or bubble trails, generated from the passage of any incorporated air bubbles through the melt. During SEM micro-analysis, all of the oxide films appeared to have similar thicknesses, and there was no evident difference in the appearance of oxides, that could give clues as to their origin, though there were some morphological differences, which will be discussed later.

It might be that heating and compacting the swarf chips into a semi-solid ball, and plunging it subsurface assisted its addition into the melt. This would have allowed it to break through the surface melt – where the surface oxide and surface tension act as barriers – but it might have also enhanced its wettability. For example, when the oxide was held in the semi-solid state, it was observed to 'sweat' eutectic droplets. The contact of these droplets may have improved the wettability of the oxide films – as the solid-liquid contact angle has been observed to decrease with increasing contact time [54]. However, it is not clear whether the 3 hours of holding at ~580°C would be sufficient for wetting to develop (a contact angle <90°). Nevertheless, a thick dross layer was formed on the surface of the melt

during this experiment, which would indicate that a large fraction of the oxides were floating out of the melt.

The thick dross layer that was formed on the surface of the melt in DM was probably the result of the floatation of some of the oxides – namely the exogenous oxides. Previous authors [181], [182] have reported that 'large oxides', introduced into the melt from scrap, has a strong propensity to float out of the melt. Kvithyld et al [183] used LiMCA to directly measure the melt cleanliness of scrap-loaded melts, and showed that the oxide content of scrap-loaded melts decreased over time due to the gradual flotation (or sedimentation) of oxide films. Although this experiment differed greatly in the type of alloys used and melt conditions, it showed that the reduction of inclusions occurred on the scale of tens of minutes. This means that stirring of the melt just prior to sampling (1 – 2 minutes before), probably would incorporated the floated inclusions long enough to be captured during sampling.

The most likely scenario is that the melt contained a combination of entrained exogenous and endogenous oxide films. However, because of the opposing forces of the floatation of oxide films from the material and the top-stirring to reincorporate floated oxide films, their content over the course of the experiment should be considered highly variable and somewhat random.

The size of these films inside the melt was also probably highly variable. Oxides originating from the outside of the swarf films would be considered to be very large, while endogenous oxides could potentially be much smaller. Large oxide films were shown to be present using high the high resolution EDX mapping (**Figure 7.11**), though it is unclear as to from where these oxides originate.

9.1.3 The Effect of Rotary Degassing on Melt Cleanliness

The rotary degassing treatment that was performed in this work was likely very inefficient as the size of the bubbles was probably relatively large [101]. Two reasons for this are that the ratio of the rotor and crucible size were not matched, and the argon purge gas was not preheated prior to injection – which would have caused the bubbles to massively expand inside the hot melt [180]. Nevertheless, degassing was performed for 1 hour, and the results show that this was successful in reducing the hydrogen content of the melt to ~0.1 ml $100g^{-1}$ (**Figure 7.4**), and considered highly reproducible from the perspective of hydrogen control.

Rotary degassing is widely considered to clean inclusions from molten metal by floating them from the melt [38], [64], [102]–[104], which may describe the relatively low PoDFA TIC, which was comparable to the clean metals (**Figure 7.7**). However, at the same time, the vortex that is generated in the melt during the process may have continuously generated and entrained endogenous oxide films from the surface of the melt [3], which explains the origin of the numerous films that were seen during the SEM micro-analysis (**Figure 7.12**). There have been few studies, if any, on the removal of film inclusions from molten aluminium, therefore a mechanism by which such inclusions are removed can only be speculated. Campbell [3] has suggested that large oxides may be removed by bubbles, and small oxide film fragments might simply slip around the periphery of a bubble in the streamlines as shown in **Figure 9.1** a) and b). Large oxide films are also probably sheared by the rotor into small entrained fragments [71], [184], [185] – much smaller than those from experiment DM which was only hand stirred.

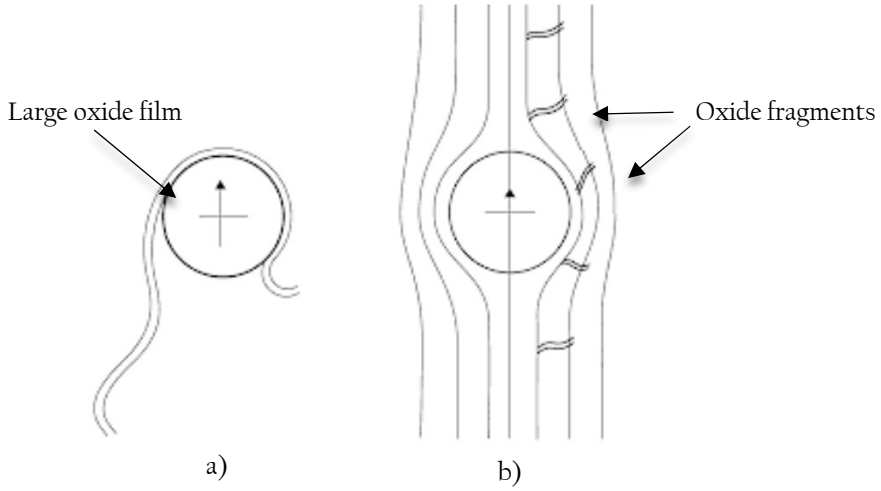

Figure 9.1 The effect of bubble size on the interaction of bubbles with a) a large oxide film, which contacts the bubble and floats out, and b) small oxide films, which do not contact the bubble and follow the streamlines of the rising bubble. Adapted from Campbell [3].

Whatever the mechanism, it is for the said reasons that only small fragments of oxide films were seen in the RD Prefil samples. The morphologies of these entrained films is discussed further in 9.3.

9.2 Complexities in the Assessment of Oxide Films

Premetz and PoDFA analysis were unable to reliably show differences in the oxide film contents between the clean and dirty melts.

9.2.1 Premetz

Premetz did not measure consistent differences in the MC values of the samples taken from the clean and dirty metals, despite the very large differences in the oxide contents that were observed with SEM micro-analysis.

There are conflicting reports about the efficacy of using Premetz or the Prefil curve for determining the oxide film content of a material. Some previous research [186], [187] has demonstrated that the raw Prefil filtration curve (even when un-normalised) is able to reveal significant differences in the oxide content in various melts of fresh- and remelted metal. Though conversely, Riestra et al. [181] were unable to resolve differences in the oxide levels of melts that contained varying amounts when using the Premetz MC value. The discrepancy likely lies in the nature of the oxide films that are inside the material.

Riestra et al. [181] and others [182] attributed this to the floatation of most of the large oxides out of the metal, which leaves primarily the smaller oxide films inside the metal. It is the large oxides that interact most with the filter and impede the filtration curve, and hence, the MC value. Campbell and Dispinar [3], [75] have suggested very small films might simply pass through the filter due to their small size. Alternatively, when these oxides do contact the filter, they might simply wrap around onto the surface of the filter. The efficacy of Premetz therefore depends on the content of large oxide films in the metal at the time of

sampling, and not the small oxide films, which would explain the scattered results observed here.

It is known that large oxide films may 'bridge' and block pores of the filter [188], so perhaps the sensitivity of the test depends on the relative size of the Prefil filter pores and the oxide films, and their ability to bridge the pores.

9.2.2 PoDFA Analysis

PoDFA analysis did not show consistent differences in the content of the oxide films between the clean and dirty metals, despite the very large differences in the oxide contents that were observed with SEM micro-analysis. This shortfall has also been reported by some others [11], [173], but not extensively.

A likely explanation for the ineffectiveness of PoDFA analysis is that a majority of the films that were present in the Prefil sample were too small in size to be detect using visible light microscopy using the PoDFA protocol. This was due to:

- The very small size of the areas of the oxide film that are intersected by the analysis plane. As is illustrated in **Figure 9.2** a). These can be less than a few microns in width, and sometimes only a few microns in length as shown in the SEM micrographs in **Figure 7.10**, for example. And,
- The segregation and concentration of the oxide films to the interdendritic regions, where they have poor contrast with surrounding inclusions and secondary-phases (such as the β-Si plates and Fe-IMCs) when viewed with visible light as shown in **Figure 9.3**. The Al-7Si alloy solidifies with ~50% eutectic, which results in the formation of a large number of β-Si plates in the interdendritic regions, which make it particularly difficult

to detect the small oxides. In contrast, wrought alloys, for which PoDFA was developed [46], typically do not solidify with a large volume fraction of eutectic, and therefore make the detection of oxides in the interdendritic regions comparatively easier.

All the PoDFA analyses in this work were conducted at 100× magnification, and the technique itself is rarely performed at magnifications beyond 200×. As **Figure 9.3** shows, even at 200× magnification, the small oxides indicated with the red arrows may be easily overlooked amongst the masses of β-Si plates.

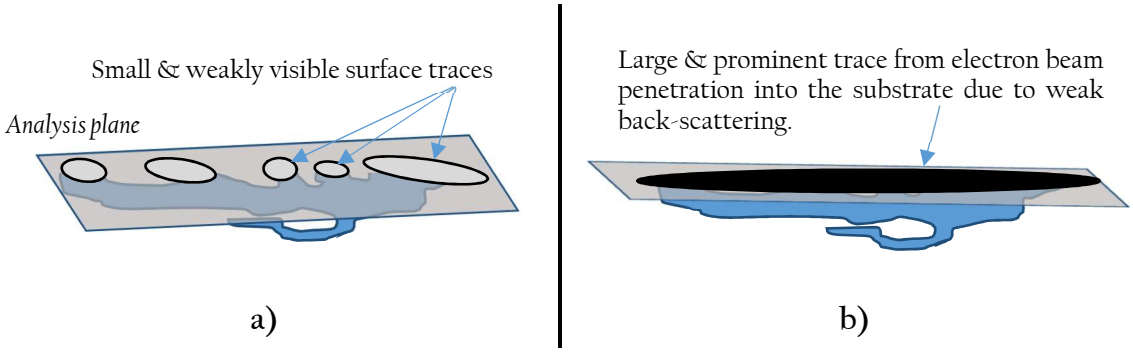

Figure 9.2 Comparison of how oxides are seen with a) visual light microscopy and b) Back Scattered Electron Imaging (BSEI) using an SEM. The latter allows for a larger trace of oxide to be seen with a higher contrast compared to its surroundings.

However, despite all that has been said, it should be emphasised that PoDFA analysis can reliably detect larger and coarser oxide films [75], [182], [186], which appear more prominent in the image (providing they are present and have not been floated out!), as indicated by the green arrows on **Figure 9.3**. It is interesting to note that in the results of these experiments (especially experiment DM) that there does not seem to be a correlation between the number of large oxides in the material, which are detected by PoDFA, and the number of small oxides that are detected by SEM.

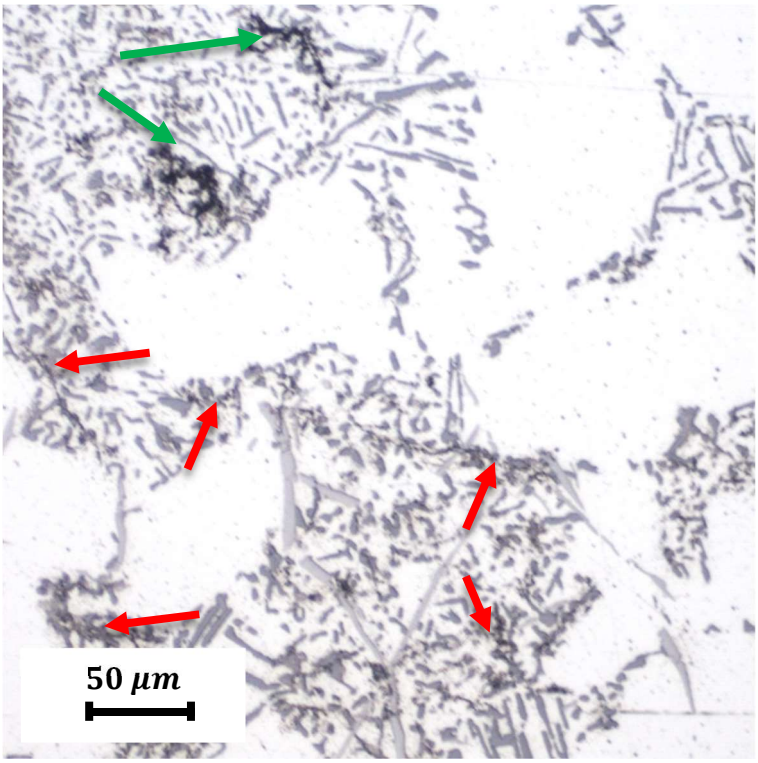

Figure 9.3 Visual light micrograph of the inclusion band of Prefil 3 from DM taken using a 200× lens. The green arrows are used to indicate oxides that are relatively easily seen compared to the relatively hard to see oxides indicated by the red arrows. These difficult to detect oxides are not typically counted during PoDFA for various reasons.

9.2.3 SEM Analysis

Had SEM not been conducted, and only the Premetz or PoDFA analysis results used to draw conclusions, very different conclusions would have been drawn from this work. For example, it would not be possible to explain the huge difference in the PND between clean and dirty metals based on the number of oxide films in the material, which would have otherwise been extremely confounding.

SEM microanalysis using BSE imaging proved to be one of the few effective techniques for characterising oxides captured in the Prefil residues. This was also reported by Yao et al.

[11] who, given the shortfalls of PoDFA analysis, used SEM to characterise small oxide bifilms.

The combination of backscattered electron (BSE) imaging and the high magnifications (500×) produced a strong contrast between the oxides and the other inclusions that were segregated to the interdendritic regions. It also allows for a greater portion of the oxide tin addition to just the points that intersect the surface to be imaged, due to penetration of the beam into the substrate as illustrated in **Figure 9.2** b).

However, the key limitation to these results presented here is that they are qualitative. The attempt that was made to quantify differences in the oxide film content in the BSE micrographs with DIA proved partially successful, and did manage to discern some differences, but requires further work. Another approach could be to perform a PoDFA style analysis on the SEM micrographs.

In conclusion, it is very likely that the combination of the propensity for large inclusions to float out of the melt, and the overlooking of small oxides by the typical PoDFA analysis that are responsible for confounding the results of previous published studies. It also raises some interesting questions about the current understanding of the effects of metal cleanliness, much of which has been built using PoDFA analysis – especially in casting alloys due to the effect that the eutectic has on obscuring oxide films from the analysis.

9.3 Oxide Film Morphology

The SEM microanalyses of the Prefil filters showed that there were oxide films with apparent non-folded, and bifilm-like morphologies, as illustrated in **Figure 9.4** a) and b). The oxide film 'pockets' that can be seen in some of the micrographs are probably bifilms too. As will be discussed in the forthcoming section, 9.4.19.3, these oxide films are probably responsible for nucleating bubbles. This however, raises a key question: *do bubbles nucleate from cracks on non-folded films or from bifilms, or from both?* Unfortunately, the experimental evidence is inconclusive on this, and this area requires further work.

Another key question, which is relevant to the results of experiment DM, was *are the endogenous oxides or exogenous oxides responsible for nucleating porosity*? Perhaps the exogenous oxides were thicker and contained deep crevices and cracks on their non-wetted sides which could nucleate bubbles in the classical fashion. Moreover, those oxide 'pockets that were observed **Figure 7.10**.

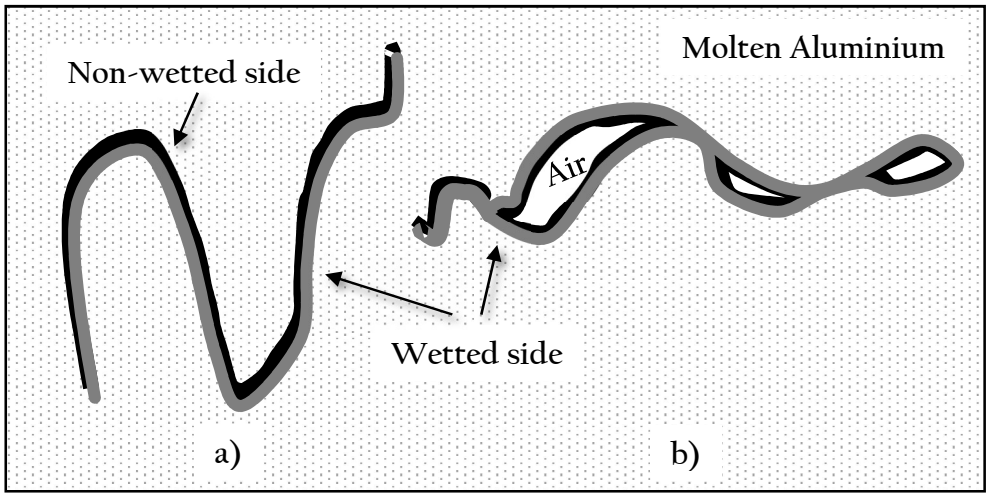

Figure 9.4 Illustrations of a) a non-folded oxide film, and b) an oxide bifilm.

9.4 Melt Quality & the Formation of Porosity during the RPT

The results summarised in **Table 7.7** give an indication of the respective roles of hydrogen and oxide films in porosity formation.

Hydrogen can be thought of as providing the 'fuel' for gas bubble formation, which provides the nucleation impetus, and feeds the expansion of the nucleated bubbles. On the other hand, oxide films act as nuclei for the bubbles, providing a means for the supersaturated hydrogen to come out of solution.

9.4.1 Pore Nucleation & the Influence of the RPT

A key result of this work was that the pore number density (PND), as measured by metallography and macro-CT was more or less constant in the RPT samples cast from the clean metals, but much higher in the samples cast from the dirty metals. This indicates that there were more instances of bubble nucleation in the dirty metal, which strongly implicates oxide films as bubble nuclei as the presence of an increased number of oxide films was the only major difference that as observed compared to the clean metal.

Interestingly, these results run counter to the results of others [96], [109]–[111], [189], who showed that increasing the hydrogen content also increased the PND in cast aluminium due to the trade-off between nucleation and growth of the hydrogen bubbles. The reason for this difference probably comes down to the fact that the RPT was used in this work and not in the others. The application of vacuum during the RPT might have had the effect of prematurely 'activating' pore nuclei early on during solidification – though this has not been well studied. In the ancillary experimental work presented in Appendix IV, bubbles were

observed to be floating from the melt early during solidification, which would support this notion.

This may occur by the 'unfurling' (opening up) of entrained bifilms in the liquid due to the expansion of their internal gas cavities [3], [77], [93], [190] (as shown in **Figure 2.9**), alternatively, the small crevices or pores [47] on the non-wetted surfaces of entrained oxide films might also contain a small amount of gas, and the application of the partial vacuum (reduced pressure) may cause this gas to blow up into a bubble. In both cases, the bubble nuclei can be considered to be 'activated' as they provide a ready embryo into which the hydrogen can diffuse as soon as supersaturation is reached. This therefore gives bubble nucleation a 'kick start' and the subsequent growth of the activated nuclei may dominate over further nucleation. In other words, bubble formation during the RPT is probably a growth process of the activated nuclei, and not a competition between nucleation and growth, as it normally would be.

9.4.2 The Effect of Hydrogen and Oxide Films on the Growth of Bubbles

The RPT samples cast from the clean melts developed a lower f_p compared to those samples cast from dirty metals with low hydrogen contents (less than very approximately ~0.3 ml $100g^{-1}$, in this work). At higher hydrogen contents (more than ~0.3 ml $100g^{-1}$, in this work), however, there was not a significant difference between the f_p, which seemed mainly to be dependent on hydrogen, and not so much on the melt cleanliness. This suggests that the oxide film content of the melt plays an increasingly important role in the formation of porosity as the hydrogen content decreases. A possible explanation for this relates to the total surface area of bubbles within the liquid. The mechanisms at play are very complex and have multi-factorial dependence.

The total surface area that the bubbles have with the liquid in a solidifying RPT sample is governed by the number of bubbles in the liquid, and the size of bubbles in the liquid. The ability for hydrogen in the liquid to reach a bubble is determined by the total surface area. If hydrogen is unable to reach a bubble surface, and come out of solution, it will remain frozen in the material.

At low hydrogen contents, hydrogen supersaturation occurs at higher solid fractions, meaning that and hydrogen comes out of solution later during solidification, and that pore growth is slower [26], [189]. In the dirty metals hydrogen needs only to diffuse a short distance to reach a bubble surface and come out of solution, because of the dense distribution of activated nuclei. Conversely, in the clean metal, hydrogen is required to diffuse larger distances to reach a bubble surface. Consequently an increased fraction of hydrogen is unable reach a bubble and is frozen into the metal, trapped in solid solution. In simple words, oxides create activated bubbles which assist in freeing supersaturated hydrogen from the liquid. This would explain the lower f_p formed in the clean metals compared to the dirty metals when the hydrogen content is low (very roughly ~0.3 ml $100g^{-1}$).

Increasing the hydrogen content increases the size of the pores (**Figure 7.19**), which in turn increases the surface area. The supersaturation is also reached earlier, meaning that hydrogen is able to come out of solution earlier, and growth is faster [26], [189]. This would mean that hydrogen is more easily able to reach a bubble surface to come out of solution – especially when bubbles are large. This would explain why the f_p developed in clean and dirty metals become closer with increasing hydrogen content. Eventually, there comes a point where the hydrogen is sufficient to nucleate pores early enough in the solidification process that the pores are able to grow to a sufficient size to have a sufficient surface area to

absorb most of the hydrogen even towards the last stages of solidification. It is at this point that parity in the f_p developed in clean and dirty metals is achieved, and in this work, using the given RPT conditions, this occurred at very approximately ~0.3 ml $100g^{-1}$.

9.5 Effects of Hydrogen & Oxide Films on the Structure of Pores

Here what has been discussed in the preceding section will be related to the resulting structure of porosity in the RPT samples.

9.5.1 Pore Number & Size

The RPT samples cast from the dirty melts developed a higher PND than those cast from the clean metals and was seemingly independent of the melt hydrogen content (**Figure 7.29** and **Figure 7.30**). Changing the PND had mixed effects though this had the effects on the average size of the pores in the samples.

At low hydrogen contents, a higher number of larger pores were formed in the dirty metal compared to in the clean metals (**Figure 7.24**), though the mean pore size was not greatly changed. This is because a larger amount of hydrogen is liberated into the pores in the dirty metal, compared to the clean metal for the reasons discussed in the preceding section. At higher hydrogen contents, above very roughly ~0.3 ml $100g^{-1}$, mean pore size in dirty metals decreases compared to the clean metals. This result is consistent with those that have been reported in microanalyses of porosity by others who have studied the effect of oxides on porosity [19]. The reason for this is straightforward – for a given volume of hydrogen, it can be distributed as a few large pores, or many small pores.

9.5.2 Pore Morphology

Quantitative measurement of the morphology of the pores was not so straightforward, as it was difficult to measure accurately. In 2D, with metallography, this was due to pore deformation; in 3D, with macro-CT, this was due to the low spatial resolution.

Hydrogen Content

Qualitatively, the macro-CT slices showed that the pores in the RPT samples took on an increasingly interdendritic shape as the initial melt hydrogen content decreased (**Figure 7.15**). This could probably because supersaturation of the melt is reached at increasingly higher solid fractions, which in turn means that gas bubbles are restricted to expand within the interdendritic mesh of solid during their slow growth. Whereas at high initial melt hydrogen content, the supersaturation is reached at lower solid fractions, and also bubbles grow faster, which means that bubbles able to reach an adequate size and internal pressure to compel the surrounding solid or liquid to take on their shape [62].

Oxide Film Content

When the number density of activated pore nuclei is high, hydrogen may more readily be able to reach the bubbles and expand them into a more spherical shape during the earlier stages of solidification due to their higher density in the melt, and the shorter distances between them. This would explain the increased number of pores with gas like morphologies in the dirty metal at low hydrogen content (Pair 1 in **Figure 7.21** and **Figure 7.22**). In the later stages of solidification, the pores are restricted to expand in the interdendritic regions.

From Pairs 2 and 3 in **Figure 7.21** and **Figure 7.22**, it can be seen that at higher hydrogen contents, the RPT samples cast from the dirty metals developed a higher number of

low-sphericity (shape factor pores) pores – both shrinkage pores and gas pores. Riestra et al. [181] observed similar shaped pores in their RPT samples cast from a high-oxide film melt of remelted scrap, and they attributed this to the incomplete unfurling of bifilms during the test. Perhaps the crumpled oxide films could expand in some places, but largely remain folded in other places, which would create gas pores with numerous shrinkage 'tendrils'. A complimentary effect could be that oxide films may physically block the interdendritic channels and inhibit metal feeding during solidification, which would in turn exacerbate the effects of shrinkage and result in increasing the interdendritic porosity. Oxide films have been reported to cause the blockage of feeders [3], [181], so it is plausible that they might also do this to the narrow interdendritic channels of a solidifying casting. This might especially be the case for the samples taken from DM because unlike the RD sample, it probably contains numerous larger oxides that would be very effective at bridging interdendritic channels.

9.6 Melt Quality & the Formation of Porosity under Atmospheric Pressure

The key result from the micro-CT was that the dirty metals consistently developed more interconnected, interdendritic porosity than the clean metals, although there was a great scatter in the results. This might be explained by segregation of the oxides to the interdendritic regions during solidification – as was observed during SEM microanalysis of the Prefil samples.

Modelling by Atwood and Lee [189] has shown that critical melt supersaturation must occur for a bubble to nucleate on bubble nuclei - thus activating them for further growth.

This a fundamental difference to the solidification in the RPT the application of reduced pressure expands and activates the nuclei at the start of solidification. Gas porosity is therefore expected to form later during solidification, and consequently, when the oxides are more concentrated in the interdendritic regions of the casting.

The SEM micrographs of the Prefil samples show that the oxides were segregated to the interdendritic regions of the casting. This would be occurring in the APT samples during solidification too - although the oxide films would be 10,000× [87], [186] far less concentrated than in the Prefil samples. To give a very rough indication of what the oxide film concentration might be like: the Al-7Si alloys used here begin eutectic solidification at approximately 50% solid fraction, which means that concentration of inclusions in the interdendritic region is doubled at this point.

The segregated films may have two simultaneous effects; firstly these films may nucleate individual gas bubbles, which proceed to grow and expand in size. Adjacent bubbles may then coalesce together form a single, continuous bubble chain within the interdendritic channels of the solidifying materials. The second, and synergistic effect of oxide films is that they may block off liquid feeding, which can exacerbate the effects of shrinkage.

Finally, the micro-CT analyses were mainly conducted on samples with a relatively high hydrogen level >0.3 ml 100 g^{-1}. Had samples with a lower hydrogen content, pores in the clean metal may have been increasingly interdendritic in shape and the conclusions to this work would be very different.

9.7 Pore Formation in the Dross Layer

RPT samples cast during DM formed a layer of pores at their top surface (**Figure 7.25**) which was attributed to the expansion of oxides in the dross layer. The stirring would have inevitably introduced air bubbles and bifilms into this layer, where they would be trapped in the labyrinth of oxide films and molten metal that composes this layer. When picked up on the surface of RPT samples, and subjected to reduced pressure, it is likely that these air bubbles and bifilms would then expand into pores. This demonstrates, that should a bifilm, or a 'sandwich' of dross become entrained into the melt and stay there (after all, entrained air was the reason that the dross had the propensity to float) it can expand into a pore. This would not only be possible due to the negative pressure of the RPT, but could also be facilitated by the shrinkage that occurs during freezing [3].

Riestra et al. [181] reported similar results, but came to a different conclusion about its effect. As shown in **Figure 9.5**, they suggested that gas pores nucleated from bifilms or other nuclei would simply float to the surface of the melt when vacuum is applied. This might be partially the case here, as the stirring prior to sampling may have entrained some air bubbles and oxide films / bifilms which would have quickly expanded when vacuum was applied and floated to the surface, and become entrapped in the dross layer. However, a large fraction of oxide films would still remain inside the body of the RPT sample, as cropping of the dross layer from the macro-CT volume still showed a much higher PND than the clean metals (**Figure 7.27**).

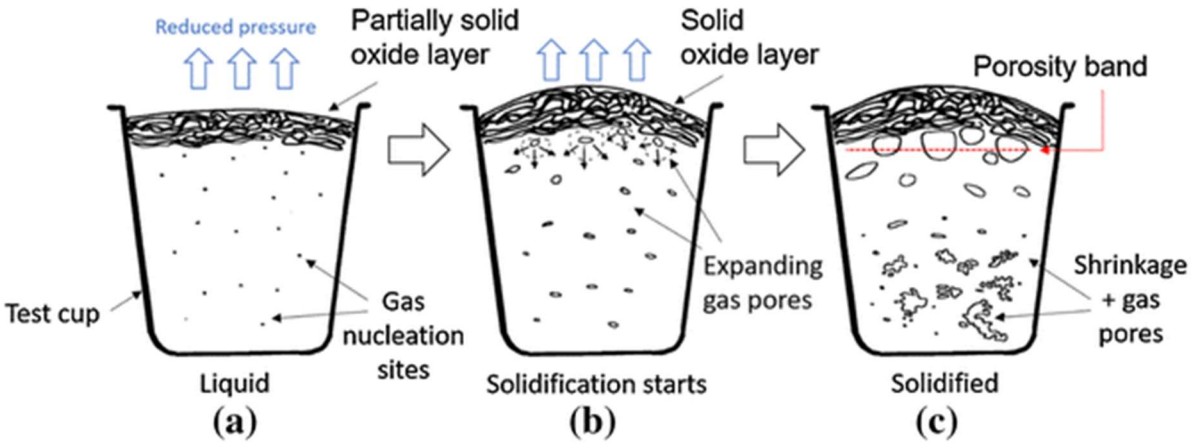

Figure 9.5 Proposed mechanism by Riestra et al. [181] for the creation of the dross layer at the surface of the RPT samples. Nucleation sites in the melt a) expand into pores with the application of vacuum b) which then proceed to float up under the dross layer. From Riestra et al. [181].

9.8 Determination of Melt Quality Using the RPT

Based on the discussion above, the interpretation of the RPT melt quality results can be discussed in a new light.

9.8.1 Density Measurements

Current wisdom holds that the f_p (commonly roughly measured by the Density Index, *DI*) developed in the RPT sample represents a measure of the overall melt quality. The results here confirm this, and illustrated that the oxide film content of a melt played a crucial role in governing the f_p that was formed. This was at least the case below a critical hydrogen threshold of approximately 0.3 ml $100g^{-1}$. Above this threshold it was not possible to discern differences in the in f_p between the clean and dirty samples as the hydrogen was able to come completely out of solution in both cases.

The sensitivity of the test to oxide films would likely vary heavily with cooling rate (and provided solidification may fully complete), and higher cooling rates the sensitivity to melt

cleanliness would be increased due to the decreased time for pore growth, which would leave more hydrogen trapped in solution unless bubbles were able to form on potent nuclei [62], [96].

9.8.2 Bifilm Index

As has been described in Section 2.6.4, the Bifilm Index (BI) is used to measure the total length of bifilms inside an RPT sample.

The results **Figure 7.35** showed that that BI is indicative of the f_p or the hydrogen content in RPT samples rather than the length of bifilms. It is often taken that higher BI means that there are more pore nuclei in the sample, however here there was no discernible difference between the clean and dirty materials. This therefore limited the usefulness of the BI in this study.

Contrary to the results here, Dispinar and Campbell [7] demonstrated that there should be a direct correlation between the BI and the number of pores. The reason for this discrepancy is unclear, but it may relate to differences in the efficacy of each approach in detecting pores.

9.8.3 Melt Quality Determination by the Analysis of Pore Structure

The results have indicated that the oxide film content could be determined by measuring the PND of the RPT samples, with the PND increasing with the number of oxide films in the material.

Using the current metallographic assessment method, the PND of pores with d_{eq}>0.5mm serves as a reasonable indicator, especially the volumetric Saltikov PND. However, the major limitation is that as the hydrogen content decreases, the reliability of the technique decreases too. Below a threshold hydrogen level of ~0.3 ml $100g^{-1}$, the accuracy of this approach was lost due to the decreasing number of gas pores with d_{eq}>0.5mm. Unfortunately it was not possible to lower this size threshold as it was found to be too heavily influenced by shrinkage pores, which drowned out the PND measurement. Hence, this was only a good indicator for RPT samples with higher hydrogen contents.

Macro-CT analysis of the volumetric PND of RPT samples was found to be a good indicator of the oxide film content of the melts. However, it is extremely impractical and time consuming, and is therefore not suited for practical melt quality determination; and SEM and BSE imaging of Prefil samples would be more straightforward from a practical perspective.

Chapter 10

Effect of Grain Refiner on Porosity Formation

The effect of TiB_2 grain refiner on porosity formation will be discussed in this chapter based on the results of the Grain Refiner Addition experiments in Chapter 8.

10.1 Effect of Grain Refiner Addition on Grain Structure

The addition of Al-3Ti-1B or Al-5Ti-1B into the Al-7Si alloy resulted in a significant reduction in the cast grain size. Interestingly, even after settling, when most of the TiB_2 particles were settled out of the melt, there was still significant refinement of the grain structure.

Two hours of settling would probably be sufficient for most of the TiB_2 particles to settled out of the material, except for the smallest of them due to their slow settling rate [99], [166] and any possible convection in the melt. However, these small TiB_2 particles might be less likely to nucleate grains, because, according to Greer's free growth model [191], particles must be at least a critical size to develop a solid nucleus cap that is sufficiently large to be energetically favourable. In addition to this, the potency of TiB_2 particles may be further deteriorated by the presence of the high silicon content. TiB_2 particles are well known to be poisoned by the silicon solute when it is present in the melt in concentrations >2wt.% [192]–[194]. Qiu et al. [194] have shown that a probable mechanism for is that the Al_3Ti layers that are formed on the surface of TiB_2 particles are themselves coated with a Ti_5Si_3 shell during poisoning, which deactivates the Al_3Ti layer as a nucleant substrate for α-Al [195]. This

therefore leaves fewer active TiB_2 particles in the melt. Therefore after settling very few active nucleants would be expected in the melt.

This may indicate that the growth restricting effect of the additional titanium solute may be primary mechanism that is responsible for the refinement of grains, at least in the settled metal. Titanium has been reported to give a high growth restricting effect, at least in pure aluminium [196], and work by Schmidt-Fetzer et al. [197] has suggested that this is also the case for Al-Si-Ti alloys. However, it should be noted that the growth restriction factor (Q) is difficult to determine in high solute multicomponent systems, and therefore would require further investigation before hard conclusions can be drawn. Tracking of the melts' titanium contents (**Figure 8.3**) revealed that the titanium content was relatively high even when the melt was settled, which would support the notion that growth restriction [198] is responsible for the grain refinement that is seen in the settled metal. It would also play a critical role in the grain refiner added and restirred melt conditions, but active TiB_2 particles would also very likely be at work.

10.2 Origins of Endogenous Borides & their Effect on Porosity

10.2.1 Origin

Endogenous borides were one of the most prolific inclusions in the melts throughout this project. Their presence was first noted from the Prefil filtration curves, in melts where the presence of fine particulate was not expected. This prompted an SEM analyses, which initially showed that they were Ti and V rich particles (**Figure 8.6**) – suggesting that they were likely borides, which was confirmed by the subsequent high resolution SEM analysis (**Figure 8.7**).

Titanium and vanadium are common elemental impurities that found are smelter-aluminium, introduced from the petroleum coke and the bauxite raw materials used in the Hall-Heroult process [199]. They are subsequently removed from the metal in the casthouse when their control is necessary (such as when producing electrical-grade aluminium) by boron treatment, where Al-B master alloys are added into the metal to precipitate *in-situ*, and sediment out the borides of titanium, vanadium, and other transition metals (TiB_2, VB_2, etc.) [98], [200]. In the case of vanadium, one possible reaction by which this can occur is [201]:

$$V + 2B = VB_2 \tag{10.1}$$

Because the base metals, when melted in a separate, well coated crucible, did not contain fine particulates (**Figure 8.4**), it can be deduced that the endogenous borides in this work precipitate *in-situ* during the experiments. The only possible source of boron to the metal is by its leaching from the crucible and/or its glazing during melt holding. This is a seemingly infinite source as it continually supplied melts with enough boron to precipitate borides in successive experiments using the same crucible.

The addition of excess titanium into the melt in the Al-Ti-B master alloys may have enabled the precipitation of more of these borides, especially during the long holding duration allowed for settling. These borides were likely constantly precipitating and settling out of the metal during this time. This would explain, at least in part, the trace boride content found in the settled Prefil sample, and the higher boride content in the restirred Prefil sample than that measured in the freshly grain refined material.

10.2.2 Effect on Porosity

In the GR2 Prefil samples, settling saw a 35-fold decrease in the MC value of the melt relative to the *Baseline* condition, and PoDFA analysis indicated that the boride content in the melt decreased by 400% (though it should be remembered that PoDFA gives only an estimate). However, despite this, there was little change in the porosity between the RPT samples. For example the fraction of porosity (f_p) decreased only 8.5% in the *Settled* metal compared to the *Baseline* metal, while the PND of gas pores (d_{eq}>0.8mm) measured by macro-CT only decreased by 4%. This demonstrates 2 key points:

1. Endogenous borides do not cause a marked increase in f_p, as grain refiner addition does (although the concentration of these particles is much less than that of the grain refiner).
2. If it is assumed that the PND indicates the number of bubble nuclei in the melt, then the number of pores should be indicative of the number of endogenous borides that are present in the melt. However, this is not the case.

The small variations in the f_p and PND probably arise due to reduction in the number of suspended oxides (and potentially other pore forming inclusions) in the settled metal, and

not because of a change in the endogenous boride content. Overall, it can be concluded that the endogenous borides probably have little or no effect on the formation of gas porosity, at least in the concentrations that they are present in this work.

It is difficult to say what their effect on the micro-porosity in the micro-CT samples is because the micro-CT results are often subject to significant variability.

10.3 The Role of TiB_2 on Gas Porosity Formation

The results show that the addition of Al-(3,5)Ti-1B grain refiner increases the propensity for Al-7Si to form gas pores during solidification. This was found to be the case for RPT and APT samples. These results agree with those of Tynelius [109] and Anyalebechi [62], who respectively observed increases in the fraction, number density, and size of pores when grain refiner was added.

Anyalebechi [62] postulated that increases in porosity might arise from increases in the melt's hydrogen solubility due to the increased titanium content. However, the titanium content in the settled metal is significantly higher in the settled condition than the baseline condition, but the porosity that is formed in the samples is almost the same. It is therefore not possible that increased titanium can explain the increased gas porosity developed in the *Grain Refined* and *Settled* melt conditions.

It can therefore be concluded that the TiB_2 particles themselves, or something associated with them, is responsible for influencing the formation of gas pores, because:

1. A refined grain structure is formed in the samples cast from the melt in the settled condition, indicating refinement in the near absence of TiB_2 particles.
2. There is an increased overall f_p, PND, and sphericity of gas pores when grain refiner is suspended in the melt (the *Grain Refined* and *Restirred* samples) compared to the baseline condition. If it is assumed that the PND is indicative of the number of nuclei in the melt, this directly indicates that there are increased instances of bubble nucleation.

These changes are seen in both GR1 and GR2. Perhaps the grain structure may also have some influence, but the data here, at least for solidification during the RPT, show that it is weak.

10.3.1 A Possible Mechanism

It has been suggested that TiB_2 particles themselves [109] or some associated oxide with them [62] might act as pore nuclei, though this has not been studied.

During solidification only ~1-2% of the added TiB_2 particles are thought nucleate α-Al, while the remainder remain inactive and are not enveloped by the solid due to their lower potency, and in turn are pushed to the grain boundaries during solidification [198]. It would be these inactive TiB_2 particles, or particle clusters, could go on to nucleate bubbles, as they behave essentially as free inclusions in the melt.

The potency of a TiB_2 particle is complex, and is known to depend on numerous factors. Perhaps the most important factor is the presence of an Al_3Ti layer on its surface, which is believed to be the active substrate for nucleating α-Al [195]. However, as mentioned in the preceding section, silicon solute can poison this layer. This Al_3Ti layer, and the Ti_5Si_3 shell that is formed during poisoning would be expected to be well-wetted as it formed from the melt, and therefore are probably not the responsible substrates for bubble nucleation.

The Al_3Ti aluminide layer also acts as an adhesive to hold together agglomerates of TiB_2 particles into a cluster [195], [202]. Clustering reduces the number of effective nuclei and allows them to sink faster than other particles (which leads to a phenomenon referred to as fading) [193]. It can therefore be expected that these clusters would be absent from the samples taken from the melt in the settled state. These TiB_2 clusters might also entrap other

inclusions, such as residual salts [203], or oxides. SEM micro-analysis (**Figure 8.8**) of the Al-5Ti-1B rod showed clustering of the particles, and further EDX analysis showed that there was a weak oxygen trace associated with the TiB_2 clusters, which could possibly suggest the association of oxide films with these clusters. The associated oxides could be fragments of oxide stringers the cluster has picked up during the manufacturing of the master alloy. Alternatively, poorly wetted crevices in the particle clusters themselves may act as nucleation sites for pores, or perhaps the intra-TiB_2 cracks might act as crevices from which bubbles may nucleate. The observation of cracked boride particles in the *Grain Refined* Prefil sample (**Figure 8.7** b)) would indicate that cracked particles remain intact when added into the melt. Further work is needed in these areas to substantiate these speculations.

Whatever the mechanism that is at play, it seems to be a very potent pore nucleation mechanism, given the significant increase in the number of gas pores. The increase in the overall f_p in both the RPT and APT samples suggests that more hydrogen is able to come out of solution and form pores. This coupled with the increased sphericity of the gas pores, measured by macro-CT in the RPT samples may indicate that pores are forming earlier during solidification, as gas pores that form earlier during solidification will better preserve their spherical shape. It is important to again emphasise that macro-CT smooths out the edges of pores, so the effects of any fine contours at the edges of pores will not be resolvable, and therefore gives only an estimation of the 'macro-morphology' of pores.

It is worth noting that there does not seem to be much of a difference in the porosity of the freshly grain refined (*Gran Refined)* and *Restirred* material in GR2, and the small variation in the data may be a result of slight changes in the hydrogen content of the melt over the experiment. It is not possible to determine any change from GR1 either, again due to the

change in the hydrogen content over the experiment. It might be that there normally would be a difference in the porosity that is formed in the RPT samples cast from freshly grain refined and restirred metal after settling of the grain refiner, due to the agglomeration of the TiB_2 into clusters at the bottom of the melt. Perhaps the reason that this is not seen in this work is because of the very high concentration of TiB_2 that was used (at least in GR2), which 'drowns out' any of the subtle changes in porosity that might be occurring.

Micro-CT analysis showed that the f_p in the micro-CT samples decreased and pores became less interconnected when grain refiner was present. This indicates that grain refiner reduced the shrinkage porosity, which occurs at the sample centres. This is probably because of better liquid feeding while the material is in the semi-solid state, which reduces shrinkage [204], whilst there are simultaneously more gas pores forming throughout the entire sample, due to increased bubble nucleation.

Part V
Conclusions

Chapter 11

Conclusions & Future Work

11.1 Conclusions

Three main areas of work were conducted; the first being the development of metallographic and macro-CT image analysis routes for the quantitative characterisation of the structure of porosity in RPT samples. The second and third areas of work were experimental, and investigated the role of hydrogen and oxide films, and TiB_2 grain refiner additions in the melt, respectively, on the formation of gas porosity. The effects of each of these factors on the resulting gas porosity are summarised in **Table 11.1**.

Table 11.1 Summary of the effects of melt hydrogen, oxide films, and TiB_2 grain refiner on gas porosity.

	Vol. Frac. Porosity (f_p) (%)	Areal & Volumetric Pore No. Density (PND) (pores cm$^{-2,3}$)	Eq. Circ. & Spher. Diam. (d_{eq}) (mm)	Circ. & Spher. (Shape Factor)
Hydrogen	↑↑	-	↑	↑
Oxide Films	↑	↑↑	↓	↓
Grain Refiner	↑↑	↑↑	↑	↑

The key conclusions from each area of work can be summarised as follows:

Characterisation Methods: Metallography & Macro-CT

- Metallographic and XCT analysis can both be used to measure changes in gas porosity in cross-sections or entire volumes of RPT samples with a range of porosity fractions (f_p), though the measurements for both techniques are most accurate when the pores are large in size.
- Although straightforward and widely accessible, metallographic measurements can be highly unreliable when shrinkage pores are present as their numerosity on the plane of analysis can skew and 'drown out' meaningful measurements of gas pores – particularly when the gas pores are small in size. Metallographic measurements of gas pores should therefore only include pores that are larger than the typical size of shrinkage pores (d_{eq}>0.5 mm is a good estimate for the RPT). Also, the shape of gas pores may be physically distorted during metallographic preparation.
- 'Macro-CT' can map and analyse the porosity in RPT samples using a relatively large nominal voxel size of ~44 µm. The accuracy of the technique is limited by the voxel size, which can lead to misleading measurements of small pores and small pore features.

The Effect of Melt Quality on Porosity Formation

- Premetz and PoDFA analysis are unable to reliably give an indication of the total oxide film content of a melt, as they are insensitive to small films, and only detect the large oxide films in the melt. SEM microanalysis with Back-Scattered Electron (BSE) imaging is better capable of resolving the oxide films that these techniques overlook. There is a need to develop a reproducible method for quantifying oxide films using SEM.

- The application of vacuum during the RPT probably 'activates' bubble nuclei, which the process of pore formation into a process that is governed more by bubble growth, rather than a competition between nucleation and growth.
- Hydrogen provides the impetus for gas porosity formation, and the fuel for the expansion of the nucleated bubbles. Oxide films act as nuclei for bubbles, and provide a means for the supersaturated hydrogen to come out of solution during solidification. The higher the oxide film content of a melt, the greater the fraction of hydrogen that may be released from solution. However, increasing the oxide content increases the amount of interdendritic shrinkage porosity that is formed.
- The fraction of porosity (f_p) in RPT samples serves as a good measure of the overall melt quality (a combination of the hydrogen and oxide film content). The pore number density (PND) can give a good indication of the oxide film content – however this can be difficult to accurately determine by metallography when the hydrogen content is low. The hydrogen content by itself can be difficult to determine.
- Under atmospheric conditions, the oxide films are concentrated to the interdendritic regions of the semi-solid casting, which increases the amount of porosity formed in these regions and the resultant porosity is more interdendritic in shape. This might be because the gas bubbles that are nucleated from oxide films combine together to form extensive interdendritic bubbles; and/or because of increased shrinkage, due to blockage of the interdendritic liquid-feeding channels by the oxide films.

The Effect of TiB_2 on Porosity Formation

- Al-7Si alloys were grain refined by the addition of Al-Ti-1B master alloy rod. Settling for 2 hours sedimented nearly all TiB_2 from the material, however the cast samples were still

observed to retain a refined grain structure. This was attributed to growth restriction effects of the free titanium that was added into the melt from the Al-Ti-B master alloy.

- The presence of TiB_2 grain refiner particles in the melt increases the f_p and the PND in RPT samples. This is not due to the effects of changes in the grain structure, but because of bubble nucleation on the particles themselves. TiB_2 particle clusters might be the type of particle that is responsible for this.
- The presence of TiB_2 grain refiner decreases the shrinkage porosity that is formed in the RPT sample. This is not due to grain refinement, but due to the enhanced nucleation of gas bubbles by the TiB_2 particles.
- Endogenous $(Ti,V)B_2$ boride particles, in the concentrations that they were present in these experiments, do not cause appreciable refinement of the grain structure of Al-7Si, nor do they seem to influence the porosity that is formed.

11.2 Recommendations of Future Work

This thesis has seemingly asked more questions than it has solved, thus leaving a great scope of potential future work. Some key recommendations for future work in each area of work are suggested here.

11.2.1 Method Development & Porosity Characterisation

There is room for further work in developing the metallographic and XCT methods. In regards to the metallographic route suggestions improvements would be:

- Develop an approach for analysing the spatial distribution of pores, and interpore distances, especially using the macro-CT analysis method. This may provide further insight into any potential competition between nucleation and growth, and also help in

verifying whether the solidification under RPT conditions is growth dominated. Once a method has been developed, this could be extended to investigate nucleation and growth of pores in samples solidified under normal (non-RPT) pressure.

A potential improvement for XCT studies of RPT samples would be to conduct the studies on miniaturised RPT samples. Smaller samples would allow for improved spatial resolutions using XCT devices. These XCT analyses could also focus exclusively on gas pores, by discriminating them from shrinkage pores by the placement markers for the MBWT.

11.2.2 Melt Quality Experiments

One of the key questions that was raised in this area of work was: *are bubbles nucleated from unfolded oxide films or bifilms*?

A good starting point for future research would be to identify how the films primarily exist inside the material – as unfolded films or bifilms – which could involve conducting the work using an alloy that contains a low content of magnesium, ideally an Al-7Si-Mg alloy (such as A356). The magnesium content of the alloy should be sufficient to permit the formation of $MgAl_2O_4$ spinel. Work by Guo [164] has suggested that 0.2wt.% magnesium will permit its formation from pure aluminium; moreover, it is also commonly formed from A356 [187]. $MgAl_2O_4$ spinel forms on the wetted-sides of Al_2O_3 oxide films, which might allow it to 'mark'; the wetted sides of the oxide films, and therefore give insight into how the oxides are folded.

This could be put into action two ways. The first option would be to use a melt of an Al-7Si-Mg melt, and use a shearing device (such as a rotary degasser) to generate and entrain

endogenous oxide films into the melt. A second approach would be to add machine chips of an Al-7Si-Mg into an Al-7Si melt – this could be assisted by the use of a melt shearing device (though this would break down large exogenous oxides). Prefil samples could then be taken and the oxide films examined metallographically with SEM. The oxide films may also be extracted from the metal using the practice described here [205] and then examined with SEM in order to further examine the wetted and non-wetted sides of the films.

A completely different area of future work that is worthy of mention is that concerning the development of a technique to for the quantification of the oxide film content in metal. The most straightforward suggestion would be do adopt a PoDFA-style counting protocol during SEM micro-analysis. An alternative approach would be to develop a method using digital image analysis to automatically count the number of oxides.

11.2.3 Grain Refiner Experiments

One of the key questions that was raised in this area work was: *what type of inclusion Al-Ti-B in grain refiner is responsible for nucleating porosity in cast aluminium*?

The first step in this work could be to further investigate what type of particles are present in the master alloy. This could be done by settling. Grain refiner rod could be added to a melt in a tall crucible, which could then be held for a calculated period of time to create an 'inclusion gradient' over the height of the metal. The largest inclusions, the TiB_2 clusters, settle fastest [99] and would be expected to be found at the bottom of the crucible. Examination of the bottom region would allow it to be determined whether TiB_2 clusters are actually present.

If TiB_2 clusters are present, the settling approach could be used to make a concentrate that could be added back into a melt to see if a higher fraction of porosity is observed in the sample. Conversely, a TiB_2 cluster-free concentrate could be made and added into the material, and its effect on the porosity observed. In addition, the TiB_2 clusters should be examined at high resolution in order to determine whether there are any oxide films associated with them.

The experiments here could also be repeated, but with lower additions of the Al-Ti-B master alloy, in order to investigate what effect, if any, that settling and restirring has on the porosity formed in the casting.

Finally, high-resolution (<1µm voxel size) XCT studies could be conducted on small specimens cut from APT samples to determine any association between boride particles and gas pores. This probably could not be performed on RPT samples, due to the large pore size, and the clusters (if they do act as nuclei), would probably be ripped apart by the expansion of the bubble. However, by examining pores in samples solidified under atmospheric pressure in this way, it might be possible to implicate boride clusters with pores and determine their role (if any) in pore formation.

Reference List

[1] J. Malisano, S. Kumar, C. Lui, and K. O'Reilly, "X-Ray Computed Tomography versus Metallography for Porosity Analysis in Aluminium RPT Castings," in *Proceedings of the 6th Decennial International Conferences on Solidification Processing*, 2017.

[2] P. C. Varley, *The technology of aluminium and its alloys*. CRC Press, 1970.

[3] J. Campbell, *Complete casting handbook: metal casting processes, metallurgy, techniques and design*. Butterworth-Heinemann, 2015.

[4] P. Le Brun, "Melt Treatment — Evolution and Perspectives," in *Light Metals 2016*, J. F. Grandfield and D. G. Eskin, Eds. Cham: Springer International Publishing, 2016, pp. 59–64.

[5] P. Waite, "A Technical Perspective on Molten Aluminum Processing," in *Essential Readings in Light Metals 2016*, Springer, 2002, pp. 51–58.

[6] J. Campbell, "Entrainment defects," *Mater. Sci. Technol.*, vol. 22, no. 2, pp. 127–145, Feb. 2006.

[7] D. Dispinar and J. Campbell, "Porosity, hydrogen and bifilm content in Al alloy castings," *Mater. Sci. Eng. A*, vol. 528, no. 10–11, pp. 3860–3865, Apr. 2011.

[8] M. Tiryakioğlu, P. Yousefian, and P. D. Eason, "Quantification of Entrainment Damage in A356 Aluminum Alloy Castings," *Metall. Mater. Trans. A*, 2018.

[9] S. Akhtar, D. Dispinar, L. Arnberg, and M. Di Sabatino, "Effect of hydrogen content, melt cleanliness and solidification conditions on tensile properties of A356 alloy," *Int. J. Cast Met. Res.*, vol. 22, no. 1–4, pp. 22–25, Aug. 2009.

[10] E. Bergsmark, C. J. J. Simensen, and P. Kofstad, "The oxidation of molten aluminum," *Mater. Sci. Eng. A*, vol. 120–121, pp. 91–95, Nov. 1989.

[11] L. Yao, S. Cockcroft, C. Reilly, and J. Zhu, "Factors Affecting the Nucleation Kinetics of Microporosity Formation in Aluminum Alloy A356," *Metall. Mater. Trans. A*, vol. 43, no. 3, pp. 1004–1016, 2012.

[12] R. N. Lumley, R. G. O'Donnell, D. R. Gunasegaram, and M. Givord, "Heat Treatment of High-Pressure Die Castings," *Metall. Mater. Trans. A*, vol. 38, no. 10, pp. 2564–2574, 2007.

[13] Q. G. Wang, D. Apelian, and D. A. Lados, "Fatigue behavior of A356-T6 aluminum cast alloys. Part I. Effect of casting defects," *J. Light Met.*, vol. 1, no. 1, pp. 73–84, Feb. 2001.

[14] Y. Murakami and M. Endo, "Effects of defects, inclusions and inhomogeneities on fatigue strength," *Int. J. Fatigue*, vol. 16, no. 3, pp. 163–182, Apr. 1994.

[15] G. Nicoletto, G. Anzelotti, and R. Konečná, "X-ray computed tomography vs. metallography for pore sizing and fatigue of cast Al-alloys," *Procedia Eng.*, vol. 2, no. 1, pp. 547–554, 2010.

[16] T. Pabel, G. F. Geier, D. Habe, J. Rosc, P. Schumacher, T. Petkov, and M. & M. S. (TMS) The Minerals, "Correlation of Porosity Detected by Computed Tomography and Fatigue Strength of Aluminium Alloys," in *Supplemental Proceedings*, John Wiley & Sons, Inc., 2011, pp. 803–805.

[17] M. E. Schlesinger, *Aluminum recycling*. CRC Press, 2013.

[18] E. M. Williams, R. W. McCarthy, S. A. Levy, and G. K. Sigworth, "Removal of Alkali Metals from Aluminum BT - Essential Readings in Light Metals: Volume 3 Cast Shop for Aluminum Production," J. F. Grandfield and D. G. Eskin, Eds. Cham: Springer International Publishing, 2016, pp. 71–79.

[19] T. Ludwig, M. Di Sabatino, L. Arnberg, and D. Dispinar, "Influence of oxide additions on the porosity development and mechanical properties of A356 aluminium alloy castings," *Int. J. Met.*, vol. 6, no. 2, pp. 41–50, 2012.

[20] J. P. Anson and J. E. Gruzleski, "The Quantitative Discrimination between Shrinkage and Gas Microporosity in Cast Aluminum Alloys Using Spatial Data Analysis," *Mater. Charact.*, vol. 43, no. 5, pp. 319–335, 1999.

[21] D. E. J. Talbot, *The effects of hydrogen in aluminium and its alloys*, vol. 724. Maney Pub, 2004.

[22] D. E. J. Talbot, "Effects of hydrogen in aluminium, magnesium, copper, and their alloys," *Int. Metall. Rev.*, vol. 20, no. 1, pp. 166–184, 1975.

[23] C. Gu, Y. Wei, F. Yu, X. Liu, and L. She, "Cellular Automaton Study of Hydrogen Porosity Evolution Coupled with Dendrite Growth During Solidification in the Molten Pool of Al-Cu Alloys," *Metall. Mater. Trans. A*, vol. 48, no. 9, pp. 4314–4323, 2017.

[24] M. Felberbaum, "Porosity in Aluminum Alloys: Visualization, Characterization, and Modeling," ÉCOLE POLYTECHNIQUE FÉDÉRALE DE LAUSANNE, 2010.

[25] P. N. Anyalebechi, "Analysis of the effects of alloying elements on hydrogen solubility in liquid aluminum alloys," *Scr. Metall. Mater.*, vol. 33, no. 8, pp. 1209–1216, Oct. 1995.

[26] R. C. C. Atwood, S. Sridhar, W. Zhang, and P. D. D. Lee, "Diffusion-controlled growth of hydrogen pores in aluminium–silicon castings: in situ observation and modelling," *Acta Mater.*, vol. 48, no. 2, pp. 405–417, Jan. 2000.

[27] T. S. Piwonka and M. C. Flemings, "Pore formation in solidification," *Aime Met Soc Trans*, vol. 236, no. 8, pp. 1157–1165, 1966.

[28] G. Couturier and M. Rappaz, "Effect of volatile elements on porosity formation in solidifying alloys," *Model. Simul. Mater. Sci. Eng.*, vol. 14, no. 2, p. 253, 2006.

[29] Y. Liu, W. Jie, Z. Gao, and Y. Zheng, "Investigation on the formation of microporosity in aluminum alloys," *J. Alloys Compd.*, vol. 629, pp. 221–229, Apr. 2015.

[30] C. E. Ransley, "The solubility of hydrogen in liquid and solid aluminium," *J. Inst. Met.*, vol. 74, pp. 599–620, 1948.

[31] R. Y. Lin and M. Hoch, "The solubility of hydrogen in molten aluminum alloys," *Metall. Trans. A*, vol. 20, no. 9, pp. 1785–1791, 1989.

[32] P. N. Anyalebechi, D. E. J. Talbot, and D. A. Granger, "The solubility of hydrogen in liquid binary Al-Li alloys," *Metall. Trans. B*, vol. 19, no. 2, pp. 227–232, 1988.

[33] G. K. Sigworth, "Gas Fluxing of Molten Aluminum. Part 1: Hydrogen Removal," *Essent. Readings Light Met. Cast Shop Alum. Prod.*, vol. 3, pp. 226–233, 2013.

[34] ABB Inc., *AlScan Model "F" User's Manual*, 1st–5th ed. Quebec, Canada, Canada: ABB Inc., 2003.

[35] H. Liu, M. Bouchard, and L. Zhang, "An experimental study of hydrogen solubility in liquid aluminium," *J. Mater. Sci.*, vol. 30, no. 17, pp. 4309–4315, 1995.

[36] P. N. Anyalebechi, "Analysis and thermodynamic prediction of hydrogen solution in solid and liquid multicomponent aluminum alloys," in *Essential Readings in Light Metals 2016*, Springer, 1998, pp. 185–200.

[37] P. N. Anyalebechi, "Attempt to predict hydrogen solubility limits in liquid multicomponent aluminum alloys," *Scr. Mater.*, vol. 34, no. 4, pp. 513–517, Feb. 1996.

[38] V. S. Warke, S. Shankar, and M. M. Makhlouf, "Mathematical modeling and computer simulation of molten aluminum cleansing by the rotating impeller degasser: Part II. Removal of hydrogen gas and solid particles," *J. Mater. Process. Technol.*, vol. 168, no. 1, pp. 119–126, Sep. 2005.

[39] J. A. Dantzig and M. Rappaz, *Solidification*. EPFL press, 2009.

[40] M. Felberbaum, E. Landry-Désy, L. Weber, and M. Rappaz, "Effective hydrogen diffusion coefficient for solidifying aluminium alloys," *Acta Mater.*, vol. 59, no. 6, pp. 2302–2308, Apr. 2011.

[41] P. D. Lee, "The formation of hydrogen porosity during the solidification of aluminium alloys." University of Oxford, 1994.

[42] P. N. Anyalebechi, "Techniques for determination of the Hydrogen Content in Aluminium and its Alloys—a Review," *Cast Met.*, vol. 3, no. 4, pp. 182–201, Oct. 1990.

[43] J. P. Martin, G. Tremblay, and G. Dube, "HyDRAL: a New and Simple Technique for In-Line Analysis of Hydrogen in Aluminium Alloys," in *Light Metals 1989*, P. G. Campbell, Ed. The Metals, Minerals, and Materials Society, 1989, pp. 903–912.

[44] A. M. Samuel and F. H. Samuel, "Various aspects involved in the production of low-hydrogen aluminium castings," *J. Mater. Sci.*, vol. 27, no. 24, pp. 6533–6563, 1992.

[45] T. M. Gansemer, B. C. Reynolds, J. N. Hart, and D. C. Chesonis, "Improvement in Hydrogen Measurement Technique for Molten Aluminum," in *Light Metals 2007*, 2007, pp. 685–689.

[46] P. Enright, "Personal Communications." 2018.

[47] S. N. Tiwari and J. Beech, "Origin of gas bubbles in aluminium," *Met. Sci.*, vol. 12, no. 8, pp. 356–362, Aug. 1978.

[48] J. C. Fisher, "The fracture of liquids," *J. Appl. Phys.*, vol. 19, no. 11, pp. 1062–1067, 1948.

[49] J. Campbell, *Castings*. Elsevier, 2003.

[50] W. L. Ryan and E. A. Hemmingsen, "Bubble Formation in Water at Smooth Hydrophobic Surfaces," *J. Colloid Interface Sci.*, vol. 157, no. 2, pp. 312–317, May 1993.

[51] S. F. Jones, G. M. Evans, and K. P. Galvin, "Bubble nucleation from gas cavities — a review," *Adv. Colloid Interface Sci.*, vol. 80, no. 1, pp. 27–50, Feb. 1999.

[52] L. Drenchev, J. Sobczak, S. Malinov, and W. Sha, "Gasars: a class of metallic materials with ordered porosity," *Mater. Sci. Technol.*, vol. 22, no. 10, pp. 1135–1147, 2006.

[53] S. G. Bankoff, "Entrapment of gas in the spreading of a liquid over a rough surface," *AIChE J.*, vol. 4, no. 1, pp. 24–26, 1958.

[54] A. Sangghaleh and M. Halali, "An investigation on the wetting of polycrystalline alumina by aluminium," *J. Mater. Process. Technol.*, vol. 197, no. 1, pp. 156–160, 2008.

[55] S. Bao, A. Kvithyld, S. Gaal, T. ENGH, and M. Tangstad, "Wetting of Pure Aluminium on Filter Materials Graphite, AlF3 and Al2O3," *Light Met.*, pp. 767–773, 2009.

[56] G. Levi and W. D. Kaplan, "Oxygen induced interfacial phenomena during wetting of alumina by liquid aluminium," *Acta Mater.*, vol. 50, no. 1, pp. 75–88, Jan. 2002.

[57] R. Raiszadeh and W. D. Griffiths, "A method to study the history of a double oxide film defect in liquid aluminum alloys," *Metall. Mater. Trans. B*, vol. 37, no. 6, pp. 865–871, 2006.

[58] B. Farhoodi, R. Raiszadeh, and M.-H. Ghanaatian, "Role of Double Oxide Film Defects in the Formation of Gas Porosity in Commercial Purity and Sr-containing Al Alloys," *J. Mater. Sci. Technol.*, vol. 30, no. 2, pp. 154–162, Feb. 2014.

[59] D. Dispinar, S. Akhtar, A. Nordmark, M. Di Sabatino, and L. Arnberg, "Degassing, hydrogen and porosity phenomena in A356," *Mater. Sci. Eng. A*, vol. 527, no. 16–17, pp. 3719–3725, Jun. 2010.

[60] B. Mirzaei, S. Akhtar, and R. E. Aune, "On the effect of oxide level in gravity cast A356 aluminium alloy," in *2013 International Conference on Aerospace Science & Engineering (ICASE)*, 2013, pp. 1–11.

[61] P. D. Lee and J. D. Hunt, "Measuring the nucleation of hydrogen porosity during the solidification of aluminium-copper alloys," *Scr. Mater.*, vol. 36, no. 4, pp. 399–404, Feb. 1997.

[62] P. Anyalebechi, "Hydrogen-induced gas porosity formation in Al–4.5 wt% Cu–1.4 wt% Mg alloy," *J. Mater. Sci.*, vol. 48, no. 15, pp. 5342–5353, 2013.

[63] J.-Y. Buffière, S. Savelli, P. H. Jouneau, E. Maire, and R. Fougères, "Experimental study of porosity and its relation to fatigue mechanisms of model Al–Si7–Mg0.3 cast Al alloys," *Mater. Sci. Eng. A*, vol. 316, no. 1–2, pp. 115–126, Nov. 2001.

[64] L. Liu and F. H. Samuel, "Effect of inclusions on the tensile properties of Al–7% Si–0.35% Mg (A356.2) aluminium casting alloy," *J. Mater. Sci.*, vol. 33, no. 9, pp. 2269–2281, 1998.

[65] D. Dispinar, "Determination of metal quality of aluminium and its alloys." University of Birmingham, 2006.

[66] H. Fujita and T. Tabata, "The effect of grain size and deformation sub-structure on mechanical properties of polycrystalline aluminum," *Acta Metall.*, vol. 21, no. 4, pp. 355–365, 1973.

[67] W. C. Sleppy, "Oxidation of Molten High-purity Aluminum in Dry Oxygen," *J. Electrochem. Soc.*, vol. 108, no. 12, pp. 1097–1102, 1961.

[68] X. CAO and J. CAMPBELL, "OXIDE INCLUSION DEFECTS IN Al-Si-Mg CAST ALLOYS," *Can. Metall. Q.*, vol. 44, no. 4, pp. 435–448, Jan. 2005.

[69] S. Impey, D. J. Stephenson, and J. R. Nicholls, "A study of the effect of magnesium additions on the oxide growth morphologies on liquid aluminum alloys," in *International conference on the microscopy of oxidation, Institute of Metals, University of Cambridge, England*, 1990, pp. 238–244.

[70] G. B. Schaffer, "Powder processed aluminium alloys," in *Materials forum*, 2004, vol. 28, pp. 65–74.

[71] Y. Wang, H.-T. Li, and Z. Fan, "Oxidation of Aluminium Alloy Melts and Inoculation by Oxide Particles," *Trans. Indian Inst. Met.*, vol. 65, no. 6, pp. 653–661, 2012.

[72] R. Fuoco, E. R. Correa, M. de Andrade Bastos, and L. S. Escudero, "Characterization of Some Types of Oxide Inclusions in Aluminum Alloy Castings (99-85)," *Trans. FOUNDRYMENS Soc.*, pp. 287–294, 1999.

[73] S. A. Impey, D. J. Stephenson, and J. R. Nicholls, "Mechanism of scale growth on liquid aluminium," *Mater. Sci. Technol.*, vol. 4, no. 12, pp. 1126–1132, Apr. 1988.

[74] A. Verma, "No Title," University of Oxford, 2015.

[75] D. Dispinar and J. Campbell, "A comparison of methods used to assess aluminium melt quality," in *136th TMS Annual Meeting, Shape Casting: 2nd International Symposium, Orlando, Florida, USA,(February 2007)*, 2007, pp. 11–18.

[76] J. T. Staley Jr, M. Tiryakioglu, and J. Campbell, *Effect of various hip conditions on bifilms and mechanical properties in aluminum castings*. 2007.

[77] D. Dispinar and J. Campbell, "Critical assessment of reduced pressure test. Part 2: Quantification," *Int. J. Cast Met. Res.*, vol. 17, no. 5, pp. 280–286, Oct. 2004.

[78] R. Raiszadeh and W. D. Griffiths, "A Semi-empirical Mathematical Model to Estimate

the Duration of the Atmosphere within a Double Oxide Film Defect in Pure Aluminum Alloy," *Metall. Mater. Trans. B*, vol. 39, no. 2, pp. 298–303, 2008.

[79] D. N. Miller, L. Lu, and A. K. Dahle, "The role of oxides in the formation of primary iron intermetallics in an Al-11.6Si-0.37Mg alloy," *Metall. Mater. Trans. B*, vol. 37, no. 6, pp. 873–878, 2006.

[80] X. Cao and J. Campbell, "Morphology of β-Al‹SUB›5‹/SUB›FeSi Phase in Al-Si Cast Alloys," *Mater. Trans.*, vol. 47, no. 5, pp. 1303–1312, 2006.

[81] S. Terzi, J. A. Taylor, Y. H. Cho, L. Salvo, M. Suéry, E. Boller, and A. K. Dahle, "In situ study of nucleation and growth of the irregular α-Al/β-Al5FeSi eutectic by 3-D synchrotron X-ray microtomography," *Acta Mater.*, vol. 58, no. 16, pp. 5370–5380, Sep. 2010.

[82] X. Cao and J. Campbell, "The nucleation of Fe-Rich phases on oxide films in Al-11.5Si-0.4Mg cast alloys," *Metall. Mater. Trans. A*, vol. 34, no. 7, pp. 1409–1420, 2003.

[83] A. J. Gerrard and W. D. Griffiths, "The Formation of Hydrogen Related Porosity by Double Oxide Film Defects in Al Alloys BT - Shape Casting: 5th International Symposium 2014," M. Tiryakioğlu, J. Campbell, and G. Byczynski, Eds. Cham: Springer International Publishing, 2014, pp. 269–276.

[84] R. Raiszadeh and W. D. Griffiths, "The behaviour of double oxide film defects in liquid Al alloys under atmospheric and reduced pressures," *J. Alloys Compd.*, vol. 491, no. 1–2, pp. 575–580, Feb. 2010.

[85] P. V Evans, P. G. Enright, and R. A. Ricks, "Molten Metal Cleanliness: Recent Developments to Improve Measurement Reliability - Light Metals 2018," 2018, pp. 839–846.

[86] P. G. Enright, I. R. Hughes, J. Pickering, A. Simard, and J. Proulx, "Characterisation of molten metal quality using the pressure filtration technique," 2003.

[87] A. Simard, J. Proulx, D. Paquin, F. H. Samuel, and H. Habibi, "Capability study of the improved PREFIL-footprinter to measure liquid aluminum cleanliness and comparison with different techniques," in *AFS 6th International conference on molten aluminium processing*, 2001, pp. 93–112.

[88] D. Doutre, B. Gariépy, J. P. Martin, and G. Dubé, "Aluminium cleanliness monitoring: methods and applications in process development and quality control," in *Essential Readings in Light Metals*, Springer, 2016, pp. 296–304.

[89] Technology Strategy Consultants, "Premetz: Fine Inclusions," 2018. [Online]. Available: https://premetz.com/pages/inclusions.

[90] P. V. Evans, P. G. Enright, and R. A. Ricks, "Premetz: Reliable Analysis of Prefil Tests," in *Solidification Processing 2017: Proceedings of the 6th International Conference on Solidification Processing*, 2017, pp. 525–529.

[91] I. R. Hughes and P. Enright, "Metallographic Analyses (PoDFA Analysis) Report,"

Oxford, 2018.

[92] J. Pickering and P. Enright, "The Prefil Technique for Molten Metal Cleanliness Measurement," in *67th World Foundry Congress (wfc06): Casting the Future*, 2006, p. 46/1-46/10.

[93] S. Fox and J. Campbell, "Visualisation of oxide film defects during solidification of aluminium alloys," *Scr. Mater.*, vol. 43, no. 10, pp. 881–886, 2000.

[94] D. Dispinar and J. Campbell, "Reduced Pressure Test (RPT) for Bifilm Assessment," in *Shape Casting: 5th International Symposium 2014*, 2014, pp. 243–251.

[95] D. Dispinar and J. Campbell, "Effect of casting conditions on aluminium metal quality," *J. Mater. Process. Technol.*, vol. 182, no. 1–3, pp. 405–410, Feb. 2007.

[96] R. C. Atwood and P. D. Lee, "A three-phase model of hydrogen pore formation during the equiaxed dendritic solidification of aluminum-silicon alloys," *Metall. Mater. Trans. B*, vol. 33, no. 2, pp. 209–221, 2002.

[97] F. Frisvold, T. A. Engh, S. T. Johansen, and T. Pedersen, "Removal of inclusions—A Survey and Comparison of Principles," in *Essential Readings in Light Metals*, Springer, 2016, pp. 324–331.

[98] A. Khaliq, M. A. Rhamdhani, G. Brooks, J. Grandfield, J. Mitchell, and C. Davidson, "Analysis of transition metal (V, Zr) borides formation in aluminium melt," *Proc. EMC 2011*, pp. 825–838, 2011.

[99] G. S. Vinod Kumar, B. S. Murty, and M. Chakraborty, "Settling behaviour of TiAl3, TiB2, TiC and AlB2 particles in liquid Al during grain refinement," *Int. J. Cast Met. Res.*, vol. 23, no. 4, pp. 193–204, Aug. 2010.

[100] P. Le Brun, *Hydrogen removal efficiency of in-line degassing units*. 2002.

[101] G. K. Sigworth, E. M. Williams, and D. C. Chesonis, "Gas Fluxing of Molten Aluminum: An Overview BT - Essential Readings in Light Metals: Volume 3 Cast Shop for Aluminum Production," J. F. Grandfield and D. G. Eskin, Eds. Cham: Springer International Publishing, 2016, pp. 65–70.

[102] T. A. Engh and T. Pedersen, "Removal of hydrogen from molten aluminium by gas purging," in *Essential Readings in Light Metals*, Springer, 2016, pp. 218–225.

[103] T. A. Engh and G. K. Sigworth, "Molten Aluminium Purification," in *Essential Readings in Light Metals*, Springer, 2016, pp. 208–217.

[104] P. Waite and R. Thiffault, "The Alcan Compact Degasser-A Trough-Based Aluminum Treatment Process. Part I: Metallurgical Principles and Performance," *Light Met.*, pp. 1001–1006, 1996.

[105] L. Zhang, J. Aoki, and B. G. Thomas, "Inclusion removal by bubble flotation in a continuous casting mold," *Metall. Mater. Trans. b*, vol. 37, no. 3, pp. 361–379, 2006.

[106] L. Wang, H.-G. Lee, and P. Hayes, "Prediction of the Optimum Bubble Size for

Inclusion Removal from Molten Steel by Flotation," *ISIJ Int.*, vol. 36, no. 1, pp. 7–16, 1996.

[107] M. Mostafaei, M. Ghobadi, G. Eisaabadi B., M. Uludağ, and M. Tiryakioğlu, "Evaluation of the Effects of Rotary Degassing Process Variables on the Quality of A357 Aluminum Alloy Castings," *Metall. Mater. Trans. B*, vol. 47, no. 6, pp. 3469–3475, 2016.

[108] M. A. Easton, M. Qian, A. Prasad, and D. H. StJohn, "Recent advances in grain refinement of light metals and alloys," *Curr. Opin. Solid State Mater. Sci.*, vol. 20, no. 1, pp. 13–24, 2016.

[109] K. Tynelius, "A parametric study of the evolution of microporosity in aluminum-silicon foundry alloys." ProQuest Dissertations Publishing, 1992.

[110] Q. T. Fang, P. N. Anyalebechi, and D. A. Granger, "Measurement of hydrogen porosity in unidirectionally solidified aluminum alloys," *Light Met.*, pp. 477–486, 1988.

[111] Q. T. Fang, P. N. Anyalebechi, J. R. Q'malley, and D. A. Granger, "Effect of solidification conditions on hydrogen porosity. Formation in unidirectionally solidified aluminum alloys," *Solidif. Process. Inst Met*, pp. 33–39, 1987.

[112] G. Kasperovich, J. Haubrich, J. Gussone, and G. Requena, "Correlation between porosity and processing parameters in TiAl6V4 produced by selective laser melting," *Mater. Des.*, vol. 105, pp. 160–170, 2016.

[113] C. T. Rueden, J. Schindelin, M. C. Hiner, B. E. DeZonia, A. E. Walter, E. T. Arena, and K. W. Eliceiri, "ImageJ2: ImageJ for the next generation of scientific image data," *BMC Bioinformatics*, vol. 18, no. 1, p. 529, 2017.

[114] D. Snelling, H. Blount, C. Forman, K. Ramsburg, A. Wentzel, C. Williams, and A. Druschitz, "The effects of 3D printed molds on metal castings," in *Proceedings of the Solid Freeform Fabrication Symposium*, 2013, pp. 827–845.

[115] D. L. Sahagian and A. A. Proussevitch, "3D particle size distributions from 2D observations: stereology for natural applications," *J. Volcanol. Geotherm. Res.*, vol. 84, no. 3–4, pp. 173–196, Sep. 1998.

[116] E. E. Underwood, *Quantitative stereology*. Addison-Wesley Pub. Co., 1970.

[117] S. Fintová, G. Anzelotti, R. Konečná, and G. Nicoletto, "Casting pore characterization by X-ray computed tomography and metallography," *Arch. Mech. Eng.*, vol. 57, no. 3, pp. 263–273, 2010.

[118] G. F. Vander Voort, *Metallography, Principles and Practice*. ASM International, 1999.

[119] A. A. Emelyanov, E. L. Furman, I. P. Conacova, and V. A. Beloglazov, "Microstructure and mechanical properties of porous cast aluminium composite," *Adv. Compos. Mater.*, vol. 3, no. 1, pp. 1–5, 1993.

[120] D. J. Nolan and M. Samandi, "Revealing true porosity in WC-Co thermal spray

coatings," *J. Therm. spray Technol.*, vol. 6, no. 4, pp. 422–424, 1997.

[121] E. Maire and P. J. Withers, "Quantitative X-ray tomography," *Int. Mater. Rev.*, vol. 59, no. 1, pp. 1–43, 2014.

[122] J. Hiller and L. M. Reindl, "A computer simulation platform for the estimation of measurement uncertainties in dimensional X-ray computed tomography," *Measurement*, vol. 45, no. 8, pp. 2166–2182, 2012.

[123] S. R. Stock, "X-ray microtomography of materials," *Int. Mater. Rev.*, vol. 44, no. 4, pp. 141–164, 1999.

[124] V. Cnudde and M. N. N. Boone, "High-resolution X-ray computed tomography in geosciences: A review of the current technology and applications," *Earth-Science Rev.*, vol. 123, pp. 1–17, Aug. 2013.

[125] T. Li, S. Shimasaki, S. Taniguchi, S. Narita, and K. Uesugi, "Three-dimensional observation of nonmetallic inclusion clusters in Solid Metal by X-ray Micro-CT," *ISIJ Int.*, vol. 56, no. 11, pp. 1989–1995, 2016.

[126] J. P. P. Kruth, M. Bartscher, S. Carmignato, R. Schmitt, L. De Chiffre, and A. Weckenmann, "Computed tomography for dimensional metrology," *CIRP Ann. - Manuf. Technol.*, vol. 60, no. 2, pp. 821–842, Jan. 2011.

[127] ZEISS Germany, "ZEISS Xradia 520 Versa," 2018. [Online]. Available: https://www.zeiss.com/microscopy/int/products/x-ray-microscopy/zeiss-xradia-520-versa.html. [Accessed: 20-Aug-2008].

[128] S. R. Stock, "Recent advances in X-ray microtomography applied to materials," *Int. Mater. Rev.*, vol. 53, no. 3, pp. 129–181, 2008.

[129] E. Maire, J.-Y. Buffière, L. Salvo, J. J. Blandin, W. Ludwig, and J. M. Letang, "On the Application of X-ray Microtomography in the Field of Materials Science," *Adv. Eng. Mater.*, vol. 3, no. 8, pp. 539–546, 2001.

[130] L. A. Feldkamp, L. C. Davis, and J. W. Kress, "Practical cone-beam algorithm," *J. Opt. Soc. Am. A*, vol. 1, no. 6, pp. 612–619, Jun. 1984.

[131] M. Sakamoto, H. Nishiyama, H. Satoh, S. Shimizu, T. Sanuki, K. Kamijoh, A. Watanabe, and A. Asahara, "An implementation of the Feldkamp algorithm for medical imaging on cell," *IBM White Pap.*, 2005.

[132] W. D. Griffiths, A. J. Gerrard, and Y. Yue, "Oxide film defects in Al alloys and the formation of hydrogen-related porosity," in *IOP Conference Series: Materials Science and Engineering*, 2016, vol. 117, no. 1, p. 12070.

[133] K. Haberl, P. Schumacher, G. Geier, and B. Stauder, "Characterization of the melt quality and impurity content of an LM25 alloy," *Metall. Mater. Trans. B*, vol. 40, no. 6, p. 812, 2009.

[134] A. K. Cziegler, T. Pabel, D. Habe, and P. Schumacher, "Evaluation of the effect of

artificial re-gassing of aluminium melts after ultrasonic treatment," *Int. J. Cast Met. Res.*, vol. 30, no. 1, pp. 30–33, Jan. 2017.

[135] D. Eskin, N. Alba-Baena, T. Pabel, and M. da Silva, "Ultrasonic degassing of aluminium alloys: basic studies and practical implementation," *Mater. Sci. Technol.*, vol. 31, no. 1, pp. 79–84, Jan. 2015.

[136] E. N. Landis and D. T. Keane, "X-ray microtomography," *Mater. Charact.*, vol. 61, no. 12, pp. 1305–1316, 2010.

[137] B. K. Shreyamsha Kumar, "Image denoising based on non-local means filter and its method noise thresholding," *Signal, Image Video Process.*, vol. 7, no. 6, pp. 1211–1227, 2013.

[138] A. Buades, B. Coll, and J. M. Morel, "A non-local algorithm for image denoising," in *2005 IEEE Computer Society Conference on Computer Vision and Pattern Recognition (CVPR'05)*, 2005, vol. 2, pp. 60–65 vol. 2.

[139] C. Solomon and T. Breckon, *Fundamentals of Digital Image Processing: A practical approach with examples in Matlab*. John Wiley & Sons, 2011.

[140] C. Tomasi and R. Manduchi, "Bilateral filtering for gray and color images," in *Computer Vision, 1998. Sixth International Conference on*, 1998, pp. 839–846.

[141] S. M. Smith and J. M. Brady, "SUSAN—a new approach to low level image processing," *Int. J. Comput. Vis.*, vol. 23, no. 1, pp. 45–78, 1997.

[142] A. Buades, B. Coll, and J.-M. Morel, "A review of image denoising algorithms, with a new one," *Multiscale Model. Simul.*, vol. 4, no. 2, pp. 490–530, 2005.

[143] F. Yu and V. Koltun, "Multi-scale context aggregation by dilated convolutions," *arXiv Prepr. arXiv1511.07122*, 2015.

[144] P. Iassonov, T. Gebrenegus, and M. Tuller, "Segmentation of X-ray computed tomography images of porous materials: A crucial step for characterization and quantitative analysis of pore structures," *Water Resour. Res.*, vol. 45, no. 9, 2009.

[145] I. Maskery, N. T. Aboulkhair, M. R. Corfield, C. Tuck, A. T. Clare, R. K. Leach, R. D. Wildman, I. A. Ashcroft, and R. J. M. Hague, "Quantification and characterisation of porosity in selectively laser melted Al–Si10–Mg using X-ray computed tomography," *Mater. Charact.*, vol. 111, pp. 193–204, Jan. 2016.

[146] A. C. Moreira, C. R. Appoloni, I. F. Mantovani, J. S. Fernandes, L. C. Marques, R. Nagata, and C. P. Fernandes, "Effects of manual threshold setting on image analysis results of a sandstone sample structural characterization by X-ray microtomography," *Appl. Radiat. Isot.*, vol. 70, no. 6, pp. 937–941, 2012.

[147] N. Otsu, "A threshold selection method from gray-level histograms," *IEEE Trans. Syst. Man. Cybern.*, vol. 9, no. 1, pp. 62–66, 1979.

[148] S. Tammas-Williams, H. Zhao, F. Léonard, F. Derguti, I. Todd, and P. B. Prangnell, "XCT analysis of the influence of melt strategies on defect population in Ti–6Al–4V

components manufactured by Selective Electron Beam Melting," *Mater. Charact.*, vol. 102, pp. 47–61, Apr. 2015.

[149] X. Cai, A. A. Malcolm, B. S. Wong, and Z. Fan, "Measurement and characterization of porosity in aluminium selective laser melting parts using X-ray CT," *Virtual Phys. Prototyp.*, vol. 10, no. 4, pp. 195–206, 2015.

[150] T. B. Kim, S. Yue, Z. Zhang, E. Jones, J. R. Jones, and P. D. Lee, "Additive manufactured porous titanium structures: Through-process quantification of pore and strut networks," *J. Mater. Process. Technol.*, vol. 214, no. 11, pp. 2706–2715, 2014.

[151] F. Léonard, S. Tammas-Williams, and I. Todd, "CT for Additive Manufacturing Process Characterisation: Assessment of melt strategies on defect population," in *iCT 2016: 6th Conference on Industrial Computed Tomography*, 2016, pp. 1–8.

[152] B. Leszczyński, A. Gancarczyk, A. Wróbel, M. Piątek, J. Łojewska, A. Kołodziej, and R. Pędrys, "Global and Local Thresholding Methods Applied to X-ray Microtomographic Analysis of Metallic Foams," *J. Nondestruct. Eval.*, vol. 35, no. 2, p. 35, 2016.

[153] P. Iassonov and M. Tuller, "Application of segmentation for correction of intensity bias in X-ray computed tomography images," *Vadose Zo. J.*, vol. 9, no. 1, pp. 187–191, 2010.

[154] F. Meyer and S. Beucher, "Morphological segmentation," *J. Vis. Commun. Image Represent.*, vol. 1, no. 1, pp. 21–46, 1990.

[155] S. Beucher and F. Meyer, "The morphological approach to segmentation: the watershed transformation," *Opt. Eng. York-Marcel Dekker Inc.*, vol. 34, p. 433, 1992.

[156] M. De Giovanni, J. M. Warnett, M. A. Williams, and P. Srirangam, "3D imaging and quantification of porosity and intermetallic particles in strontium modified Al-Si alloys," *J. Alloys Compd.*, 2017.

[157] M. De Giovanni, J. M. Warnett, M. A. Williams, N. Haribabu, and P. Srirangam, "X-ray tomography investigation of intensive sheared Al–SiC metal matrix composites," *Mater. Charact.*, vol. 110, no. Supplement C, pp. 258–263, 2015.

[158] J. Mathew, A. Mandal, J. Warnett, M. A. Williams, M. Chakraborty, and P. Srirangam, "X-ray tomography studies on porosity and particle size distribution in cast in-situ Al-Cu-TiB2 semi-solid forged composites," *Mater. Charact.*, vol. 118, pp. 57–64, Aug. 2016.

[159] N. Khdhair, N. El abbadi, E. Hamood, and E. Al-saadi, *Blood vessels extraction using mathematical morphology*, vol. 9. 2013.

[160] X. Bai, F. Zhou, and B. Xue, "Image enhancement using multi scale image features extracted by top-hat transform," *Opt. Laser Technol.*, vol. 44, no. 2, pp. 328–336, 2012.

[161] G. Ziółkowski, E. Chlebus, P. Szymczyk, and J. Kurzac, "Application of X-ray CT method for discontinuity and porosity detection in 316L stainless steel parts produced

with SLM technology," *Arch. Civ. Mech. Eng.*, vol. 14, no. 4, pp. 608–614, Aug. 2014.

[162] B. M. Patterson, J. P. Escobedo-Diaz, D. Dennis-Koller, and E. Cerreta, "Dimensional Quantification of Embedded Voids or Objects in Three Dimensions Using X-Ray Tomography," *Microsc. Microanal.*, vol. 18, no. 2, pp. 390–398, 2012.

[163] A. (Aluminium C. of C. Lld.), *Handbook of Aluminium Alloys*, Second Edi. Montreal: The Herald Press Limited, 1947.

[164] G. Wu, "Understanding the Role of Oxidation in Bonding of Aluminium Alloys," University of Oxford, 2014.

[165] R. H. Davies, A. T. Dinsdale, J. A. Gisby, J. A. J. Robinson, and S. M. Martin, "MTDATA-thermodynamic and phase equilibrium software from the national physical laboratory," *Calphad*, vol. 26, no. 2, pp. 229–271, 2002.

[166] S. Srimanosaowapak, "Precipitation and Sedimentation of Particles in Molten Aluminium Alloys," University of Oxford, 2006.

[167] M. Bryant, "The evolution of fused refining fluxes," *Aluminium Times*, 2015.

[168] J. Schindelin, I. Arganda-Carreras, E. Frise, V. Kaynig, M. Longair, T. Pietzsch, S. Preibisch, C. Rueden, S. Saalfeld, and B. Schmid, "Fiji: an open-source platform for biological-image analysis," *Nat. Methods*, vol. 9, no. 7, p. 676, 2012.

[169] J. Darbon, A. Cunha, T. F. Chan, S. Osher, and G. J. Jensen, "Fast nonlocal filtering applied to electron cryomicroscopy," in *2008 5th IEEE International Symposium on Biomedical Imaging: From Nano to Macro*, 2008, pp. 1331–1334.

[170] A. Buades, B. Coll, and J.-M. Morel, "Non-local means denoising," *Image Process. Line*, vol. 1, pp. 208–212, 2011.

[171] D. Legland, I. Arganda-Carreras, and P. Andrey, "MorphoLibJ: integrated library and plugins for mathematical morphology with ImageJ," *Bioinformatics*, vol. 32, no. 22, pp. 3532–3534, Nov. 2016.

[172] G. Lehmann and D. Legland, "Efficient N-Dimensional surface estimation using Crofton formula and run-length encoding," *Effic. N-Dimensional Surf. Estim. using Croft. formula run-length encoding, Kitware INC*, 2012.

[173] S. Akhtar, L. Arnberg, M. Di Sabatino, D. Dispinar, and M. Syvertsen, "A Comparative Study of Porosity and Pore Morphology in a Directionally Solidified A356 Alloy," *Int. J. Met.*, vol. 3, no. 1, pp. 39–52, 2009.

[174] R. Deriche, "Using Canny's criteria to derive a recursively implemented optimal edge detector," *Int. J. Comput. Vis.*, vol. 1, no. 2, pp. 167–187, 1987.

[175] Thermo Fisher Scientific (FEI), "Amira-Avizo Software." Thermo Fisher Scientific (FEI).

[176] L. Brabant, J. Vlassenbroeck, Y. De Witte, V. Cnudde, M. N. Boone, J. Dewanckele, and L. Van Hoorebeke, "Three-Dimensional Analysis of High-Resolution X-Ray

Computed Tomography Data with Morpho+," *Microsc. Microanal.*, vol. 17, no. 2, pp. 252–263, 2011.

[177] S. Katuwal, T. Norgaard, P. Moldrup, M. Lamandé, D. Wildenschild, and L. W. de Jonge, "Linking air and water transport in intact soils to macropore characteristics inferred from X-ray computed tomography," *Geoderma*, vol. 237–238, pp. 9–20, 2015.

[178] S. A. Saltikov, "The Determination of the Size Distribution of Particles in an Opaque Material from a Measurement of the Size Distribution of Their Sections BT - Stereology," 1967, pp. 163–173.

[179] W. Pabst, E. Gregorová, and T. Uhlířová, "Microstructure characterization via stereological relations — A shortcut for beginners," *Mater. Charact.*, vol. 105, pp. 1–12, 2015.

[180] P. Evans, *Private Communications*. 2018.

[181] M. Riestra, A. Bjurenstedt, T. Bogdanoff, E. Ghassemali, and S. Seifeddine, "Complexities in the Assessment of Melt Quality," *Int. J. Met.*, vol. 12, no. 3, pp. 441–448, 2018.

[182] M. Di Sabatino, L. Arnberg, S. Rørvik, and A. Prestmo, "The influence of oxide inclusions on the fluidity of Al–7 wt.%Si alloy," *Mater. Sci. Eng. A*, vol. 413–414, pp. 272–276, Dec. 2005.

[183] A. Kvithyld, J. A. Sæter, M. Syvertsen, H. Fossheim, A. Nordmark, R. Sottar, and T. A. Engh, "Discussion of Bi-Film Index and LiMCA Data in Industrial Aluminum Remelting Trials," in *TMS Annual Meeting & Exhibition*, 2018, pp. 855–861.

[184] S. Kumar, N. Hari Babu, G. M. Scamans, and Z. Fan, "Influence of Intensive Melt Shearing on the Microstructure and Mechanical Properties of an Al-Mg Alloy with High Added Impurity Content," *Metall. Mater. Trans. A*, vol. 42, no. 10, pp. 3141–3149, 2011.

[185] H.-T. Li, Y. Wang, and Z. Fan, "Mechanisms of enhanced heterogeneous nucleation during solidification in binary Al–Mg alloys," *Acta Mater.*, vol. 60, no. 4, pp. 1528–1537, Feb. 2012.

[186] A. A. Simard, F. Dallaire, J. Proulx, and P. Rochette, "Cleanliness measurement benchmarks of aluminum alloys obtained directly at-line using the prefil-footprinter instrument," *Light Met.*, vol. 2000, pp. 739–744, 2000.

[187] L. Liu and F. H. Samuel, "Assessment of melt cleanliness in A356.2 aluminium casting alloy using the porous disc filtration apparatus technique: Part I Inclusion measurements," *J. Mater. Sci.*, vol. 32, no. 22, pp. 5901–5925, 1997.

[188] E. Lae, H. Duval, C. Rivière, P. Le Brun, and J.-B. Guillot, "Experimental and numerical study of ceramic foam filtration," in *Essential Readings in Light Metals*, Springer, 2016, pp. 285–290.

[189] R. C. Atwood and P. D. Lee, "Simulation of the three-dimensional morphology of

solidification porosity in an aluminium–silicon alloy," *Acta Mater.*, vol. 51, no. 18, pp. 5447–5466, Oct. 2003.

[190] S. Fox and J. Campbell, "Liquid metal quality," *Int. J. Cast Met. Res.*, vol. 14, no. 6, pp. 335–340, May 2002.

[191] A. . L. Greer, A. . M. Bunn, A. Tronche, P. . V Evans, and D. . J. Bristow, "Modelling of inoculation of metallic melts: application to grain refinement of aluminium by Al–Ti–B," *Acta Mater.*, vol. 48, no. 11, pp. 2823–2835, Jun. 2000.

[192] G. S. V. Kumar, B. S. Murty, and M. Chakraborty, "Grain refinement response of LM25 alloy towards Al–Ti–C and Al–Ti–B grain refiners," *J. Alloys Compd.*, vol. 472, no. 1–2, pp. 112–120, 2009.

[193] S. A. Kori, V. Auradi, B. S. Murty, and M. Chakraborty, "Poisoning and fading mechanism of grain refinement in Al-7Si alloy," in *Materials Forum*, 2005, vol. 29, pp. 387–393.

[194] D. Qiu, J. A. Taylor, M.-X. Zhang, and P. M. Kelly, "A mechanism for the poisoning effect of silicon on the grain refinement of Al–Si alloys," *Acta Mater.*, vol. 55, no. 4, pp. 1447–1456, Feb. 2007.

[195] P. Schumacher and A. L. Greer, "High-resolution transmission electron microscopy of grain-refining particles in amorphous aluminum alloys," in *Light metals 1996*, 1996.

[196] M. Easton and D. StJohn, "Grain refinement of aluminum alloys: Part I. the nucleant and solute paradigms—a review of the literature," *Metall. Mater. Trans. A*, vol. 30, no. 6, pp. 1613–1623, 1999.

[197] R. Schmid-Fetzer and A. Kozlov, "Thermodynamic aspects of grain growth restriction in multicomponent alloy solidification," *Acta Mater.*, vol. 59, no. 15, pp. 6133–6144, 2011.

[198] D. H. StJohn, M. Qian, M. A. Easton, and P. Cao, "The interdependence theory: the relationship between grain formation and nucleant selection," *Acta Mater.*, vol. 59, no. 12, pp. 4907–4921, 2011.

[199] F. Vogt, R. Tonti, M. Hunt, and L. Edwards, "A preview of anode coke quality in 2007," in *LIGHT METALS-WARRENDALE-PROCEEDINGS-*, 2004, pp. 489–494.

[200] P. S. Cooper and M. A. Kearns, "Removal of transition metal impurities in aluminium melts by boron additives," in *Materials Science Forum*, 1996, vol. 217, pp. 141–146.

[201] A. Khaliq, M. A. Rhamdhani, G. Brooks, and J. Grandfield, *Removal of Vanadium from Molten Aluminum-Part I. Analysis of VB2 Formation*. 2013.

[202] I. G. G. Watson, M. F. F. Forster, P. D. D. Lee, R. J. J. Dashwood, R. W. W. Hamilton, and A. Chirazi, "Investigation of the clustering behaviour of titanium diboride particles in aluminium," *Compos. Part A Appl. Sci. Manuf.*, vol. 36, no. 9, pp. 1177–1187, Sep. 2005.

[203] S. Lakshmi, L. Lu, and M. Gupta, "In situ preparation of TiB2 reinforced Al based

composites," *J. Mater. Process. Technol.*, vol. 73, no. 1, pp. 160–166, 1998.

[204] D. G. McCartney, "Grain refining of aluminium and its alloys using inoculants," *Int. Mater. Rev.*, vol. 34, no. 1, pp. 247–260, Jan. 1989.

[205] S. Kumar and K. A. Q. O'Reilly, "Influence of Al grain structure on Fe bearing intermetallics during DC casting of an Al-Mg-Si alloy," *Mater. Charact.*, vol. 120, pp. 311–322, 2016.

[206] ABB Inc., "Prefil-Footprinter, Pressure filtration melt cleanliness analyzer, A quick and thorough inclusion control solution," *Prod. Inf. Broch.*, no. Rev. B 01.2016, 2016.

[207] J. Campbell and R. Harding, "TALAT Lecture 3202 The Liquid Metal," 1994.



APPENDICES

Appendices to the thesis submitted for the degree of
Doctor of Philosophy in Materials

Contents

Appendix I **Supplementary Background Information** 2

I.1 Summary of Hydrogen Measurement Techniques 2

I.2 Inclusion Assessment using LiMCA 5

Appendix II **Supplementary Material on the Materials & Methods** 6

II.1 Hydrogen Analysis using LECO 6

II.2 Volume Fraction of Porosity Uncertainty Analysis 9

II.3 Supplementary Material to the Porosity Characterisation Methods 12

Appendix III **Supplementary Material for Part III** 20

III.1 Experiment DMX 20

III.2 SEM Analysis of the 'Particle Cluster' Inclusions Present in CM1 28

III.3 Additional Metallographic Measurements 30

III.4 Grain Refiner Addition Studies: Solidification Curves 36

Appendix IV **Ancillary Experimental Work RPT Porosity Retention Experiments** 38

References In The Appendices 66

Appendix I
Supplementary Background Information

I.1 Summary of Hydrogen Measurement Techniques

This section provides a brief overview of some of the common hydrogen measurement techniques that are employed in aluminium industry.

I.1.1 Bubble Formation Techniques

The most simple of the techniques for on-line hydrogen measurement bubble formation tests. The two standard techniques of this family will be briefed here.

In the **First Bubble Test t**he quantity of hydrogen in a melt is estimated based on the temperature at which the first bubble appears at the surface of a sample solidified at reduced pressure [1]. The measured temperature at which this occurs can then be used to obtain the hydrogen content from a nomogram. Like the RPT, this test is probably confounded by melt cleanliness.

The Reduced Pressure Test (RPT) is also sometimes used [2], [3]. Sometimes the sample density is used, and sometimes the sample is sectioned and the porosity inside the sample is compared to a reference chart. It is well known that the RPT influenced by the melt cleanliness, but is nevertheless still used as a rough foundry floor estimate.

I.1.2 Direct Measurement Techniques

Direct measurements techniques, as the name suggests, directly measure the amount of hydrogen that is trapped within a sample of a known mass.

The most common method these days is **LECO**, an off-line method. The technique involves casting off a small sample in a well-fed *Ransley Casting* [4] (also known colloquially as a *Gas Pin*) from the melt, and then machining a small sample (3.0 to 6.5 g) from it. The sample is then melted and the hydrogen that is liberated from the sample is measured, and normalised by weight. The major advantage of these techniques is that they do not require the solubility of hydrogen inside the melt to be estimated, unlike some other methods [5]. However, the measurements are subject to errors arising from potential contamination of the samples during machining.

The **Hyscan** is an on-line variation that measure the hydrogen given off from liquid metal samples [6].

I.1.3 Gas Recirculation Techniques

The most industrially widespread of the on-line measurement techniques as they allow for accurate on-line measurements of hydrogen to be made. As shown in **Figure I.1**, these techniques rely on the recirculation of an inert gas through the melt using an immersed probe, which picks up dissolved hydrogen from the melt [1], [7], which is then measured downstream, inside the instrument – just like the ABB **AlScan**, the most popular member of this family of instruments. Although measurement is fast (~10 minutes) and convenient, the major drawback of this technique is that it requires the hydrogen content to be estimated

using alloy correction factors – which may introduce significant error The Alcoa **Telegas** was the original commercially widespread method to employ this principle.

The (FMA) **CHAPEL** is a variation of this technique that does not use a recirculating gas (but is mentioned here as it is otherwise hard to classify), but instead directly measures the P_{H_2} [8]. This is done by equilibrating the P_{H_2} inside.a small evacuated volume inside the device with that of the melt by using a probe, immersed in the melt, to take up hydrogen.

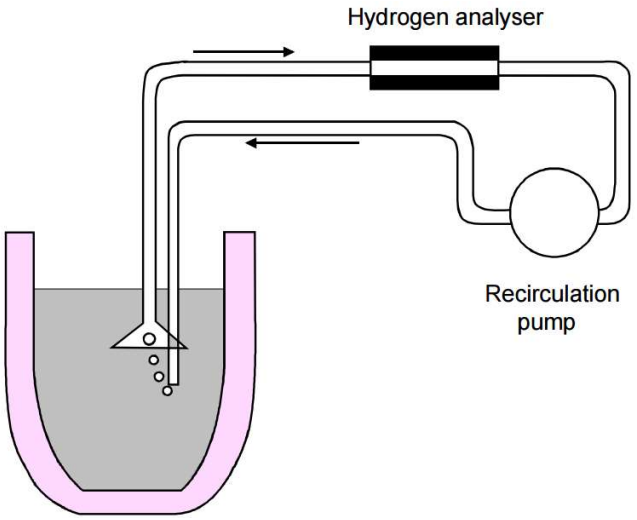

Figure I.1 Basic operating principle of the Telegas, a melt-hydrogen measuring instrument based on the recirculating gas measurement system. From Campbell and Harding [9].

I.1.4 Electrochemical Techniques

These are the most modern of the industrial instrument for on-line hydrogen measurement. They measure the P_{H_2} that is built up inside a small hollow volume in the head of a probe that is immersed into the melt. Using a solid-state reference standard ($CaZrO_3$-In [10], [11] in the AlSpek), the change in the conductivity across a proton conducting membrane is measured, and the hydrogen level is measured. Like the carrier gas recirculation

methods, one of the issue with these methods that they requires the use of alloy correction factors to estimate the hydrogen content. The key instruments of this family are the EMC **Hycal**, and the Foseco **AlSpek**.

I.2 Inclusion Assessment using LiMCA

LiMCA is widely considered throughout industry to be considered the 'premier' method for melt cleanliness assessment [12], as it is able to accurately provide real time, on-line, continuous, quantitative measurements of the inclusion population inside molten metal [13], [14]. The device is based on a Coulter counter, which detects inclusions that are suspended in the metal by measuring changes in the electrical conductivity on the melt that passes through the probe [15]; the device is designed for large-scale production, for use in launders, and requires metal flow. It is able to measure the size and number of inclusions in the range of 20 to 300 µm in the liquid metal, but it is not able to discern inclusion species, nor is it able to discern differences between micro-bubbles and inclusions – which limits its use downstream of in-line degassers [16].

Appendix II
Supplementary Material on the Materials & Methods

II.1 Hydrogen Analysis using LECO

II.1.1 Procedure

LECO was employed to give complimentary hydrogen measurements over the experiments as a kind of 'control' to ensure that the AlScan measurements were realistic, when processing the data, that is, it was used to give ancillary measurements of the melt hydrogen content. It was only used as the primary measurement method for experiment GR1 in the Grain Refiner Addition experiments.

Analysis off-site by Sci-Lab Analytical (Tattenhall, United Kingdom) with a LECO RH402 instrument. Analysis was conducted on small samples machined from Ransley mould castings [4] – known colloquially as *gas-pins* – taken at intervals during the experiments.

When casting the gas pins, the mould was first preheated by taking a 'dummy-casting', which was subsequently discarded, then approximately one minute later, the 'analysis sample' was cast. The analysis was conducted on small samples of approximately 3 to 5 g that were machined from the bottom region of the gas pins (**Figure II.1**). The results are generally given in ppm but can be converted to ml $100g^{-1}$, the AlScan's units, using the relationship [17]: $1\ ml\ 100g^{-1} = 1.1932\ ppm$.

The resolution of this technique is 0.001 ppm hydrogen (~0.0012ml $100g^{-1}$), though in practice there are limitations, such as the escape of hydrogen from the material solidification, and contamination of the analysis specimen during machining.

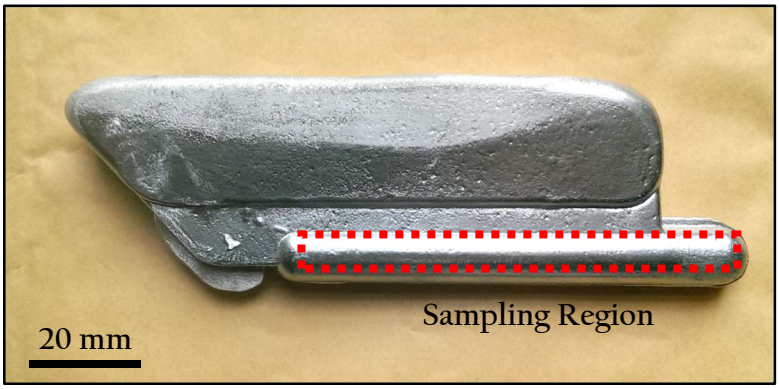

Figure II.1 A Ransley Mould 'Gas Pin' casting, with the sample collection area for LECO analysis shown.

II.1.2 Comparison of AlScan and LECO

Generally there was a good agreement between the hydrogen content that was measured by the AlScan and by LECO at contents $\lessapprox$ 0.4 ml $100g^{-1}$ as shown in **Figure II.2**. This suggests that the AlScan was giving a reasonable measurement for the Al-7Si alloys, despite risk of potential errors arising from its use alloy factors in calculating the hydrogen content. This is in better agreement than that which has been reported by others in the literature [18].

However, at high hydrogen contents $\gtrapprox$0.4ml $100g^{-1}$, the discrepancy between the techniques increased. This can be explained based on the fundamental differences between the two techniques, namely, the AlScan measures (approximately) the hydrogen dissolved in the molten metal, whereas LECO measures the hydrogen that is entrapped in the solidified metal. In the LECO gas pin samples, a small amount of hydrogen loss is expected due to the

combination of high casting temperature and high mould temperature, which (slightly) slows solidification which allows a small window of time for hydrogen to escape the material. At high hydrogen levels, bubbles form earlier during solidification, meaning that a higher fraction may escape as the content increases. A hydrogen level of 0.4 ml $100g^{-1}$ is approximately the point at which hydrogen can escape.

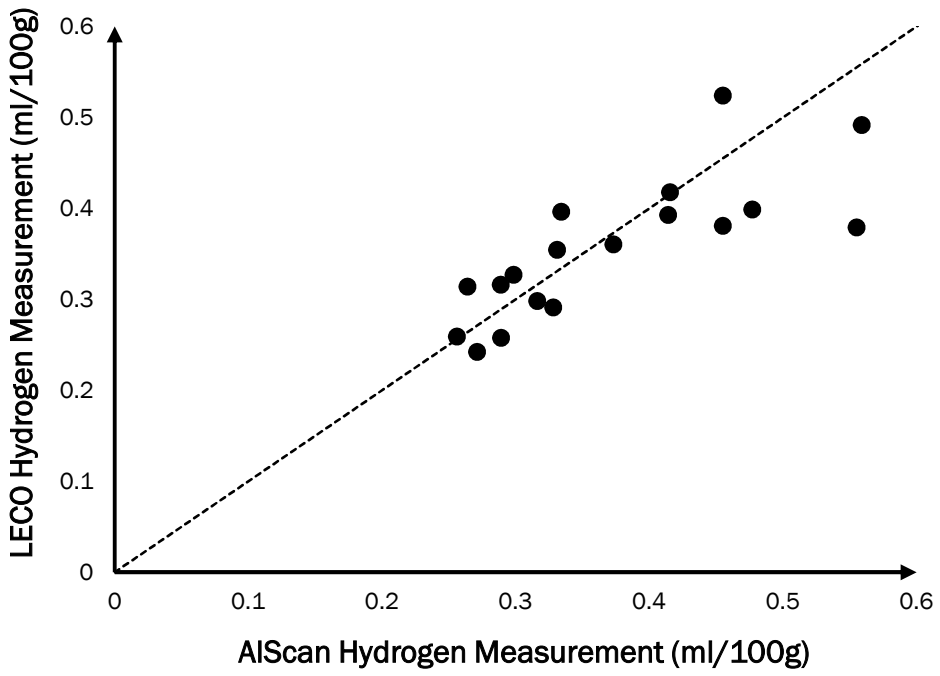

Figure II.2 Comparison melt hydrogen content measured by AlScan and LECO obtained from various experiments during this project.

II.2 Volume Fraction of Porosity Uncertainty Analysis

This section gives an overview of the uncertainty associated with the calculated volume fraction, f_p, in the RPT samples, and presents a calculation of the maximum permissible range of f_p as a result of these uncertainties.

II.2.1 Sources of Uncertainty

RPT Sample Density

The density of the RPT samples is calculated using equation 4.1 (reproduced below). The measurement uncertainty is considered to come from the measurements of the sample mass using the density balance, which was taken as ± 0.02 g, the typical variability.

$$\rho = \frac{m_a}{m_{a_2} - m_w}\rho_w \tag{II.1}$$

Where m_a, m_w, and m_{a_2} are the mass of the sample in air, the mass when immersed, and the mass in air after immersion, respectively, and ρ_w is the density of water, 0.998 g cm^{-3}.

f_p is subsequently calculated using equation 4.2 (reproduced below).

$$f_p = \left(1 - \frac{\rho}{\rho_t}\right) \times 100\% \tag{II.2}$$

Where ρ_t is the theoretical alloy density.

Theoretical Alloy Density

The theoretical density (ρ_t) of Al-7Si was calculated to be 2.67 g cm^{-3} using MTData thermodynamic software with the MTAL database v6.1 [165]. This was confirmed by additional calculations to be 2.67 g cm^{-3} using the rule of mixtures, with densities of

2.70 g cm^{-3} and 2.33 g cm^{-3} for Al and Si, respectively, and a 1.2wt.% solid solubility of Si in Al.

In the case that the Si content of the experimental alloy varied, its density would also vary. Calculations with MTDATA showed that a variation of ±0.5wt.%Si around the nominal composition (7wt.%Si) would only cause ρ_t of the alloy to vary between 2.68 g cm^{-3} to 2.67 g cm^{-3}. The uncertainty of this is therefore taken to be ±0.01 g cm^{-3}.

II.2.2 Maximum Variation

Given the uncertainties listed above, the maximum upper and lower bounds of the calculated sample density, ρ_+ and ρ_-, respectively, are:

$$\rho_+ = \frac{m_a + 0.02}{\left(m_{a_2} - 0.02\right) - \left(m_w + 0.02\right)}\rho_w \tag{II.3}$$

$$\rho_- = \frac{m_a - 0.02}{\left(m_{a_2} + 0.02\right) - \left(m_w - 0.02\right)}\rho_w \tag{II.4}$$

These values can then be used to calculate the maximum upper and lower bounds of the volume fraction of porosity, f_{p+} and f_{p-}, respectively, using:

$$f_{p+} = \left(1 - \frac{\rho_-}{2.68}\right) \times 100\% \tag{II.5}$$

$$f_{p-} = \left(1 - \frac{\rho_+}{2.67}\right) \times 100\% \tag{II.6}$$

The difference in the f_p from its nominal value, Δf_p, is therefore given as:

$$\Delta f_{p+} = f_{p+} - f_p \tag{II.7}$$

$$\Delta f_{p-} = f_p - f_{p-} \tag{II.8}$$

The maximum uncertainty in the measured f_p of a number of Al-7Si RPT samples taken during this project is plotted as a function of f_p in **Figure II.3**. The figure shows that the maximum uncertainty range decreases as f_p increases; b) shows that the maximum relative error, $\Delta f_p/f_p \times 100$, is most significant when the f_p is low (as one might expect), as is the case in the rotary degassed samples from RD, or the APT samples, however, even then, the maximum Δf_p.

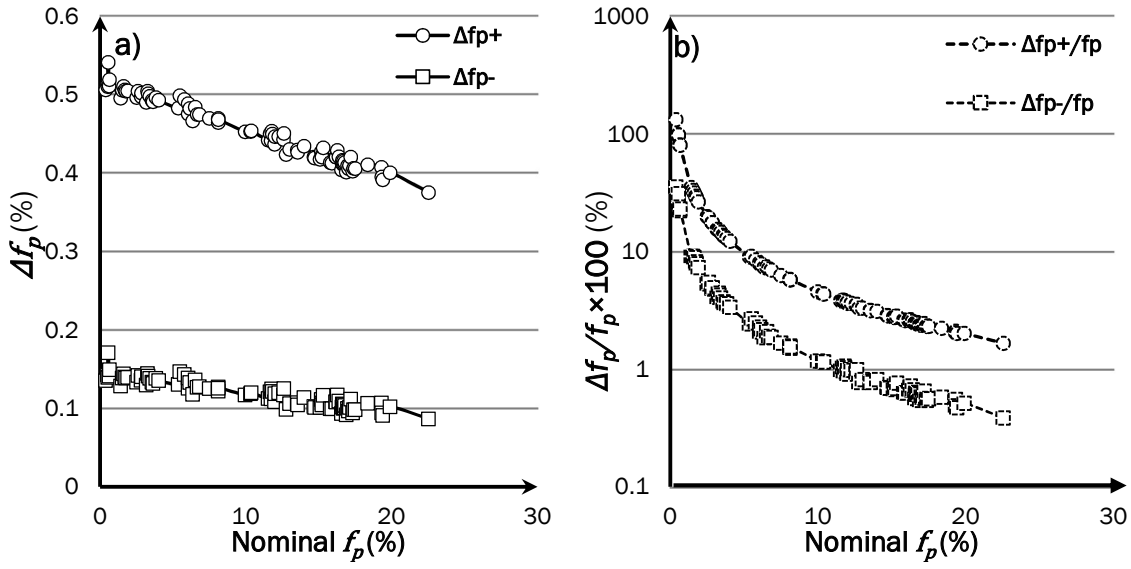

Figure II.3 a) Δf_p vs f_p, and b) $\Delta f_p/f_p$ vs f_p of a large number of Al-7Si RPT samples.

II.3 Supplementary Material to the Porosity Characterisation Methods

This section presents further details on the image analysis procedures used for the metallographic, macro-CT, and micro-CT analyses of pores.

Metallographic Analysis Workflow: Figure II.4 & Table II.1.

Macro-CT Analysis Workflow: Figure II.5, **Figure II.6**, and **Table II.2**.

Micro-CT Analysis Workflow: Figure II.7 & Table II.3.

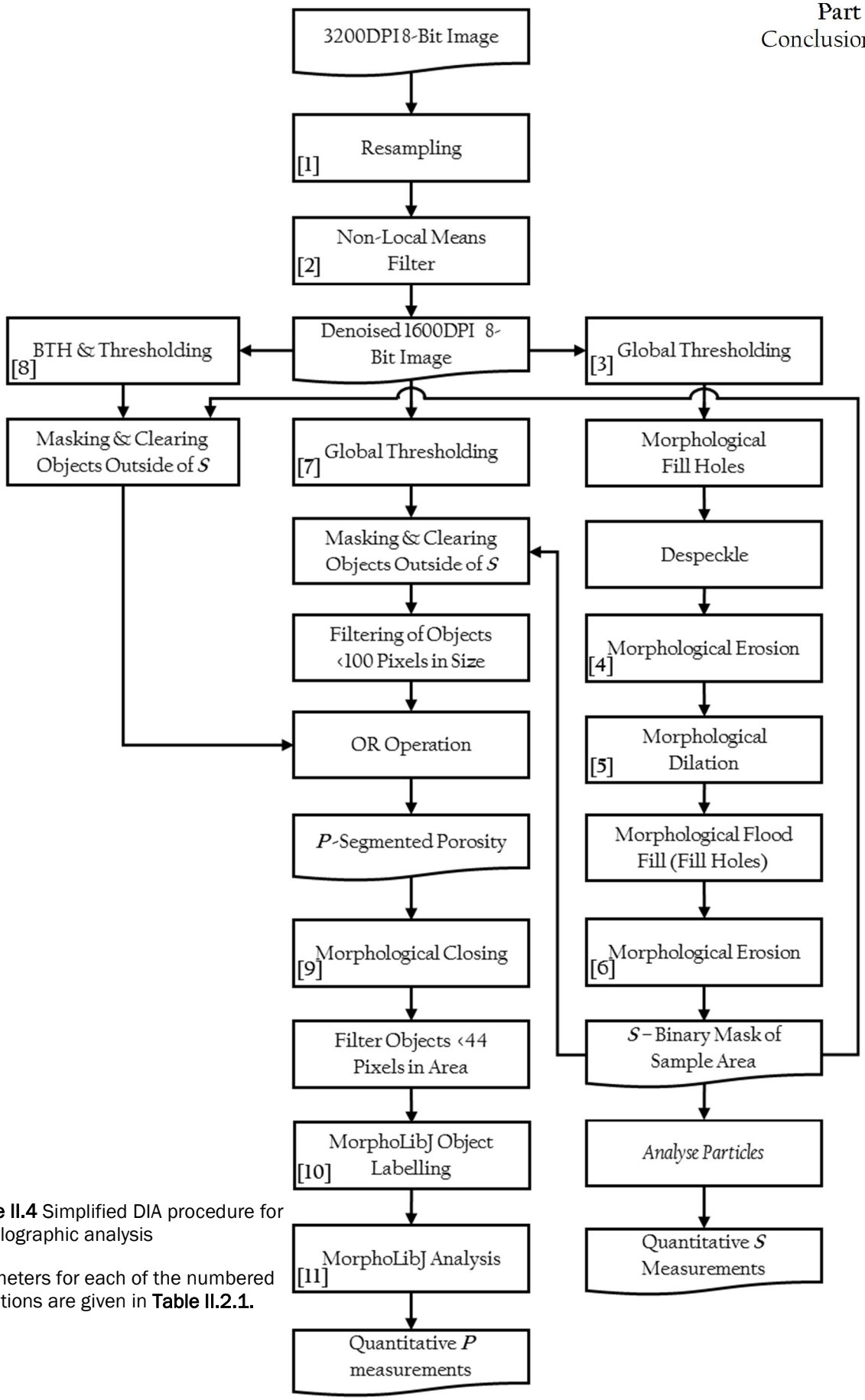

Figure II.4 Simplified DIA procedure for metallographic analysis

Parameters for each of the numbered operations are given in **Table II.2.1.**

Table II.1 Parameters used in processing & segmentation of metallographic images of RPT sample cross-sections.

Operation		User Inputs
Image Processing		
1	Image Resampling	*Mode:* Bicubic. *x- & y- rescaling factor:* 0.5
2	NLM Filter	*Sigma:* 5 *Smoothing Factor:* 1
Segmentation of RPT Area from Background		
3	Global Threshold	*Mode:* Otsu
4	Morphological Erosion	*Iterations:* 50
5	Morphological Dilation	*Iterations:* 75
6	Morphological Erosion	*Iterations:* 40
Segmentation of Porosity		
7	Global Threshold	*Intensity Range:* 0 - 125
8	Black Top hat Transformation [19] & Global-Thresholding	*Structuring Element*: Disk *Size (Radius)*: 22 *Threshold*: 50 – 255
8	MorphoLibJ [19] Object Labelling	*Module:* 'Connected Components Labelling' *Connectivity:* 8 (Pixel vertices or sides) *Type of result:* 16 bit
9	MorphoLibJ [19] Analysis	*Module:* 'Region Morphometry

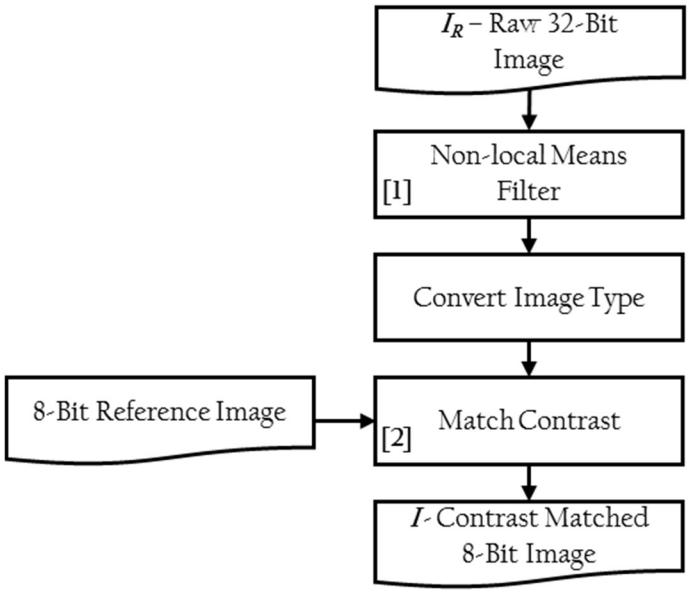

Figure II.5 Image processing procedure for macro-CT images.

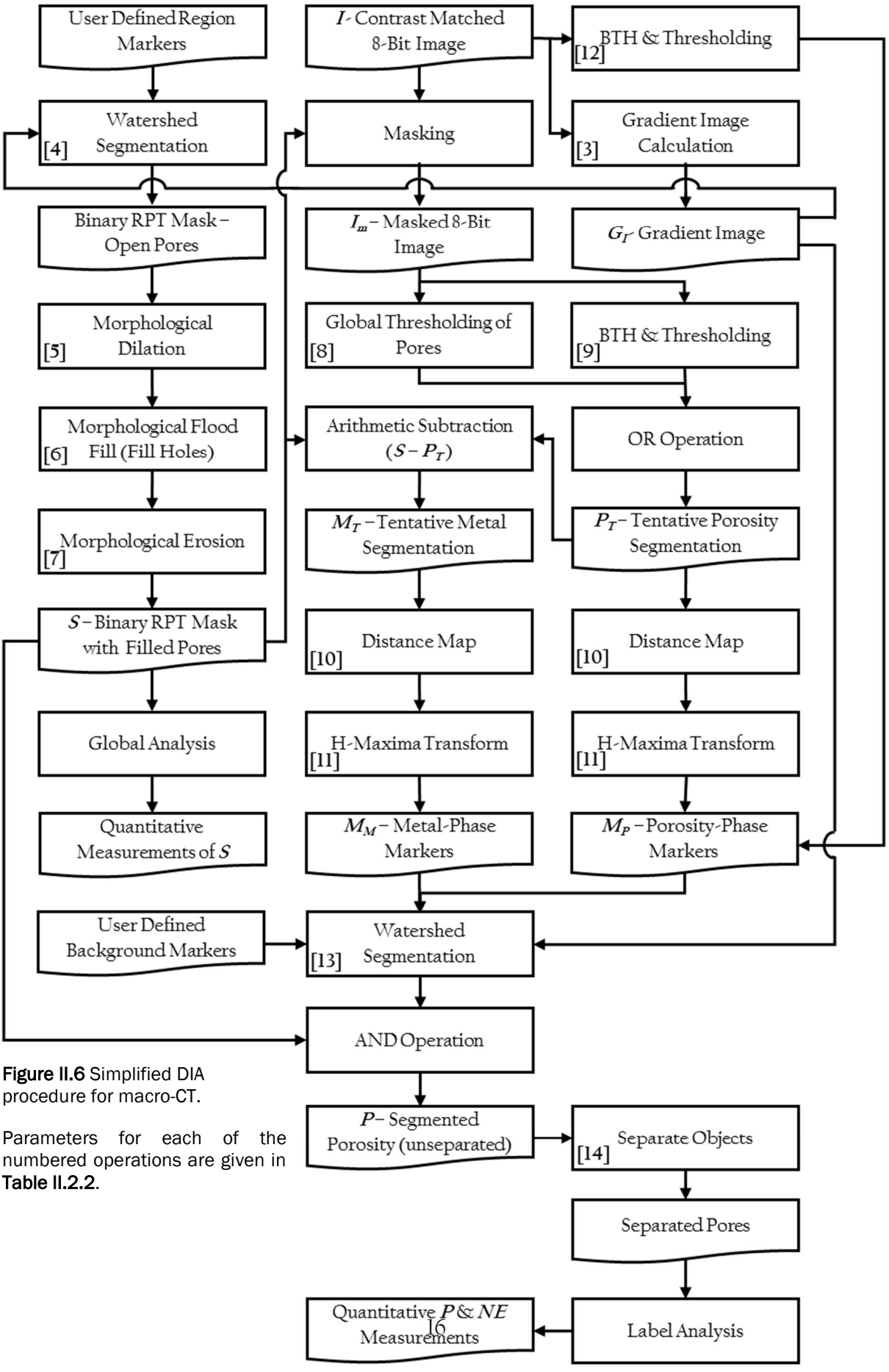

Figure II.6 Simplified DIA procedure for macro-CT.

Parameters for each of the numbered operations are given in **Table II.2.2**.

Table II.2 Parameters used in processing & segmentation of macro-CT images.

Operation		Parameters
Image Processing		
1	Non-Local Means Filter	*Search Window Kernel:* 16 voxels *Local Neighbourhood Kernel:* 4 voxels *Similarity Value:* 0.6
2	Match Contrast	*Mode:* Mean & Variance
Segmentation of RPT Casting from Background		
3	Calculate Gradient Image	*Interpretation:* 3D *Gradient Type:* Canny-Deriche [20] *Gradient Options:* Amplitude (max of input) *Standard Deviation:* 60
4	Marker-Based Watershed	*User defined markers of phases* *Split Type:* Side-by-side *Output:* Basins
5	Morphological Dilation	*Structuring Element Shape:* Ball (sphere) *Structuring Element Radius:* 13 voxels
6	Fill Holes	*Mode:* 3D *Neighbourhood:* 26 Voxel
7	Morphological Erosion	*Structuring Element:* Cube *Radius:* 16 voxels
Tentative Segmentation of Porosity		
8	Global Threshold	*Intensity Range:* 0 – 100
9	Black Top-Hat Transform	*Structuring Element:* Ball *Structuring Element Radius:* 3 voxels *Intensity Range:* 10 – 255
Defining Watershed Markers for the Metal & Porosity Phases		
10	Distance Map	*Mode:* Chamfer
11	H-Maxima Transform	Contrast Factor: 4
12	Black Top-Hat Transform	*Structuring Element:* Ball *Structuring Element Radius:* 1 voxels *Intensity Range:* 10 – 255
Segmentation of Porosity for Analysis		
13	Marker-Based Watershed	*User defined markers of background & sample holder & calculated phase markers.* *Split Type:* Side-by-side *Output:* Basins
14	Separate Objects	Contrast Factor: 4

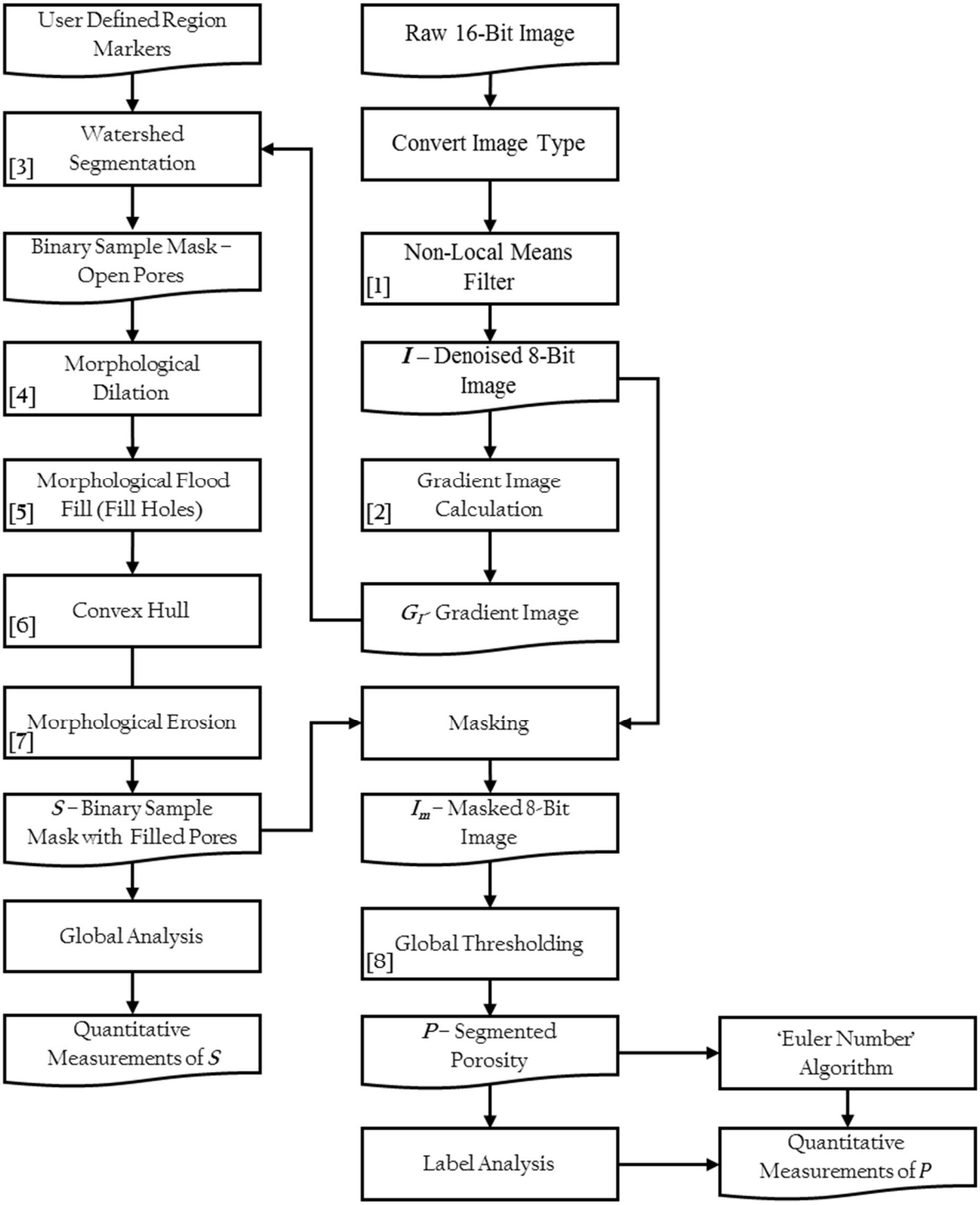

Figure II.7 Simplified DIA procedure for micro-CT. Parameters for each of the numbered operations are given in **Table II.2**.

Table II.3 Parameters used in processing & segmentation of micro-CT images.

Operation		User Inputs
Image Processing		
1	Non-Local Means Filter	*Search Window Kernel:* 16 voxels *Local Neighbourhood Kernel:* 4 voxels *Similarity Value:* 0.6
Segmentation of RPT Casting from Background		
2	Calculate Gradient Image	Canny-Deriche method [20]
3	Marker-Based Watershed	*User defined markers of phases* *Split Type:* Side-by-side *Output:* Basins
4	Morphological Dilation	*Structuring Element:* Ball *Structuring Element Radius:* 55 voxels
5	Fill Holes	*Mode:* 3D *Neighbourhood:* 26 Voxel
6	Convex Hull	*Mode:* 2D (x-y slices)
7	Morphological Erosion	*Structuring Element:* Cube *Radius:* 16 voxels
Segmentation of Porosity		
8	Global Threshold	*Mode:* 3D (entire volume) *Calculated by Otsu's Method*

Appendix III
Supplementary Material for Part III

III.1 Experiment DMX

This experiment was originally intended to be presented in the body of the thesis, as part of the Melt Quality experiments. However, due to its variable results, it was decided that it would be most appropriate to relegate it to the Appendix.

The key takeaway of this work is that the upgassing caused the removal of the oxide films that were initially added into the melt at the start of the experiment. Therefore, only the samples taken prior to upgassing can be considered dirty. It is these dirty samples that have been used in the meta-analysis that is presented in Section 7.8 of the thesis body to assist the interpretation of the results.

III.1.1 Procedure

In this experiment an attempt was made at increasing its oxide film content by adding in exogenous dross skimmings that were collected from previous experiments. A work flow of the experiment is shown in **Figure III.1**.

The dross was skimmed and collected from the melts of previous experiments using Al-7Si alloys. The skimmings contained primarily oxide films with some metallic aluminium. The dross skimmings were dried off by holding them in an oven at 300°C overnight to bake off trapped moisture, and heated over the top of the furnace to bring them up to temperature prior to its addition. The dross skimmings were then added to the melt to give a nominal

constitution of ~15wt.%. The melt was vigorously hand stirred for ~3 minutes to aid its incorporation into the melt.

Two important aspects of this work was that the surface oxide was intermittently skimmed off, and that the melt was bottom stirred (as shown in Figure 4.10 of the thesis body) to prevent settling of the inclusions prior to sampling.

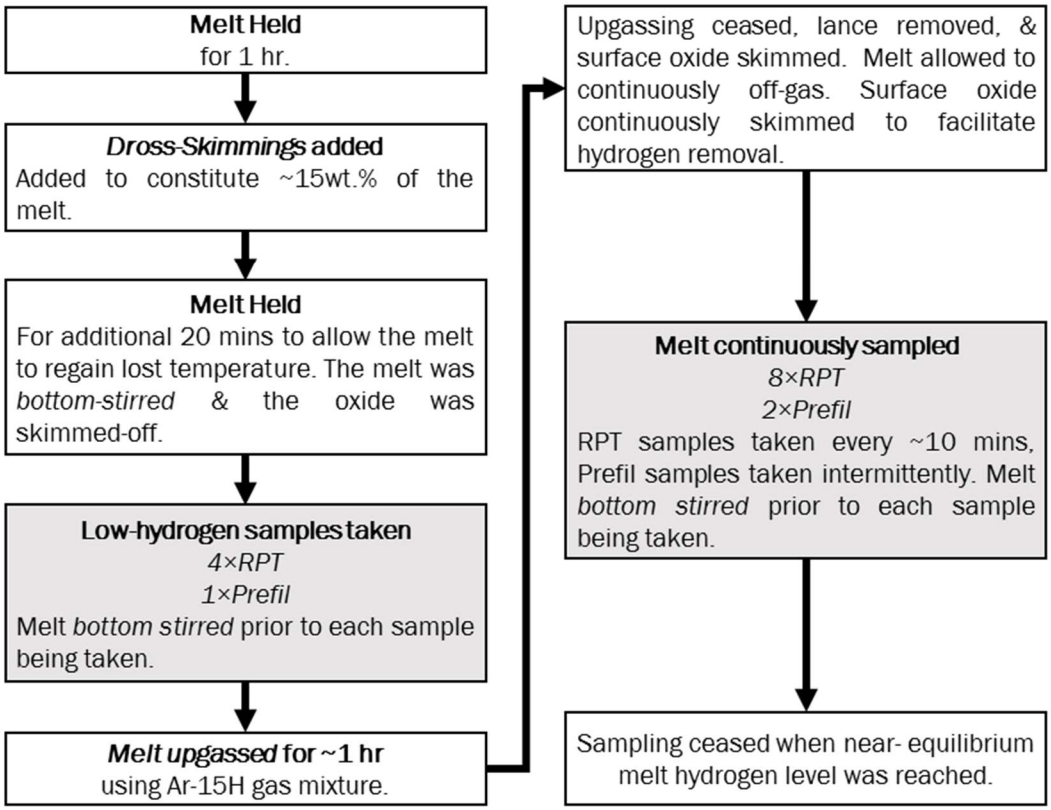

Figure III.1 Experimental procedure for experiment DMX.

III.1.2 Results

Changes in the f_p and hydrogen content are given in **Figure III.2**. Only the samples that are indicated were used in the meta-analysis in Section 7.8 of the thesis body. The results of the PoDFA analysis of the Prefil samples taken over the course of the experiment (as

indicated on **Figure III.2**) are given **Table III.1**. Micrographs from the SEM microanalysis of the Prefil samples are shown in **Figure III.3**, and a summary of observations and the 'Cleanliness Rating' made based on the microanalysis are given in **Table III.2**.

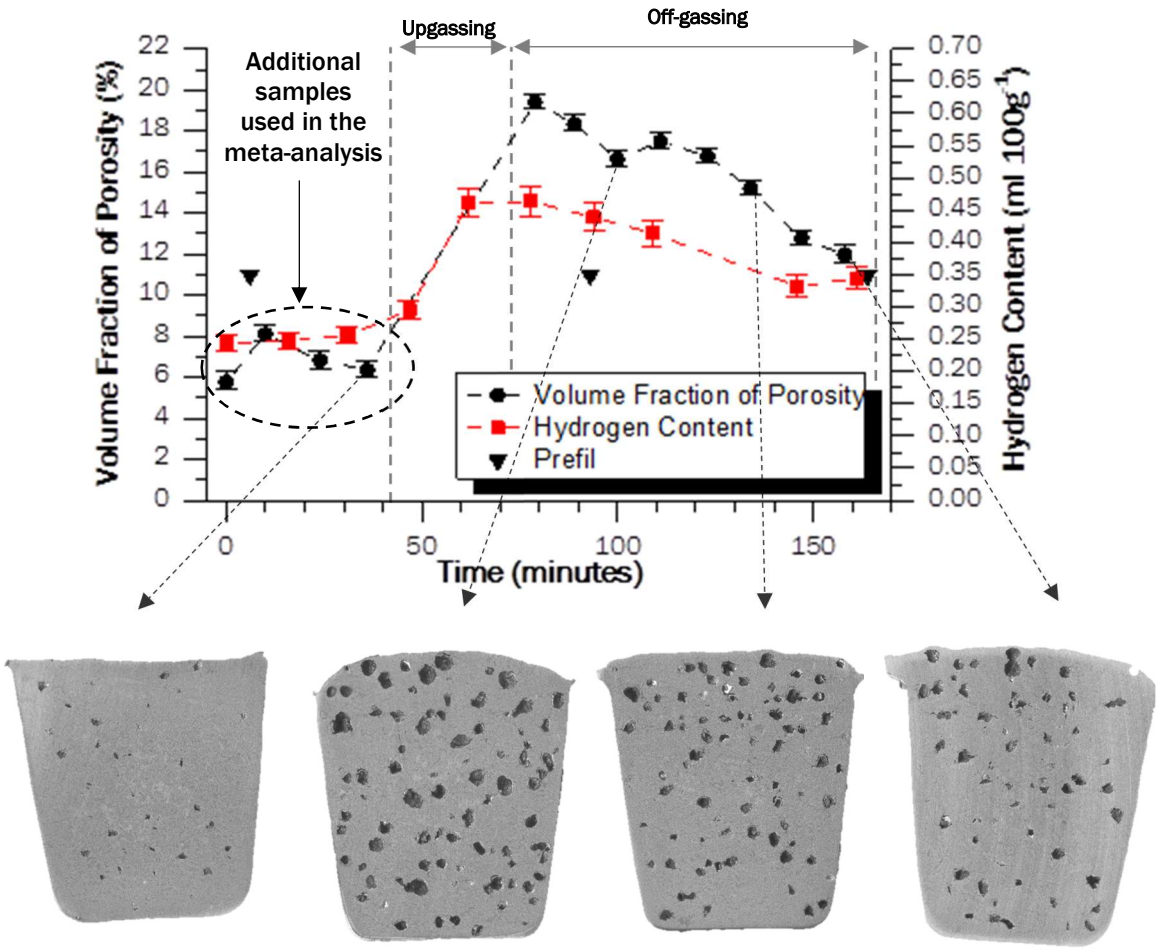

Figure III.2 f_p and melt hydrogen content versus time, and selected of metallographic cross-sections of RPT samples, from experiment DMX.

Table III.1 Premetz MC values and complete PoDFA analysis results from DMX experiments.

Exp.	Sample #	Relative Sampling Time (min)	MC	PoDFA						
				Oxide Films (#/kg)	Refractory		Crucible Fragments (mm^2/kg)	α-Al_2O_3 (mm^2/kg)	Borides (mm^2/kg)	Total Inclusion Count (mm^2/kg)
					Reacted (mm^2/kg)	Unreacted (mm^2/kg)				
DMX	1	6	8.6	43	0.0004	0.012	0.057	0.012	0.029	0.101
	2	93	3.2	33		0.033	0.010	0.002	0.004	0.048
	3	164	3.4	15		0.001	0.004	0.017	0.001	0.023

Blank cells indicate that no amount of the given inclusion species were measured, while 'trace' indicates that trace amounts of the inclusion species were observed, though not in measurable amounts.

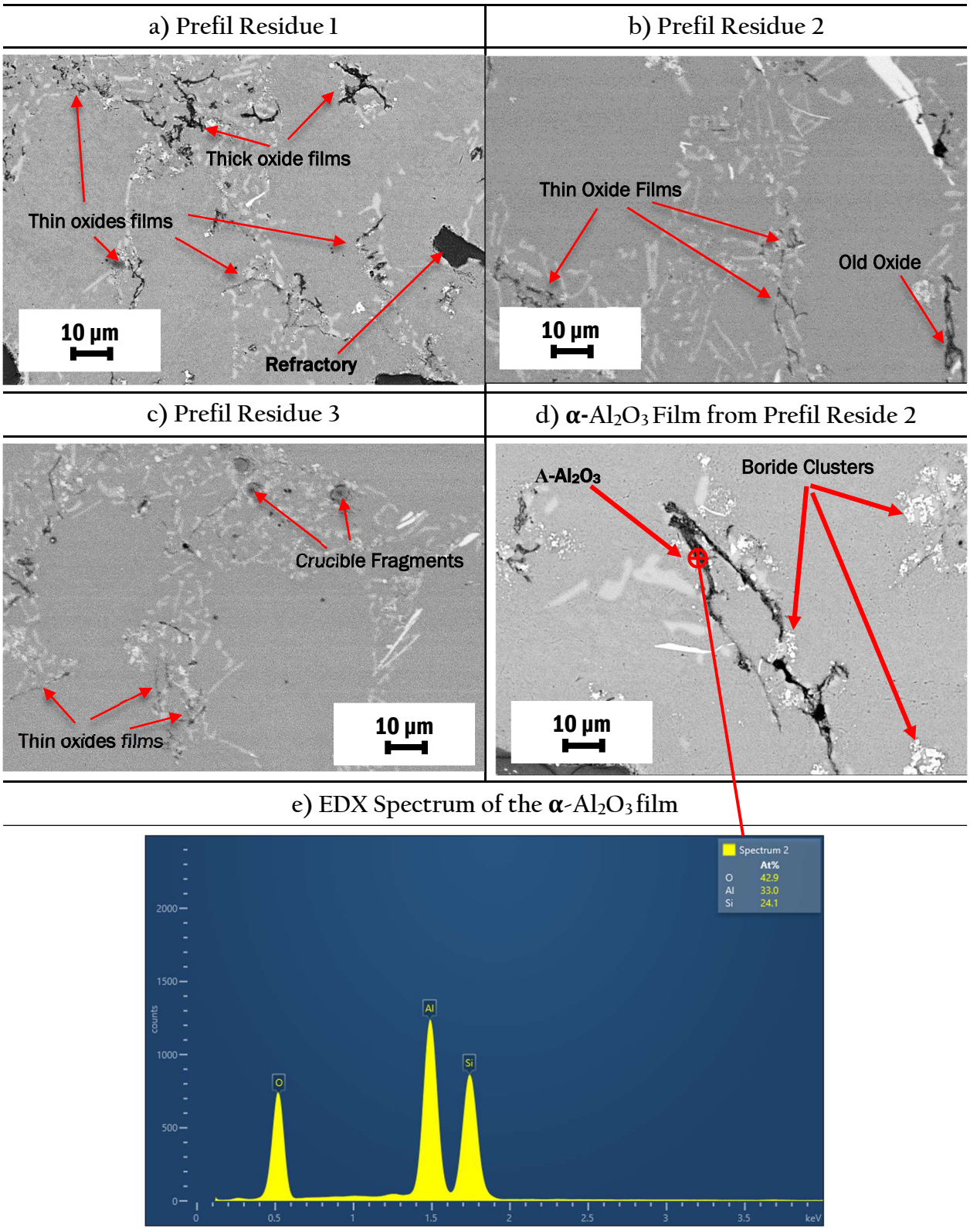

Figure III.3 BSE micrographs from DMX Prefil samples, showing a), b), and c) typical microstructures, d) an example of an old oxide film fragment, and e) and EDX spectrum of the old oxide fragment in d).

Table III.2 The 'Cleanliness Rating' of each Prefil Sample from SEM (BSE) microanalysis and a summary of the observations. The Cleanliness Rating givens a qualitative estimate of the number of oxide films in the material made by the SEM user based on the observations that were made during the analysis. A value of 1 represents a clean metal, with a very low oxide content, whilst a value of 10 represents a dirty metal, with a high oxide film content. This should be taken only as a ballpark estimate of the relative oxide contents between the experiments.

Prefil No.	Cleanliness Rating (1 – 10)	Summary of Observations
1	7	Numerous oxide films (**Figure III.3**a)) along with many thin, and probably young, oxide films that were generally small in size were observed. A relatively large fraction of thick, and probably old, oxide films which likely originate from the exogenous dross skimmings, or from scrap on the crucible wall were also seen. EDX analysis (**Figure III.3** e)) confirms the composition of old oxides to be oxygen rich, and when Si is omitted from the spectrum the stoichiometry of the particle is very close to that of Al_2O_3 at 44(at.%)Al-56(at.%)O.
2	4	Few and sparely distributed young oxides, though there were still some thick, old oxides present in the melt. The overall number of oxide films had been significantly reduced by the upgassing process. Old oxides might remain because of resuspension during bottom stirring.
3	4	

III.1.3 Discussion on the Effect of Upgassing on Melt Cleanliness

Based on the results, it seems that the addition of dross skimmings in DMX seems to have had mixed effects on the oxide film content of the melt. A combination of thin and thick oxide films were observed in the melts prior to upgassing (Prefil 1), though after upgassing, far fewer oxide films were observable, which is a result of their assisted floatation by the gas bubbles [13],[22]. Once at the surface of the melt, the dross layer, and the oxide films were skimmed off! In retrospect, this is clearly what largely cleaned up the melt – as the floated inclusions were not reincorporated back in by stirring. The constant bottom stirring of the melt after upgassing may have resuspended any sedimented films and other inclusions in the melt – which would explain the high levels of refractory and other inclusions in the metal.

Because there is not an appreciable change in the PND of the RPT samples after upgassing, it can be concluded that the resuspended inclusion species that were found in the do not have a significant effect on porosity, at least at the concentrations that they are present in the experiment. This is an important result that will be discussed further in the coming sections.

If the oxide films act as nuclei for pores – as has been discussed in Section 9.4 of the body of the theses – the pore number density (PND) should be indicative of the number of nuclei. **Figure III.4** shows, the PND in DMX drops sharply after upgassing which would evidence their removal from the metal. A decrease in PND with upgassing can also be seen in CM2, though to a much lesser extent. This would explain the decrease in the number of oxide films that were observed during SEM microanalysis of the Prefil samples that taken after upgassing – though the melt was subsequently dirtied as the melt was handled, which results in a small increase in the PND.

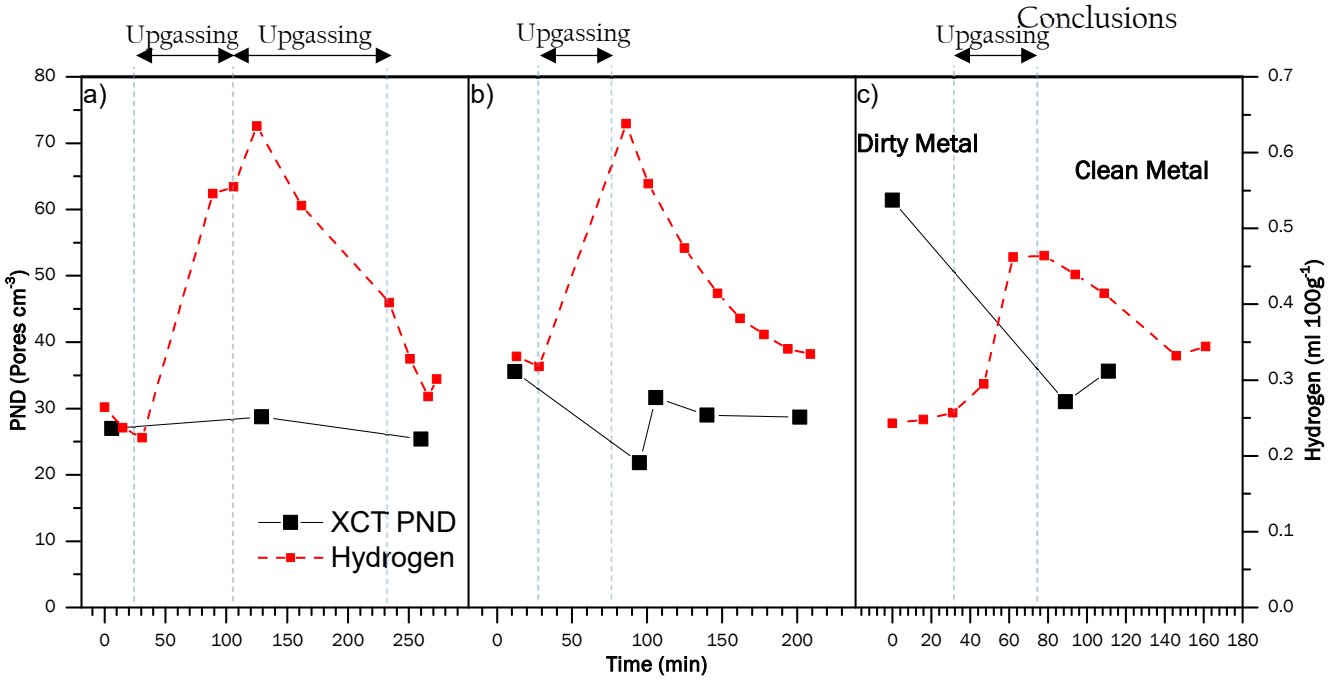

Figure III.4 The change in PND and NED measured by macro-CT in a) CM1, b) CM2, and c) DMX.

III.2 SEM Analysis of the 'Particle Cluster' Inclusions Present in CM1

PoDFA analysis of the Prefil samples taken from CM1 revealed the presence of an unknown 'particle cluster' species of inclusion as shown in **Figure III.5**.



Figure III.5 Visual light micrograph taken at 500× magnification showing the presence of numerous Oxide Film Inclusions

EDX analysis of these inclusions (**Figure III.6**) revealed that they were rich in copper. It is likely that these particles are $CuAl_2$, and traces of the other elements are simply the result of interaction of the beam with the surrounding substrate, as phases and inclusions containing these elements are all segregated to the interdendritic regions. $CuAl_2$ forms in copper containing alloys during the final stages of solidification.

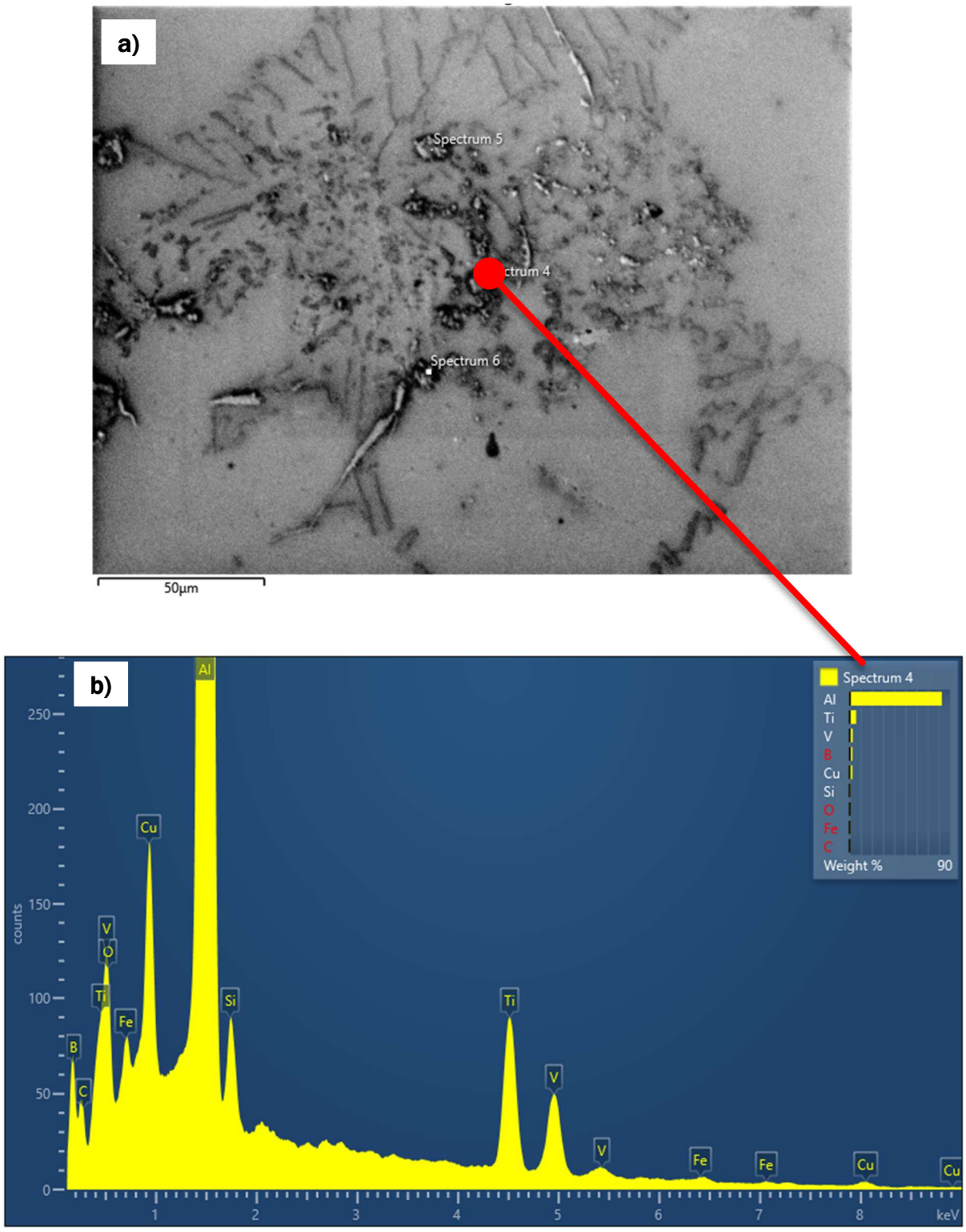

Figure III.6 a) Secondary electron image of the particle cluster inclusions, and b) the EDX spot-analysis spectrum.

III.3 Additional Metallographic Measurements

Here some additional metallographic of the porosity in RPT sample sections are presented.

III.3.1 Melt Quality Experiments

The areal size-shape distributions of pores in the clean RPT samples versus their hydrogen content are shown in **Figure III.7**, supplementary plots to the results in Section 7.6.1.

A comparison of the areal size-shape distributions of pores in clean and dirty RPT samples are shown in **Figure III.8**, supplementary plots to the results in Section 7.7.1.

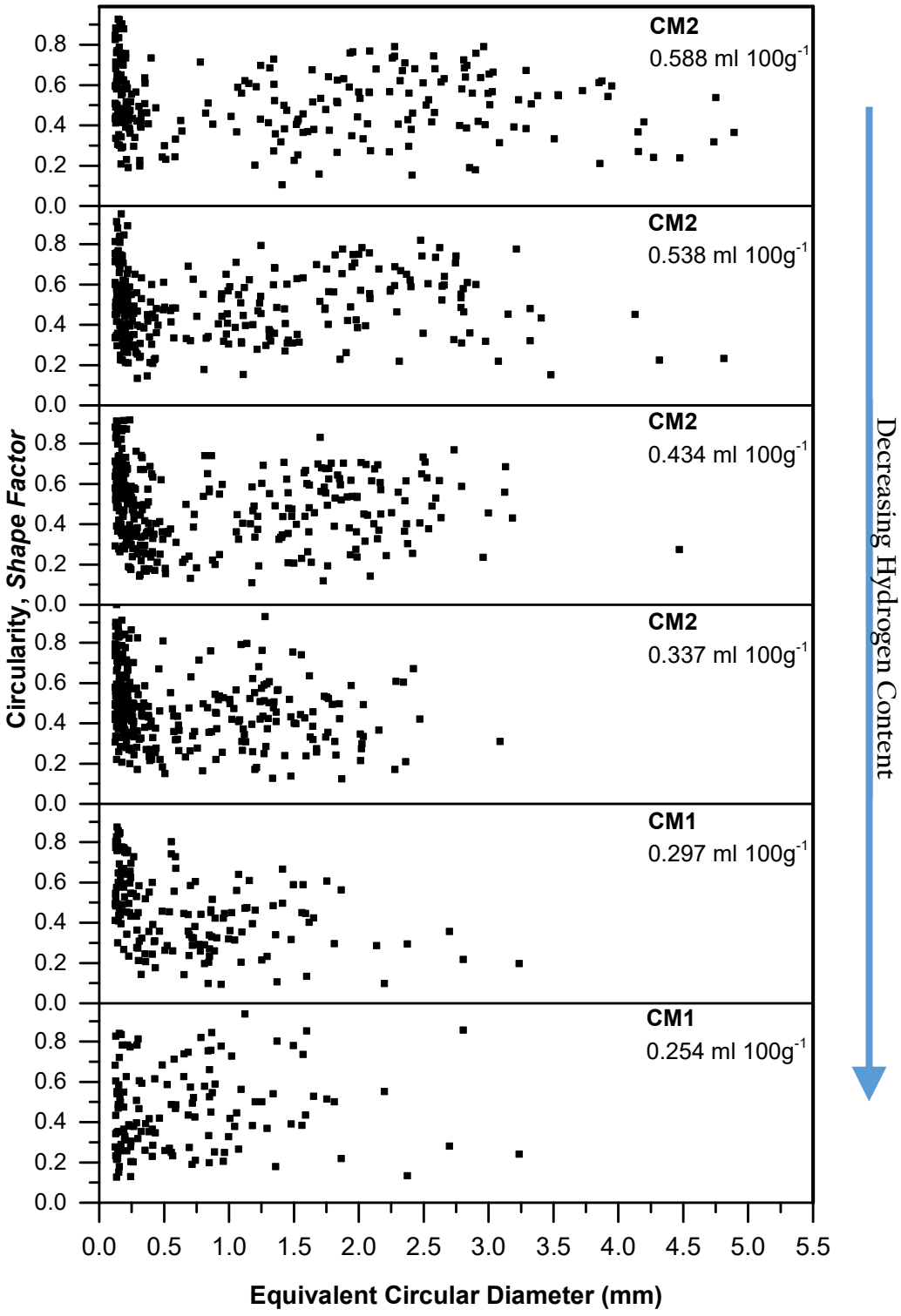

Figure III.7 2D metallographic pore size-shape distribution in clean metals with different hydrogen contents.

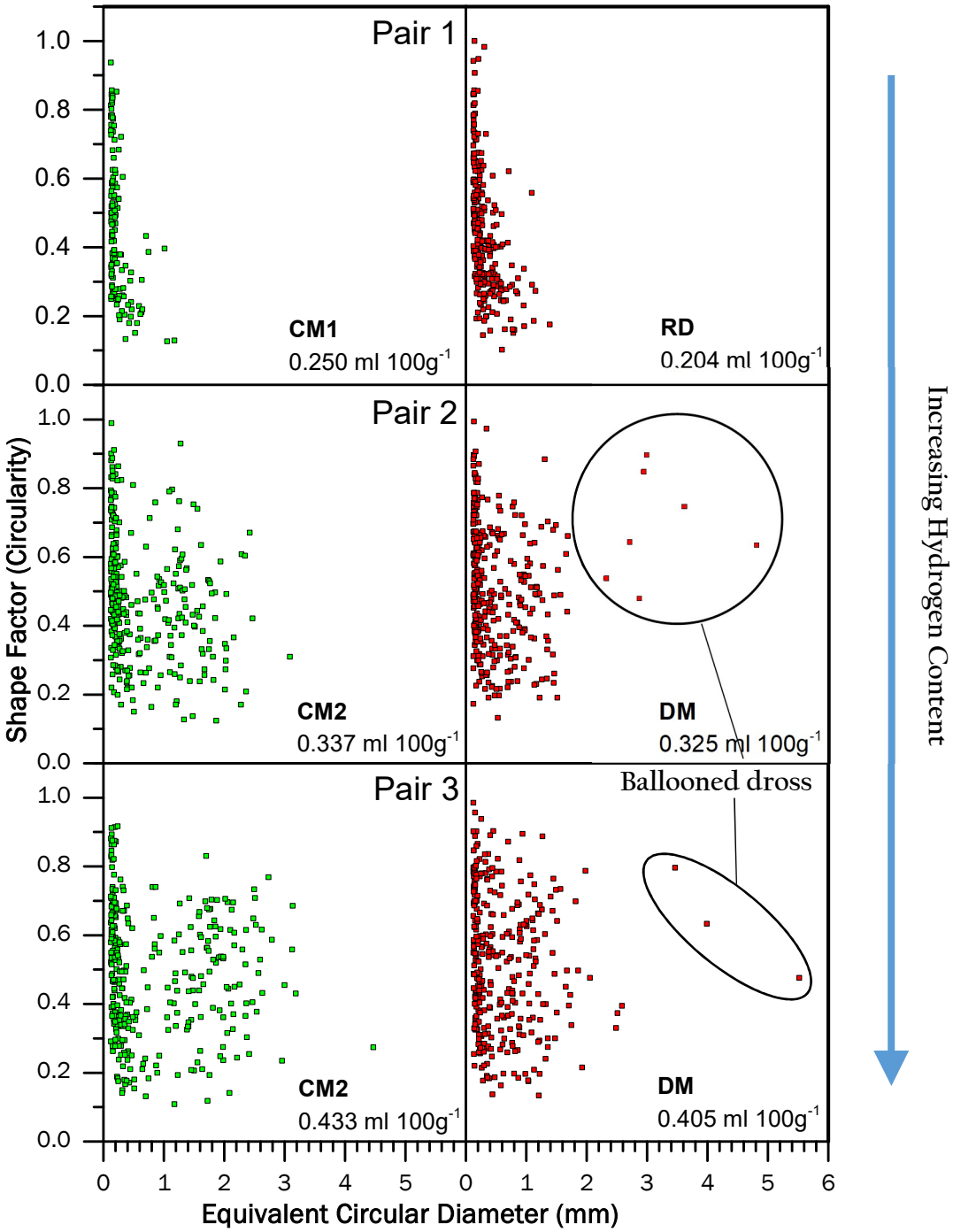

Figure III.8 2D size-shape distribution of pores in clean and dirty metal, measured by metallographic analysis

III.3.2 Grain Refiner Addition Experiments

The areal size-shape distributions of pores in RPT samples from GR1 shown in **Figure III.9**, supplementary plots to the results in Section 8.5.1.

A comparison of the areal size-shape distributions of pores in RPT samples from GR1 are shown in **Figure III.8**, supplementary plots to the results in Section 8.5.2.

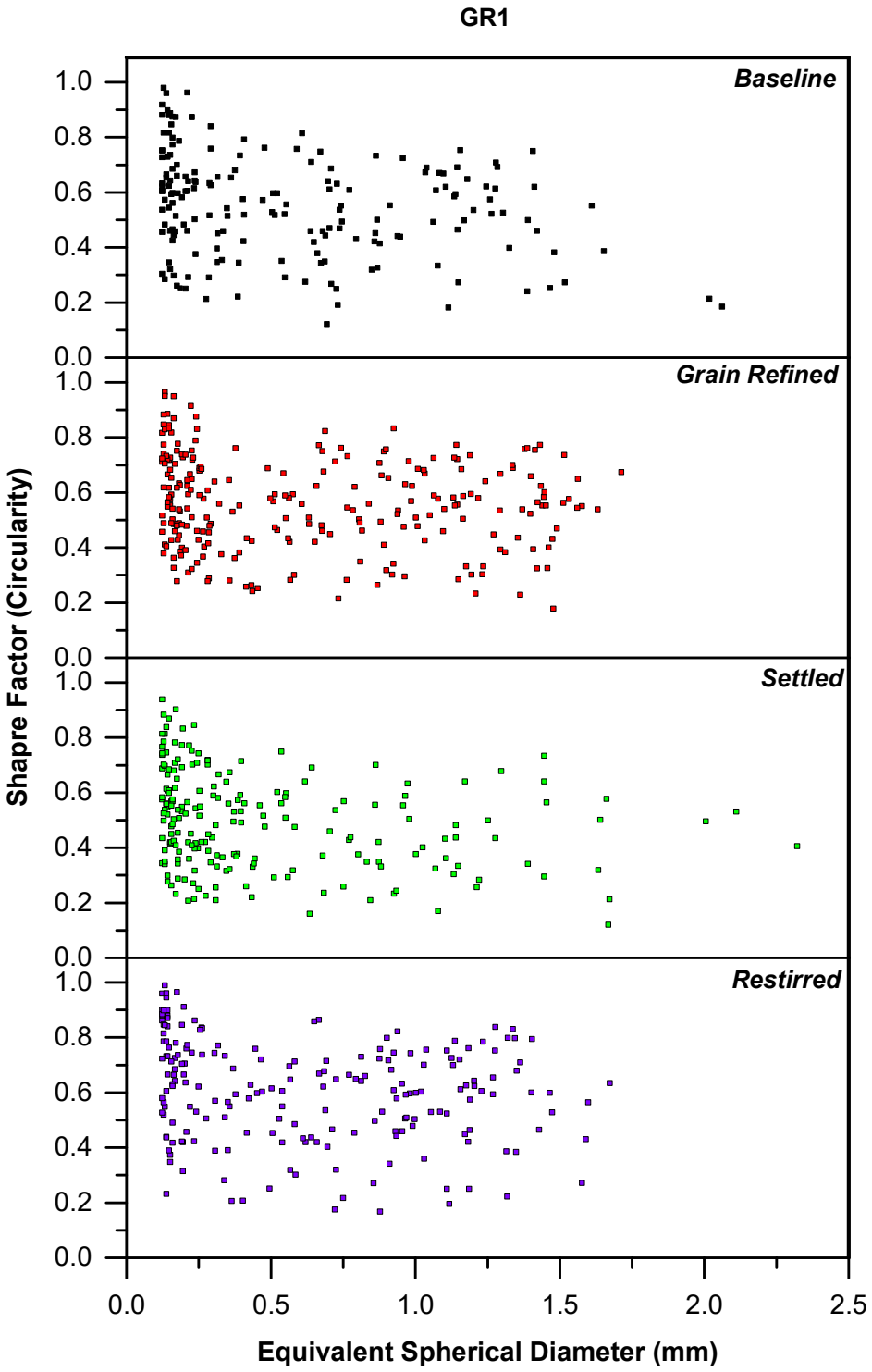

Figure III.9 Pore size-Shape distribution from the metallographic analysis of selected RPT samples from GR1

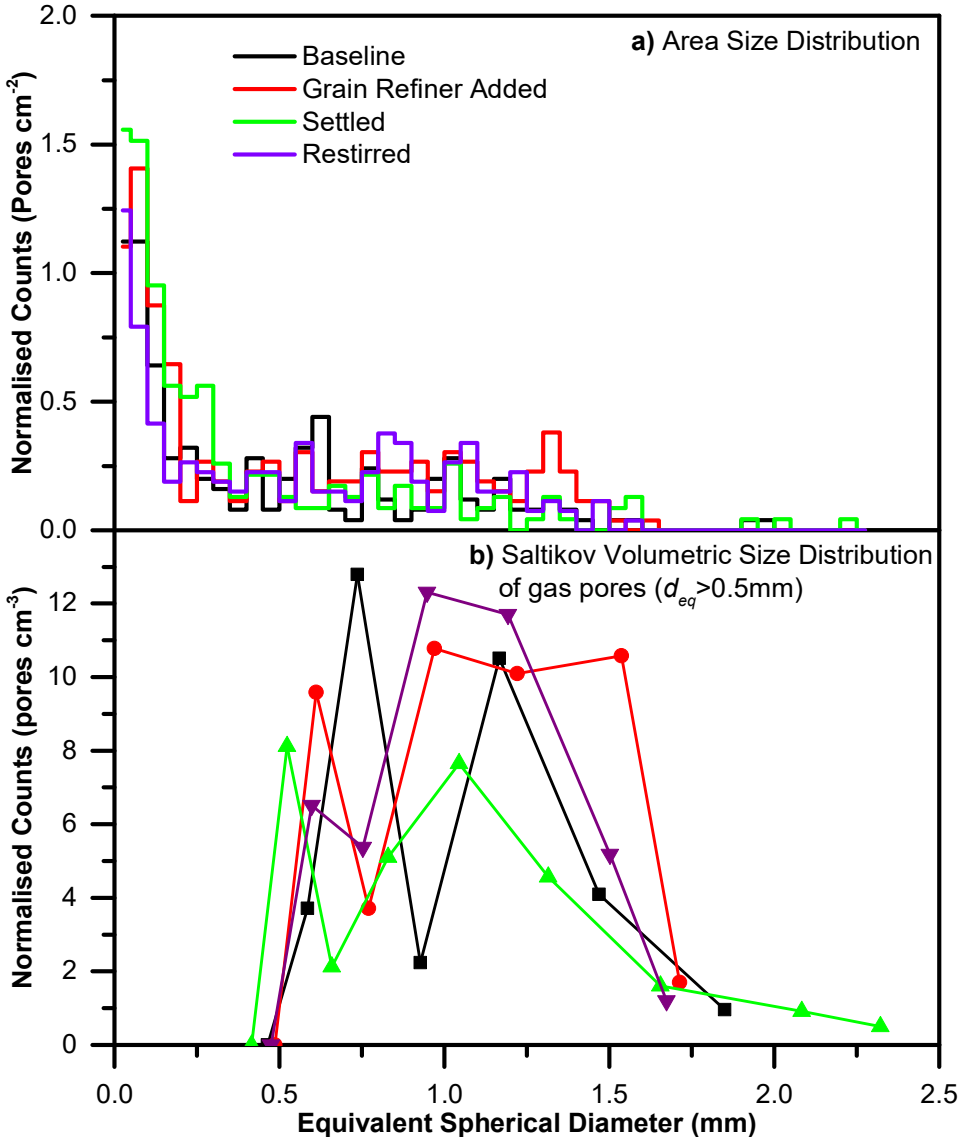

Figure III.10 a) areal size distribution of pores, and b) volumetric distribution of gas pores in selected RPT samples from GR1 measured by Metallographic analysis.

III.4 Grain Refiner Addition Studies: Solidification Curves

Temperature-time solidification curves were measured *in situ* during the RPT for the *Baseline* and *Grain Refined* melts in GR1 in order to understand if grain refiner caused any major changes to the solidification time of the alloy. This was conducted using the procedure described in Appendix IV.1.1.2. **Figure III.11** shows that the addition of grain refiner did not have a measurable effect on the solidification times of the α-Al or the eutectic solidification, but it did decrease the undercooling required to nucleate these phases.

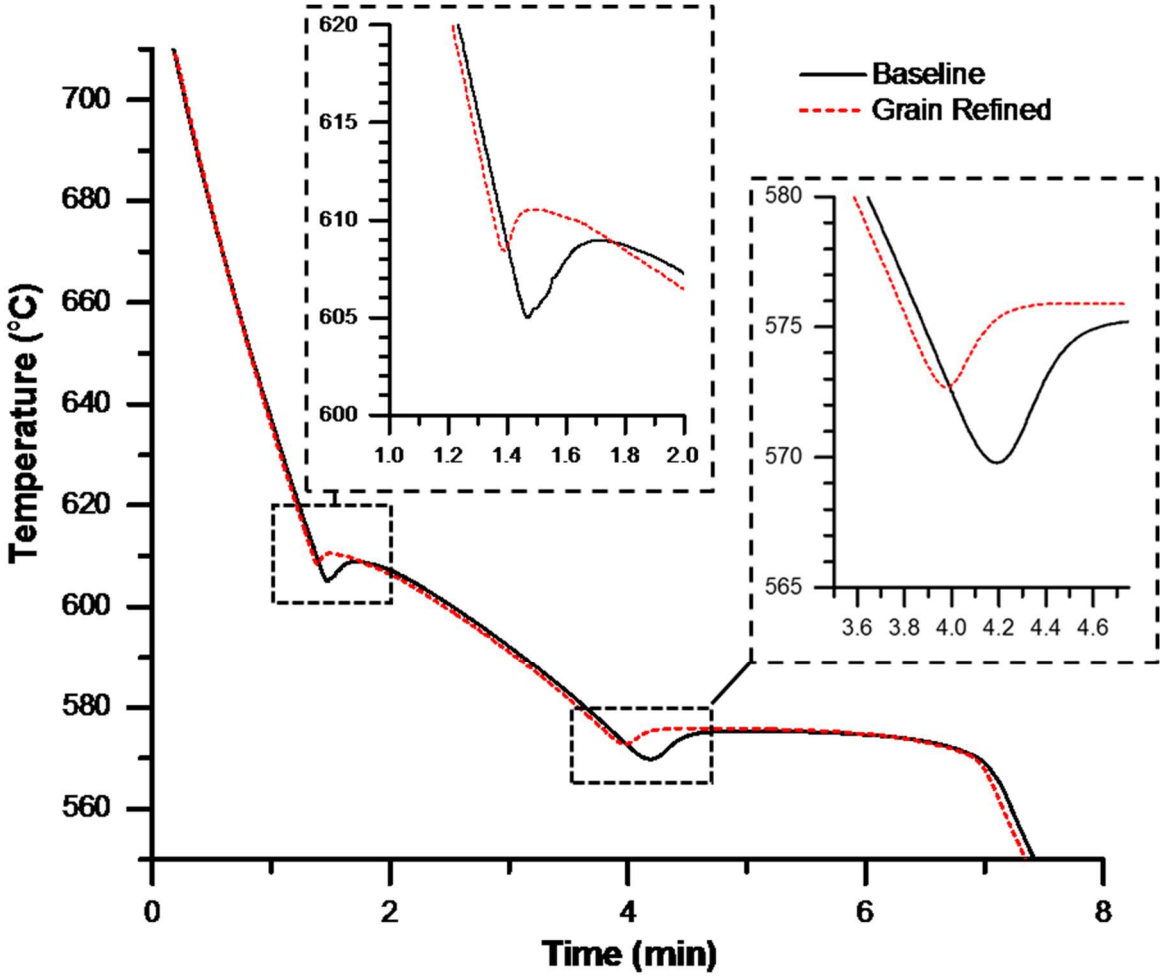

Figure III.11 Temperature-time cooling curves measured *in-situ* during the RPT during the *Baseline* and *Grain Refined* in experiment GR1 of the Grain Refiner Addition experiments.

Appendix IV
Ancillary Experimental Work
RPT Porosity Retention Experiments

This ancillary work was originally intended to be the first chapter of experimental work to be presented in this thesis. Although, as the scope of the thesis was refined, in the interest of brevity, it was deemed necessary relegate to the Appendices. This ancillary experimental work investigated the dependency of the porosity formed during the Reduced Pressure Test (RPT) on the solidification characteristics of the Al-7Si test alloy.

This work was spurred by the inconsistent porosities formed in RPT samples in experimental work that was performed early on during this project. An example of this is given in **Figure IV.1**, which shows that repeated trials with the RPT yielded different volume fractions and structures of porosity in successive samples cast under similar conditions.

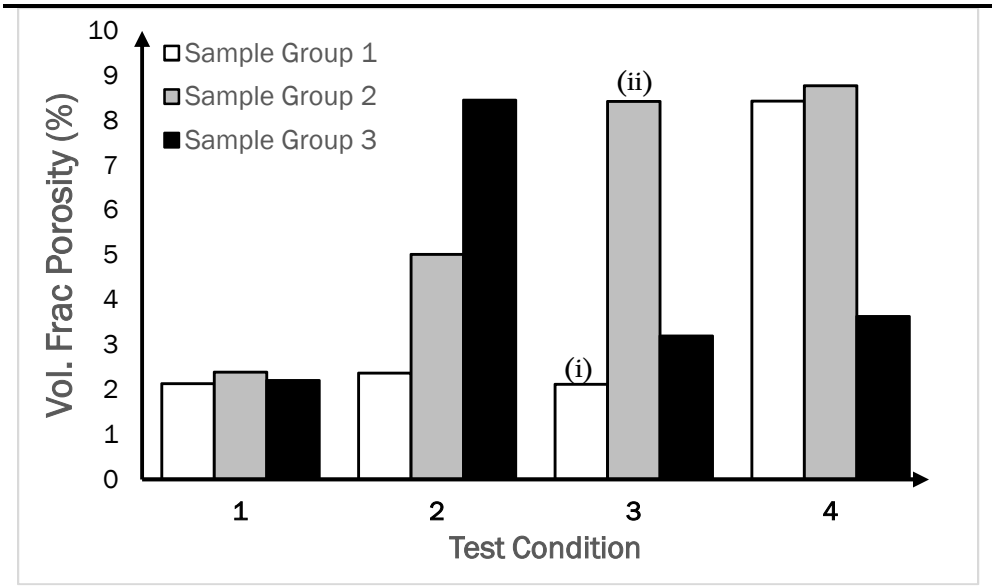

a)

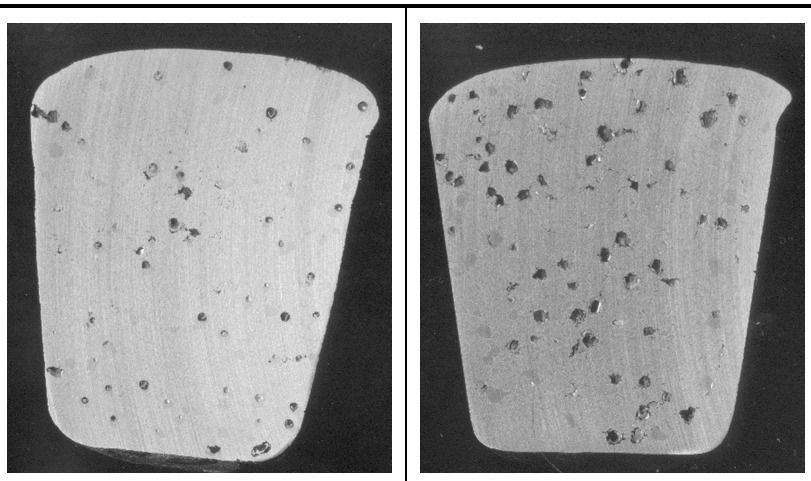

Condition 3 Sample (i) | Condition 3 Sample (ii)

b)

Figure IV.1 An example of an experiment where inconsistencies in the a) volume fraction of porosity, and b) the structure porosity in RPT samples taken in successive sample groups (trials).

IV.1.1 Experimental Procedures

In the first phase of experiments, an investigation was conducted to determine the effect of alloy solidification characteristics on the outcome of the RPT, and to select suitable RPT parameters based on the findings.

Binary Al-7Si alloys were used for the majority of the experiments, though on this occasion only, ancillary experiments were also conducted using a binary Al-3Si alloy so that the effects of the solid fraction and the formation of the eutectic phase could be examined. A list of the experiments that were performed is given in **Table IV.1**.

Table IV.1 Experimental IDs for RPT Parameter Selection.

ID	Alloy	Experiment
VD1	Al-7Si	*RPT duration (Vacuum duration)*
VD2		
VD3		
VD4	Al-3Si	
SC1	Al-7Si	*Temperature-time solidification curves*
SC2		
SC3		
SC4	Al-3Si	

The melts were prepared as described in Section 4.1 in the main thesis body, and held for 2 hours to allow for *self-cleaning* (as is outlined in Section 4.5.5).

IV.1.1.1 Selection of RPT Duration

Experiments were conducted where the duration of the applied vacuum was varied in order to examine what effect its termination at various stages during sample solidification

would have on the porosity inside the samples. RPTs were conducted as described below in Section 4.4 of the main thesis body, with the only difference being the variable test durations.

Upon termination of the vacuum in each test, the sample was left undisturbed for 9 minutes to ensure that it was fully solidified before it was handled to prevent any disturbance of the pores in the semi-solid material.

IV.1.1.2 In Situ Temperature – Time Solidification Curves

Temperature-time solidification curves were collected *in situ* from RPT samples to determine the solidification behaviour of the Al-7Si. A diagram of the experimental setup is shown in **Figure IV.2**. The primary objective of this work was to obtain the shape of the cooling curve, and the times at which each phase formed during the RPT.

K-type thermocouples (RS Components Ltd.) were used to measure the temperature at the centre of the solidifying samples and the data were logged using a PicoTechnology TC-08 data logger at 100ms intervals. The accuracy of these thermocouples is ±0.75% of the measured temperature. Prior to the experiments the thermocouples were dipped into the melt alongside a designated reference k-type thermocouple to check for any discrepancies in their measurements, however none was observed for any of the thermocouples.

The RPTs were taken in accordance with the procedure in Section 4.4 of the main thesis body, though the vacuum was terminated manually after the sample cooled below 500°C. Temperature-time curves were measured for a variety of cooling rates by varying the temperature of the refractory cup holders used in the tests. Tests were conducted with the cup holders at room temperature, and at ~250°C, and at ~500°C. The cup holders at elevated

temperature were heated in ovens that were set 10°C above their target temperatures, for at least 2 hours.

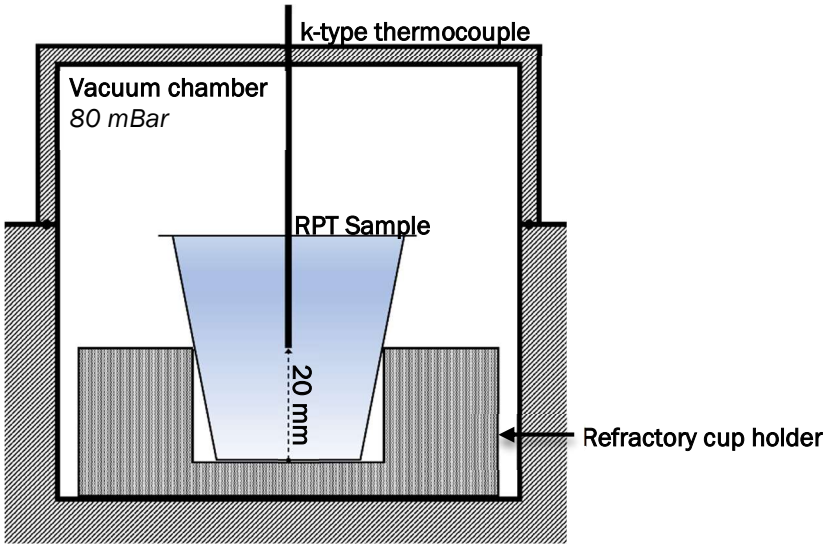

Figure IV.2 Diagram of the setup for the *in situ* measurement of the temperature-time solidification curve during the RPT.

IV.1.2 Melt Compositions

A summary of melt compositions from each experiment are listed below in Table **IV.2**.

Table IV.2 Alloy compositions by experiment. The Al-3Si alloy is indicated in grey.

Exp.	Elemental Content (wt.%)								
	Si	**Fe**	**Cu**	**Mg**	**Zn**	**Ti**	**V**	**Al**	**Others**
VD1	6.8	0.21	0.001	0.007	0.013	0.006	0.006	92.93	0.05
VD2	7.4	0.23	0.012	0.004	0.006	0.006	0.003	92.34	0.03
VD3	7.0	0.24	0.010	0.004	0.006	0.006	0.004	92.69	0.02
VD4	3.3	0.21	0.003	0.006	0.005	0.004	0.005	96.42	0.03
SC1	6.8	0.21	0.001	0.007	0.013	0.006	0.006	92.93	0.05
SC2	7.4	0.23	0.012	0.004	0.006	0.006	0.003	92.34	0.03
SC3	7.5	0.02	0.001	0.005	0.005	0.006	0.005	92.47	0.01
SC4	3.3	0.21	0.003	0.006	0.005	0.004	0.005	96.42	0.03

IV.1.3 RPT Duration & Retained Porosity

IV.1.3.1 Observations of Bubble Formation during the RPT

The solidifying samples were monitored through a viewing port at the top of in the RPT vacuum chamber to determine at which point gas bubbles were formed during solidification. A freeze-frame sequence taken from a video recording of the solidification of one of the samples cast in experiment VD3-Trial 2 is shown in Figure **IV.3**. Unfortunately because of the old age of the RPT apparatus, its viewing port has become obscured, which made video recording difficult. This combined with the small size of the bubbles means that bubbles are extremely difficult to resolve in this image sequence. Anecdotal evidence is therefore provided, as bubbles at the surface of the casting and other characteristics were still clearly observable by the operator. Moreover, the point at which bubbles nucleate is likely highly dependent on the hydrogen level, and would occur earlier on in RPTs cast from melts with high hydrogen contents.

Approximately 20 seconds after the start of the RPT, bubbles were observed to be breaking at the surface of the sample. This continued until approximately the 3 minute mark when the sample began to 'mushroom' (Figure **IV.3** b)). The sample seemed to mushroom to its maximum height approximately 3 minutes and 10 seconds after test initiation (Figure **IV.3** c)). In the tests where the vacuum was terminated prior to approximately 4 minutes and 20 seconds, the mushrooming collapsed, whereas when the vacuum was terminated at time after approximately 4 minutes and 20 seconds, the mushrooming of the samples was retained and no change to their external shape was observed. Although anecdotal evidence, and highly subjective, these observations suggest that porosity that is measured in the RPT

samples after the termination of the test is not simply a measure of the porosity formed, but a measure of the *retained porosity*.

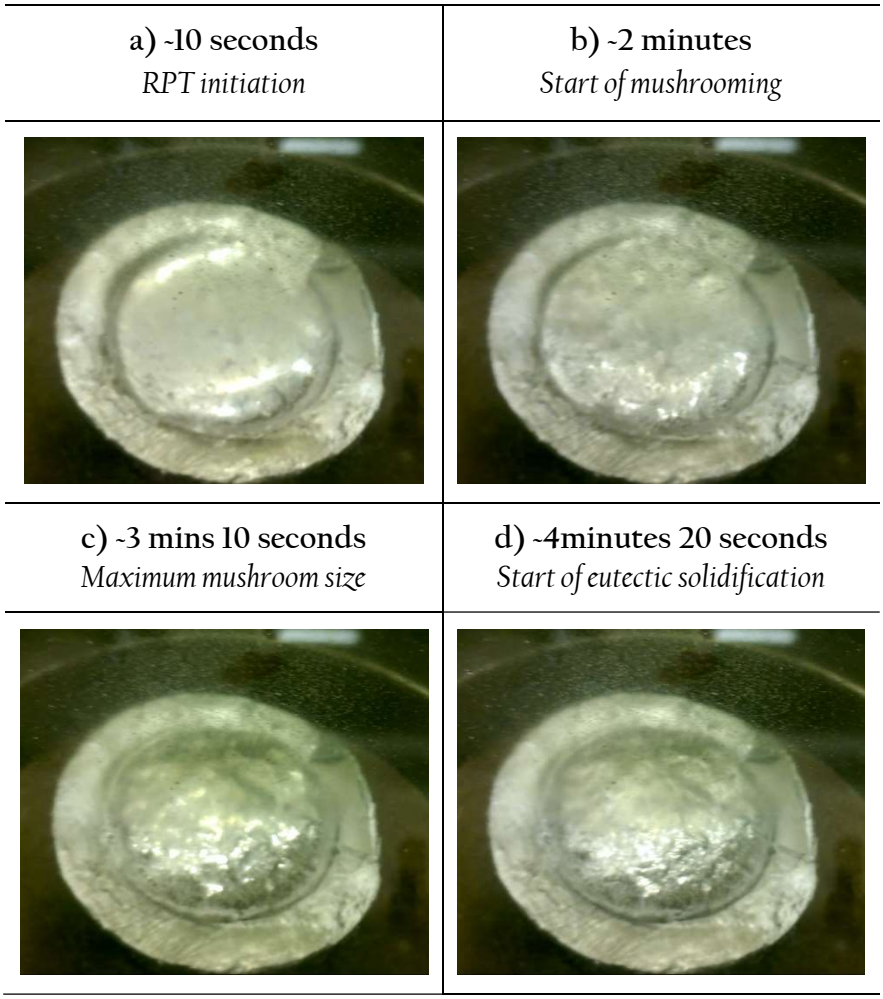

Figure IV.3 Freeze frames of alloy solidification in the RPT.

IV.1.3.2 Retained Porosity versus RPT Duration

Figure IV.4 shows a plot of the *retained porosity* in the samples versus the RPT duration. Each experiment was conducted with the melt hydrogen at equilibrium with the environment, hence, as a result higher volume fractions of porosity were developed in samples when the melt hydrogen level was higher. The melt hydrogen content range over the

duration of each trial is listed in Table **IV.3**. Despite the broad range of hydrogen contents of the melts used in the trials, a common trend can be observed in the data, where the retained porosity in the samples remains relatively low until approximately 4 minutes and 20 seconds, after which it spikes sharply. The retained porosity seems to plateau after this point, with further vacuum time yielding no appreciable increase in the volume of retained porosity. In the samples with test durations of less than 4 minutes and 20 seconds, it can be seen that the retained porosity in the RPT samples gently increases with vacuum time.

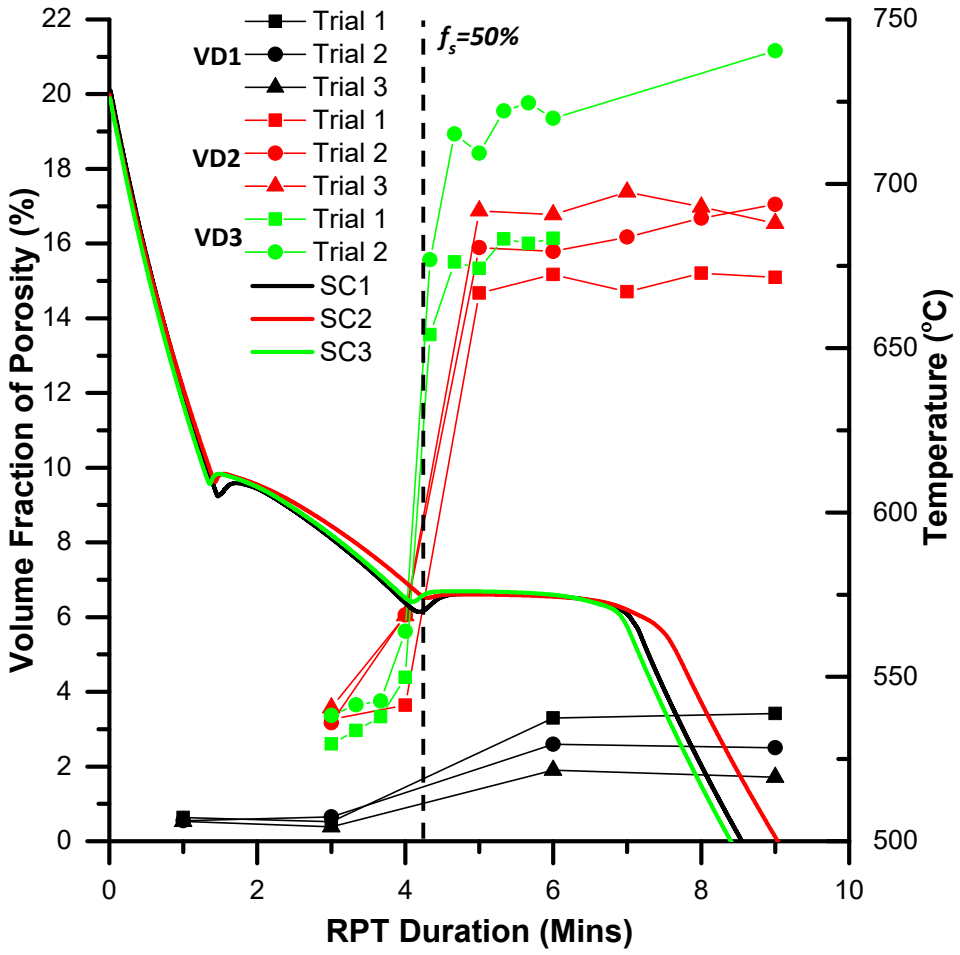

Figure IV.4 RPT duration versus fraction of retained porosity in the RPT samples, and *in situ* temperature-time solidification curves.

Table IV.3 Melt hydrogen contents in each trial of the RPT vacuum duration experiments measured using the AlScan.

	Melt Hydrogen Content ($ml\ 100g^{-1}$)		
	Trial 1	*Trial 2*	*Trial 3*
VD1	0.23 – 0.25	0.23 – 0.24	0.22
VD2	0.40 – 0.42	0.43 – 0.45	0.44 – 0.5
VD3	0.36 – 0.37	0.39 – 0.46	-

IV.1.4 Temperature-Time Solidification Curves

The temperature-time solidification curves collected *in situ* from the samples during the RPT from multiple experiments are shown overlaid on Figure **IV.4**. Notable measurements from the *in situ* solidification curves are listed in **Table IV.4**.

Table IV.4 Solidification characteristics of Al-7Si alloys during the RPT. The given values are averaged from measurements taken during SC1, SC2, and SC3.

Parameter	Approximate Value
α-Al Start Time	~1 min 20 s
α-Al Solidification Time (Calculated from the average of the measurements from SC1, SC2, and SC3)	~2 min 40 s
Eutectic Start Time	~4 min 20 s
Total Solidification Time (to solidus temperature)	~8 min 30 s

The effect heating of the refractory cup holders on the temperature time solidification curves was also examined and is shown in **Figure IV.5**. As expected, heating the refractory cup holder reduces the cooling rate and extends the solidification time of the sample, which

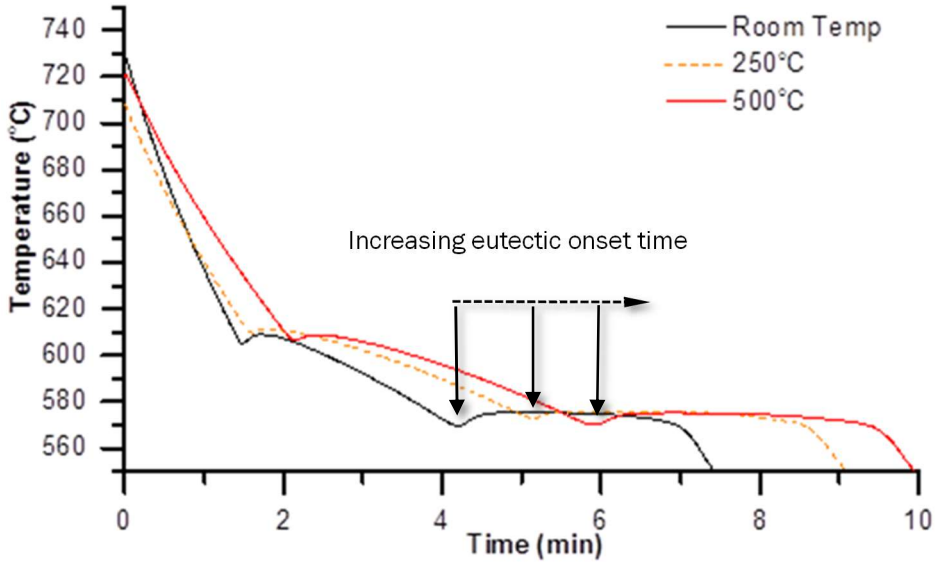

Figure IV.5 Temperature-time solidification curves cast with heated cup holders.

in turn prolongs the onset of eutectic solidification - which does not begin until approximately 6 minutes when the cup holder is heated to 500°C.

IV.1.5 Solid Fraction Calculations

Scheil solidification calculations were performed using the thermodynamic software package (NPL) MTDATA [23] (using the MTAL database v6.1) to estimate the solid fraction as a function of temperature (Figure IV.6). They indicate that just prior to the onset of eutectic solidification, the solid fraction of primary α-Al in Al-7Si alloys is approximately 50%. The solid formed at this stage is highly dendritic in nature (as is shown in the example micrograph in Figure IV.10). The presence of these dendrites confers strength to the solidifying semi-solid, and it may be that 50% solid fraction is the threshold required to develop enough strength in the dendritic network to retain the pores in the solidifying RPT samples after termination of the vacuum. Therefore, in order to elucidate whether the onset of eutectic solidification or the development of a mechanically strong dendritic network was

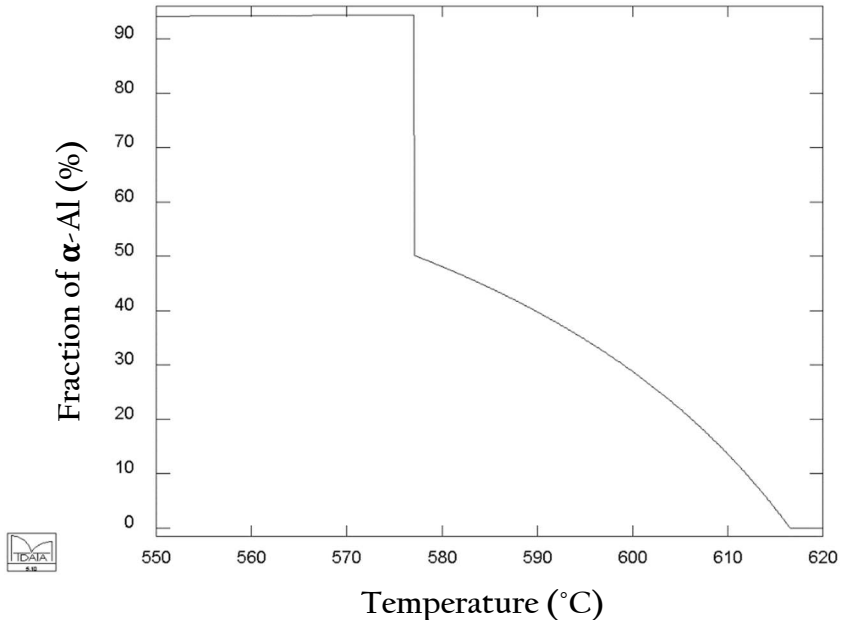

Figure IV.6 – Fraction of α-Al vs temperature in Al-7Si alloys based on Scheil-solidification calculations using MTData.

responsible for retention of the porosity, further ancillary studies were conducted using an Al-3Si alloy, the results of which are presented in the following section.

IV.1.6 Ancillary Studies using an Al-3Si Alloy

Ancillary studies were conducted using a binary Al-3Si alloy – this was the only time a non-Al-7Si alloy was used in the work presented in this thesis – to elucidate the effect of eutectic solidification and solid fraction on the retention of porosity at the termination of the vacuum during the RPT. This alloy was selected as it underwent eutectic solidification after a larger amount of primary α-Al forms. The Scheil-solidification calculation in Figure **IV.7** indicates that the solid fraction of this phase just prior to eutectic solidification in Al-3Si alloys is ~86%. Based on the cooling curve of this alloy shown in Figure **IV.8**, this occurs at approximately 5 minutes and 40 seconds into the RPT. In comparison, a 50% fraction of solid is reached at approximately 3 minutes and 20 seconds.

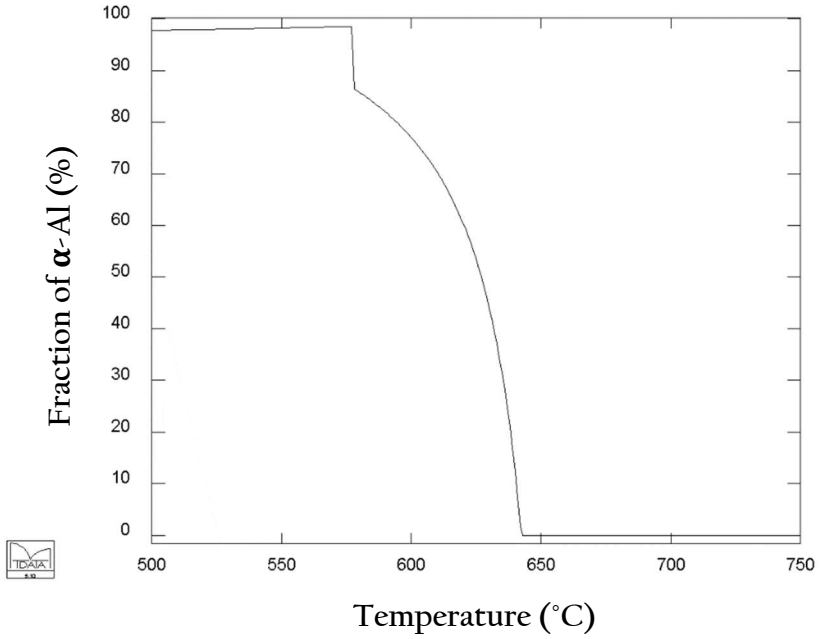

Figure IV.7 Scheil solidification calculation of the solid fraction of α-Al in Al-3Si

The volume fraction of retained porosity versus the duration of the RPT in Figure **IV.8** shows that the fraction of retained porosity in the RPT samples spikes between 5 and 6 minutes, which again, according to the temperature-time curve, corresponds to the onset of eutectic solidification in the same way that it does in the Al-7Si alloys. This supports the

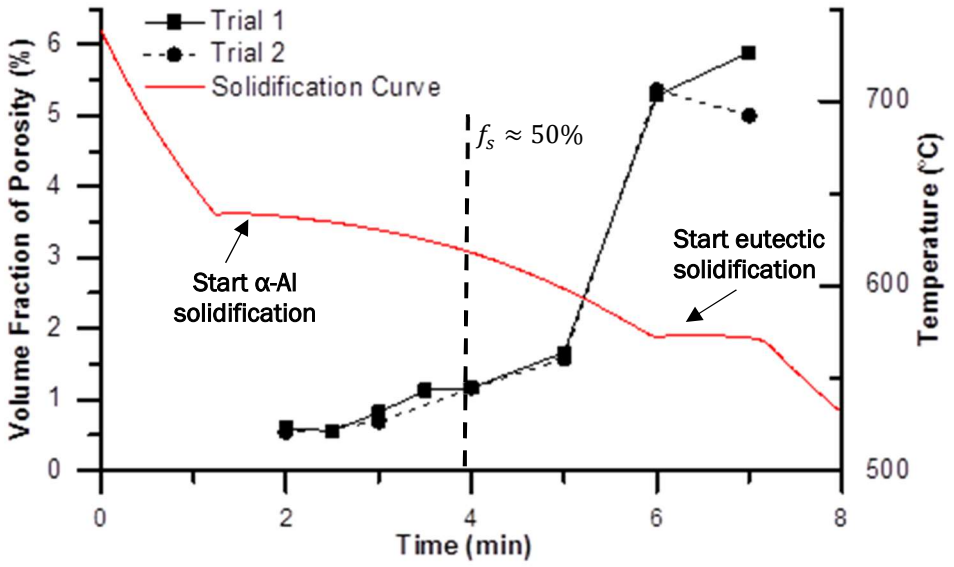

Figure IV.8 RPT duration versus fraction of retained porosity in the RPT samples, and *in situ* temperature-time solidification curves using Al-3Si alloys (VD4 and SC4).

notion that the onset of eutectic solidification is responsible for retaining the porosity after the termination of the RPT rather than the effect of solid fraction.

IV.1.7 Metallographic Analysis

Metallographic analysis was performed on micro- and macro- scales in order to investigate the structure of pores and the surrounding phases.

IV.1.7.1 Micro-Analysis

Pore Structure

Micrographs from the microstructural analysis by light (optical) microscopy of samples solidified under 4 minutes, 5 minutes, and 9 minutes of vacuum duration in experiment VD2 are presented in Figure **IV.9**. Figure **IV.9** a) shows a gas pore in the sample solidified with a 4 minute RPT duration, which is highly spherical and surrounded largely by eutectic. In the sample solidified after 5 minutes of RPT duration, a large number gas pores as well as interdendritic pores (Figure **IV.9** b)) were observed. In the sample solidified after 9 minutes of RPT duration, these small interdendritic pores are much few in number, and the larger gas pores tend to be contoured by dendrites.

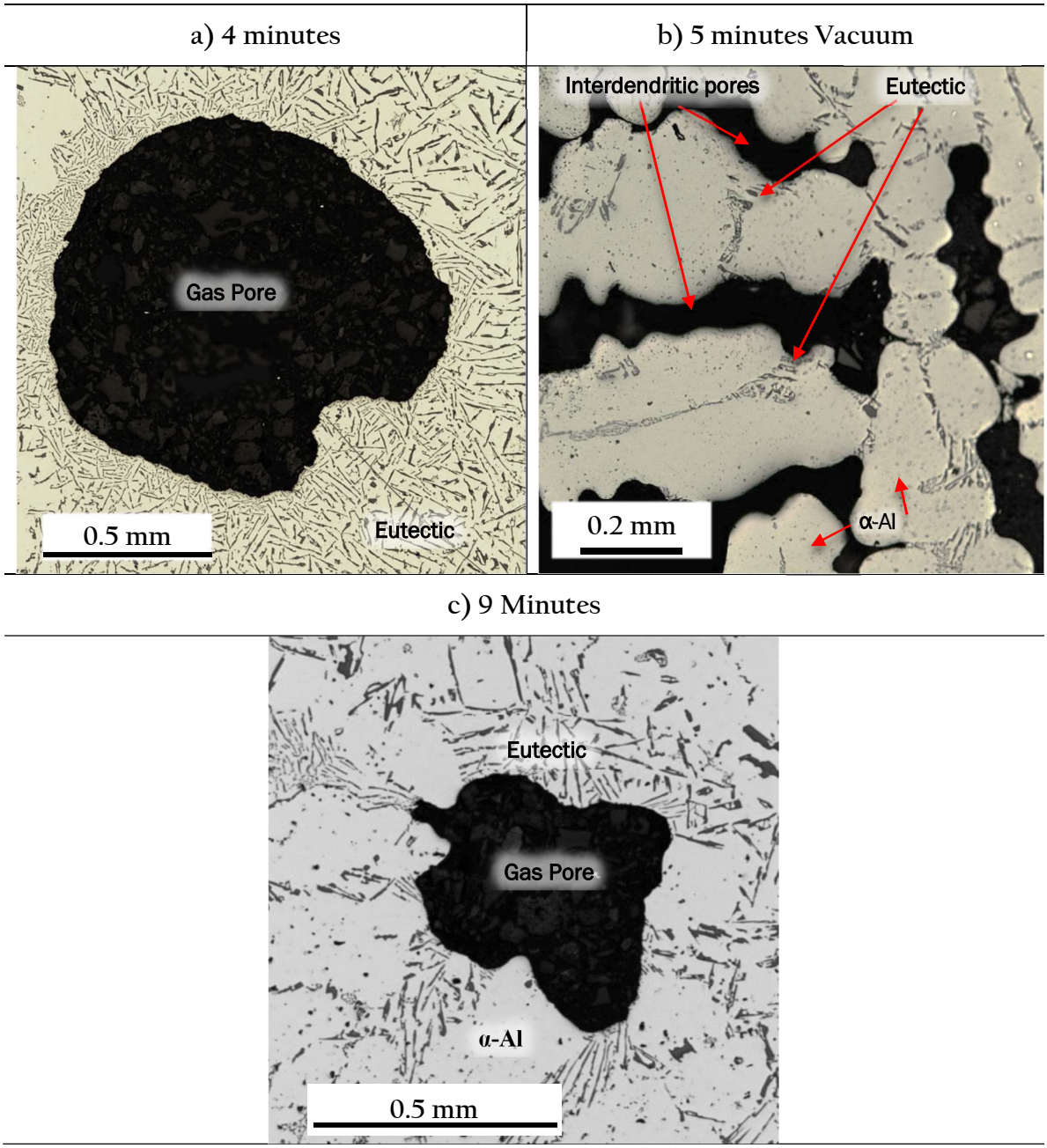

Figure IV.9 Micrographs of porosity inside RPT samples cast with different RPT durations.

Secondary Dendrite Arm Spacing & Local Cooling Rate

The cooling rate through the thickness of the RPTs was estimated by analysing the secondary dendrite arm spacing (λ_2) [24], [25]. Analysis was conducted along the mid-planes of selected RPT samples, 20 mm from the base of the sample, the same height where

the thermocouple was placed when taking the solidification curves. A minimum of 10 measurements were taken from at least 4 micro-graphs for each position, and λ_2 was calculated using [26]:

$$\lambda_2 = \frac{L}{N-1}$$

Where L is the measured length, perpendicular to the secondary dendrite arms, and *N* is the number of arms.

As shown in Figure **IV.11**, the SDAS in the samples was relatively constant at an average of 64±21 µm throughout the sample, indicating that the local cooling rate is approximately constant over the radius of the sample.

The cooling rate can be calculated from the the SDAS, λ_2, by [24], [27]:

$$\lambda_2 = A(t_{sl})^n \qquad \text{(IV.1)}$$

The coefficient *A* is dependent on the Si content, and can be calculated as 13.2 for Al-7Si alloys by linear regression of the data given by Bamberger et al. [27] as shown in **Figure IV.12**. t_{SL} is the local solidification time, which was calculated as 173 seconds, from the average α-Al solidification times in the solidification curves. The exponent *n* has been reported to range between 0.3 to 0.5 [24], [27], [28] reported for the SDAS in Al-Si alloys [29]. Using the values of *A* and t_f in equation IV.1, it was calculated that in this work *n*=0.31, which falls at the lower end of the reported range.

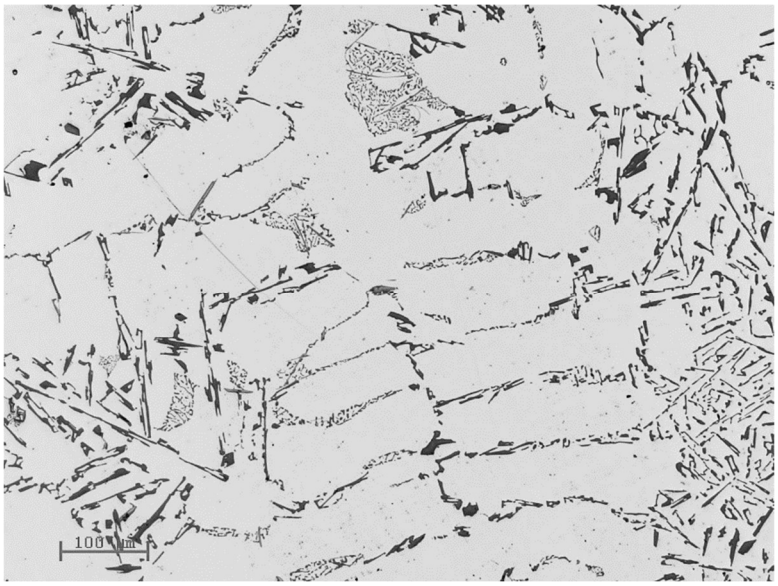

Figure IV.10 Typical micrograph used for analysis of the SDAS.of pores.

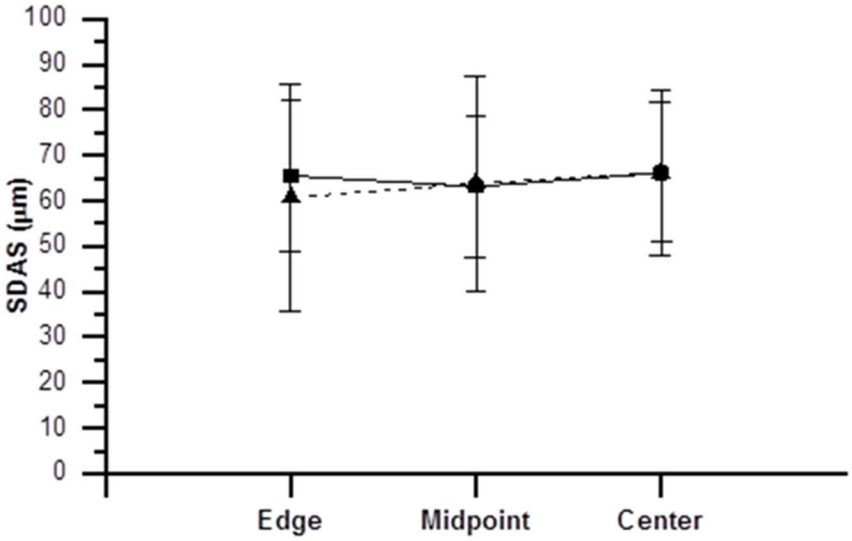

Figure IV.11 SDAS measured by metallographic analysis of micrographs. The error bars represent the spread in the measured values.

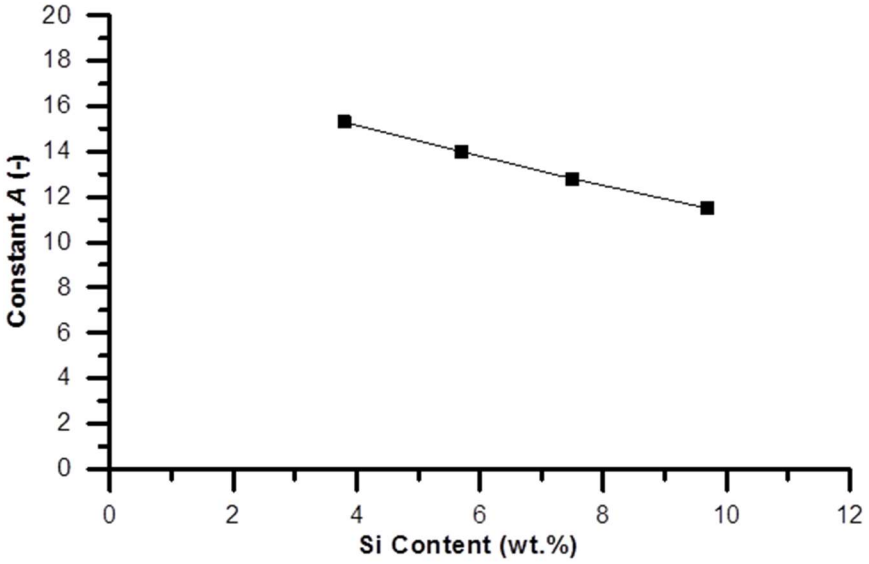

Figure IV.12 – Relationship between *A* and Si content in Al-Si alloys using the data from [27].

IV.1.7.2 Macro-Analysis

A comparison of metallographic images of cross-sectioned RPT samples solidified under 4, 5, and 9 minutes of RPT duration are shown in Figure **IV.13**. The structure of the porosity in these images is reminiscent of that of the samples shown in Figure **IV.1**.

In the sample cast with a 4 minute RPT duration (Figure **IV.13** a)), the pores are on average smaller in diameter, more spherical in shape, and fewer in number than the sample solidified under 5 (Figure **IV.13** b))minutes of RPT duration. Qualitatively, there seems to be very little difference between the structure of pores in the samples cast with 5 minute and 9-minute (Figure **IV.13** c)) RPT durations.

Finally, by comparing Figure **IV.13** a) and d) it can be seen the pores in the sample solidified with a 4 minutes RPT duration has fewer, but much larger and prominent pores than its equivalent APT sample.

a) 4 minutes	b) 5 minutes
	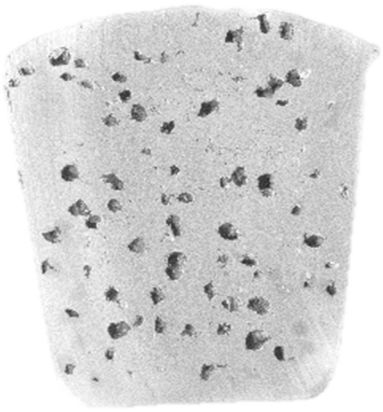
c) 9 minutes	**d) APT paired with a)**
	

Figure IV.13 Metallographic Sections of RPT samples from experiment VD2-Trial 2 solidified with different vacuum durations.

Image analysis was performed on the metallographic cross-sections of RPT samples from VD2 to quantify the effect of the RPT duration on the structure of porosity inside the sample, the results of which are shown in **Figure IV.14**. **Figure IV.14** a) shows that the pore number density (PND) follows a similar trend, but it shows a spike in the samples solidified under 5 minutes of vacuum. This spike reflects numerous small pores that were observed in the

micro-analysis (Figure **IV.9** b)). Including only pores with an equivalent circular diameter (d_{eq}) >0.5mm in the analysis shows a steady incline and plateau in the pore number density. These trends are somewhat further reflected in **Figure IV.14** b) which shows the average equivalent pore diameter, d_{eq}, where there is a slight depression at 5 minutes, due to the presence of the small pores in the sample, though this is less evident than the spike in PND. Finally, **Figure IV.14** c) shows the average area weighted shape factor of the pores decreases with increasing RPT duration. Prior to 5 minutes, pores are more spherical in shape, especially large pores. There is a downward perturbation in pore sphericity at 5 minutes vacuum duration, which is due to the formation of interdendritic shrinkage pores, and the formation of numerous interdendritic tendrils at the edges of large gas pores.

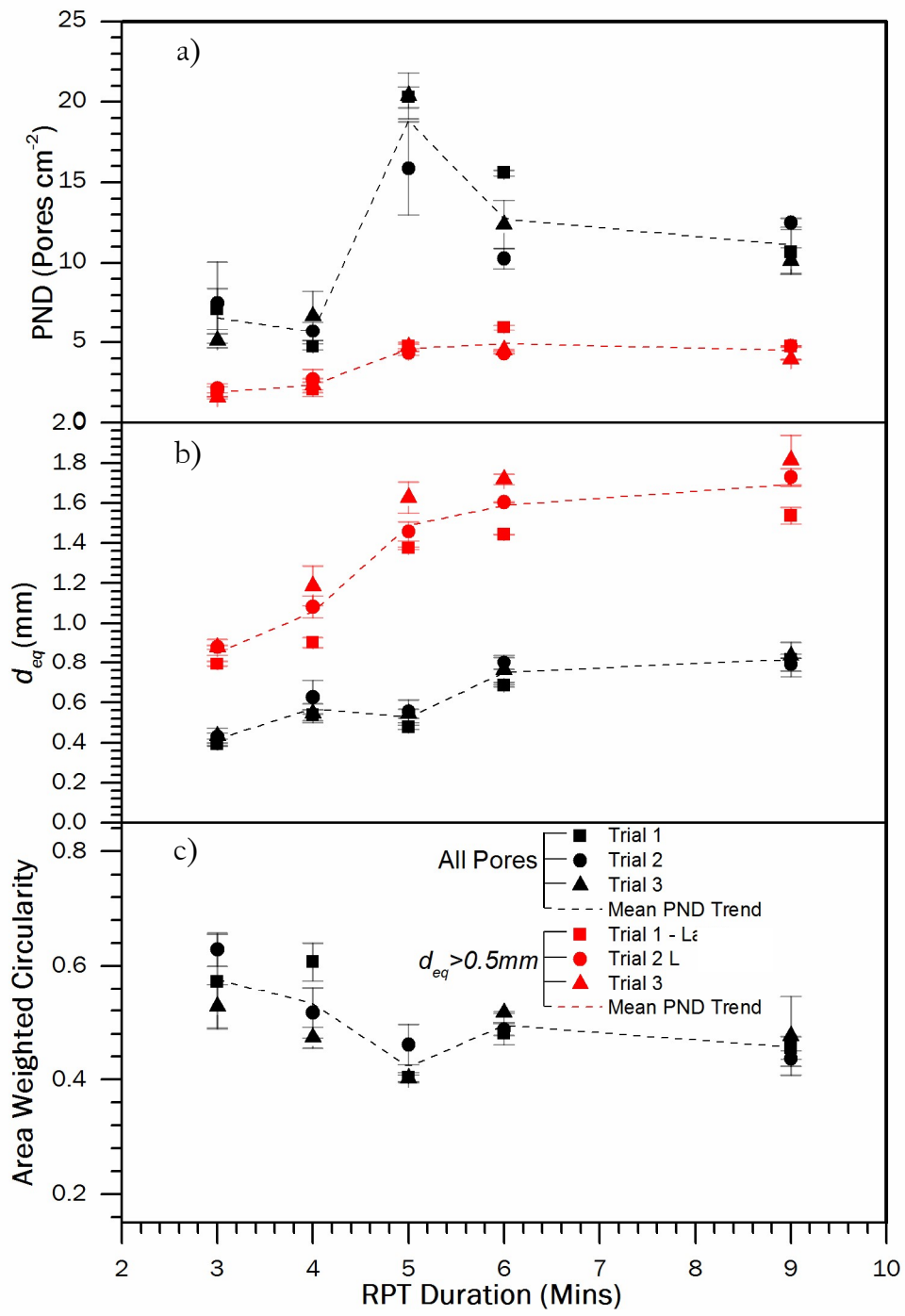

Figure IV.14 – Quantitative metallographic image analysis of porosity in RPT samples cast during experiment VD2 showing the variation of a) pore number density (PND), b) equivalent circular diameter (d_{eq}), and c) area weighted circularity (shape factor) of gas pores with the RPT duration.

IV.1.8 Discussion

IV.1.8.1 Porosity Retention in Semi-Solid Alloys

The results showed that bubbles form early on during solidification in the RPT – at least in alloys containing relatively high amounts of hydrogen; however, the amount of porosity that is retained in the solidified RPT sample depends on the phases that present in the semi-solid alloy at the point at which the test is terminated.

Termination of the partial vacuum that is applied to the solidifying metal during the RPT is equivalent to applying an overpressure, or load to it. For the applied vacuum of 80 mBar, which was used here, the applied overpressure is equivalent to ~93 kPa (nearly 1 atm). In fully molten alloys, the overpressure is transferred through the liquid and to the suspended bubbles, which in turn forces them to collapse down to 8% their 'atmospheric' size. Whereas, in fully solidified alloys, which may easily support this pressure through the bulk metal, which prevents the collapse of the pores..

In the semi-solid material, the application of pressure has a combination of effects, which are microstructure dependent, which act together to alter the structure porosity that is formed in the RPT samples, and ultimately governing the result of the RPT. When overpressure is applied to the semi solid material, it is transferred through the solid, liquid, and the gas bubbles. In response the gas bubbles again collapse down, though the degree to which this occurs depends on the amount of pressure that is transferred to them, as some of the pressure is taken up by the dendritic skeleton of the semi-solid material. Concurrent with this, the pressure also squeezes the liquid through the interdendritic channels – in a process known as *interdendritic feeding* [30], [31] – to fill the volume left by the collapsed pores.

The ability of a semi-solid alloy to bear load is dependent on its solid fraction and the interaction of its dendrites [32], [33]. At low solid fractions, before the dendrites have impinged on each other, the semi-solid material has no strength and the dendritic slurry may still easily flow to fill the volume left by the collapsed pores by *mass feeding* [31]. At higher solid fractions where the dendrites begin to impinge and interlock with each other (starting at a solid fraction known as the dendrite coherency point (f_{coh})) the material begins to develop some strength and semi-solid material ceases to flow, though the dendrites may still rearrange under load [32]. It is likely that it is at the dendrite coherency point that the surface of the sample begins to 'balloon' or 'mushroom', as the growing bubbles may lift up the dendritic skeleton with their expansion. If overpressure is applied to the sample at this point, the dendrites rearrange – at least partially – which collapses the bubbles down, and squeezes the liquid to fill the freed up volume around them. These areas of solute rich liquid go on to be the last to solidify, which explains why some pores are entirely surrounded by eutectic phase (**Figure IV.9**). Also, because the bubbles are surrounded by liquid at this stage, they are able to take on a spherical shape (**Figure IV.14**).

The amount of pressure that is transferred to the bubbles, which governs the degree to which they collapse, depends on the solid fraction of the material at the time of overpressure application. **Figure IV.4** showed that increasing volumes of porosity are retained in the alloys with increasing RPT duration, which is due to directly corresponds to increase in the solid fraction.

As mentioned above, strength develops continuously after the $f_{coh.}$ In unrefined Al-7Si alloys this has been reported to occur at a solid fraction of 0.16 for Al-Si alloys of various compositions [34], though this would likely vary with the grain size and structure [35]. A

further increase in alloy strength is expected at the dendrite maximum packing solid fraction, f_{spk},, the point where the dendrites are heavily interlocked and cannot rotate to rearrange anymore, and the dendrite arms must be broken for deformation to occur [32]. f_{spk} has been shown to occur at 0.35 and 0.4 in Al-7Si-1Cu and Al-7Si-4Cu alloys, respectively, which develop highly dendritic microstructures [32], [36]. Even in Al-4Cu alloys with highly globular structures, f_{spk} occurred at 0.6 [32]. At this point, one might expect to see no change in the volume of porosity after this point. However the results of the RPT duration tests using Al-3Si alloys in **Figure IV.6** indicate the contrary. The f_p gradually increased up until eutectic solidification, at a solid fraction of 0.85, at which point it spiked. It is only after the onset of eutectic solidification that the pores are retained at their 'reduced pressure' size. Given that hypoeutectic Al-Si alloys normally solidify with a dendritic microstructure, a solid fraction of 0.85 is well beyond the expected point of f_{spk}. This probably because even at f_{spk} the dendritic skeleton material is not strong enough to prevent the collapse under ~93kPa of applied pressure – though it does prevent some, hence the increasing volume of porosity with RPT duration prior to the onset of eutectic solidification.

It is only at the onset of eutectic solidification that the movement of interdendritic liquid in the solidifying materials is arrested. During eutectic solidification Al-Si alloys form α-Al and β-Si platelets, which have coherent and incoherent interfaces with the α-Al dendrites, respectively. The α-Al likely act as a kind of 'glue' between adjacent dendrites, whereas the latter mechanical impediments to the motion of dendrites, which act together to prevent deformation of the solid during pressure application. Dahle et al. [32] found that Al-Si-Cu alloys displayed a sharp increase in mechanical strength with the formation of the eutectic, to which they attributed to the coherency with the α-phase. In addition, and more

significantly, the formation of these phases occurs in the interdendritic canals, which shuts them off to interdendritic fluid flow. This combination means that when the vacuum of the RPT is terminated after the onset of eutectic solidification, there is a very strong resistance to the collapse and rearrangement of the bubbles in the material. This can be considered the point where the bubbles begin to be 'locked into' the solid as pores.

This process is not instantaneous, and engages gradually as eutectic solidification proceeds. **Figure IV.4** shows that eutectic solidification in the Al-7Si alloy lasts for approximately 4 min 10 s. It may be that early on during eutectic solidification, the semi-solid material is still able to slightly deform and partially collapse gas bubbles, and rearranging the remaining interdendritic liquid. This rearrangement of pores may explain the appearance of the interdendritic shrinkage type pores in the samples solidified with a 5 minute RPT duration (**Figure IV.9** & **Figure IV.14**). However, if this is the case, the collapse of pores after eutectic formation does not occur to an such an extent to appreciably influence the effect on the overall f_p, as indicated by the retained porosity versus RPT duration curves (**Figure IV.4** and **Figure IV.8**), though it is enough of an influence to change their 2D appearance on a metallographic plane as a number of small pores (**Figure IV.9** & **Figure IV.14**). Nevertheless, one might expect some detectable, albeit minor change in the measured retained porosity fraction.

IV.1.8.2 Reproducibility of the RPT & Parameter Selection

The original and primary aim of this area of experimental work was to elucidate the cause of the spurious results that were frequently attained in the early experiments of this project, in order to select RPT parameters to improve test reproducibility. This was successfully achieved.

The results show that the porosity that is formed in RPT samples is determined by the point at which the vacuum is terminated during solidification. **Figure IV.4** and **Figure IV.8** demonstrate that the RPT duration should be no shorter than the beginning of eutectic solidification in order for pores of significant size to form, and ideally no less than 6 minutes to prevent pore rearrangement – though this likely would continue to occur to some extent until the material was fully solid (~8 minutes).

The spurious results obtained in the early experiments (**Figure IV.1**) can be explained based on the premature termination of the RPT prior to the onset of eutectic solidification in combination with operator error. Originally, samples were cast using a 4 minute RPT duration, the standard setting for the RPT, and the melt sampled using a large iron spoon into cups heated on the RPT's on-board heater. Because of the comparatively large volume of the spoon compared to the small melt sample, if it was heated incompletely – and there was not initially a great deal of care attached to doing so – it would siphon a great amount of heat from the metal prior to pouring. This would therefore often cause the melt to be poured at a lower than intended temperature. This combination would allow the sample to cool sufficiently fast and enter the eutectic solidification regime just prior to vacuum termination. Small interdendritic pores were often observed in the Al-7Si alloys cast in these experiments – for example that presented in previous published work [37] (**Figure IV.15**) – which indicates that the vacuum was terminated soon after eutectic formation. However, when successive RPTs were taken, in rapid succession, the refractory cup holder and the apparatus itself became heated, the cooling rate decreased and the time taken before the onset of eutectic solidification in the sample was extended (**Figure IV.5**). As a result, the vacuum would then terminate prior to eutectic solidification which would cause a loss of

large amounts of porosity from the sample. Such a loss would constitute a spurious RPT result. It can be seen by comparing **Figure IV.1** and **Figure IV.13**, that the structure of the porosity in the spurious result is the same as in the sample from the experiments in this chapter that had its RPT vacuum terminated prior to the onset of eutectic solidification.

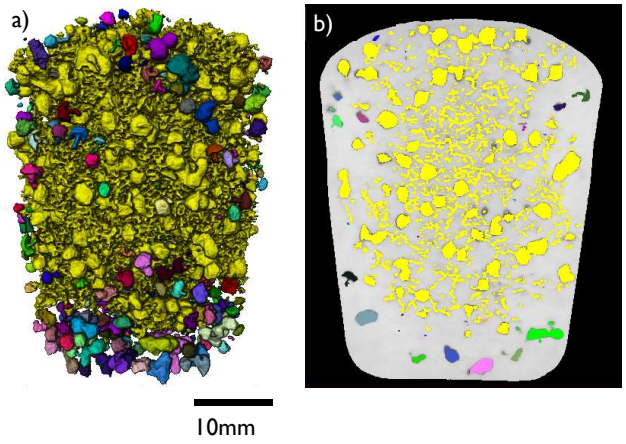

Figure IV.15 An example of extensive interdendritic porosity in an Al-7Si RPT sample shown as a) a 3D reconstruction, and b) a slice of macro-CT data. This formed as the result of the RPT vacuum soon after the onset of eutectic solidification. Adapted from [37].

In response to these findings, care was taken to control the heat of the refractory cup holder during subsequent experiments. To aid this a set of 8 cup holders of the same material were produced in house, and used cyclically throughout each experiment. Secondly, the RPT duration used in the subsequent experiments was extended to 9 minutes. Though the results do not explicitly indicate that this was necessary, it was not known whether handling of the semi-solid samples after the onset of eutectic solidification would have disturbed the internal porosity, and was therefore left undisturbed until fully solid. Indeed, this is because it is believed that the vacuum was terminated prior to 6 minutes, there may be some minor collapse and rearrangement of pores in the eutectic liquid. Finally, the melt samples were

taken by dipping the RPT cups into the melt, and holding them there for 30 seconds. This eliminated for spoon pouring, thus allowing better control of the initial melt temperatures.

References In The Appendices

[1] P. N. Anyalebechi, "Techniques for determination of the Hydrogen Content in Aluminium and its Alloys—a Review," *Cast Met.*, vol. 3, no. 4, pp. 182–201, Oct. 1990.

[2] J. B. Patel, J. Lazaro Nebredaand, and Z. Fan, "Efficient De-gassing of Aluminium Alloy Melts by High Shear Melt Conditioning Technology."

[3] A. M. Samuel and F. H. Samuel, "The reduced pressure test as a measuring," *Metall. Trans. A*, vol. 24, no. 8, pp. 1857–1868, 1993.

[4] D. E. J. Talbot, *The effects of hydrogen in aluminium and its alloys*, vol. 724. Maney Pub, 2004.

[5] LECO Corporation, *Inorganic Application Note: Determination of Hydrogen in Aluminum and Aluminum Alloys*. St. Joseph, M, M: LECO Corporation, 2003.

[6] D. Dispinar, "Determination of metal quality of aluminium and its alloys." University of Birmingham, 2006.

[7] ABB Inc., *AlScan Model "F" User's Manual*, 1st–5th ed. Quebec, Canada, Canada: ABB Inc., 2003.

[8] X.-G. Chen and S. Engler, "Measuring Hydrogen Content in Molten Aluminium Alloys using the CHAPEL Technique," *Cast Met.*, vol. 6, no. 2, pp. 99–108, Jul. 1993.

[9] J. Campbell and R. Harding, "TALAT Lecture 3202 The Liquid Metal," 1994.

[10] T. M. Gansemer, B. C. Reynolds, J. N. Hart, and D. C. Chesonis, "Improvement in Hydrogen Measurement Technique for Molten Aluminum," in *Light Metals 2007*, 2007, pp. 685–689.

[11] T. M. Gansemer and J. N. Hart, "Method and apparatus for measuring gas concentration levels in liquids." Google Patents, 08-Aug-2006.

[12] P. V Evans, P. G. Enright, and R. A. Ricks, "Molten Metal Cleanliness: Recent Developments to Improve Measurement Reliability - Light Metals 2018," 2018, pp. 839–846.

[13] P. Le Brun, "Melt Treatment — Evolution and Perspectives," in *Light Metals 2016*, J. F. Grandfield and D. G. Eskin, Eds. Cham: Springer International Publishing, 2016, pp. 59–64.

[14] C. Dupuis and R. Dumont, "The impact of LIMCA technology on the optimization of metal cleanliness," in *Essential Readings in Light Metals*, Springer, 2016, pp. 332–337.

[15] M. E. Schlesinger, *Aluminum recycling*. CRC Press, 2013.

[16] T. N. Ware, M. Cooksey, and M. J. Couper, "Measurement of the performance of in-line processes using LiMCA," in *7th Australian Asian Pacific Conference on Aluminium Cast*

House Technology, ed. PR Whiteley (Warrendale, PA: The Minerals, Metals & Materials Society, 2001), 2001, pp. 45–54.

[17] ABB Bomem, "AlSCAN Result Conversion ml/100g to ppm," *AlSCAN Engineering Bulletin No. 14*, Oct-1999.

[18] C. Dupuis, Z. Wang, J. P. Martin, and C. Allard, "An Analysis of Factors Affecting the Response of Hydrogen Determination Techniques for Aluminium Alloys," in *Light Metals*, 1992, pp. 1055–1067.

[19] D. Legland, I. Arganda-Carreras, and P. Andrey, "MorphoLibJ: integrated library and plugins for mathematical morphology with ImageJ," *Bioinformatics*, vol. 32, no. 22, pp. 3532–3534, Nov. 2016.

[20] R. Deriche, "Using Canny's criteria to derive a recursively implemented optimal edge detector," *Int. J. Comput. Vis.*, vol. 1, no. 2, pp. 167–187, 1987.

[21] G. Lehmann and D. Legland, "Efficient N-Dimensional surface estimation using Crofton formula and run-length encoding," *Effic. N-Dimensional Surf. Estim. using Croft. formula run-length encoding, Kitware INC*, 2012.

[22] G. K. Sigworth, E. M. Williams, and D. C. Chesonis, "Gas Fluxing of Molten Aluminum: An Overview BT - Essential Readings in Light Metals: Volume 3 Cast Shop for Aluminum Production," J. F. Grandfield and D. G. Eskin, Eds. Cham: Springer International Publishing, 2016, pp. 65–70.

[23] R. H. Davies, A. T. Dinsdale, J. A. Gisby, J. A. J. Robinson, and S. M. Martin, "MTDATA-thermodynamic and phase equilibrium software from the national physical laboratory," *Calphad*, vol. 26, no. 2, pp. 229–271, 2002.

[24] M. C. Flemings, "Solidification processing," *Metall. Trans.*, vol. 5, no. 10, pp. 2121–2134, 1974.

[25] M. D. Peres, C. A. Siqueira, and A. Garcia, "Macrostructural and microstructural development in Al–Si alloys directionally solidified under unsteady-state conditions," *J. Alloys Compd.*, vol. 381, no. 1–2, pp. 168–181, Nov. 2004.

[26] E. Vandersluis and C. Ravindran, "Comparison of Measurement Methods for Secondary Dendrite Arm Spacing," *Metallogr. Microstruct. Anal.*, vol. 6, no. 1, pp. 89–94, 2017.

[27] M. Bamberger, B. Z. Weiss, and M. M. Stupel, "Heat flow and dendritic arm spacing in chill-cast Al–Si alloys," *Mater. Sci. Technol.*, vol. 3, no. 1, pp. 49–56, 1987.

[28] K. P. Young and D. H. Kerkwood, "The dendrite arm spacings of aluminum-copper alloys solidified under steady-state conditions," *Metall. Trans. A*, vol. 6, no. 1, pp. 197–205, 1975.

[29] T. Okamoto and K. Kishitake, "Dendritic structure in unidirectionally solidified aluminum, tin, and zinc base binary alloys," *J. Cryst. Growth*, vol. 29, no. 2, pp. 137–146, Jun. 1975.

[30] T. S. Piwonka and M. C. Flemings, "Pore formation in solidification," *Aime Met Soc Trans*, vol. 236, no. 8, pp. 1157–1165, 1966.

[31] J. Campbell, *Complete casting handbook: metal casting processes, metallurgy, techniques and design*. Butterworth-Heinemann, 2015.

[32] A. K. Dahle *et al.*, "Relationship between tensile and shear strengths of the mushy zone in solidifying aluminum alloys," *Metall. Mater. Trans. A*, vol. 34, no. 1, pp. 105–113, 2003.

[33] N. L. M. Veldman, A. K. Dahle, D. H. StJohn, and L. Arnberg, "Dendrite coherency of Al-Si-Cu alloys," *Metall. Mater. Trans. A*, vol. 32, no. 1, pp. 147–155, 2001.

[34] R. Xu, H. Zheng, F. Guo, Y. Zhang, S. Ding, and X. Tian, "Effect of Silicon Concentration on the Dendrite Coherency Point in Al–Si Binary Alloys," *Trans. Indian Inst. Met.*, vol. 67, no. 1, pp. 95–100, 2014.

[35] G. Chai, L. BÄckerud, T. RØlland, and L. Arnberg, "Dendrite coherency during equiaxed solidification in binary aluminum alloys," *Metall. Mater. Trans. A*, vol. 26, no. 4, pp. 965–970, 1995.

[36] T. Sumitomo, D. H. StJohn, and T. Steinberg, "The shear behaviour of partially solidified Al–Si–Cu alloys," *Mater. Sci. Eng. A*, vol. 289, no. 1–2, pp. 18–29, 2000.

[37] J. Malisano, S. Kumar, C. Lui, and K. O'Reilly, "X-Ray Computed Tomography versus Metallography for Porosity Analysis in Aluminium RPT Castings," in *Proceedings of the 6th Decennial International Conferences on Solidification Processing*, 2017.